MAPPING SURFACE WATER IN COMPLEX AND HETEROGENEOUS ENVIRONMENTS USING REMOTE SENSING

TSITSI BANGIRA

Dissertation presented for the degree of Doctor of Philosophy in the Faculty of Science at Stellenbosch University

Promotor: Prof Adriaan van Niekerk

Co-Supervisor: Prof Massimo Menenti

Co-Supervisor: Dr Zoltán Verkedy

March 2019

DECLARATION

By submitting this research dissertation electronically, I declare that the entirety of the work contained therein is my own, original work, that I am the sole author thereof (save to the extent explicitly otherwise stated), that reproduction and publication thereof by Stellenbosch University will not infringe any third party rights and that I have not previously in its entirety or in part submitted it for obtaining any qualification.

With regard to Chapters 3, 4 and 5 the nature and scope of my contribution were as follows:

Chapter	Nature of contribution	Extent of contribution (%)
Chapter 2	This chapter is being prepared as a review article for submission to a scientific journal. The preliminary title is: The trade-offs between resolution, techniques and environmental complexity for mapping land surface water using earth observation data: A review. The chapter was written by me, with some inputs from my supervisors.	T. Bangira 90% M. Menenti 2% Z. Vekerdy 2% A.van Niekerk 6%
Chapter 3	This chapter was published as a journal article (Bangira T, Alfieri S, Menenti M, Van Niekerk A & Vekerdy Z 2017. A Spectral Unmixing Method with Ensemble Estimation of Endmembers: Application to Flood Mapping in the Caprivi Floodplain. Remote Sensing 9: 1013) and was co-authored by my supervisors who helped in the conceptualisation and writing of the manuscript. S. M. Alfieri helped with coding. I carried out the literature review, data collection and analysis components and produced the first draft of the manuscript.	T. Bangira 75% M. Menenti 10% S.M. Alfieri 10% Z. Vekerdy 2% A.van Niekerk 3%
Chapter 4	This chapter will be submitted for publication as a journal article (Bangira T, Iannini L, Menenti M, Van Niekerk A & Vekerdy Z 2018. Flood extent mapping within the Caprivi floodplain using Sentinel-1 time series analysis) and was co-authored by my supervisor who helped in the conceptualisation and writing of the manuscript. L. Iannini helped with coding and development of the model. I carried out the literature review, data collection and analysis and produced the first draft of the manuscript.	T. Bangira 80% M. Menenti 6% L. Iannini 10% Z. Vekerdy 1% A. van Niekerk 3%
Chapter 5	This chapter is under review (Bangira T, Van Niekerk A, Menenti M & Alfieri S 2018. Comparing thresholding with machine learning classifiers for mapping complex water bodies. Remote Sensing) and was co-authored by my supervisors who helped in the conceptualisation and writing of the manuscript. S. M. Alfieri helped with coding. I carried out the literature review, data collection and analysis components and produced the first draft of the manuscript.	T. Bangira 85% M. Menenti 3% S.M. Alfieri 2% A. van Niekerk 15%

Signature of candidate: Declaration with signature in possession of candidate

Signature of supervisor: Declaration with signature in possession of Supervisor

Date:

SUMMARY

Global climate change characterised by rising temperatures and changes in the magnitude and intensity of precipitation is projected to affect the spatial and temporal distribution of land surface water (LSW) resources. Accurate and reliable information on the dynamics of LSW is valuable in understanding and monitoring the occurrence and impacts of floods and droughts. This knowledge is also critical for appropriate planning and impact assessment. Research has showed that droughts and floods are the two major hydrological disasters in developing countries such as southern Africa. This is mainly due to the lack of accurate and robust methods and reliable data sources necessary for monitoring the spatial and temporal dynamics of LSW resources. Satellite remote sensing (RS) technology is a promising primary data source and provides techniques suitable for repeated mapping water bodies and flood plains. However, many flood plains and water bodies are characterised by the presence of submerged vegetation, dissolved and suspended substances. These characteristics limit the application of RS in monitoring LSW resources.

This study evaluated the potential of remotely sensed data with different temporal, spatial and radiometric properties to map LSW in such challenging environments. Three experiments were carried out. The first experiment evaluated a new spectral indices-based unmixing algorithm that uses a minimum number of spectral bands. The algorithm was applied to Medium Resolution Imaging Spectrometer Full Resolution (MERIS FR) imagery to map open water and partly submerged vegetation. MERIS FR imagery has high (three days) temporal, but low (300 m) spatial resolution. The quality of the flood map derived from MERIS data was compared to high (30 m) spatial, but low (16 day) temporal resolution Landsat Thematic Mapper (TM) images on two different flooding dates (17 April 2008 and 22 May 2009). The findings show that, despite the low resolution of MERIS, both the spatial and frequency distribution of the water fraction extracted from the MERIS data were in good agreement with the high-resolution TM retrievals. This suggests that the proposed technique can be used to produce reliable and frequent flood maps using low spatial resolution imagery.

The use of synthetic aperture radar (SAR) has become increasingly relevant for mapping and monitoring flooded vegetation (FV). In a second experiment, a procedure was constructed and validated based on a time series of Sentinel-1 SAR data for mapping floods in a vegetated floodplain. For each newly available image, the probability of temporary flooded conditions is tested against the probability of not-flooded conditions. The changes in land cover characteristics are considered by the technique. The modelling and testing components were applied

independently to the vertical transmit and horizontal receive (VH) polarisation, vertical transmit and vertical receive (VV) and VH/VV ratio. The resulting flood maps were compared to those obtained from Landsat-8 Operational Land Imager (OLI) and ground truthing. Overall classification accuracies showed that the maps produced from the fused Sentinel-1 products (VH and VH/VV) were most accurate (84.5%) and significantly better than when only the VH polarisation was used (78.7%). These results demonstrate that the fusion of VH/VV and VV polarisations can improve flood mapping in vegetated floodplains.

The third experiment involved using automatic thresholding of near-concurrent normalized difference water index (NDWI) (generated from Sentinel-2) and VH backscatter bands (generated from Sentinel-1) to map waterbodies with diverse spectral and spatial characteristics. The resulting maps were compared to the classification performances of five machine learning algorithms (MLAs), namely decision tree (DT), k-nearest neighbour (k-NN), random forest (RF), and two implementations of the support vector machine (SVM). The results show that the combination of multispectral indices with SAR data is highly beneficial for classifying complex waterbodies and that the proposed thresholding approach classified waterbodies with an overall classification accuracy of 89.3%. However, the varying concentrations of suspended sediments (turbidity), dissolved particles and aquatic plants negatively affected the classification accuracies of the proposed method, whereas the MLAs (SVM in particular) were less sensitive to such variations.

The LSW maps and techniques developed in this study are critical for flood status monitoring, water resources planning and disaster management, and will as such reduce the impact of floods and droughts on vulnerable communities living in southern Africa. Furthermore, the results of this study will hopefully inspire the remote sensing community to make use of the new generation of freely available multispectral and SAR data (such as those provided by the Sentinel constellations) for operational drought and flood monitoring.

KEYWORDS

Remote sensing, land surface water mapping, turbid, eutrophic, heterogeneous, thresholding, machine learning, spectral unmixing, time series, SAR, multispectral imagery

OPSOMMING

Globale klimaatsverandering gekenmerk deur stygende temperature en veranderinge in die grootte en intensiteit van presipitasie word geprojekteer om die ruimtelike en temporale verspreiding van hulpbronne vir grondoppervlakwater (GOW) te beïnvloed. Akkurate en betroubare inligting oor die dinamika van GOW is nuttig om die voorkoms en impak van vloede en droogtes te verstaan en te monitor. Hierdie kennis is ook van kritieke belang vir toepaslike beplanning en impakbepaling. Navorsing het getoon dat droogtes en vloede die twee grootste hidrologiese rampe in ontwikkelende lande, soos Suider-Afrika, is. Dit is hoofsaaklik te wyte aan die gebrek aan akkurate en robuuste metodes, tesame met ‘n tekort aan betroubare databronne wat vir die monitering van die ruimtelike en temporale dinamika van GOW-hulpbronne benodig word. Satelliet afstandswaarneming (AW)-tegnologie is 'n belowende primêre databron en bied tegnieke wat vir herhaalde kartering van waterliggame en vloedvlaktes geskik is. Baie vloedvlaktes en waterliggame word egter deur die teenwoordigheid van ondergedompelde plantegroei en opgeloste en gesuspendeerde stowwe gekenmerk. Hierdie eienskappe beperk die toepassing van AW in die monitering van GOW-hulpbronne.

Hierdie studie het die potensiaal van afstandswaarnemingdata met verskillende tydelike, ruimtelike en radiometriese eienskappe geevalueer om GOW in sodanige uitdagende omgewings te karteer. Drie eksperimente is uitgevoer. Die eerste eksperiment het 'n nuwe spektrum indeks-gebaseerde ontmenging-algoritme geëvalueer wat gebruik maak van 'n minimum aantal spektrale bande. Die algoritme is toegepas op Medium-Resolusie Beeldvormende Spektrometer Volle Resolusie (MERBS VR) beeldmateriaal om oop water en plante wat gedeeltelik gedompel is te karteer. MERBS VR beeldmateriaal het 'n hoë (drie dae) temporale resolusie, maar 'n lae (300 m) ruimtelike resolusie. Die kwaliteit van die vloedkaart wat afgelei is van die MERBS-data is teen hoë (30 m) ruimtelike resolusie, maar lae (16 dae) temporale Landsat Tematiese Karteerder (TK) beelde van twee verskillende datums (17 April 2008 en 22 Mei 2009) waartydens oorstromings plaasgevind het, geëvalueer. Die bevindings toon dat, ten spyte van die lae resolusie van MERBS, beide die ruimtelike en frekwensieverspreiding van die waterfraksie wat vanuit die MERBS-data verkry is goed ooreengestem het met die hoë-resolusie TK-herwinnings. Dit dui daarop dat die voorgestelde tegniek gebruik kan word om betroubare en gereelde vloedkaarte te produseer deur van lae-ruimtelike-resolusie-beelde gebruik te maak.

Die gebruik van sintetiese diafragma-radar (SDR) het toenemend relevant vir die kartering en monitering van oorstroomde plantegroei (OP) geword. In 'n tweede eksperiment is ’n prosedure, gebaseer op 'n tydreeks van Sentinel-1 SDR-data, vir die kartering van oorstromings in 'n

vloedvlakte met plante ontwikkel en gevalideer. Vir elke nuwe beskikbare beeld word die waarskynlikheid van tydelik-oorstroomde toestande getoets teen die waarskynlikheid van nie-oorstroomde toestande. Veranderinge in grondbedekkingseienskappe word deur die tegniek oorweeg. Die modellering- en toetskomponente is onafhanklik op die vertikale transmissie en horisontale ontvangs (VH), vertikale transmissie en vertikale ontvangs (VV) en VH/VV verhouding polarisasies toegepas. Die resulterende vloedkaarte is met dié van Landsat-8 Operasionele-grondbeelder (OGB) en grondslag-getrouheid vergelyk. Algehele klassifikasie-akkuraatheid het getoon dat die kaarte wat uit die aaneengesmelte Sentinel-1 produkte (VH en VH/VV) vervaardig is, die akkuraatste (84,5%) was en aansienlik beter was as wanneer slegs die VH polarisasie gebruik is (78,7%). Hierdie resultate toon dat die samesmelting van VH/VV en VV-polarisasies die vloedkartering in beplante vloedvlaktes kan verbeter.

Die derde eksperiment het die gebruik van outomatiese drempelbepaling van naby-gelyktydig genormaliseerde verskil-natheid-indeks (GVNI) (gegenereer met Sentinel-2 beelde) en VH-terugverspreidingbande (gegenereer met Sentinel-1 data) behels om waterliggame met uiteenlopende spektrale en ruimtelike eienskappe te karteer. Die resulterende kaarte is vergelyk met die klassifikasieprestasies van vyf masjienleer-algoritmes (MLAs), naamlik besluitboom (BB), k-naaste buurman (k-NN), ewekansige woud (EW) en twee implementasies van die ondersteuningsvektormasjien (OVM). Die resultate toon dat die kombinasie van multispektrale indekse met SDR data uiters voordelig vir die klassifikasie van komplekse waterliggame is en dat die voorgestelde drempelbepalingbenadering waterliggame met 'n algehele klassifikasie-akkuraatheid van 89,3% geklassifiseer het. Die wisselende konsentrasies van gesuspendeerde sedimente (turbiditeit), opgeloste deeltjies en waterplante het egter die klassifikasie-akkuraatheid van die voorgestelde metode negatief beïnvloed, terwyl die MLAs (OVM in die besonder) minder sensitief vir sodanige variasies was.

Die GOW-kaarte en -tegnieke wat in hierdie studie ontwikkel is, is van kritieke belang vir vloedstatusmonitering, waterhulpbronbeplanning en rampbestuur en sal sodanig die impak van vloede en droogtes op kwesbare gemeenskappe in Suider-Afrika verminder. Daarbenewens sal die resultate van hierdie studie hopelik die afstandswaarneminggemeenskap inspireer om van die nuwe generasie, vrylik-beskikbare multispektrale en SDR-data gebruik te maak om operasionele droogte en vloede te monitor (soos die wat deur die Sentinel-konstellasies verskaf word).

TREFWOORDE

Afstandswaarneming, grondoppervlakwaterkartering, turbied, eutropies, hetereogenies, drempelbepaling, masjienleer, spektrale ontmenging, tydsreeks, SDR, multispektrale beeldmateriaal

ACKNOWLEDGEMENTS

I sincerely thank:

- Professor Adriaan van Niekerk, Professor Massimo Menenti and Dr Zoltán Vekerdy, my supervisors, for their guidance, support and suggestions.
- Sebbie, my husband, for his encouragement, tolerance and patience throughout this study.
- My sons (Sebastian and Christian), my mum, brothers and sisters for their unconditional support.
- The Graduate School, Stellenbosch University, for awarding me a scholarship for this study.
- European Space Agency (ESA) for funding this research under the Alcântara Initiative, which was facilitated by Delft University of Technology (The Netherlands) and Stellenbosch University (South Africa).
- ESA for providing MERIS, Sentinel-1 and Sentinel-2 data under the project ID C1F.3105.
- Dr Silvia Maria Alfieri and Dr Lorenzo Iannini (TU Delft University, the Netherlands) for the scientific and technical expertise and guidance shared with me throughout the entire period of study.
- Linguafix for editorial work on this dissertation.
- Friends and colleagues (Dr Timothy Dube, Nyasha Magadzire and 2015 Graduate School cohort) who walked with me throughout this project.

"With God nothing is impossible, and his mercies endure forever." Having been raised on a remote farm and village of Guruve, Zimbabwe, studying for a Doctorate was not on the agenda of my wishes neither in my dreams. Nevertheless, God has proven otherwise and awarded me with this overwhelming opportunity.

Thank you Lord for taking me this far!

CONTENTS

TABLES

FIGURES

ACRONYMS AND ABBREVIATIONS

AGRHYMET	Agro-meteorology and operational hydrology
ANN	Artificial neural networks
ATWT	À trous wavelet transform
AVHRR	Advanced very high resolution radiometer
AVIRIS	Airborne visible infrared imaging radiometer suite
AWEI	Automated water extraction index
CCI	Climate Change Initiative
CNES	Centre National d'Etudes Spatiales
CSA	Canadian Space Agency
DEM	Digital elevation model
DORIS	Doppler orbitography radiopositioning integrated by satellite
DSM	Digital surface model
DT	Decision tree
EMS	Electromagnetic spectrum
ENSO	El Niño southern oscillation
Envisat	Environmental satellite
EO	Earth observation
ERS	European remote sensing satellite
ERTS	Earth resources technology satellite
ES	Expert systems
ESA	European Space Agency

ETM	Enhanced thematic mapper
EVI	Enhanced vegetation index
FLAASH	Fast line-of-sight atmospheric analysis of spectral hypercubes
GCM	Global climate models
GEE	Google earth engine
GIS	Geographic information systems
GLCM	Grey level co-occurrence matrix
GLDV	Grey level difference vector
GMES	Global monitoring for environment and security
GPS	Global positioning system
GRD	Ground range detected
HH	Horizontal transmit and horizontal receive
HIS	Hue, saturation and intensity
HV	Horizontal transmit and vertical receive
IBSU	Index based spectral unmixing
InSAR	Interferometric synthetic aperture radar
ISODATA	Iterative self-organising data analysis
IW	Interferometric wide
JAXA	Japan Aerospace Exploration Agency
K-NN	K-nearest neighbour
LEDAPS	Landsat ecosystem disturbance adaptive processing system
LiDAR	Light detection and ranging

LST	Land surface temperature
LSU	Linear spectral unmixing
LSW	Land surface water
LSWI	Land surface water index
MERIS	Medium resolution imaging spectrometer
MIR	Mid-infrared radiation
MLA	Machine learning algorithms
MNDWI	Modified normalized difference wetness index
MSS	Multispectral scanner
MWR	Microwave radiometer
MWR	Microwave radiometer
NASA	National Aeronautics and Space Administration
NDMI	Normalised difference moisture index
NDVI	Normalised difference vegetation index
NDWI	Normalised difference wetness index
NESZ	Noise equivalent sigma zero
NIR	Near infrared
NRT	Near real-time
OLCI	Ocean and land colour instrument
OLI	Operational land imager
OSH	Optimal separating hyperplane
PALSAR	Phase Array type L-band SAR

PCA	Principal component analysis
PDBT	Polarisation difference brightness temperature
PDF	Probability density function
RADAR	Radio detection and ranging
RADARSAT	Radio detection and ranging satellite
RBF	Radial basis function
RF	Random forest
RGDP	Regional gross domestic product
ROI	Region of interest
SAR	Synthetic aperture radar
SAVI	Soil and vegetation index
SDGs	Sustainable development goals
SLICE	Supervised learning and image classification environment
SLSTR	Sea and land surface temperature radiometer
SNAP	Sentinel application platform
SPOT	Satellite positioning and tracking
SPSS	Statistical package for social sciences
SRAL	SAR altimeter
SU	Spectral unmixing
SVM	Support vector machine
SWIR	Short-wave infrared
TCWI	Tasselled cap wetness index

TM	Thematic mapper
TOA	Top of atmosphere
TRMM	Tropical rainfall measuring mission
TSS	Total suspended solids
UAV	Unmanned aircraft vehicle
USAID	United States agency for international development
UTM	Universal transverse Mercator
VV	Vertical transmission and vertical receiving
WRC	Water research commission
WRI	Water ratio index
WS	Wide swath mode

CHAPTER 1: INTRODUCTION

> "Man must rise above the Earth – to the top of the atmosphere and beyond – for only thus will he fully understand the world in which he lives" (Socrates, 500 BC).

Global climate change characterised by rising temperatures and changes in the magnitude and intensity of precipitation is projected to have significant positive or negative impacts on land surface water (LSW) resources (Kundzewicz et al. 2014; Mueller et al. 2016). LSW refers to permanent water bodies such as dams or reservoirs, but it can also include temporarily inundated areas (Martinis et al. 2015). Global climate models (GCMs) are projecting that many parts of the Earth will become either extremely wet or dry (Dosio & Panitz 2016; Mishra & Singh 2010). Mason & Goddard (2001) have argued that, although climate change is resulting in decreased precipitation in most parts of the world, it is also triggering extreme rainfall events that often lead to flooding and drought. These forecasts, coupled with growing populations, paint a bleak picture for future generations, especially for those in the developing world where resilience against climate change is relatively low.

Floods and droughts are among Earth's most destructive natural hazards (Mishra & Singh 2010; Teng et al. 2017). The impacts of these disasters is most devastating in river valleys and floodplains where large populations have settled to take advantage of its rich natural resources (e.g. freshwater, fertile soils, places of recreation, alluvial mineral resources, fishing opportunities). These areas have consequently become the world's most densely populated areas (Huang et al. 2008). Consequently, more than 11% of the global communities are living in flood-prone regions and about 1% are exposed to floods each year (Kundzewicz et al. 2014). There is a need to monitor flood extent and changes in small water bodies to improve resilience to floods and droughts respectively.

A number of recent researches have reported increases in floods and droughts globally (Aimar 2017; Ali et al. 2013; Borga et al. 2011; Desai et al. 2015), with some regions being affected more than others. Recently, the underlying climate oscillations of the El Niño Southern Oscillation (ENSO) had affected southern Africa, leading to significant changes in the timing and amount of precipitation received in the region (Gaughan et al. 2016). During the 2010 to 2011 El Niño period, above normal and below normal rainfall events were observed over large parts of southern Africa (Hoell et al. 2017a; Malherbe et al. 2016). Floods and droughts can lead to the displacement of living organisms, destruction of property and even loss of life (Long, Fatoyinbo & Policelli 2014). In January 2011, some stations in Mozambique reported daily

rainfall of above 200 mm, leading to more than 100 deaths and loss of shelter for more than 200 000 people (Manhique et al. 2015). Conversely, droughts have resulted in a depletion of managed freshwater. Water stored in small reservoirs are critical for food security in developing economies where water storage infrastructure is limited (Botai et al. 2017). The 2011 drought resulted in more than 200 deaths and afflicted about 10 million people in southern Africa (Winkler, Gessner & Hochschild 2017). Recently, the Western Cape Province of South Africa has been affected by the worst water shortage in 113 years (Botai et al. 2017), resulting in a dramatic decline in agriculture production, increases in food prices and implementation of water rationing.

Recognising the threat of droughts and floods, heads of states are putting in place international agreements that are designed to reduce and mitigate the impacts of extreme climatic events (Desai et al. 2015). For instance, the Sendai Framework for Disaster Risk Reduction 2015–2030 stipulates targets for the post-2015 development agenda. Many of these targets aim to substantially reduce the number of people affected by hydrological disasters, economic losses and damage to critical infrastructure (Kelman 2015). In this context, operational and cost-effective methods for mapping surface water dynamics, small water reservoirs and for monitoring extreme hydrological events are needed to improve resilience to floods and droughts. Prominent work has been done in Europe (Clement, Kilsby & Moore 2018), Asia (Pham-Duc, Prigent & Aires 2017) and China (Du et al. 2016; Yesou et al. 2016), but little has been done in other parts of the world. Although the Food Aid Organisation (FAO) and the United States Agency for International Development (USAID) have established early drought warning systems in Africa, such as (AGRHYMET) (Traore et al. 2014), the systems focuses on food security for the West African Sahel region. In particular, very little work on the monitoring of flood plains and small water bodies has been done in southern Africa despite the immediate need for monitoring floods and droughts in the region.

This chapter provides a critical perspective on using remote sensing to monitor extreme hydrological events arising from global climate change to improve flood and drought resilience. A short overview of existing work is given, and some research gaps are highlighted. This is followed by a formulation of the research problem, an aim statement and an outline of the study objectives. The chapter concludes with an overview of the research methodology applied in the research.

1.1 LAND SURFACE WATER (LSW) MAPPING

In essence, LSW mapping was defined as the activity of tracking the extent and dynamics of water on the Earth's surface, excluding soil moisture (Li et al. 2013). Note that the word "land" is included to separate it from ocean water. LSW mapping plays an important role in drought and flood monitoring, wetland observations, flood disaster assessment and inland water resources management (Feyisa et al. 2014; Li et al. 2013; Pierdicca et al. 2013). LSW can be mapped using conventional in situ techniques such as ground-based surveys, but such activities are laborious, time-consuming, expensive and sometimes difficult or impossible to carry out (Du et al. 2014). For instance, during flood events, water bodies are often inaccessible or dangerous to enter. Telemetric techniques, such as radio-transmitted gauges, are also often used to monitor water levels and flood extents (Fan et al. 2016; Momo et al. 2015). The information provided by these gauges is location-specific, and a dense network of stations is required to get a regional overview of LSW dynamics. Moreover, in southern Africa, most water bodies are ungauged, and the few gauges that are installed are often poorly maintained.

Remote sensing offers an alternative approach to in situ surveys and telemetry by consistently providing near real-time, cost-effective and reliable data at wide spatial coverage (Čotar, Oštir & Kokalj 2016; Du et al. 2016; Du et al. 2014). Satellite sensors can observe areas that are remote, inaccessible or dangerous to enter (Mueller et al. 2016). These sensors have the potential to perform frequent, regular measures and have the capability to characterise LSW in different regions of the electromagnetic (EM) spectrum. Although shorter wavelengths (optical and thermal) can be obscured by clouds, some sensors, such as radar, can operate in all seasons, any time of day and even in poor weather conditions.

1.2 REMOTE SENSING FOR LAND SURFACE WATER MAPPING: AN OVERVIEW

Campbell & Wynne (2011) defined remote sensing as the acquisition of information about the properties of a target without being in physical contact with it. The value of satellite remote sensing technology for LSW mapping was first recognised in the early 1970s when the images from NOAA AVHRR (1 km resolution) and Earth Resources Technology Satellite 1 (80 m resolution) were used for flood mapping in the Mississippi (Wiesnet, McGinnis & Pritchard 1974) and in south-western Iowa (Hallberg, Hoyer & Rango 1973) and River basins respectively. Early satellite images were of coarse spatial resolution, prohibitively expensive and affordable to only a few government and private institutions. Imagery became much more affordable with the

establishment of the USA`s Land Remote Sensing Policy Act of 1992 and the subsequent dramatic increase in the number of Earth observation (EO) satellites (Goward et al. 2001).

The concurrent improvements in computer hardware and software, especially in the ability of personal computers to handle large amounts of remotely sensed data, have made satellite data accessible to many users and applications. Today, satellite remote sensing technology is being used in a very wide variety of applications such as crop health analysis, precision agriculture, crop yield estimation, urban planning, land use and land cover mapping, and aids environmentalists in monitoring natural hazards (Chuvieco 2016). These applications, coupled with advances in aerospace and aeronautical technology, have given impetus to space agencies such as National Aeronautics and Space Administration (NASA), Canadian Space Agency (CSA), European Space Agency (ESA) and Centre National d'Etudes Spatiales (CNES) to launch satellites with higher spatial, temporal and spectral resolutions (Berger et al. 2012; Donlon et al. 2012). For instance, ESA initiated the Copernicus programme in 2014, which consisted of five Sentinel satellite missions, with each consisting of a pair of satellites (Manakos & Lavender 2014). The main aim of the Sentinel missions is to provide robust datasets with better spatial (10 m) and temporal (six days) resolution to manage and protect the environment and natural resources and ensure civil security (Gascon et al. 2014). Sentinel-1 is a polar-orbiting radar imaging mission carrying a C-band SAR sensor that is capable of observing the Earth under any weather conditions throughout the day (Geudtner et al. 2014). Sentinel-2 carries a multispectral, high-resolution optical sensor ideal for land and inland water monitoring (Gascon et al. 2014). Sentinel-3 is a multi-sensing platform carrying a Sea and Land Surface Temperature Radiometer (SLSTR); an Ocean and Land Colour Instrument (OLCI); a SAR Altimeter (SRAL); a Doppler Orbitography Radiopositioning Integrated by Satellite (DORIS) and MicroWave Radiometer (MWR) for ocean, atmospheric and land applications (Nieke et al. 2015). The Sentinel-4 and Sentinel-5 missions are committed to atmospheric monitoring services (Berger et al. 2012).

From the preceding overview of remote sensing, it should be clear that remotely sensed techniques have evolved to an extent that the reasonably quickly changing inundations (floods) can be monitored with satellite images. The following subsections provide more detail of multispectral and active microwave (SAR) sensors and the techniques used for mapping LSW.

1.2.1 Multispectral imagery for LSW mapping

Multispectral (optical) sensors capture the solar reflectance of the Earth's surface or atmosphere (Martinis et al. 2015). Multispectral images enable the extraction of physical water-related aspects such as turbidity, colour (Heege et al. 2014) and in transparent and shallow water areas, even water depth (Jay & Guillaume 2014). Examples of multispectral sensors used for LSW mapping are carried on, e.g., the Landsat-7, Landsat-8, Sentinel-2, SPOT-6 and SPOT-7 EO satellites.

Multispectral methods discriminate water from non-water features based on the notion that open water has a much higher visible reflectance than near infrared (NIR) reflectance. The spectral response of LSW is also contrasted with that of vegetation, which has a much higher reflectance in the NIR range of the EM spectrum (Huang et al. 2014). Most multispectral remote sensing techniques delineate LSW through general feature (land cover) mapping or feature extraction (Li et al. 2013). Land cover mapping often involves unsupervised or supervised image classification techniques. Unsupervised classification algorithms assign pixels to classes (clusters) based on statistics (Canty 2014). These techniques incorporate no prior knowledge of the characteristics of the themes (informational classes) being studied. ISODATA and K-means are the most used clustering algorithms for LSW mapping (Thomas et al. 2015). In the supervised classification approach, an operator uses known information (training samples) to specify pixel/object values (spectral signatures) to classify pixels/objects of unknown identity (Canty 2014). The training process greatly influences the outcome of supervised classification (Li et al. 2013). To attain a comprehensive characterisation of each class in the feature space, a broad training set is usually recommended (Foody & Mathur 2004). However, large sets of training samples are not usually achievable owing to the high costs in most cases associated with field surveys. Applications of popular supervised classification algorithms include: maximum likelihood (ML) (El-Magd & Tanton 2003), random forest (RF) (Breiman 2001), decision trees (DTs) (Davranche, Lefebvre & Poulin 2010; Giardino et al. 2010), artificial neural networks (ANNs) (Skakun 2012) and support vector machine (SVM) (Mountrakis, Im & Ogole 2011). The output of land cover mapping is usually a full cover ("wall-to-wall") thematic classification of all pixels/objects in the image, although in special cases pixels may remain unclassified.

Feature extraction methods produce a binary (two-class) output image that has only two possible values for each pixel/object, namely true or false (Canty 2014). These methods can be based on thresholding of single bands (Jain et al. 2005) or spectral indices (Du et al. 2016; Xu 2006). Due to their simplicity, low cost and performance, water indices are widely used for the identification

of surface water (Acharya et al. 2016). The most well-known water indices are the normalised difference wetness index (NDWI) (McFeeters 1996) and modified NDWI (MNDWI) (Xu 2006). NDWI juxtaposes the high reflectance of water in the green band with its low reflectance in the near infrared (NIR) band to maximise surface water identification, while the modified normalised difference water index (MNDWI) replaces NDWI's NIR band with a short-wave infrared (SWIR) band. Most studies that have adopted spectral indices for LSW mapping applied a range of thresholds to differentiate water from other land surface features. Identifying a threshold that produces the highest possible accuracy is a demanding and tedious assignment, as threshold values are unstable and vary with location and water characteristics (Feyisa et al. 2014).

Feature extraction and land cover classification methods can be combined to increase the accuracy of water extraction, especially in heterogeneous environments (Jiang et al. 2012; Sun et al. 2012). For instance, Sun et al. (2012) combined thresholding of spectral indices with maximum likelihood classification. Thresholding alone achieved a producer's accuracy of 92%, whereas the integrated method produced a higher (95%) producer's accuracy.

The use of multispectral data for LSW mapping has several limitations. Although LSW has lower reflectance in the visible and NIR wavelengths than other land covers, the reflectance ranges are relatively small (Marcus & Fonstad 2008). This often leads to confusion between water and other low NIR reflectance features, such as areas in shadow or dark man-made features. Water is a highly irregular target as its spectral properties differ as a function of depth, concentrations of chlorophyll, total suspended solids (TSS) and coloured dissolved organic matter (CDOM) (Pekel et al. 2016). According to Marcus & Fonstad (2008), the sun-target-sensor geometry can also negatively affect the use of multispectral imagery for LSW mapping as specular reflection can change the appearance of water, depending on the time of day and year. Certain sun-sensor angles can cause sun glint, resulting in the sensor-received radiance to be higher than the actual water-leaving radiance. This is particularly problematic for imagery acquired off-nadir (at an angle). Water turbidity, water depth, the sediment type and dissolved substances also affect how light is reflected by LSW (D'Andrimont, Marlier & Defourny 2017). Arguably, the greatest limitation of multispectral data for LSW mapping is its inability to provide meaningful information during overcast conditions (i.e. when the Earth's surface is obscured by clouds). This limitation is especially problematic during flood events when cloud cover is most prevalent. Moreover, multispectral sensors are unable to observe water under

closed vegetation canopies and are restricted to daytime use (when solar illumination is provided).

1.2.2 SAR data for LSW mapping

Radar sensors, such as the synthetic aperture radars (SAR), are active sensors that transmit microwaves with the ability to propagate through the atmosphere regardless of the weather or (natural) lighting conditions (Gstaiger et al. 2012). As such, SAR images can be generated during overcast periods and at night. Microwaves at certain frequencies and polarisations also can penetrate vegetation canopies (Plank et al. 2017). Examples of popular satellites with SAR sensors on board that are suitable for LSW mapping are Sentinel-1, ALOS-PALSAR, RADARSAT-2 and TerraSAR-X.

SAR techniques discriminate water features based on the substantial distinction between the dielectric properties and surface roughness of water and other land covers (Gao et al. 2017). SAR sensors transmit and measure an EM wave with a distinct polarisation, frequency and amplitude (Chan & Koo 2008). When the wave traverses with a target, part of the wave energy is scattered back and its amplitude and arrival time is registered at a specific polarisation. The backscattered wave is sensitive to the dielectric and geometric features of the target, which enables the discrimination between surface features. Water surfaces are generally much smoother than the surrounding dry land and act as a mirror-like reflector, resulting in lower backscatter than other features (Horritt, Mason & Luckman 2001; Teng et al. 2017).

Different methods have been used to delineate water from SAR data. This includes visual interpretation (Di Baldassarre et al. 2010), thresholding (Hong et al. 2015), texture analysis (Pradhan et al. 2014), fuzzy classification (Twele et al. 2016), region growing (Mason et al. 2012), object-based classification of different SAR polarisations (Pradhan, Sameen & Kalantar 2017) and active contour modelling (Bessinger 2016; Horritt et al. 2003) methods. Most of these techniques are semi-automatic, usually configured through visual analysis of the image histograms and finally adjusted by the operator based on an instinctive impression of the result (Matgen 2011). To date, image thresholding and classification have been the most commonly used approaches to delineate surface water with SAR imagery.

A number of challenges relating to the use of SAR data for LSW mapping exist, particularly in complex environments. Martinis et al. (2015) stated that radar backscatter is strongly altered by surface conditions and changes in water surface roughness (e.g. due to waves caused by wind), which can lead to stronger return pulses. Water surfaces with floating or partially submerged

vegetation can also appear brighter due to double-bounce reflection between the water surface and the emergent vegetation parts (Pulvirenti et al. 2011b). The double-bounce reflection can cause LSW to be confused with other land covers and lead to omissions. Conversely, non-water areas with low backscatter, such as smooth agricultural cropland, bare ground, pavements, sand dunes and radar shadow, can cause overestimations (commissions) of LSW extent (Martinis et al. 2015).

Sensor parameters such as viewing angle, frequency and polarisation play a significant role in LSW mapping with SAR systems (Pierdicca, Pulvirenti & Chini 2013). Horritt et al. (2003) found that lower incidence angles will shorten the distance between the point at which microwaves enter the canopy and reach the water surface, thereby minimising scattering from the canopy and making a specular reflection off from the sensor`s view direction more probable. As a result, small incidence angles are more suitable for detecting water in vegetated environments such as wetlands and floodplains (Töyrä et al. 2002). Frequency and polarisation are also principal factors, with L-band wavelengths being more successful at penetrating canopies than those in the C-band (Ramsey, Rangoonwala & Bannister 2013). Canopy backscatter is also greater in VV polarisations compared to those with HH configurations (Wang et al. 1995).

1.2.3 Multisensor approaches for LSW mapping

Multisensor approaches synergistically combine data from several sensors to provide more information than can be derived from the individual sensors alone (Kumar & Acharya 2016). Since EO satellites provide data at different spatial, temporal and spectral resolutions, the combination of different data can increase understanding capabilities and produce stable LWS mapping results (Kaplan & Avdan 2018; Töyrä, Pietroniro & Martz 2001). Multisensor approaches can also be used to resolve the incompleteness of sensor data (Sandholt et al. 2003; Wang, Colby & Mulcahy 2002). For example, Hong et al. (2015) achieved an overall classification accuracy of 83.7% when SAR amplitude information was used for delineating surface water extent, but when Landsat data was incorporated into the classification, the overall classification accuracy increased to 96.4%. However, the combination of data from multiple sensors leads to large datasets that often limit its implementation to small areas and number of images (Franceschetti & Lanari 2018; Mleczko & Mróz 2018). In addition, the successful combination of datasets requires them to be of the same (or at least similar) date and spatial resolution, which can raise the cost and practical complexity.

There are many aspects to be considered when choosing remote sensing data for LSW mapping, among which spatial resolution and revisit time are of great importance. High spatial resolution data is often preferred to coarse spatial resolution, but such data often have poor temporal resolutions. Coarse spatial resolution data are generally acquired more frequently but often lead to a poor delineation of LSW, especially in complex environments (Sun, Yu & Goldberg 2011; Zhang, Zhu & Liu 2014). This is attributed to the measured signal being influenced by interactions of EM radiation with various components within each pixel. For example, a mixture of water, vegetation and soil cover hinders the accurate delineation of water features in heterogeneous floodplains (Keshava & Mustard 2002).

1.3 RESEARCH PROBLEM

The Caprivi floodplain in the northern part of Namibia experiences annual floods. The area is characterised by savannah vegetation, including grass, sporadic shrubs and woodlands (Figure 1.1a and b). During the 2009 flood, Skakun et al. (2014) estimated that approximately 60 000 to 90 000 people in the Caprivi were impacted by the flood, at least 38 000 people were displaced, and 102 lives were lost. Despite these detrimental impacts, people continue to settle in these flood-prone areas due to favourable geographic conditions such as food production (fertile land) and fishing activities. During flood events, the Caprivi floodplain cannot be monitored by ground surveys since the area is very large (about 2 000 km^2) and difficult to access by road. The area is also the habitat of wild animals such as elephants, lions, crocodiles and hippos, which inhibits travel on foot or by boat. In the age of satellite technology, the integration of information extracted through Geographical Information System (GIS) and remote sensing (RS) with other datasets provides tremendous potential for monitoring and impact assessment of flood disaster for relief agencies.

Reservoirs are monitored for drought preparedness (before drought occurs), drought response (during the drought) and drought mitigation (after drought has occurred). All these phases require good estimates of the areal extent and shape of water bodies at a particular time. In the time of the writing of this thesis, the Western Cape Province of South Africa is experiencing its worst water shortage in 113 years. The Western Cape Province receives most of its rainfall during winter and as such relies on irrigation during the summer months for agricultural production. Agricultural activities in the Western Cape contribute 23% towards the gross domestic product of region (GDPR). More than 10 million hectares (89%) of the province's land surface is presently producing over 55% of South Africa's total agricultural exports, of which the major products are fruit (27%), winter grain (22%), poultry (21%), wine (21%) and green

vegetables (18%) (DAFF 2018). The water storage levels of the major reservoirs in the province were reportedly at 20.8% of their normal capacity in March 2018, which equates to effectively 12.3% of the accessible reservoir water volume (Evans 2018). Authorities were confronted with difficult decisions about how to best manage the limited available water resources and minimise the inevitable socio-economic impacts. Many limitations of existing procedures and gaps in available information sources were exposed. One of the biggest needs was to determine how resilient the agricultural industry, in particular the perennial crops sector, would be to severe water restrictions. This proved to be challenging given that no operational systems are in place to quantify and monitor how much water is stored in privately owned and managed reservoirs (dams).

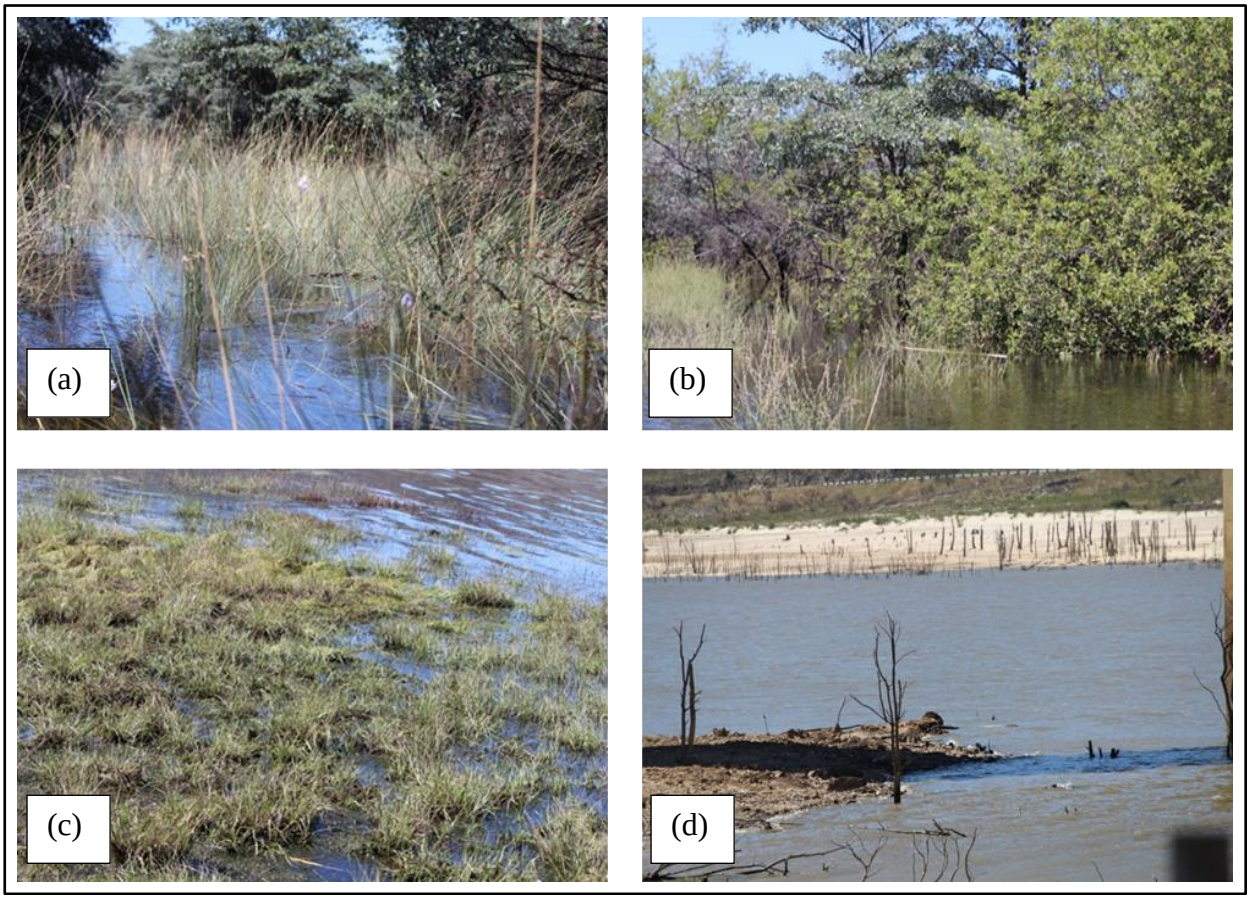

Figure 1.1 Examples of complex LSW environments, namely (a & b) vegetated floodplains in Caprivi and (c & d) turbid and optically shallow water in the Western Cape

In South Africa, and specifically in the Western Cape Province, surface water is stored in reservoirs (dams) of varying sizes and depths. In many cases, the water is turbid, optically shallow or eutrophic (Figure 1.1c and d). In the Caprivi, flooded areas are often obscured by woody vegetation (e.g., trees and shrubs) or characterised by partially submerged vegetation. EO-based detection, delineation, and monitoring of such LSW will likely pose challenges, but the few studies that have been done on EO-based LSW mapping in southern Africa (Crétaux et

al. 2011; Gumindoga et al. 2016) targeted clear, large and open water bodies. Very little is thus known about how partial vegetation cover influences classification results. The effect that the surrounding landscape (e.g. land cover and terrain) has on classification accuracies is also not well understood. This is particularly relevant when using coarse spatial resolution data (due to the mixed pixel effect), but it is also relevant when using high spatial resolution imagery for mapping small water bodies located in mountainous terrain (Cheruiyot et al. 2014; Plank et al. 2017). These uncertainties need to be investigated before fully automated EO techniques can be established to produce accurate, reliable and timeous LSW maps in heterogeneous environments such as those of the Caprivi floodplain and Western Cape Province.

Previous applications of remote sensing techniques for LSW mapping in complex environments have used imagery with high to medium spatial resolution and low temporal resolution (Bangira et al. 2017; Zhang, Zhu & Liu 2014). The dynamic changes and heterogeneity of surface water were thus not previously considered. Given the complexity of the floodplains and the rapid changes (often within 10 days) of LSW extents during flood events, flood mapping using imagery acquired at low temporal resolutions will be of little value. Ideally, EO data at both high temporal (1-3 days) and spatial (10-30 m) resolutions are required to adequately monitor the temporal and spatial dynamics of LSW. However, due to technical constraints, a trade-off between spatial and temporal resolutions often needs to be made. One solution is to make use of data from multiple sensors, whereby high temporal and coarse spatial resolution data are integrated with low temporal, but high spatial resolution data. Multisensory approaches also allow for the combination of SAR and optical data to maximise the advantages of each type of data. The recent development and launching of satellites carrying multispectral and SAR sensors with better spatial, temporal and spectral resolution opened up many new research opportunities. In particular, the ESA Sentinel satellite constellation holds much potential for mapping and monitoring heterogeneous LSW bodies for flood and drought resilience. Maps show a more direct and view of the spatial extent of the floods and depletion of water reservoirs for disaster management. This research intends to capitalise on these developments for flood and drought monitoring by addressing the following research questions:

i. *What are the limitations of existing EO methods for mapping LSW in heterogeneous environments?*

ii. *How can flooded areas in heterogeneous environments be mapped using low spatial and high temporal resolution optical imagery?*

iii. *How effective are multisensory approaches for automated classification of LSW?*

iv. *What role does the Sentinel satellite constellation play in monitoring LSW changes, particularly in data-scarce regions?*

1.4 AIMS AND OBJECTIVES

The primary aim of this research is to evaluate the potential of remotely sensed data with different temporal, spatial and radiometric properties to map LSW under flooded vegetation and shallow, turbid and eutrophic water. Various techniques will be assessed to understand better the capabilities and limitations of using SAR and multispectral data for LSW mapping in complex and heterogeneous environments.

The research will seek to achieve the following objectives:

1. Review the literature on existing remote sensing data and techniques for LSW mapping and highlight the advantages and respective limitations of the methods;
2. Develop and validate a technique whereby vegetated LSW can be mapped using high temporal and low spatial resolution imagery;
3. Construct and validate a procedure based on time series of Sentinel-1 SAR data for mapping floods in a heterogeneous floodplain;
4. Develop a method based on combining multispectral and SAR data for mapping small and spectrally diverse LSW bodies; and
5. Synthesise the research work in relation to the primary aim.

The approach taken for achieving these aims and objectives is described in the next section.

1.5 RESEARCH METHODOLOGY AND DISSERTATION STRUCTURE

This research uses statistical methods for the analysis and validates the results with field observations and satellite data. The intended goal is to develop and evaluate techniques for LSW mapping in heterogeneous environments, with flood and drought monitoring being the ultimate purpose. The developed techniques were tested on two study areas in southern Africa, namely the Caprivi floodplain and the Cape Winelands District of the Western Cape Province. The Caprivi floodplain is densely vegetated with shrubs, trees, and grass. The Cape Winelands

District has complex water bodies that are turbid and eutrophic. Statistics were used to analyse results and to give argumentative answers to the research questions (Rogers & Kearney 2004).

The research design is shown in Figure 1.2 and involves six steps, each representing a chapter. The structure of the dissertation and content of each chapter are summarised in Table 1.1. The dissertation consists of six chapters that are arranged in four sections: (i) General overview and contextualisation (Chapter 1 and Chapter 2), (ii) Flood mapping in heterogeneous environments (Chapter 3 and Chapter 4), (iii) Mapping of complex water bodies (Chapter 5), and (iv) Conclusion and synthesis (Chapter 6). Some components of Chapters 2–5 are duplicated as they were written as stand-alone articles meant for publication in scientific journals.

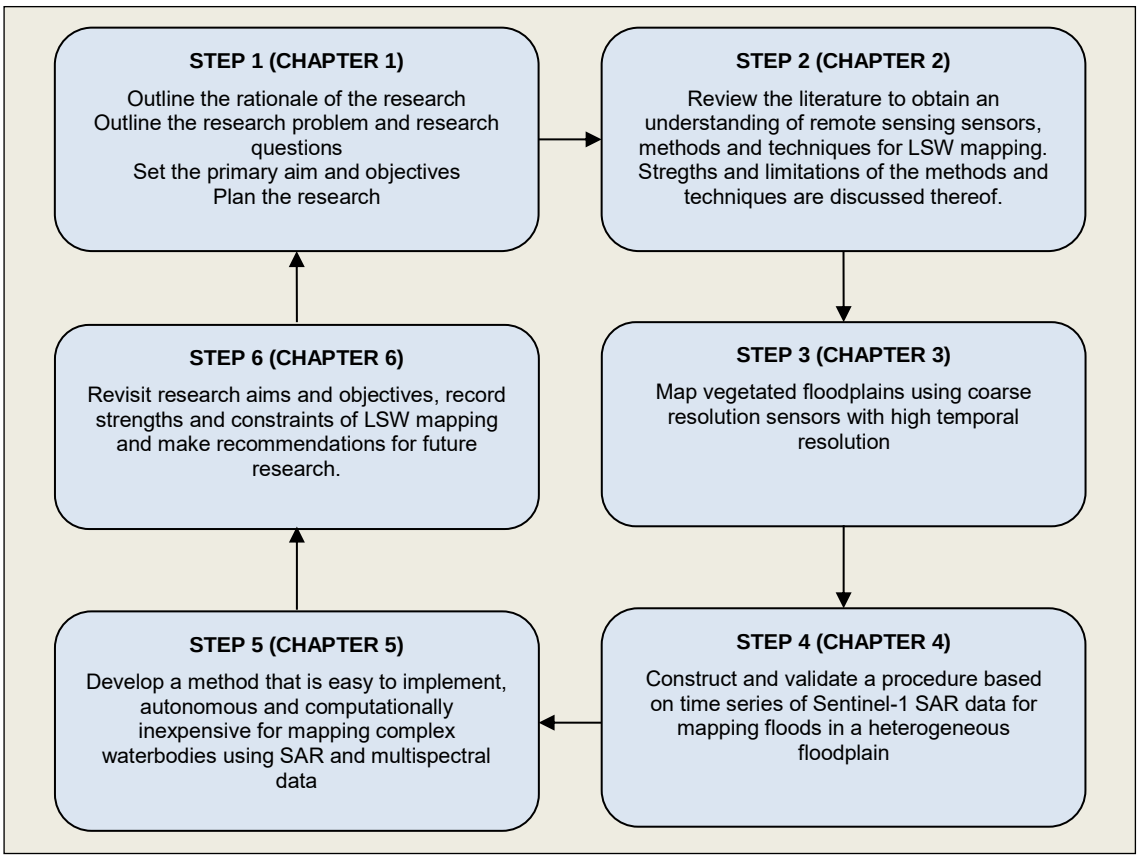

Figure 1.2 Research design, consisting of eight steps

This chapter serves as an introduction and a contextualisation of the research. It highlighted the impact of global climate change on the occurrence of extreme hydrological events such as floods and drought. The chapter further elaborated on the importance of remote sensing techniques for mapping and monitoring the dynamics of LSW for improving flood and drought resilience. A brief overview of different remote sensing techniques used for LSW mapping was provided. In addition, the chapter described the research problem and stated aims and objectives of the study.

The next chapter, Chapter 2, provides a review of the relevant literature and overviews the existing methods used for LSW mapping. The literature review associates specifically to the first research objective (Objective 1). It aims to describe the research gaps and motivate the need for developing cost-effective methods for accurate and consistent LSW mapping in complex environments, with flood and drought monitoring being the focus.

Flood mapping in heterogeneous environments requires remote sensing data with high temporal and high spatial resolution. However, there is a trade-off between spatial and temporal resolution in remote sensing data. To address Objective 2, Chapter 3 describes a technique that uses spectral unmixing with ensemble estimation of endmembers to improve surface water area estimates in vegetated floodplains using low spatial but high temporal resolution satellite imagery.

Table 1.1 Dissertation structure and chapter content

Chapter no.	Chapter title	Main points
1	Introduction	A rationale for LSW mapping Research problem Primary aim and objectives Research methodology and design
2	Reviewing the trade-offs between resolution, techniques and environmental complexity for mapping land surface water using earth observation data (In preparation for submission to a journal)	Remote sensing sensors for LSW Remote sensing techniques for LSW mapping Potential and limitations of the use of SAR data for LSW mapping in complex environments Trade-offs between satellite data availability, costs, applicability and techniques for LSW mapping
3	A spectral unmixing method with ensemble estimation of endmembers: Application to flood mapping in the Caprivi floodplain (Published journal article)	Trade-off between spatial and temporal resolution for mapping vegetated floodplains Linear spectral unmixing Indices-based spectral unmixing Automatic selection of endmembers
4	Flood extent mapping within the Caprivi floodplain using Sentinel-1 time series analysis (In review)	Temporal analysis of VH, VV and VH/VV backscatter over different flooded pixels Comparison between Sentinel-1 and Landsat-8 OLI flood maps Accuracy assessment using ground truthing
5	Comparing thresholding with machine learning classifiers for mapping complex water (Waiting for submission to a journal)	Mapping complex water bodies using automatic techniques Comparison between thresholding and machine learning classifiers for mapping complex water bodies Accuracy assessment using ground truth
6	Land surface water mapping using remote sensing in complex and heterogeneous environments: A synthesis	Research aim and objectives revisited Research value and contribution Limitations, recommendations and recommendations for future studies Conclusion

SAR sensors provide an advantage over optical sensors by being able to collect data under overcast conditions, a condition often experienced during flood events. SAR sensors also can observe inundated areas obscured by woody vegetation, which is one of the characteristics of the

Caprivi floodplain. Thus, Chapter 4 investigates the use of a time series of SAR (Sentinel-1) data and Bayesian probability for flood mapping in the heterogeneous Caprivi floodplain. Chapter 4 consequently addresses Objective 4.

There is a need for autonomous EO methods to map and monitor water bodies. Chapter 5 integrates freely available Sentinel-1 (SAR) and Sentinel-2 (multispectral) data and evaluates a range of thresholding and machine learning algorithms for mapping the complex water bodies of the Cape Winelands District, thereby addressing research Objective 3.

The final chapter, Chapter 6, critically assesses the extent to which the research objectives were met. It provides a synthesis of the findings and conclusions are drawn based on the preceding chapters. The chapter makes recommendations for forthcoming research based on the highlighted limitations of this study.

CHAPTER 2: REVIEWING THE TRADE-OFFS BETWEEN RESOLUTION, TECHNIQUES AND ENVIRONMENTAL COMPLEXITY FOR MAPPING LAND SURFACE WATER USING EARTH OBSERVATION DATA

2.1 ABSTRACT

Increased impacts of climate change are causing changes in land surface water (LSW), which have resulted in floods and water shortages. Changes in the extent of LSW can have considerable ecological, social and economic consequences. Timely and accurate monitoring of LSW dynamics is therefore essential in prioritising relief efforts and planning mitigation measures against the impact of floods and droughts. Earth observation (EO) has been recognised as an effective alternative to conventional methods of monitoring LSW as it generally reduces costs and time associated with obtaining information about the extent of LSW. This chapter assesses, based on literature review, the application of EO for LSW mapping, particularly within heterogeneous and complex environments such as flooded vegetation (FV) or where waterbodies are turbid, eutrophic or optically shallow. The review found that EO is currently being used mainly for LSW mapping in clear and open water environments, while being underutilised in complex and heterogeneous environments. EO data for LSW mapping is frequently being used in Asia, Europe, Australia and America, but comparatively few applications of this technology were found in Africa. There seems to be many opportunities for the application of EO for monitoring LSW in Africa where in situ data about LSW is particularly scarce. The new generation of satellites (e.g. the Sentinel constellation) that has become available in recent years have opened up new possibilities for combining coarse and fine spatial resolution data – with different revisit times and generated from different types of sensors (e.g. multispectral and synthetic aperture radar) – for the operational monitoring of LSW in complex environments.

Keywords: Earth observation (EO), land surface water (LSW) mapping, water security, flood, SAR, multispectral

2.2 INTRODUCTION

Climate change will affect the spatial and temporal variability of precipitation causing extreme hydrological events such as droughts and floods (Haddeland et al. 2014; Kundzewicz et al. 2018; Kusangaya et al. 2014). The increase in greenhouse gases in the atmosphere will continue, leading to global warming and an intensification of the hydrological cycle, making extreme hydrological events more complex and more challenging (Kelman 2015; Kusangaya et al. 2014).

A warmer atmosphere has a larger capacity to hold water vapour, which will increase the frequency of heavy rainstorms in many places and contribute to droughts in others. The Intergovernmental Panel on Climate Change (IPCC) forecasts that major changes in precipitation patterns will be experienced more in Africa than anywhere else (IPCC 2014). Southern Africa was identified as a climate change hotspot (De Sherbinin 2014), and recent studies have documented a high frequency of droughts and floods, linked to the El Niño effect, in this region (Hoell et al. 2017b; Kusangaya et al. 2014).

The recognition of climate change as a potential cause of increasing extreme rainfall events have resulted in the development of many LSW monitoring methods. Changes in LSW can be observed with the use of either conventional (e.g. gauges and ground surveys) or EO (e.g. in situ, aerial and satellite-based) methods. Conventional techniques involving ground surveys are important for LSW monitoring because they offer a local perspective. However, when the case is on a large scale, such methods are time-consuming, expensive and even impractical due to prohibitive weather conditions. The prevailing economic situation in many countries requires cheap, quick and reliable methods for LSW monitoring (Kusangaya et al. 2014). An alternative option is provided by satellite remote sensing (RS) technology.

Satellite RS encompasses a series of techniques that collect, process and disseminate information about the Earth's surface (Campbell & Wynne 2011). The science of RS for monitoring LSW has gained popularity owing to its superiority over in situ data gathering techniques (Levin 1999). Generally RS can reduce the costs and time associated with obtaining information about the extent of LSW and can be set up to provide operational (autonomous) monitoring of surface water resources (Du et al. 2016). Satellites provide a synoptic view and most are operational for many years, enabling consistent measurements over extended periods. EO also allows for repeated image acquisitions over the same locations, which are necessary for the detection of temporal changes in LSW. In addition, remotely sensed data are stored in a digital format that can easily be combined with ancillary data in a geographic information system (GIS) for further analysis (Tehrany, Pradhan & Jebur 2014). The coverage of extensive areas enables regional surveys on diverse themes and the monitoring of huge features (e.g. floodplains), and a single remotely sensed image can be analysed and used to achieve various objectives. RS also plays an important role in disaster management. For example, it can be used to map the extent of flooded areas, which can aid mitigation planning and rescue operations (McCallum et al. 2016).

Considering these advantages, researchers have used passive (Thanh Noi & Kappas 2018; Yang & Du 2017) and active (Manavalan 2017; Martinis et al. 2015; Martinis, Plank & Ćwik 2018)

EO sensors for LSW mapping, with varying levels of accuracy. According to Zhou et al. (2017), an effective operational EO sensor for LSW mapping should have the following characteristics: a) short revisit time, along with fast product production; b) high spatial, radiometric and spectral resolution; and c) wide image coverage. However, owing to technical limitations there is usually a trade-off between the pixel size[1] of EO imagery and the revisit time (temporal resolution) (Huang et al. 2016). Since water flow can be rapid, many flood-mapping studies choose to compromise on high spatial resolution (more detailed images) in favour of high temporal resolution (more frequent images). However, images with low spatial resolution are problematic when small and narrow waterbodies are being considered, or when complex, heterogeneous flooded landscapes such as urban areas and vegetated floodplains are being studied (Ferro-Famil & Pottier 2016).

Currently, there is no operational RS sensor dedicated to monitoring LSW dynamics, but several sensors – such as those mounted on the constellation of Sentinel satellites – have recently become operational and provide images with high spectral, temporal and spatial resolutions. Most of the LSW mapping methods whose conception was based on images produced by these new sensors were developed outside southern Africa (e.g. in Europe), and it is not clear how these datasets and methods will perform in the heterogeneous LSW environments of southern Africa.

The purpose of the following sections is to: give an overview the LSW mapping studies that have been carried out; briefly introduce the RS sensors often used for LSW mapping; investigate the trade-offs between temporal and spatial resolution for LSW mapping; and critically review the literature on LSW mapping using EO data in heterogeneous environments.

2.3 REMOTE SENSING SENSORS FOR LSW MAPPING

RS sensors are instruments that acquire images or other measurements of the Earth's surface without direct contact with the target (Sivakumar et al. 2004). These sensors can be carried on satellites or mounted on aircrafts or can be ground-based. There are two main types of EO satellite sensors that are suitable for LSW mapping: those that actively illuminate the Earth's surface with their own radiation energy (active sensors); and those that passively use the sun's

[1] Pixel size is determined by the instantaneous field of view of the sensor (Cracknell 1998)

energy reflected off the Earth's surface or measure thermal infrared energy emitted from the Earth (passive sensors) (Lillesand, Kiefer & Chipman 2014). Figure 2.1 compares passive and active sensors and the parts of the electromagnetic spectrum (EMS) most often used in each type of data.

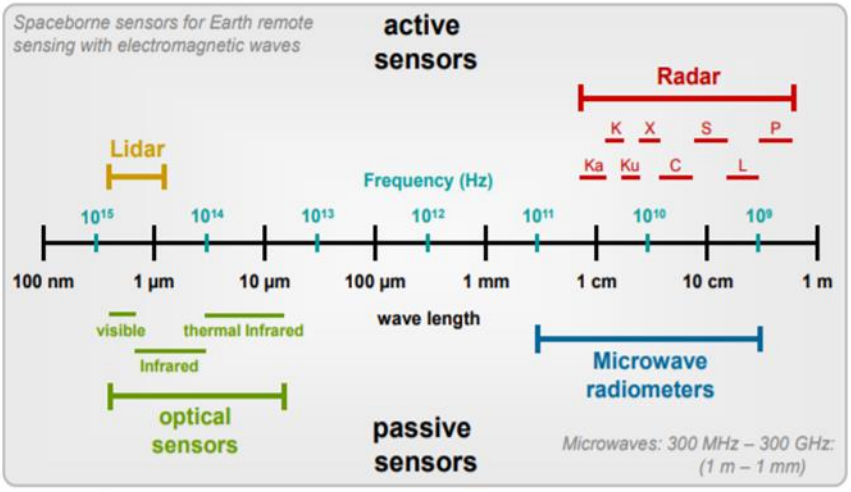

Adapted from Moreira (2013)

Figure 2.1 Types of remote sensors

Passive and active sensors are explained in more detail in the following subsections.

2.3.1 Passive sensors

Passive sensors detect and record electromagnetic energy occurring in the target's environment (Tempfli et al. 2009). These sensors measure reflectance in specific wavelength bands such as visible (390–700 nm), infrared (750 nm–1 mm), ultraviolet (100–400 nm) and microwave (15 mm–30 cm). The energy can be either reflected – as in the case of visible, infrared and ultraviolet wavelengths – or absorbed and then re-emitted – as in the case of thermal infrared and microwave wavelengths. Sensors with several (i.e. 3–20) wide bands are known as "multispectral" sensors; whereas those with many narrow bands (generally 20 or more) are known as "hyperspectral" sensors.

Technically, a sensor requires a minimum quantity of electromagnetic energy to acquire an image (Lillesand, Kiefer & Chipman 2014). A detector sensitive to wavelengths in a narrow band (fine spectral resolution) thus has to observe a larger area (coarse spatial resolution) compared to a detector sensitive to a wider dimension of wavelengths (total energy of the entire wavelength range). The spatial, temporal and spectral resolutions of a sensor are thus closely linked; a fine spatial, temporal and spectral resolution automatically leads to an image with a coarser spectral, spatial and temporal resolution or vice versa. Given the current limited

availability of space-borne hyperspectral sensors, the rest of the section focusses on multispectral imagery.

Multispectral imagery can be grouped into two categories. The first group is characterised by images with high to medium spatial resolutions and longer revisit times. These include, for example, images from Landsat and Sentinel-2 (S2), which provide images with 10–100 m pixel sizes, but at relatively longer revisit cycles (5–16 days). The second group includes imagery from MODIS, MERIS and Sentinel-3 (S3), which provide relatively coarse spatial resolutions (250–1000 m) but shorter revisit times (one or more observation per day).

The use of passive sensors is dependent on weather and time of day as cloud cover and the absence of natural light can hamper image acquisition. Given that flood events are often associated with cloud cover and the dynamic nature of floods – especially in small to medium-sized basins (catchments) – reliable and continuous monitoring of flooded areas with passive sensors is often problematic and this has paved the way for active sensors (Matgen 2011).

2.3.2 Active sensors

Active sensors provide their own source of energy for illuminating the Earth's surface (Finkl & Makowski 2017) and image acquisition is consequently independent of atmospheric conditions and time of day (Kuenzer et al. 2013). Active sensor technologies include radar (radio detection and ranging), lidar (light detection and ranging) or sonar (sound navigation and ranging) (Woodhouse 2017). However, most of the active satellite sensors used for LSW mapping carry radar antennas that transmit microwave signals at a fixed frequency, directed towards a specific target from which the reflected energy is detected (Campbell & Wynne 2011). The radar antenna is designed to transmit and receive EM waves of a specific polarisation. The most common polarisations for LSW mapping are horizontal linear (H) and vertical linear (V). Thus a radar system can have different levels of polarisation complexity, namely single polarised — VV or HH or HV or VH; dual polarisation — HH and HV or VV and VH or HH and VV; and quad polarisations — HH, VV, HV and VH. Due to the interaction with the target, polarisations have a significant impact on LSW mapping, as discussed in 2.5.4.

Radar systems work in the microwave section of the EMS (100 nm to 1m), which is delimited into different frequency bands Table 2.1). The characteristics of the radar system are directly proportional to the transmitted frequency. The greater the frequency of a radar system, the more it is sensitive to atmospheric conditions such as haze, rain and clouds. These specific

characteristics of the frequency bands influence their applications in different environments. The L, C and X bands are the most suitable for LSW mapping.

Table 2.1 Microwave bands, frequency, wavelength and examples of mission satellites

Band	Frequency (GHz)	Wavelength (cm)	Examples of satellites
P-band	0.3 – 1	30 – 100	BIOMASS*
L-band	0.75 – 1.1	15 – 30	ALOS-PALSAR
S-band	2 – 4	7.5 – 15	NovaSAR-S*
C-band	4 – 8	3.8 – 7.5	Sentinel-1 and RADARSAT-2
X-band	8 – 12.5	2.4 – 3.8	TerraSAR-X
Ku-band	12.5 – 18	1.7 – 2.4	Telstar 5,6 and 7
K-band	18 – 26.5	1.1 – 1.7	GRACE
Ka-band	26.5 – 40	0.75 – 1.1	GRACE

NOTE: * Not yet launched

Radar systems are often categorised into non-imaging (e.g. altimeter and scatterometer), imaging (e.g. SAR, or interferometric synthetic aperture radar (InSAR)) systems. Non-imaging systems take measurements in a single dimension, as opposed to the bi-dimensional representation of imaging systems (Levin 1999). SAR is most widely used for LSW mapping (Manavalan 2017) and is the focus of the rest of this section.

A SAR is a side-looking radar system that utilises the flight path of the platform to electronically imitate a very large antenna or aperture (Ferro-Famil & Pottier 2016). The relative motion between the antenna and ground-based target is processed such that it produces a fine spatial resolution image (Ouchi 2013). SAR sensors have some drawbacks. Relatively high energy supply is required, which can limit the feasibility of SAR time series data and even the collection of individual images in some regions (Tsyganskaya et al. 2018b). Due to its side-looking nature, some areas of the Earth's surface may not be detectable to the sensor due to radar shadowing and layover generated by topography, taller buildings or vegetation (Tsyganskaya et al. 2018b). These effects increase with small viewing angles and steep terrain. Corrections of these effects have to be applied to lower their influence (O'Grady, Leblanc & Bass 2014). Furthermore, SAR images are generated by the coherent interaction of the transmitted microwave with the objects; they suffer from the consequence of speckle noise and have no spectral characteristics, making their interpretation difficult for inexperienced users (Argenti et al. 2013). Speckle may lead to uncertainties in measurements and may result in decreases in classification accuracies (Tsyganskaya et al. 2018b). Speckle reduction can be realised in two ways, namely multi-look processing and spatial filtering.

Multi-look processing involves the summing and averaging of narrow sub-beams to form a single output image (Dasari et al. 2015). Spatial filtering is implemented after data acquisition and involves the application of a moving window consisting of a few pixels in dimension (e.g. 3 × 3 or 5 × 5) over each pixel in the image. A numerical computation (e.g. averaging) is applied to the pixel values in the window and the central pixel's value is replaced by the calculated value (Argenti et al. 2013; Dasari et al. 2015). The window is moved one pixel at a time in both the row and column dimensions until the entire image has been filtered. A smoothing effect is realised and the visual appearance of the speckle is minimised by calculating the (weighted) average of a small window around every pixel (Argenti et al. 2013). The choice of the window size and filter type affects the result (Giustarini et al. 2015). Generally, the larger the window size, the more the resolution is reduced and the more blurred (generalised) the image appears. As a result, the edges are smoothed and the textural information is diminished (Dong, Milne & Forster 2000). Similar filtering can be done along the time axis too, i.e., using a set of consecutive images. This method is used for surface objects, which do not change in time.

Multi-looking and spatial filtering processes reduce speckle at the cost of pixel size (Argenti et al. 2013), while temporal filtering reduces the temporal resolution. Thus, the proportion of speckle reduction must be selected according to the specific application and the amount of detail required. Levin (1999) suggested little or no speckle filtering should be done if fine detail and high resolution are required. In this study, all the speckle filter methods available in Sentinel Application Platform (SNAP) software package were evaluated.

2.4 REMOTE SENSING TECHNIQUES FOR LSW MAPPING

The techniques used for LSW mapping with RS data are strongly influenced by whether multispectral or SAR datasets are being used. The different spectral features of water and non-water features form the foundation for the development and implementation of algorithms and techniques for retrieving LSW from multispectral data (Martin 2014). Water is differentiated from non-water features on the basis that it has very different reflectance and absorption inertia properties compared to other Earth surface materials such as vegetation and soil (Figure 2.2). Specifically, clear and deep water has a low spectral response (<10%) in the visible region but at longer wavelengths (NIR and SWIR) has an even greater absorption of all the incoming radiation (Feyisa et al. 2014; Mueller et al. 2016). However, the presence of vegetation and dissolved and suspended substances in water result in complex spectral characteristics (Martin 2014). Specifically, turbid water has higher visible and infrared reflectance compared to clear water (Figure 2.2).

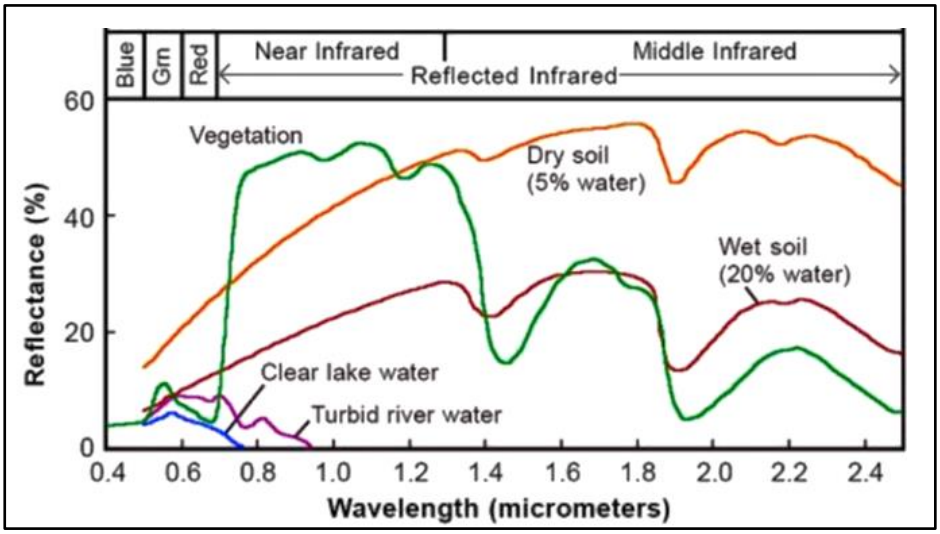

Source: Smith (2012)

Figure 2.2 Typical spectral reflectance curves of popular physical Earth surface objects in the visible and near to the mid-infrared range of the electromagnetic spectrum

LSW mapping using SAR imagery is possible because LSW pixels are in most cases associated with low backscatter values, thanks to the principle that smooth and calm water surfaces act as 'specular' reflectors (Figure 2.3a), resulting in a large proportion of the SAR signal being reflected away from side-looking SAR sensors (Giustarini et al. 2015; Greifeneder et al. 2014). Therefore, LSW areas appear darker due to the low backscattering response, whereas non-water surfaces appear bright cause of diffused reflection (Figure 2.3b).

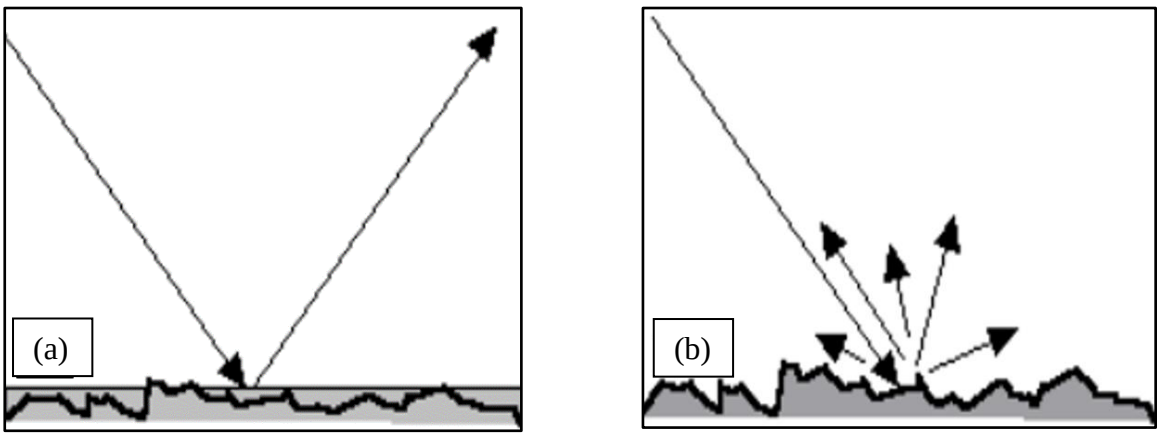

Figure 2.3 Types of reflection: (a) specular reflection from a smooth water surface and (b) diffuse reflection from a non-water surface

Although differences in backscatter are useful to delineate open water, the presence of emergent vegetation and waves caused by wind may cause diffused reflection (and an associated increase in backscatter) to such an extent that water features have similar backscatter responses to non-water features (Giustarini et al. 2015).

The techniques employed for LSW mapping with remote sensing data can be grouped into two main approaches, namely LSW extraction and land cover mapping. In LSW extraction methods, only 'water' features are targeted and other land covers are disregarded. In contrast, land cover mapping approaches group all pixels or objects in an image into one of many thematic (land cover) classes, of which some classes (often only one) relate to water. Land cover mapping and LSW extraction methods can be realised by manual delineation through visual interpretation, or by computer-assisted rule-based, supervised and unsupervised classification approaches.

2.4.1 Visual interpretation

Visual interpretation (VI) involves manually digitising LSW boundaries by visually interpreting SAR and/or multispectral images (Brivio et al. 2002). Much of the pioneering work on the application of RS for LSW mapping was accomplished by the visualisation of the Landsat-1 infrared band (0.8–1.1 µm) using tone, colour, texture, size, shape and context on the floodplains of the Iowa (Hallberg, Hoyer & Rango 1973), Arizona (Morrison & Cooley 1973) and Mississippi (Moore & North 1974; Schwertz, Spicer & Svehlak 1977) rivers. These studies achieved good LSW delineations, but some of the authors noted that suspended sediments increased NIR reflectance from water surfaces. Under such conditions, vegetation and water had identical spectral signatures in the infrared channels, which made accurate delineations difficult.

Blasco, Bellan & Chaudhury (1992) used visual interpretation of SPOT XS scenes acquired before and after flooding to evaluate the extent of floods in mangrove forests of the Ganges Delta in Bangladesh. The results from the study underestimated flooded forests by about 20%. Chopra, Verma & Sharma (2001) investigated water turbidity and seasonal water changes of the Harike wetland in India by visually analysing the false colour composites of IRS LISS-II bands 2, 3 and 4. The authors concluded that computer-assisted classification methods (see next section) are best for mapping wetlands due to the presence of mixed pixels. Similarly, Wang, Colby & Mulcahy (2002) argued that the visualisation of NIR images for delineating floods in vegetated floodplains can underestimate the flooded area, unless supplementary data such as a digital elevation model (DEM), along with expert rules, are incorporated. The authors also noticed that the presence of shadows cast by tall vegetation and topography resulted in an overestimation of LSW when VI of NIR imagery was used.

The visualisation of thermal bands can also be used for mapping LSW (Zhang et al. 2012a). This practice is based on the principle that all materials at temperatures above absolute zero (-273°C) continuously emit electromagnetic radiation (Lillesand, Kiefer & Chipman 2014). Emissivity

depends on wavelength, land surface temperature (LST) and some physical properties of the surface, e.g. water content. Materials such as water with low thermal inertia (emissivity) show a much accentuated diurnal cycle compared to land temperatures (Burke, Pricope & Blum 2016). During daytime, open waterbodies have lower temperatures (appear dark on thermal imagery), inundated forests are warmer (lighter tones) and dry land emits the most thermal radiation (appear bright). In contrast, dry land is colder than open water at night and the relationships between dry land, vegetated LSW and open water are inverted.

Few studies have applied VI of thermal imagery for LSW mapping (Burke, Pricope & Blum 2016; Moore & North 1974; Sandholt et al. 2003). Moore & North (1974) did much of the pioneering work and made use of thermal infrared bands of the ERTS satellite to map inundated forests. The authors found that the thermal infrared imagery represents the top of the tree canopy temperatures and that the underlying water was poorly represented. Fifteen years later, Barton & Bathols (1989) and Ali, Quadir & Huh (1989) applied the segmentation of temperature histograms derived from thermal bands 4 and 5 (10.30–11.30 µm) of AVHRR imagery to monitor floods along the Darling River in Australia and major rivers in Bangladesh, respectively. However, the authors in both studies reported an underestimation of flooded areas due to mixed pixels. Sandholt et al. (2003) encountered the same challenge of the augmentation of mixed pixels in the presence of vegetation when they tried to visually determine inundated areas of the Senegal River valley using AVHRR thermal imagery.

The thermal bands and high temporal resolution of the MODIS sensor motivated Zhang et al. (2012a) to visually map floods at night. The experimental results indicated that the visualisation of the MODIS thermal bands is quick at observing floods over large areas, but was ineffective at delineating FV due to the coarse (1000 m) pixel size of MODIS. More recently, D'Andrimont & Defourny (2018) used the visual interpretation of the MODIS LST product derived from thermal infrared bands 31 (10.78–11.28 µm) and 32 (11.77–12.27 µm) with a spatial resolution of 1000 m to monitor seasonal changes in waterbodies on the African continent with commission error of less than 6%.

From the literature, it seems that the visualisation of thermal images is only suitable for delineating LSW when high detail is not required, as the spatial resolution of the available imagery is generally coarse. For example, the Landsat-8 thermal infrared (TIR) bands have a spatial resolution of 100 m, while the MODIS LST and Sentinel-3 Sea and Land Surface Temperature Radiometer (SLSTR) products have a resolution of 1 km.

LSW mapping using SAR data was initially carried out using VI (Brivio et al. 2002; Di Baldassarre et al. 2011; Oberstadler, Honsch & Huth 1997). Oberstadler, Honsch & Huth (1997) and Brivio et al. (2002) used a false colour composite of two ERS-1 images and on-screen-digitising to delineate flood boundaries. Horritt, Mason & Luckman (2001) commented on the subjectivity of VI of SAR imagery and the underestimation of flood extents in areas where FV increase backscatter. To overcome this limitation, they suggested that ancillary information should be integrated with expert rules.

Generally, visual interpretation of satellite imagery is intuitive, allowing for rapid delineation of open LSW. However, in heterogeneous environments, the interpretation needs to be carried out by an experienced analyst (Di Baldassarre et al. 2011). The mapping of large LSW areas can also be very time-consuming, and the results are often inconsistent among image interpreters. These shortcomings have led to the development of computer-assisted classification techniques.

2.4.2 Computer-assisted classification

Traditionally, computer-assisted classifications of remotely sensed imagery have been grouped into two categories, namely supervised and unsupervised techniques. More recently, approaches that fall outside these approaches have been adopted, of which expert systems (ESs) is one of the most popular (Blaschke 2010; Mather & Tso 2016). The following subsections provide an overview of supervised and unsupervised classification methods, followed by an outline of expert system classification approaches.

2.4.2.1 Unsupervised classification

Unsupervised classification, also known as image clustering, groups the input data into similar classes, based on their spectral properties (Campbell & Wynne 2011). The analyst then manually relabels and joins the spectral classes' (clusters) into informational classes. Iterative self-organising data analysis (ISODATA) (Jung et al. 2014; Parmuchi, Karszenbaum & Kandus 2002) and *k*-means (Li et al. 2018; Papaioannou, Vasiliades & Loukas 2015) are examples of unsupervised classifiers. The advantages of unsupervised classification are that no a priori knowledge (e.g. training data) is required (Schowengerdt 2012). These techniques are also fairly quick and easy to run. Furthermore, clustering and segmentation based techniques are able to adapt to the characteristics of the input dataset at both local and regional scales (Lässig, Kersting & Morik 2016). One of the limitations of unsupervised classification is that the spectral classes do not always concur to informational classes. The user has to spend time defining and relabelling the classes after the classification. Unsupervised classifications furthermore are

restricted to frameworks where underlying assumptions are contravened. For example, Amitrano et al. (2018) proposed an unsupervised *k*-means clustering method for flood mapping using S1 images. The authors assumed a bi-modal allocation of the data in feature space, where each mode resembles either the non-water or the water class. However, in scenarios where the distribution of non-water and water classes are multi-modal (due to high spectral variance within land covers), the major assumptions of such a clustering-based approach is contravened, causing low classification accuracies (Karpatne et al. 2016; Lässig, Kersting & Morik 2016).

Very little attention has been given in literature to the use of unsupervised classification for LSW mapping. One notable exception is Thomas et al. (2011), who used ISODATA on a masked Landsat TM image to map inundation in a large heterogeneous vegetated floodplain, the Macquarie Marshes. The authors observed that the presence of vegetation in flooded areas caused confusion between water and other land covers. Ozesmi & Bauer (2002) argued that unsupervised classification is most successful when a large number of clusters are specified. To assess this hypothesis, Martin, Brabyn & Beard (2014) applied unsupervised classification for LSW mapping using aerial imagery, specifying various numbers of target classes. Their results revealed that the unsupervised classification accuracy can be boosted by increasing the number of spectral classes to be clustered.

Martinis, Twele & Voigt (2011) argued that unsupervised classification algorithms are effective for automated mapping of LSW features using small datasets. For example, Martinis, Kersten & Twele (2015) and Twele et al. (2016) presented fully automated services for flood mapping using TerraSAR-X and S1 data respectively in which pre-processing, unsupervised classification, as well as post classification improvement was automatically produced after satellite data delivery. However, the proposed processing chains currently employ global ancillary data sets such as global DEMs and topographic slope information, which are characterised by a spatial resolution remarkably coarser than the pixel spacing of TerraSAR-X data and S1.

2.4.2.2 Supervised classification

Supervised classification involves the use of samples of known identity (training data) to classify pixels or objects of unknown identity (Mather & Tso 2016). The underlying assumption in the use of training samples (a priori knowledge) is that the spectral response of a certain target (e.g. water class) will be almost consistent throughout the image (Campbell & Wynne 2011). In contrast to unsupervised classification that produces spectral classes that must later be assigned

to informational classes (e.g. land cover classes), supervised classification generates informational classes directly. It has, however, several shortcomings. The collection of representative training samples is expensive and time-consuming as it often requires field visits, which are difficult to carry out in inaccessible areas (Campbell & Wynne 2011). Training samples are often only usable for a limited period, because the spectral and spatial properties of classes vary over time, especially in highly dynamic target classes such as LSW (Hasmadi, Pakhriazad & Shahrin 2009; Lässig, Kersting & Morik 2016).

Supervised classifiers are generally grouped into (traditional) parametric (parallelepiped, minimum distance, and maximum likelihood (ML)) and (modern) non-parametric (support vector machine (SVM), decision tree (DT), random forest (RF) and k-nearest neighbour (k-NN)) algorithms. Parametric classifiers assume a particular (usually normal) statistical distribution in the input data (Rodriguez-Galiano et al. 2012) as they rely on statistical measures such as mean, standard deviation and probability (Aggarwal (Compiler and ed) 2014). Parametric algorithms have difficulty dealing with multi-modal input datasets (i.e. noisy and skewed training data) (Mather & Tso 2016; Petropoulos, Kalaitzidis & Vadrevu 2012). On the other hand, non-parametric classifiers build no assumptions about the statistical distribution of the input data (Campbell & Wynne 2011) and are considered to be more robust than traditional classifiers (Gilbertson, Kemp & Van Niekerk 2017).

A number of studies have evaluated supervised classification algorithms for LSW mapping (Rebelo 2010; Sisodia, Tiwari & Kumar 2014a; Sun, Yu & Goldberg 2011). The choice of the classifier is mainly determined by the level of accuracy required and the input data properties. A supervised ML classifier was applied by Sandholt et al. (2003) on Landsat-5 and AVHRR imagery to map five spectrally different water surfaces in the Senegal River valley. They concluded that mapping of LSW in turbid, eutrophic and spectrally shallow waterbodies is not an easy task. This is in agreement with Sisodia, Tiwari & Kumar (2014a) and Feyisa et al. (2014) who argued that ML is useful for mapping open waterbodies in arid regions where the water line boundary is contrasted by drier terrestrial areas, but they claim that ML does not perform well when water surfaces and surrounding areas are vegetated. MacAlister & Mahaxay (2009) achieved high accuracies when ML was applied for wetland mapping. However, they avoided confusion between wet and dry classes by first masking wetland areas that were smaller than 60x60m and occurred on slopes of more than 5% by using the ‘eliminate’ command in ArcGIS and classifying them separately. Song, Sohn & Park (2007) used ML on RADARSAT-1 data for water classification by assuming an approximate normal distribution of the water and non-water

classes. However, ML performed poorly due to its inability to distinguish water from topographic shadow. Relatively few studies have applied the parallelepiped classification and minimum distance algorithms for LSW mapping. One of them is Martinez & Le Toan (2007) who applied the parallelepiped classifier on a time series of JERS images for flood mapping in the Óbidos floodplain. Their accuracy assessment showed good results, with a kappa coefficient of about 0.8. However, significant confusion occurred with land covers (e.g. pastures and shadows) that showed very similar backscatter characteristics to those of water. This type of confusion was also encountered by Sisodia, Tiwari & Kumar (2014b) using the same classifier, but with Landsat multispectral scanner (MSS), thematic mapper (TM) and enhanced thematic mapper (ETM+) images of Rajasthan, India. In contrast, Khan et al. (2015) used the parallelepiped algorithm and a SPOT-5 image in Pakistan to classify waterbodies and achieved producer's and user's accuracies of 95% of 99% respectively.

Powerful non-parametric and parametric machine learning algorithms (MLAs) are increasingly replacing parametric classification methods. A number of examples of the use of MLAs such as DTs (Acharya et al. 2016; Mueller et al. 2016), SVM (Feng et al. 2015), RF (Corcoran et al. 2012) and *k*-NN (Pauw 2012; Tehrany, Pradhan & Jebuv 2014) for LSW mapping are available in the literature. Tulbure & Broich (2013) showed that the DTs deliver a high classification accuracy of 96% across different LSW environments while allowing fast processing, which makes them suitable for application to very large datasets. Tehrany, Pradhan & Jebuv (2014) used k-NN for classifying waterbodies with an accuracy of 91%. Liu et al. (2018) found that SVM, RF, DTs and k-NN consistently outperformed ML for waterbody mapping in wetland environments using unmanned aircraft vehicle (UAV) images, irrespective of the training sample size. This observation is in agreement with Petropoulos, Kalaitzidis & Vadrevu (2012), Jia et al. (2014) and Feng, Liu & Gong (2015) who used Hyperion hyperspectral, Landsat-8 and UAV imagery for waterbody mapping.

2.4.2.3 Expert system (rule-based) classification

Expert systems, also known as knowledge-based or rule-based classification, are computer programs that use symbolic logic (artificial intelligence) to imitate human experts and are expected to arrive at the same conclusion as human experts in image classification (Skidmore et al. 1996). These programmes are governed by a set of decision rules, which can incorporate ancillary data from diverse sources directly into the classification process. The overall premise is that experts will have a better grasp of the problem to be solved if they interact with the data and

view it through different representations; they will thus be able to design, test and fine-tune scenarios to extract the desired information (Pekel et al. 2016).

Rule-based techniques have many advantages. They are intuitive and logical and the classification rules for certain classes can be refined without affecting the rules for others or compromising the overall classification. Such refinements and the addition of more rules and datasets can be done iteratively. Additional data layers can easily be added at later stages of the classification process without affecting existing rules (Pauw 2012). The flexibility of expert systems regarding input data is advantageous as ancillary data from diverse sources can be integrated with remotely sensed data. Also, prior knowledge of distributions of target classes can be captured in knowledge rules (Masocha & Skidmore 2011). Lastly, once a pixel (or object) has been assigned to a certain class, it can be disregarded by further processing if necessary.

A major disadvantage of expert systems is the time needed to develop a successful rule-based classification system (Parent, Volin & Civco 2015). In addition, expert systems are negatively affected by increasing dimensionality of data. As the number of input layers increases, it becomes more difficult for the interpreter to comprehend their relation to the desired product classes (Pauw 2012). Regardless of these limitations, there are numerous reports in the literature of the usefulness of rule-based methods for LSW mapping.

Thresholding is a simplified rule-set that is most often applied to spectral indices. Thresholding is by far the most popular method for LSW mapping using multispectral data. Thresholding of spectral indices that emphasise water features are widely used to delineate LSW thanks to their simplicity, low computational cost and good performance. Examples of popular spectral indices are listed in Table 2.2. These indices involve the use of at least two bands and take advantage of spectral differences of water and other surfaces to extract LSW information. Most of the spectral indices used for LSW mapping are designed to exploit the relatively high reflectance of water in the visible region of the EMS and low reflectance of water in the infrared wavelengths, while also taking advantage of the high NIR reflectance of vegetation and soil features (McFeeters 1996; Xu 2006). This results in the enhancement of water features and masking of background (non-water) features.

The tasselled cap wetness (TCW) index is a by-product of tasselled cap (TC) transformation (Kauth & Thomas 1976), which provides information on the moisture content of soils and vegetation (Ouma & Tateishi 2006). TCW is based on coefficient values that are strongly influenced by the reflectance values of the SWIR bands of Landsat TM/ETM + (Huang et al.

2002). Although TCW has been shown to delineate LSW with reliable accuracy (Bhagat & Sonawane 2011; Huang et al. 2002), its application is limited when it comes to the derivation of coefficients, which are different in each sensor.

McFeeters (1996) proposed the use of the normalized difference water index ($NDWI_1$) for detecting LSW in wetland environments. The index was formulated based on the assumption that LSW will be enhanced given its relatively high green light reflectance and high NIR reflectance, while for terrestrial vegetation and soil, reflectance is relatively lower in the green range of the EMS compared to the NIR range, and will thus be suppressed (McFeeters 1996). Xu (2006) modified the $NDWI_1$ by replacing NIR with mid-NIR/SWIR to form the MNDWI (Table 2.2). MNDWI has been shown to overcome $NDWI_1$'s shortcomings by suppressing built-up and vegetated areas, while highlighting water features (Hui et al. 2008; Ji, Zhang & Wylie 2009; Lu et al. 2011).

Xiao et al. (2005) defined a land surface water index (LSWI) based on NIR and SWIR MODIS bands with a pixel size of 500 m for mapping flooded rice fields. LSWI has been used to delineate LSW in several studies with comparable accuracy (Islam, Bala & Haque 2010; Lu et al. 2011). Ouma & Tateishi (2006) developed a water index (WI) that combines TCW and $MNDW_3$ to map the saline and non-saline lakes in Kenya using Landsat TM and ETM+ data. The WI detected the shorelines with an accuracy of 98.4%, which was 22.3% higher than the TCW, and 43.2% more accurate than the NDWI. Feyisa et al. (2014) developed an automated water extraction index (AWEI) with an objective to overcome the limitations of MNDWI and NDWI in underestimating the detection of LSW in areas with shadows. However, the results showed that the AWEI underestimated the mapping of LSW in areas where water was green-brown in colour, and/or where waterbodies were small or had long perimeters causing a large proportion of mixed pixels.

LSW mapping using thresholding of spectral indices is a three-step procedure that involves: 1) derivation of the index using appropriate bands; 2) defining a threshold that adequately separates water and non-water features; and 3) applying the threshold to produce a thematic layer/map. Table 2.2 shows that positive values in water indices are in most cases associated with LSW features. However, waterbodies in urban areas are frequently small and surrounded by complex built-up areas, vegetation and shadows. The fragmented surfaces in urban areas result in a considerable amount of mixed pixels, causing confusion between water and non-water features (especially at lower resolutions). Areas with mixed water, vegetation and soils often have negative NDWI and MNDWI values (Ji, Zhang & Wylie 2009; Singh et al. 2015). In such

environments, Liu, Yao & Wang (2016) proposed manual adjustments of thresholds and the use of spectral indices in combination with other image classification algorithms and/or ancillary data.

Table 2.2 Spectral indices frequently used for land surface water feature extraction

Index	Equation	Remarks	Reference
Tasselled cap wetness	TCW = $0.1509(\rho_1) + 0.1973((\rho_2) + 0.3279((\rho_3) + 0.3406((\rho_4) - 0.7112(\rho_5) - 0.4572(\rho_7)$	Water has a positive value	Kauth & Thomas (1976)
Normalized difference water index	$NDWI_1 = \frac{Green-NIR}{Green+NIR}$	Water has a positive value	McFeeters (1996)
Normalized difference moisture index	$NDMI = \frac{NIR-MIR}{NIR+MIR}$	Water has a positive value	Wilson & Sader (2002)
Normalized difference water index	$NDWI_2 = \frac{Red-SWIR}{Red+SWIR}$	Water has a positive value	Rogers & Kearney (2004)
Land surface water index	$LSWI = \frac{NIR-SWIR}{NIR+SWIR}$	Water has a positive value	Xiao et al. (2005)
Normalized difference water index	$NDWI_3 = \frac{MIR-NIR}{MIR+NIR}$	Water has a positive value	Ouma & Tateishi (2006)
Water index	$WI = f(TCW \pm kNDWI_3)$ *f* denotes a function and *k* is a constant	Water has a positive value	Ouma & Tateishi (2006)
Modified normalized difference water index	$MNDWI = \frac{Green-SWIR}{Green+SWIR}$	Water has a positive value	Xu (2006)
Water ratio index	$WRI = \frac{Green+Red}{NIR+MIR}$	Water has a positive value	Shen & Li (2010)
Automated water extraction index	$AWEI = 4(Green - MIR) - (0.25NIR + 2.75SWIR)$	Water has a positive value	Feyisa et al. (2014)
Enhanced water index	$EWI = \frac{Green-SWIR+0.1}{Green+SWIR(NDVI\times0.5)}$	Water has a positive value	Wang et al. (2015)

Note: ρ_i = corresponds to the respective reflectance bands

Thomas et al. (2015), Menarguez (2015) and Zhou et al. (2017) generated expert rules to integrate MNDWI and vegetation indices (normalized difference vegetation index (NDVI) and NDI) to classify FV. The results revealed that such an integration was sensitive to mixed water and vegetation pixels. Pekel et al. (2016) implemented an expert system in Google Earth Engine (GEE) and incorporated ancillary data (including a DEM, the global human settlement data layer (GHSDL), spectral wetness indices and the Randolph glacier inventory) to classify each pixel in 1 823 terabytes of Landsat data as water or as land. Classification performance, measured using more than 40 000 reference points, confirmed that the classifier produced less than 1% of false water detections and missed less than 5% of water. In another example, Pradhan et al. (2014) applied a semi-automated expert system based on spectral, spatial, textural and contextual factors

for flood mapping on TerraSAR-X imagery. The system suitably extracts the spectral signatures of water with an overall accuracy of 86.18%.

The choice of band combinations has been cited as a drawback of spectral LSW indices (Lu et al. 2011) as different band combinations produce different results. For example, Xu (2006) in Fuzhou City (China) observed that MNDWI can enhance waterbodies and suppress built-up features more efficiently than $NDWI_1$. This was confirmed by a study in Italy (Venice coastland) by Du et al. (2016) in which it was observed that MNDWI can delineate LSW features with a higher accuracy (96.57%) compared to $NDWI_1$ (95.71%). A number of studies (Hui et al. 2008; Ji, Zhang & Wylie 2009; Sarp & Ozcelik 2017) have demonstrated the superiority of MNDWI over other indices. Conversely, a number of studies (Jain et al. 2005; Rokni et al. 2014; Zhou et al. 2017) have also found that $NDWI_1$ performed better than other water indices – including MNDWI – for delineating the LSW features.

When it comes to SAR data, histogram thresholding (Martinis, Twele & Voigt 2009; White et al. 2015), radiometric thresholding (Matgen et al. 2011; White et al. 2014), active contour models (Horritt et al. 2003) and segmentation (Martinis, Twele & Voigt 2009; Martinis, Twele & Voigt 2011) techniques have been successfully applied for LSW mapping. Statistical active contour models that incorporate both local tones, texture measures, land cover and Bayesian probability rules were developed by Horritt, Mason & Luckman (2001) and Horritt et al. (2003) to delineate flood boundaries using ERS-1 SAR data. Although this method was found to delineate LSW with accuracies of 70% or higher, its construction is complex and will likely be difficult to replicate. More recently, Pulvirenti et al. (2011a) and Twele et al. (2016) carried out flood mapping using fuzzy rules that mainly contextualises local conditions by considering backscatter, as well as topographical and land cover information. However, such information at suitable scale may not be available in many areas. In addition, Pricope (2013) argued that topography based methods for delineating LSW areas are not effective in semi-arid regions with porous sandy soils and low topographic gradients.

Thresholding is the most popular approach for mapping LSW using SAR data (Chini et al. 2017; Manjusree et al. 2012; Twele et al. 2016). In this approach, all pixels with a backscatter coefficient lower than a specified threshold in an intensity image are classified as water. However, the definition of an accurate threshold to separate water from other land cover components is challenging, because the physical and chemical properties of water are highly variable in space and time. Optimal thresholds vary from one image to another and cannot be restricted to one standard value (Du et al. 2016). Schlaffer et al. (2015) proposed that a suitable

threshold value can be found either by visual inspection (manual adjustment) of the grey scale histogram or by using an automatic algorithm. Martinis, Twele & Voigt (2009) argued that the manual adjustment of thresholds is time-consuming and not feasible for near real-time flood monitoring. Several studies (Du et al. 2016; Singh et al. 2015; Yang et al. 2017) have adopted automatic threshold defining methods. These methods are reported to rapidly produce reproducible (reliable) thresholds, thereby reducing delays between the delivery of satellite data (after crisis events) and the provision of satellite-derived crisis information (e.g. flood extent information) to aid emergency management authorities and decision-makers.

Sezgin & Sankur (2004) categorised automatic thresholding methods into six classes.

1. Histogram-shape-based methods involve the analysis of the peaks and valleys of the smoothed histogram (Olivo 1994).

2. Entropy-based methods determine the threshold by minimising the cross-entropy between the input image and the output binary image as a way of preserving information (Kapur, Sahoo & Wong 1985).

3. Attribute-based methods define the threshold-based on the similarity of shape, connectivity, texture and stability between the newly obtained image and the original grey scale image (Liu & Srihari 1997; O'Gorman 1997).

4. Spatial methods define the threshold-based on higher-order probability distribution or the correlation between pixels (Lie 1993).

5. Locally adaptive methods compute a threshold value based on local statistics like range (White & Rohrer 1983), variance (Sauvola & Pietikäinen 2000) or surface fitting parameters (Yanowitz & Bruckstein 1989) of the neighbouring pixels.

6. Clustering-based methods group the grey level data into two clusters, background or foreground, based on iterations (Leung & Lam 1996), minimum error (Kittler & Illingworth 1986), clustering (Otsu 1975) and fuzzy (Jawahar, Biswas & Ray 1997) thresholding.

Each of the above automatic thresholding methods is associated with challenges, particularly in situations where the target pixels constitute a smaller proportion compared to the background pixels or when the background and foreground classes possess unimodal distributions (Sezgin & Sankur 2004). For example, histogram based methods (Glasbey 1993) have high chances of

selecting a good threshold if the histogram peaks are tall, narrow, symmetric and separated by deep valleys. In situations where histograms are fuzzy, Long, Fatoyinbo & Policelli (2014) have proposed a method that iteratively smoothed the histogram using a majority filter. Conversely, algorithms that depend on iterations such as those proposed by Otsu (1975) and Leung & Lam (1996) have been reported to have difficulties in converging, producing multiple convergence points and converging to an illogical thresholding value. However, Otsu algorithm is one of the most widely used automatic threshold methods in delineating LSW features and was adopted in this study. This algorithm determines the optimal threshold by maximising inter-class (water and non-water) variance (Du et al. 2016; Otsu 1975).

Thresholding is useful for producing results quickly and inexpensively. When used on SAR data it is most effective for calm open water with a specular backscatter response, but not for wind-induced rough water surfaces or flooded vegetation with rough surfaces (White et al. 2015). White et al. (2015) and Long, Fatoyinbo & Policelli (2014) argued that the method can delineate flooded vegetation and turbid water with greater accuracy if the threshold is manually adjusted and the approach is used in combination with other techniques such as supervised and unsupervised classifiers. Martinis, Twele & Voigt (2009) stated that the manual adjustment of thresholds has a major drawback, namely that the reliability of the final result strongly depends on the skill of the operator. As a result, they proposed a completely unsupervised technique based on the automatic selection of thresholds. Due to the above mentioned limitations of thresholding, supervised classification was found to outperform thresholding of popular spectral wetness indices in Sarp & Ozcelik (2017) and Nandi, Srivastava & Shah (2017). Furthermore, Amitrano et al. (2018) reported that k-means (83.8%) outperformed SVM (82.8%), thresholding (66.8%) and k-NN (57.2%) for rapid flood mapping using S1 data. The following section expands on the potential and challenges of using SAR data for LSW mapping in complex environments.

2.5 POTENTIAL AND LIMITATIONS OF THE USE OF SAR DATA FOR LSW MAPPING IN COMPLEX ENVIRONMENTS

The potential of using SAR data for LSW mapping has been demonstrated by several previous investigations (Hess & Melack 2003; Hess et al. 1995; Horritt et al. 2003; Pulvirenti et al. 2011a; Townsend 2001). In particular, the application of SAR for mapping FV is well established, mainly because SAR technology has the capability to penetrate vegetation canopies (Klemas 2015; White et al. 2015). However, the presence of water underneath vegetated areas can cause SAR backscatter values to increase significantly due to the double- or multi-bounce interaction

between the specular reflecting water surface and vertical structures of the vegetation, such as trunks and stems (Pierdicca, Pulvirenti & Chini 2018; Pulvirenti et al. 2013). The success of SAR-based LSW mapping techniques is thus dependent on the system parameters (e.g. microwave frequency, polarisation and incident angle) and environmental parameters (canopy type, structure and density). The effects of these characteristics are not independent from each other. They are explained in detail in the following subsections.

2.5.1 Surface roughness dependency

SAR backscatter is directly proportional to surface roughness (Skakun et al. 2016). Smooth and calm waterbodies act as specular reflectors resulting in a large proportion of the SAR signals being reflected in the sensor-look direction instead of being returned to the sensor (as mentioned in previous sections). As a result, LSW features have low backscatter values and appear dark in the image. Conversely, microwaves incident on a rough surface (e.g. urban areas and vegetation canopy) are scattered in many directions (diffuse reflection) and result in brighter tones in the radar imagery (Martinis, Twele & Voigt 2009). Microwaves that have the ability to penetrate the tree canopy and interact with solid surfaces (e.g. tree trunks) and inundated land surface underneath the trees are susceptible to double-bounce or volumetric scattering. The volume scattering mechanism represents multiple scatterings, which are prevalent over forested and agricultural areas, where tree crowns, or vegetation canopy reflect the SAR signal diffusely (Costa 2004; Hess et al. 1995).

Several studies have reported that double-bounce scattering between the flooded surface and tall vegetation can result in underestimation of the flooded areas in vegetated floodplains (Horritt et al. 2003; Martinis et al. 2015; Tsyganskaya et al. 2018b). Inundated areas under forest canopy have higher backscatter values when compared to forested areas in dry conditions. The double-bounce mechanism cause a backscatter enhancement of about 3 to 10 dB based on the VH polarisation at 5.405 GHz (White et al. 2015), resulting in LSW to appear different to what is expected (Pulvirenti et al. 2016b).

Polarimetric SAR can be used to characterise and decompose double-bounce scattering (Plank et al. 2017). The output of decomposition can be used as an input to hierarchical classification to segregate forest from water. Costa (2004) used region-based segmentation of polarimetric SAR interferometry (Pol-InSAR) to reduce the effect of double-bounce on LSW mapping. The authors produced seasonally inundated maps with accuracies exceeding 95% for inundated vegetated areas. However, the interpretation and decomposition of scattering processes based on Pol-

InSAR require substantial ground truth measurements such as tree heights, diameters, density, leaf size and angular distribution, ground roughness and dielectric constant of water (Costa 2004).

The roughness of a surface influences the way in which the signal wavelength captures the surface in the image (Ozesmi & Bauer 2002). Longer wavelengths are generally less sensitive to surface roughness. A rough surface can appear smooth in the P-band (with a specular reflection) and very rough in X-band (with diffuse scattering characteristics). Costa et al. (2002) found that the difference between flooded and non-flooded areas was clearly distinguishable on JERS-1 (23.5 cm wavelengths) images, whereas on RADARSAT-1 (5.6 cm wavelengths) images were more difficult to differentiate.

2.5.2 Incident angle dependency

SAR systems are side looking, therefore the SAR backscatter of LSW features behaves differently depending on the radar incidence angle. Generally, backscatter decreases with an increase in incidence angle (Hess, Melack & Simonett 1990; Manjusree et al. 2012). An increase in incidence angle increases the route that the radar signal has to travel through the canopy layer, which means that the canopy attenuation on the radar signal also increases (Töyrä, Pietroniro & Martz 2001). Manjusree et al. (2012) found that inundated forests appeared relatively bright at incidence angles ranging from 20–49°. Some studies found that the effect of incidence angle was insignificant (Imhoff et al. 1986; Long, Fatoyinbo & Policelli 2014; Ormsby, Blanchard & Blanchard 1985), whereas in others (Hess et al. 1995; Lang, Townsend & Kasischke 2008; O'Grady, Leblanc & Bass 2014; O'Grady, Leblanc & Gillieson 2013; Wang et al. 1995) definite angular dependencies were noted, with smaller incidence angles being preferred for distinguishing flooded from non-flooded forests.

Töyrä, Pietroniro & Martz (2001) compared the response of C-band radar to water at both low (27.5^{o}) and high (47.5^{o}) incidence angles. The study came to two conclusions: 1) at high incidence angles, wind-induced effects are suppressed, while at low angles the return signal from water has similar values to those for dry land; and 2) at angles greater than 45°, the path length through the canopy cover increases and the canopy attenuation prevents the signal from penetrating the vegetation. Santoro et al. (2015) demonstrated that the dependence of the ASAR backscatter on the incidence angle was land cover specific in the São Francisco River, Brazil. LSW features showed the strongest sensitivity to incidence angle among all land cover classes (O'Grady, Leblanc & Gillieson 2013).

2.5.3 Frequency dependency

Canopy penetration is less at higher frequencies, therefore longer wavelengths are better at penetrating vegetation canopy (Töyrä, Pietroniro & Martz 2001). Microwaves at higher frequencies (e.g., C-band 3.8–7.5GHz) tend to interact primarily with the upper portion of the canopy and have less potential for discriminating between water and non-water features in inundated tall forests (Figure 2.4). White et al. (2015) stated that P-band (30−100 cm wavelengths) radar signals penetrate nearly all canopies; L-band signals (15−30 cm) penetrate many canopies; and C-band (3.75–7.5 cm) and X-band (2.4–3.75 cm) signals only penetrate open canopies or dense canopies during leaf-off conditions or if the cover story is dead.

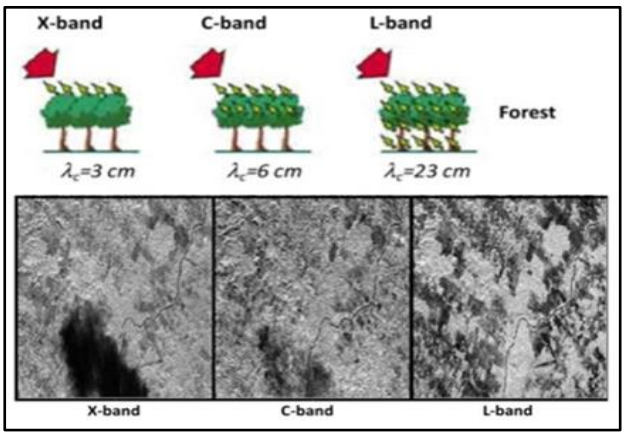

Adapted from Brisco (2015)

Figure 2.4 Response of a forest stand to X-, C- and L-band microwave energy

L-band (15.0–30.0 cm wavelengths) is recommended for LSW mapping beneath forest canopies (Hess et al. 1995; Manavalan, Rao & Krishna Mohan 2017; Pope et al. 1997; Townsend & Walsh 1998; Töyrä, Pietroniro & Martz 2001), but such data are not readily available for some areas. The high spatial resolution X-band on TerraSAR-X (Martinis, Kersten & Twele 2015) and COSMO-SkyMed (Refice et al. 2014) has also been used for mapping vegetated floodplains with encouraging accuracy. Martinis, Kersten & Twele (2015) proposed a fully automated processing chain for near real-time flood detection using high-resolution TerraSAR-X data over Germany with an accuracy of approximately 85%. Unfortunately, both TerraSAR-X and COSMO-SkyMed have poor coverage, especially in Africa (Gstaiger et al. 2012; Martinis, Kersten & Twele 2015). This limitation of L and X bands motivated the development of research in investigating the suitability of C-band SAR to map FV (Martinis, Plank & Ćwik 2018; Twele et al. 2016).

2.5.4 Polarisation dependency

The polarisation of the SAR signal has an effect on the nature and quantity of backscatter. The radar antenna can transmit and receive signals in either horizontal (H) or vertical (V) mode and sensors can be either co- (HH and VV) or cross- (VH and HV) polarised (Henderson et al. 1998). Different SAR polarisations react differently over the same land cover and several studies have evaluated the effect of polarisation for LSW mapping (Clement, Kilsby & Moore 2018; Pulvirenti et al. 2016a; Tsyganskaya et al. 2018b). Polarimetric SAR (PolSAR) sensors coherently transmit and receive both vertical and horizontal polarisations (Brisco et al. 2011). They show the backscatter of any polarisation including nonlinear polarisations. PolSAR images have both the phase and amplitude information, thus providing a wealth of information about physical properties of a surface (Franklin et al. 2018; Pulvirenti et al. 2016b). Compared to co-polarised images, high frequency and multi-polarised radar systems provide more information for differentiating complex LSW features (Hess & Melack 2003; Martinis & Rieke 2015).

Studies on the use of low-frequency (L-band) data observed several advantages of co-polarisation (HH or VV) for the separation of flooded and non-flooded forests (Hess, Melack & Simonett 1990; Manavalan, Rao & Krishna Mohan 2017). Wang et al. (1995) observed that, when the wavelength and incidence angle are identical, canopy volume scattering in flooded forests contributes more to the total backscatter at C-VV than at C-HH polarisations. Conversely, when interacting with vertically oriented vegetation, the response of the C-VV-polarised wave is greater and the penetration into the vegetation is thus reduced. Lang et al. (2015) observed that polarisation ratios, for example the ratio of L-HV and L-HH bands, are useful for distinguishing flooded versus non-FV.

Although many studies have concluded that HH polarisations provide better accuracies for LSW mapping in vegetated environments, the availability of such data is limited in Africa. In addition, Manavalan, Rao & Krishna Mohan (2017) observed that C-band VH polarised images are able to map and quantify partially submerged areas with greater accuracy than the L-band HH polarised images, and as such they may provide an alternative solution.

2.6 DATA FUSION TECHNIQUES FOR MAPPING LSW

Information provided by an individual sensor may be incomplete (e.g. due to cloud cover in multispectral images) or inconsistent and inexplicit (e.g. blurred, hazy). One solution is to make use of data acquired by multiple sensors. Data fusion is, within the context of EO, the process of combining data from multiple sources (or periods) to obtain more information about a particular

area or at a particular time, while attempting to minimise loss or distortion of the original data (Amarsaikhan et al. 2012; Whyte, Ferentinos & Petropoulos 2018). Data fusion approaches are mostly applied to solve temporal and spatial resolution issues, or to enhance image details (Irwin et al. 2017). Data fusion techniques are important for LSW mapping, particularly in heterogeneous environments, because of the complex variability in spectral responses of vegetation, sediments and dissolved substances in the water. Using multiple sources of data allows for the consideration of different interactions with the ground surface and the exploitation of feature extraction capabilities of the different sensors. For example, radar sensors record backscatter attributes in various polarisations, whereas optical sensors record the sum of radiance reflected at different wavelengths (Tiner, Lang & Klemas 2015). As a result, optical images are far more directly interpretable (due to them being comparable to what humans observe) and are rich in information content, while radar images are not easy to directly interpret, but have high confidence/certainty with respect to presence of moisture content, surface roughness and dielectric properties. The fusion of radar and optical data thus has the potential to decrease classification error and increase interpretation robustness.

According to Pohl & Van Genderen (2017), data fusion can be performed at three different processing levels, namely pixel, feature and decision processing levels (Figure 2.5). Image fusion at pixel level involves the merging of multiple datasets at the lowest processing level using techniques such as the augmented vector approach in which the image bands from the different sensors are combined into one common database and classified as if they were obtained by one single sensor (Töyrä et al. 2002). The datasets are simply resampled and co-registered to the same pixel size and map projection respectively. Fusion at feature level requires the extraction of segmented LSW features recognised in the various data sources. These segmented water features (objects) from multiple sources are then fused for further assessment using statistical approaches such as the artificial neural network (ANN) (Pohl & Van Genderen 2017). Lastly, decision level fusion is a method that combines outputs from multiple algorithms to produce a final fused information-rich product. The obtained information is finally combined (based on decision rules) to reinforce common interpretation, resolve differences and furnish a better understanding of the observed LSW objects. As an example, Shah-Hosseini, Safari & Homayouni (2018) used a decision based fusion method to fuse optical and radar LSW maps. These maps were derived from object-based SVM classification in which a voting strategy method was used.

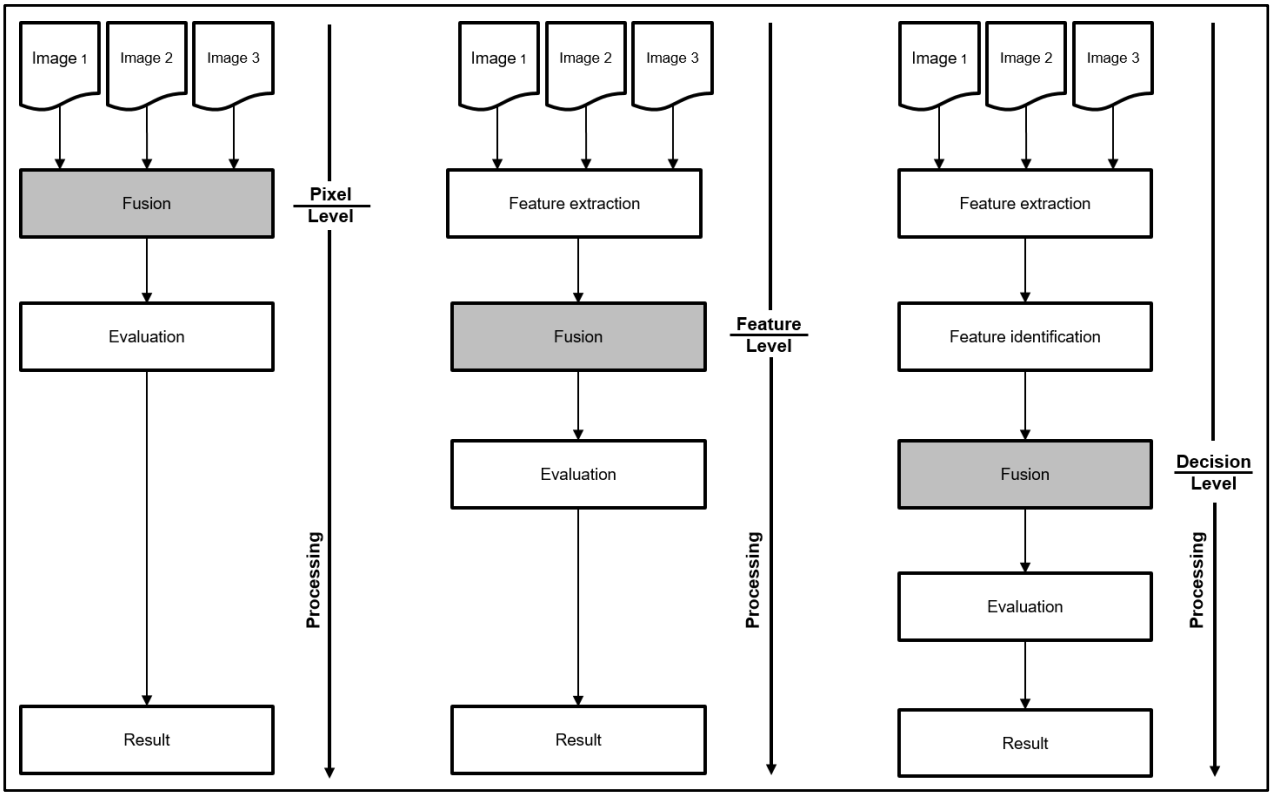

Adapted from Pohl & Van Genderen (1998).

Figure 2.5 Processing levels of image fusion

Recent developments in data fusion for LSW mapping are mainly driven by the: 1) increased availability of data from different, often complementary, sensors and sources; 2) a shift from statistical approaches to more powerful and flexible machine learning algorithms for data classification; 3) the introduction of operational image segmentation algorithms that allow for the processing of datasets at multiple scales; and 4) increased computer processing power.

Based on the above-explained processing levels (Figure 2.5), data fusion can either be done by combining images acquired by different sensors (a multisensor approach) or by the same sensor (e.g., pan-sharpening).

2.6.1 Multisensor or multisource approaches for LSW mapping

Multisensor or multisource image fusion approaches for LSW mapping involve the combination of two or more geometrically registered images (Ghassemian 2016) and can be performed by considering the temporal and spatial resolution parameters of the datasets. In this review, the focus is on multisensor image fusion that involves: 1) radar and multispectral data from different sensors (Bwangoy et al. 2010; Torbick & Salas 2015); 2) multispectral images from different sensors (Chen et al. 2017; Dao & Liou 2015; Zhang et al. 2018); and 3) radar images from different sensors (Mahdianpari et al. 2017).

Although many LSW mapping studies obtained satisfactory results using multispectral and radar RS images separately, the combination of optical and radar imagery has been reported to increase accuracy (Blaes, Vanhalle & Defourny 2005; Joshi et al. 2016). Skidmore, Woodgate & Richards (1986) were pioneers of multisensor work for LSW mapping as they combined single-date images of LANDSAT MSS and SIR-B data to classify water in the Riverine Forest, Australia. The highest classification accuracy was achieved when the two data sources were used in combination, as opposed to individually. Li et al. (1995) and Wang, Koopmans & Pohl (1996) combined ERS-1 and Landsat TM data for wetland identification and FV mapping respectively. The latter study found that the accuracy increased by 7.3% when the two data sources were used in combination, whereas Wang, Koopmans & Pohl (1996) concluded that the multisensor approach improved interpretation capability of RS data in flood mapping. Töyrä et al. (2002) used the Mahalanobis distance classifier (Mahalanobis, Vijaya Kumar & Sims 1996) for wetland mapping on a RADARSAT and SPOT scene, resulting in accuracies of 76% and 80% respectively, whereas a combination of the single-date scenes resulted in an accuracy of 92%. Maillard, Alencar-Silva & Clausi (2008) used RADARSAT-1 and the combination of RADARSAT-1 and ASTER data to delineate palm swamps. They found that the combination of SAR and multispectral-based classification did not yield better results to those that were obtained by only using the visible and NIR bands of the ASTER image. Recently, Whyte, Ferentinos & Petropoulos (2018) developed a synergistic approach for monitoring wetlands based on the multiple-date fusion of S1 and S2 data. They found that the combination of the datasets significantly increased the wetland classification by up to 2.4% in areas with overlapping wetland and non-wetland classes compared to the independent classification of either S1 or S2 images.

Few studies have fused lidar and SAR data for LSW mapping. The application of lidar data is limited by its application to small areas only, complex data processing and high acquisition costs (Joshi et al. 2016; Li & Guo 2015). One exception is Millard & Richardson (2013), who applied RF for wetland mapping using RADARSAT-2 and Reigl LMS Q680 data. Their results showed that the classification accuracy when fusing SAR imagery with lidar derivatives did not exceed the accuracy obtained when only using SAR. Conversely, Irwin et al. (2017) fused three LSW classification maps derived from SAR, optical and airborne lidar datasets. Results showed a water classification uncertainty of 4–9% when using the fused data compared to 17–23% uncertainty when using a single SAR polarisation. Based on these examples, it seems that combining a variety of data sources will increase reliability of LSW mapping in complex landscapes.

2.6.2 Pan-sharpening

Pan-sharpening (PS) or 'refining' is an example of the sharpening techniques whereby a fine-resolution multispectral image is produced by combining a lower resolution multispectral image with a finer resolution panchromatic image (Vivone et al. 2015; Zhang 2010). PS is premised on the availability of a high spatial resolution panchromatic (PAN) band of the same scene and aims to downscale the coarse multispectral imagery to the spatial resolution of the PAN band (Du et al. 2016). It is feasible to use PS with RS images that have coarse multispectral bands and a fine spatial resolution PAN band (approximately the same spectral range as the coarse-resolution bands), such as Landsat TM/ETM+/OLI, SPOT, IKONOS and Quick Bird imagery.

Many pan-sharpening methods have been proposed in literature to produce spatially enhanced multispectral images for LSW mapping (Du et al. 2016; Kaplan 2018; Yang et al. 2017). These methods are divided into two groups, namely the component substitution (CS) and multi-resolution analysis (MRA) group (Li, Jing & Tang 2017). The CS approaches are based on the replacement of a component that is attained by a spectral transformation of the multispectral bands with the PAN image (Li, Jing & Tang 2017). Examples of CS methods are the intensity-hue-saturation (IHS) (Tu et al. 2001), Gram-Schmidt (GS) (Laben & Brower 2000) and principal component analysis (Welch 1987). The CS methods are easy and quick to implement and the generated images yield higher spatial quality with sharper edges. However, the CS methods suffer from spectral distortions since these techniques do not observe different spectral response ranges between the PAN and multispectral channels (Li, Jing & Tang 2017).

The MRA techniques are based on the introduction of the spatial details that are obtained through a multi-resolution decomposition of the PAN image into the up-sampled multispectral bands (Vivone et al. 2015). Examples of MRA methods popularly used for LSW mapping are high-pass filtering (HPF) (Chavez, Sides & Anderson 1991), a trous wavelet transform (ATWT) (Ranchin & Wald 2000) and undecimated or decimated wavelet transform (Nason & Silverman 1995). MRA-based methods are better at preserving spectral information of the original multispectral images than the CS methods. However, MRA methods may cause spatial distortions, such as ringing or aliasing effects, originating shifts or obscured profiles and textures (Li, Jing & Tang 2017). There is no specific PS technique for the mapping of LSW bands as each of them is associated with strengths and weaknesses. For example, Rokni et al. (2015) found that the Gram-Schmidt PAN band provided surface water change detection maps of higher accuracy when compared with IHS and HPF derived from Landsat TM.

Although S2 does not have a PAN band, the principle of pan-sharpening can be used to downscale the lower resolution (20 and 60 m) bands to the high-resolution (10 m) bands. Generally, three approaches exist (Du et al. 2016; Wang et al. 2016). The first approach produces an artificial PAN band by averaging all the 10 m multispectral bands (Kaplan 2018). The second method uses the NIR band, which is close to the SWIR band on the EMS as a PAN-like band (Du et al. 2016). The third approach is to use the 10 m resolution channel with the highest correlation with the band being sharpened (Kaplan 2018). The selection of a PS technique has a direct influence on the derived LSW maps (Du et al. 2016; Wang et al. 2016; Yang et al. 2017). Du et al. (2016) used the HIS, ATWT, HPF and GS PS methods to produce a 10 m MNDWI from which waterbody maps were generated. ATWT was found to produce LSW maps with the highest accuracy. Yang et al. (2017) found that the LSW maps derived from images pan-sharpened with the GS technique were the most accurate as it maintained the consistency of image spectral characteristics. In contrast, Kaplan (2018) found that pan-sharpening using a wavelet principal component resulted in a MNDWI that was the most appropriate for LSW mapping. The authors concluded that more research is needed on deriving accurate high-resolution SWIR bands from S2 data for LSW mapping in vegetated and optically complex LSW environments.

2.7 TRADE-OFFS BETWEEN SATELLITE DATA AVAILABILITY, COSTS, APPLICABILITY AND TECHNIQUES FOR LSW MAPPING

The previous decade has witnessed much improvement in the application of RS in LSW mapping (Čotar, Oštir & Kokalj 2016; Du et al. 2016; Liu, Yao & Wang 2016). Still, LSW mapping using RS imagery is impaired by technical and non-technical constraints. The non-technical limitations include the lack of trained analysts, as well as socio-political and economic constraints (Rahman & Di 2017). Many local governments have mentioned monetary constraints for personnel training and acquisition of hardware and software as a hindrance to the adoption of RS technology for monitoring LSW during flood and drought events (Rahman & Di 2017; Revilla-Romero et al. 2015). Political and organisational factors, as well as resistance by authorities to adopt new science and technology, exacerbate this. It has been observed that it often takes time to convince stringent political structures, particularly in local government, to support the use of RS. Furthermore, licensing of software for manipulating RS imagery complicates the use of satellite imagery. When government agencies or practitioners purchase commercial software it comes with various licensing restrictions which may create distractions. However, the introduction of open access GIS and RS software such as QGIS (Quantum

Geographic Information Systems) and SNAP enable the free processing and analysis of satellite data.

Technical limitations include trade-offs between the temporal, spatial and spectral resolution of sensors, and dealing with contextual complexities of heterogeneous LSW environments (Teng et al. 2017; Yan et al. 2015). The major challenge facing researchers who deal with low and medium spatial resolution multispectral sensors is the issue of mixed pixels. Pierdicca, Pulvirenti & Chini (2018) showed that both high temporal and spatial resolution data are needed for LSW mapping in heterogeneous environments. Due to the fragmentation of land cover features in vegetated floodplains, as well as in landscapes where LSW features are often turbid and eutrophic, RS data with resolutions of higher than 10 m are required (Pierdicca, Pulvirenti & Chini 2018; Thomas et al. 2015). The unavailability of ground observations for the validation of RS data has also been cited as a limiting factor of EO approaches to LSW monitoring (Bello & Aina 2014).

Despite the above mentioned impediments, the future of LSW mapping using RS seems promising for a variety of reasons. The advent of freely available RS data acquired by relatively high spatial and temporal resolution, such as the constellation of Sentinel satellites, has opened up new possibilities for LSW mapping. For example, the S2 constellation increases the chances of obtaining cloud free images during flood events. Cloud-based platforms open up RS datasets and technologies to a much wider audience as users need no technical or financial capacity to establish the large computing resources and data storage devices needed for processing such data (Amitrano et al. 2018). Cloud-based techniques allow for consistent low-key updating of information which can be used for a wide variety of applications (Gorelick et al. 2017). Consequently, the continuous launching of EO satellites provides continuous, up-to-date, low cost data collection for large regions of the globe and is particularly beneficial for LSW mapping.

This literature review has shown that most studies have evaluated the utility of multispectral data for LSW mapping, whereas the use of SAR data is less prominent. The limited number of studies using SAR data can be largely attributed to the cost, availability, interpretation and processing issues associated with this data (Plank et al. 2017). However, based on recent research, the use of SAR data for LSW mapping in FV is increasing. This is attributed to the recent launch of new sensors such as the S1, which can provide data frequently and no cost for long-term. Furthermore, the realisation of the capacity of SAR sensors to penetrate cloud cover and observe

FV (unlike multispectral sensors) has resulted in an increase in the application of SAR data for LSW mapping (Plank et al. 2017; Twele et al. 2016).

Other LSW mapping studies using RS data have demonstrated that in situ observations using smartphones with high-resolution cameras and UAVs provide useful information for the validation of maps derived from satellite data (McCallum et al. 2016; Wang et al. 2018). Local communities can share photos of the onset of flooding on social media such as Facebook and Twitter. For example, the PetaJakarta twitter account in Jakarta, Indonesia, received more than 160 000 tweets and images within 24 hours of the inception of flooding on 5 February 2014 (Holderness & Turpin 2015). Feng, Liu & Gong (2015) used UAVs to collect high-resolution data and demonstrated that they have great potential for rapid and accurate detection of inundated areas in complex urban landscapes. Data from UAVs and mobile phones can enrich the hydrologist's knowledge of LSW dynamics, especially when integrated with satellite data.

A new group of studies focusing on the use of RS in LSW mapping in heterogeneous and optically complex environments has demonstrated an increased potential of employing multisource data for near real-time LSW mapping (D'Addabbo et al. 2016; Franklin et al. 2018) and solving the problem of mixed pixels (Ouled et al. 2018), observing water under FV (Martinis, Kersten & Twele 2015), and trading off between temporal and spatial resolution (Huang et al. 2016). Monitoring the changes of LSW using remotely sensed data generally requires both fine spatial resolution and short revisit time. Data fusion is the most viable solution for providing such data. Huang et al. (2016) fused coarse spatial (375 m) and high temporal (daily) resolution Visible Infrared Imaging Radiometer Suite (VIIRS) data with medium spatial (30 m) and low temporal resolution (16 days) Landsat-8 data to generate real-time LSW maps with fine spatial resolution. Rebelo (2010) combined images derived from ALOS/PALSAR and Landsat TM to map wetland sites with an accuracy of 89%. Franklin et al. (2018) combined data from RADARSAT-2 and Landsat-8 for wetland classification, with an OA of greater than 90%. Although both studies managed to classify wetlands successfully, RADARSAT-2 and ALOS/PALSAR data are not freely available and these studies were carried out in small areas. There is thus a need to evaluate freely available SAR and multispectral data with global coverage, such as the data provided by S1 and S2, for operational LSW mapping and monitoring.

2.8 CONCLUSION AND THE WAY FORWARD

The application of RS for LSW mapping is promising given the development of powerful techniques such as machine learning, data fusion and multisensor approaches, and present day

technologies such as smartphone applications, cloud-based storage and processing systems (e.g. Google Earth Engine), social media and UAVs. However, there is a cut off between academic research on RS for LSW mapping in heterogeneous environments and the operationalisation of remotely sensed data for hydrological applications. A transformation from science-driven approaches to well-defined, user-oriented applications of RS is needed for monitoring floods and the dynamics of waterbodies. Furthermore, given the poor economic situations of most developing countries, LSW mapping techniques should be robust, cheap and autonomous.

Although much progress has been made in sensor development and LSW mapping techniques, three key issues for improving LSW mapping – particularly in complex environments (e.g. vegetated floodplains and landscapes with turbid, eutrophic or optically shallow waterbodies) such as in many places of southern Africa – require more research. First, despite extensive research on land use and land cover classification; there is little research on solving the issue of mixed pixels, which is of particularly relevance to the mapping of LSW using coarse spatial, high temporal resolution imagery. Second, more research is needed to evaluate the potential of the new generation of sensors, specifically those mounted on the S1 and S2 satellites. These data sources hold much potential for LSW mapping in heterogeneous and complex environments as they are freely available, have relatively high spatial resolutions and frequent revisit periods. Finally, the emergence of datasets with high temporal resolution has created an opportunity for autonomous LSW mapping and near real-time LSW monitoring. There is thus a need to compare popular rule-based techniques (e.g. thresholding) with machine learning classification algorithms (such as SVM, k-NN, DT and RF) to determine which of these approaches will be most appropriate for LSW mapping over large and complex areas.

CHAPTER 3: A SPECTRAL UNMIXING METHOD WITH ENSEMBLE ESTIMATION OF ENDMEMBERS: APPLICATION TO FLOOD MAPPING IN THE CAPRIVI FLOODPLAIN[2]

3.1 ABSTRACT

The Caprivi basin in Namibia has been affected by severe flooding in recent years resulting in deaths, displacements and destruction of infrastructure. The negative consequences of these floods have emphasised the need for timely, accurate and objective information about the extent and location of affected areas. Due to the high temporal variability of flood events, Earth observation (EO) data at high revisit frequency is preferred for accurate flood monitoring. Currently, EO data has either high temporal or coarse spatial resolution. Accurate methodologies for the estimation and monitoring of flooding extent using coarse spatial resolution optical image data are needed in order to capture spatial details in heterogeneous areas such as Caprivi. The objective of this work was the retrieval of the fractional abundance of water (γ_w) by applying a new spectral indices-based unmixing algorithm to Medium Resolution Imaging Spectrometer Full Resolution (MERIS FR) data using a minimum number of spectral bands. These images are technically similar to the OLCI image data acquired by the S3 satellite, which are to be systematically provided in the near future. The normalized difference wetness index (NDWI) was applied to delineate the water surface and combined with normalized difference vegetation index (NDVI) to account for emergent vegetation within the water bodies. The challenge to map flooded areas by applying spectral unmixing is the estimation of spectral endmembers, i.e., pure spectra of land cover features. In our study, we developed and applied a new unmixing method based on the use of an ensemble of spectral endmembers to capture and take into account spectral variability within each endmember. In our case study, forty realisations of the spectral endmembers gave a stable frequency distribution of γ_w. Quality of the flood map derived from the Envisat MERIS (MERIS) data was assessed against high (30 m) spatial resolution Landsat Thematic Mapper (TM) images on two different dates (17 April 2008 and 22 May 2009) during which floods occurred. The findings show that both the spatial and the frequency distribution of the γ_w extracted from the MERIS data were in good agreement with the high-resolution TM retrievals. The use of conventional linear unmixing, instead, applied using the entire available

---

[2] Bangira T, Alfieri S, Menenti M, van Niekerk A & Vekerdy Z 2017. A Spectral Unmixing Method with Ensemble Estimation of Endmembers: Application to Flood Mapping in the Caprivi Floodplain. Remote Sensing 9: 1013-1021.

spectra for each image, resulted in relatively large differences between TM and MERIS retrievals.

Keywords: Remote sensing; spectral unmixing; flood mapping; NDWI; coarse-resolution; mixed pixel; fractional vegetation

3.2 INTRODUCTION

Flooding is a natural hazard that causes more damage than any other natural hazard (Dimitriadis et al. 2016; Ganaie, Hashaia & Kalota 2013; Klemas 2015). Flood plains are often densely populated and most vulnerable to flood events. Flood monitoring in such areas is consequently required to mitigate the effects of flood disasters and to assess inundation damages. Floodplain mapping and flood risk assessment are frequently assessed using one-dimensional (1-D) and two-dimensional (2-D) hydraulic models (Costabile & Macchione 2015; Dimitriadis et al. 2016; Teng et al. 2017). A key element for the reliability of such model-based analyses is the accurate setup of the river model, which is primarily related to the representation of the topography and of the land surface hydraulic properties (Costabile et al. 2015; Jafarzadegan & Merwade 2017; Papaioannou et al. 2017). Earth observation by satellites has been shown to be helpful in this respect. The estimation and mapping of hydraulic roughness by (Mtamba et al. 2015), who used Radarsat-2 and Landsat TM images for spatial parameterisation of Manning's roughness coefficient, is a good example. These authors emphasised the challenges of constructing an accurate estimator of hydraulic roughness. Accordingly, the opportunity of calibrating directly the model—estimated flooded area versus time against satellite retrievals of fractional water abundance, as proposed in this study, is a very promising approach to improve model accuracy and reliability. To reduce uncertainties in the parameters used, hydraulic models also require flow data or inundated areas for calibration purposes. Obtaining flow data is often challenging because many of the river systems that are prone to flooding are ungauged, inadequately gauged, or have gauges that are unreliable due to poor maintenance (Costabile & Macchione 2015; Jafarzadegan & Merwade 2017). For hydrological data-scarce and spatially extensive floodplains in remote regions, earth observation is the only viable and cost-effective alternative for mapping inundated areas (Ganaie, Hashaia & Kalota 2013; Klemas 2015). The lack of available flow data, augmented by restricted access, leads to data gaps that make effective and timely monitoring of river basins difficult.

Frequent and accurate quantitative mapping of inundated area using EO data is receiving much interest within the field of flood damage assessment and management (Jain et al. 2005; Long,

Fatoyinbo & Policelli 2014; Skakun et al. 2014). Recent literature documents noticeable efforts of investigating the potential of flood inundation maps, derived from optical and radar image data, to calibrate and validate hydrological models in sparsely gauged or ungauged areas (Khan et al. 2011). In particular, in Khan et al. (2011) used flood maps derived from multispectral images and a distributed hydrologic model to characterise the spatial extent of flooding and associated hazards over sparsely gauged or ungauged basins. These studies demonstrated the utility of flood spatial extent obtained from satellite data to calibrate and evaluate hydrologic models.

Several methods have been proposed to delineate inundated areas using remotely sensed data. These methods make use of: (a) reflected solar radiation (Ganaie, Hashaia & Kalota 2013; McFeeters 1996); (b) emitted thermal radiation (Brakenridge et al. 2007); and (c) microwave backscatter and/or emission (Long, Fatoyinbo & Policelli 2014; Tanguy et al. 2017). Reflected solar radiation methods are effective for assessing seasonal patterns of inundation in areas that have minimum vegetation and cloud cover (Teng et al. 2017; White et al. 2015). These methods are based on the principle that water strongly absorbs NIR radiation. Inundated areas can be mapped by thresholding NIR reflectance or by classifying normalized ratios of NIR, red, green, short-wave infrared, or middle infrared bands. Thermal radiation methods delineate water on the principle that land and water have different thermal inertia and emission properties. Passive microwave methods rely on the large difference in the emissivity of water and land area. For example, in Brakenridge et al. (2007) differentiated land and water using AMSR-E brightness temperature (T_b) values, which are normally much lower for water than for land ($T_b\, land > T_b, water$). Conversely, Shang, Jia & Menenti (2015) used a simplified radiative transfer model and linear model to retrieve the fractional area of water saturated soil (WSS) and standing water from the polarisation difference brightness temperature (PDBT) at 37 GHz measured by the Special Sensor Microwave Imager (SSM/I).

Active microwave methods are based on the assumption that calm water acts as a specular reflector, returning low backscatter to the sensor. The water features will appear darker in the image as compared to non-water features. For instance, authors in Tanguy et al. (2017) successfully (accuracy > 85%) delineated floods by combining very high-resolution Radarsat-2 (C-band, HH polarisation) data with flood return period data estimated for each point of the floodplain from a digital elevation model (DEM). SAR has become an important source of data to map flooded areas as the land surface can be observed regardless of the cloud cover, and during day or night. However, SAR data has been shown to be less effective in inundated areas

with emergent vegetation or when waves are present (e.g., in windy conditions) (White et al. 2015). Woody vegetation is particularly problematic as its relatively rough surface leads to the radar signal being scattered diffusely, with flooded vegetated areas appearing bright on the image (White et al. 2015). The effect of rough surfaces is reduced when very high spatial resolution SAR data is used, but such data—acquired frequently and over large areas—remains costly.

Spectral band ratioing has been the basis for formulating indices such as the NDWI for mapping water bodies (McFeeters 1996). NDWI has been used in many studies for mapping seasonal or long-term changes in water surfaces (Jain et al. 2005; McFeeters 1996). Authors in Jain et al. (2005) found that NDWI produced the best results compared to single-band (NIR) density slicing and Tasselled Cap wetness for mapping flood-affected areas in India using Landsat TM and IRS LISS III data. In Qiao et al. (2011), NDWI was first used to enhance water features, then a histogram segmentation method was applied on a re-defined NDWI based on a pixel-wise distance from the highest value of the NDWI.

Given the temporal variability of flooding, very high temporal resolution data is required for flood monitoring. However, the spatial resolution of current multispectral data products acquired at high (e.g., daily) temporal resolution is low (250 m or lower) which negatively affects the performance of algorithms for accurately delineating inundated areas. In addition, although NDWI thresholding has been shown to be successful in mapping flood extent, it is not suitable in highly heterogeneous areas, especially when emergent or partly submerged vegetation is present (Ji, Zhang & Wylie 2009). This is attributed to the sensitivity of NDWI to vegetation water content (Gao 1996) and to the strong reflectance of vegetation in the NIR band (which is a component of the NDWI). The presence of mixed pixels, mostly at the edges of inundated areas, but in some situations also within flooded areas increases the sensitivity of NDWI to vegetation.

Pixels in satellite images usually contain mixed spectral information due to the high variability in the distribution of land cover components. In its simplest representation, many areas include three land cover types, namely water, soil and vegetation. These types are likely to be mixed within observed targets, even at the relatively high spatial resolution (30 m) of the TM sensor. The spectral signal of a mixed pixel can be represented as a combination of the component spectral signals. The reflectance of a pixel in a particular spectral band may be represented as the sum of the reflectance values of all subpixel components (endmembers) in that band, weighted by the fractional abundance of each component (Gebbinck & Schouten 1995; Keshava & Mustard 2002; Settle & Drake 1993). To deal with the mixed pixel challenge, several approaches such as spectral unmixing (Sarker et al. 2015), fuzzy *c*-means (FCM) and possibilistic *c*-means

(PCM) (Foody 2000), and Bayesian unmixing models (Halimi et al. 2015) have been developed to attribute the fractions of each pixel to classes.

Spectral unmixing (SU) is one of the most popular techniques used for analysing mixed pixels and has been used in studies to derive flood maps in areas where water was partly covered by vegetation (Ji, Zhang & Wylie 2009; Sarker et al. 2015; Settle & Drake 1993). SU is the procedure by which the measured spectrum of a pixel is decomposed into a collection of spectral endmembers and a set of corresponding fractional abundances within the pixel (Gebbinck & Schouten 1995; Keshava 2003; Keshava & Mustard 2002). Generally, SU results are highly dependent on the quality of spectral endmembers. As a rule, the endmembers must be fewer than the number of spectral bands, and all of the endmembers in the image must be specified. A method to improve the selection of endmembers by an adaptive procedure was presented by Sarker et al. (2015). This method improved flood mapping on three different sets of Landsat TM images of three different flood events in Australia. SU can be classified into linear and nonlinear unmixing approaches. In linear SU (LSU) it is assumed that the combination of spectral signatures (endmembers) is linear, meaning that incident radiation only interacts with each component independently, unlike nonlinear unmixing that considers the multiple scattering between different components (Keshava & Mustard 2002). More importantly, in linear unmixing it is also assumed that each endmember has a unique reflectance spectrum, equal for all pixels of the endmember. Linear approaches are preferred because they are simple and flexible. Although only a few studies have applied SU for flood mapping, it has provided successful outcomes. For instance, LSU provided a relatively successful (R^2 = 0.79) overall estimate of the water area in the Senegal River Valley when it was applied to unmix just two endmembers, land and water, using NOAA AVHRR bands 4 and 5 and Landsat TM data (Sandholt et al. 2003). With the exception of Zurita-Milla et al. (2011), relatively little research has been done on unmixing MERIS data to map land cover and none specifically to delineate flooded areas. In one example, authors in Zurita-Milla et al. (2011) applied linear unmixing on MERIS data in order to extract subpixel land cover composition in the fragmented landscape of the Netherlands. This study addressed a rather different problem than ours, since it relied on fractional abundances of land—cover classes determined from land cover data at high spatial resolution.

When LSU is infeasible (Bioucas-Dias et al. 2012), nonlinear SU (NLSU) can be implemented. For instance NLSU was applied for surface water mapping by Xie et al. (2016a) using Landsat-8 OLI to detect wet pixels in a highly heterogeneous urban environment. A quantitative accuracy assessment showed that the applied method gave the best performance in water mapping with a

mean user's accuracy of 92% for test regions. A comparison of linear and nonlinear unmixing was done by Yu et al. (2017) and the study concluded that nonlinear approaches deal better with complex and mixed vegetation surfaces. For the sake of brevity, the reader is referred to Keshava (2003),Jain et al. (2005), Mazvimavi & Wolski (2006), Sarker et al. (2015) and Yu et al. (2017) for an overview, examples and comparison of SU methods. Although both linear and nonlinear approaches have achieved significant progress in decomposing mixed spectral signals, a robust technique does not yet exist, leaving end users with the difficult task of selecting the most appropriate approach (Keshava & Mustard 2002).

In this study, we propose and evaluate nonlinear SU of NDWI observed with MERIS data to map flood extent in the highly heterogeneous Caprivi region. The proposed method relies on the estimation of fractional abundance of water (γ_w by incorporating the fractional abundance of vegetation (γ_v) and three endmembers (soil, vegetation and water) in the NDWI equation. NDVI is used to estimate γ_v which gives the fraction of emergent vegetation within water bodies. The main objective of this work is to assess the methodology for mapping complex vegetated flooded areas using MERIS FR data at 300 m spatial resolution and to evaluate its performance by comparing the results against high (30 m) spatial resolution reference data obtained from Landsat TM imagery. The results are interpreted in the context of extending the method to data supplied by the recently launched S3/OLCI imaging spectrometer, which has a similar spatial resolution and spectral configuration to MERIS FR. The proposed application to Ocean and Land Colour Instrument (OLCI) on board S3 data will permit the monitoring of flood events at daily temporal resolution over large areas. The opportunity of calibrating directly the model-estimated flooded area versus time against satellite retrievals of fractional water abundance, as ours, is a very promising approach to improve model accuracy and reliability. The study also addressed a secondary objective by comparing the proposed method with the conventional LSU.

3.3 MATERIALS AND METHODS

3.3.1 Study area

The study area (Figure 3.1) comprises the Caprivi floodplain, which is about 3200 km^2 in size and is located between 17°30′ S and 18°05′ S and 24°15′ E and 25°15′ E. The Caprivi flood plain receives an annual rainfall of about 900 mm, of which most occurs during the summer months (November to April) (Long, Fatoyinbo & Policelli 2014). Summer is characterised by high temperatures, averaging 30 °C during the day and 15 °C during the night. During the dry winter

season (June to September) the mean temperature during the day is 25 °C and 2 °C at night (Hui et al. 2008).

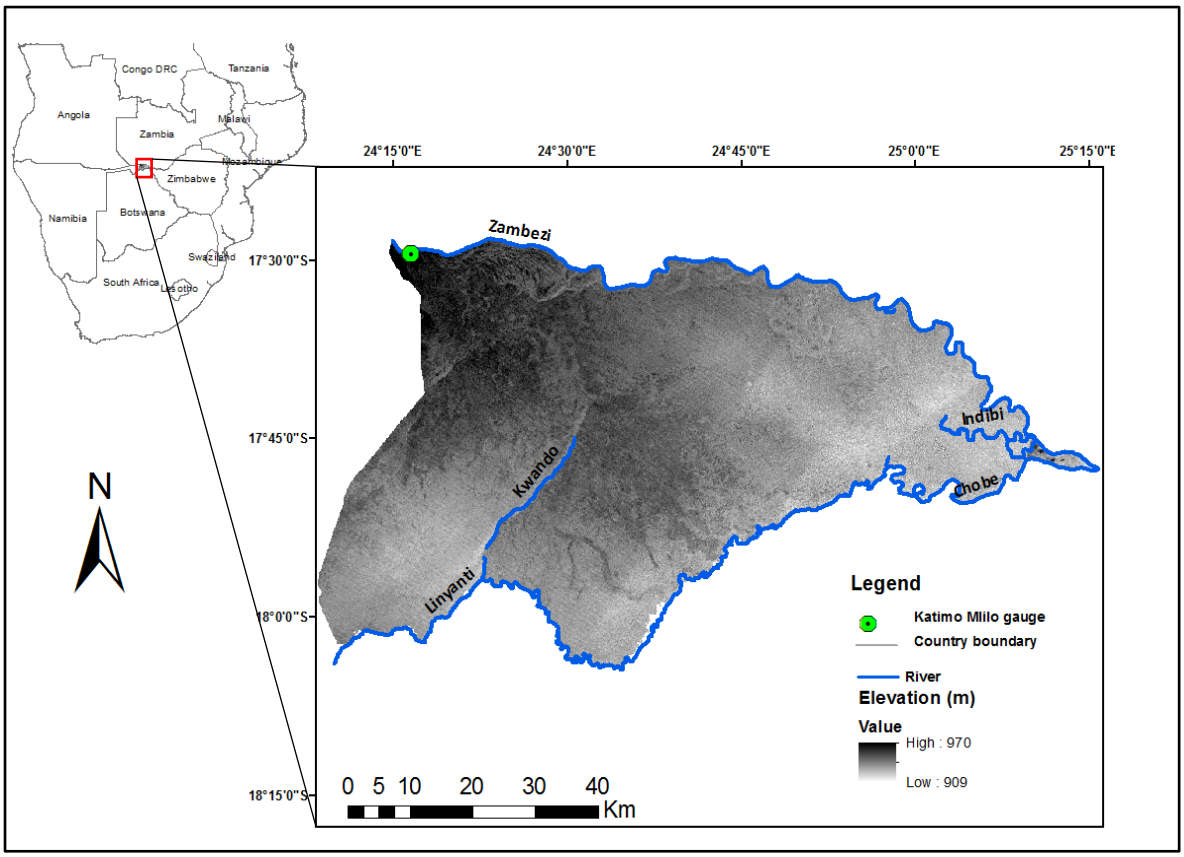

Figure 3.1 Location of the study area

The Caprivi Basin is flanked by four rivers, namely the Zambezi, Linyanti, Chobe and Kwando. The Zambezi River, which is one of the largest rivers in Africa, flows along the border between Namibia's Caprivi region and Zambia. The region is densely populated because it receives more rain than the other more arid regions of Namibia. Flooding is mainly caused by high rainfall in the upper Zambezi River Catchment area in Southern Congo, Angola's Lunda Plateau and North-Eastern Zambia. Flooding is a regular occurrence in the Caprivi, with the most devastating floods experienced in March 2004, April 2008 and 2009. During the April 2008 flood event, the Zambezi River spilled over its banks, leaving a large area inundated. Authors in Miah (1988) reported that in April 2009, the Caprivi region of Namibia experienced the worst flooding in decades after heavy torrential rains across Angola, Namibia, and Zambia increased water levels in the Chobe, Kwando and Zambezi rivers. The impact was substantial since the Caprivi region is home to approximately 60 percent of the Namibian population. Infrastructure, agricultural land, conservancies, livestock and homes were washed away during April 2009. About 2500 to 3000 people living in the area were evacuated to higher ground (UNICEF 2012).

Storm hydrographs and daily water levels at the Katimo Mlilo gauge (Figure 3.1) for the period from 2008 to 2011 are shown in Figure 3.2. The dotted lines show the flood threshold for the water level and discharge as provided by the Namibian Meteorological Department.

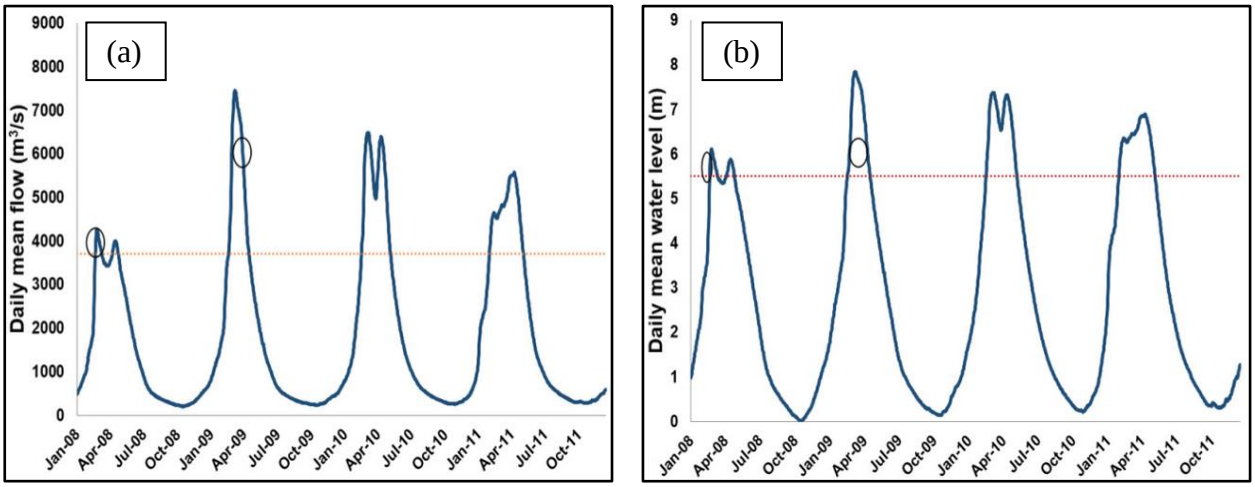

Figure 3.2 Yearly cycle of Zambezi River: (a) discharge hydrograph; and (b) water level for the period from 2008 to 2011. The dotted line shows the flood threshold whereas the black circles point out the flooding events considered in this study

3.3.2 Remote sensing data

There were 16 TM and 88 MERIS cloud free/low cloud cover images for the study area during the flood season March to May and from 2008 to 2011. Among these, only two matching pairs of high (TM) and low (MERIS) spatial resolution data products were available for testing the proposed method. Landsat 5 is a sun-synchronous, near-polar orbit satellite operating at an altitude of 705 km, with a revisit time of 16 days. The TM sensor is a whiskbroom scanner with three visible, three infrared and one thermal bands with 185 km imaging swath. The bands have central wavelengths of approximately 0.49, 0.56, 0.66, 0.83, 1.67, 11.5 and 2.24 μm, respectively. MERIS is a push broom imaging spectrometer operating in the visible and near infrared (VNIR) spectral range from 400 to 900 nm with a spatial resolution of 300 m. MERIS has a three-day revisit time and fifteen spectral bands, programmable in position and bandwidths by ground command, which were set by default to nominal centre wavelengths of 0.413, 0.443, 0.490, 0.510, 0.560, 0.620, 0.665, 0.681, 0.708, 0.753, 0.762, 0.779, 0.865, 0.885 and 0.9 μm with typical bandwidths of 10 nm.

The image dates (Table 3.1) were selected to coincide with the flood events. The choice of the image pairs was primarily based on the shortest interval between acquisition dates, and secondarily on their coverage of the study area. Given that the image pairs were acquired at more or less the same time (apart from the second TM image, which was acquired a day before the

MERIS image), we assumed similar cloud, haze and water surface roughness (due to wind) conditions. The MERIS data were considered to be the primary source of observations, while the higher resolution TM data were used as reference. According to Congalton & Green (2008), high-resolution imagery can be used as reference for land cover mapping, as long it has a ten times higher spatial resolution compared to the imagery being assessed. The 30 m TM images consequently met this requirement for the 300 m MERIS images.

Table 3.1 A summary of EO data used in this study

Image Pair	Sensor	Acquisition Date and GMT	Spatial Resolution	Temporal Resolution
Pair 1	MERIS	17 April 2008 08:09	300 m	3 days
	TM	17 April 2008 08:13	30 m	16 days
Pair 2	MERIS	23 May 2009 08:07	300 m	3 days
	TM	22 May 2009 08:12	30 m	16 days

3.3.3 Pre-processing

Surface spectral reflectance was estimated by performing atmospheric correction of the satellite Top of Atmosphere (TOA) radiance measurements. MERIS data were atmospherically corrected using the SMAC (Simplified Method for Atmospheric Corrections of satellite measurements) algorithm (Rahman & Dedieu 1994) (Processor 1.5.203) as implemented in the open source software package BEAM 5.0 Brockmann Consult, Geesthacht, Germany (Basic ERS and Envisat (A)ATSR and MERIS) (Rahman & Dedieu 1994). The algorithm is a semi-empirical approximation of atmospheric radiative transfer and takes into account the attenuation due to atmospheric absorption and scattering.

FLAASH (Fast Line-of-sight Atmospheric Analysis of Spectral Hypercubes) (Matthew et al. 2000), as incorporated in the Environment for Visualising Images (ENVI) software, was used for converting the TM at-sensor radiance to at-surface reflectance. FLAASH is an atmospheric correction code based on the MODTRAN (MODerate resolution atmospheric TRANsmission) radiative transfer model and can be applied to spectral analysis and atmospheric retrieval methods, such as per-pixel retrievals of precipitable water vapour and aerosol optical depth. Other applications include estimation of scattering for compensation of adjacency effects, cloud detection and smoothing of spectral structure resulting from an imperfect atmospheric correction. FLAASH improves the accuracy of the atmospheric correction by detecting and compensating for sensor-introduced artefacts such as optical smile and inaccurate spectral calibration. MERIS and TM image pairs were co-registered using an image-to-image first order polynomial transformation.

3.3.4 Linear spectral unmixing

The performance of the proposed method, described in Section 3.5, was compared to the conventional LSU method for mapping inundated areas. LSU is a spectral mixture analysis procedure that decomposes a mixed pixel into various distinct components. Pure components are assumed to have a unique reflectance spectrum and be uniformly distributed in separate portions within the field of view. It has been successfully applied for estimating snow-cover fraction of Andes using TM images (Vikhamar & Solberg 2003), forest species abundance in North Pindos National Park, Greece, based on CHRIS/PROBA images (Stagakis, Vanikiotis & Sykioti 2016), crop yield estimation for a grain sorghum field in south Texas using a QuickBird imagery (Yang et al. 2013), and mapping of water turbidity using a HyMap imaging spectrometer (Alcântara et al. 2009). For a given number of endmembers (n), LSU can be expressed as:

$$\rho_k = \sum_{i=1}^{n} \gamma_i \cdot \rho_{i,k} + \varepsilon_k \qquad \text{Equation 3.1}$$

where ρ_k is the observed reflectance of a pixel at wavelength (k);

$\rho_{i,k}$ is the reflectance of endmember i at wavelength (k);

γ_i is the abundance of endmember i; and

ε_k is the residual error.

The unknown fractional abundances γ_i can be estimated with least square fitting of the observed spectra to Equation 3.1, if the number of endmembers is smaller than the number of spectral bands. An over-determined LSU problem was solved using Equation 3.1 based on fifteen MERIS bands and six TM bands (excluding the thermal band) to estimate the fractional abundances of water (γ_w), vegetation (γ_v) and (γ_s). The result of LSU is a grey scale image for each endmember, with pixel values representing the abundances (γ_i) in the range 0–1. The γ_w image was selected for further analysis.

3.3.5 Indices-based spectral unmixing

In this study, endmembers were defined as pure components of water, soil, or vegetation and weighted by their fractional abundance when applying SU. Our new approach relies on the functional relationship between the γ_w and spectral indices (NDWI and NDVI). This is done by assuming that the observed pixel-wise spectral reflectance is a linear combination of the spectral reflectance of soil, water and vegetation endmembers, then using the pixel-wise spectral reflectance to determine NDWI and NDVI. The assumption is that the different components in a

pixel contribute independently to its reflectance (Cheruiyot et al. 2014). The NDWI SU equation for the estimation of γ_w is rewritten by substituting the (pixel) spectral reflectance values as linear combinations of the ones of the three endmembers, together with their abundances, where only γ_w is unknown and can be determined from observed NDWI. Because of the use of NDVI to estimate γ_v the pixel spectral reflectance appears twice in this equation, thus introducing the nonlinear SU (Barati et al. 2011). The use of NDVI modulates the reflectance spectrum of water in response to emergent vegetation. The potential advantage of this method, over conventional LSU, is the reduction of the number of spectral bands for which the endmembers have to be defined and the estimation of γ_v from NDVI. This is done by exploiting two main concepts: (1) the evidence of the strong water absorption in the near infrared and the higher green water reflectance; and (2) the reliability of using NDVI to estimate γ_v (Carlson & Ripley 1997).

Although many spectral indices have been developed for separating water from other land cover classes in remotely sensed multispectral data, NDWI is the most commonly used (McFeeters 1996; Qiao et al. 2011; Xu 2006). It has been used for flood mapping in various studies (Ganaie, Hashaia & Kalota 2013; Memon et al. 2015). NDWI is a dimensionless quantity used as an indicator of the surface wetness. The NDWI makes use of the green band because of the higher green water reflectance. The green band may be substituted by the SWIR or mid-NIR spectral bands to minimise sensitivity to the spectral reflectance of vegetation and maximise the sensitivity to the reflectance of water. In this study, the original formulation of NDWI (McFeeters 1996) was adopted, namely:

$$\text{NDWI} = \frac{\rho_G - \rho_{NIR}}{\rho_G + \rho_{NIR}} \qquad \text{Equation 3.2}$$

where ρ_g is the spectral reflectance in the green region of the spectrum (band 2) and

ρ_{NIR} is the spectral reflectance in the near infrared region of the spectrum (band 4).

NDWI (Equation 3.2) was computed using the TM green and near infrared bands (i.e., band 2 and 4) centred at 560 nm and 830 nm; while with MERIS it was calculated using bands 5 and 13 centred at 559.7 nm and 864.9 nm, respectively.

NDWI values range from −1 to 1, with soil and terrestrial vegetation features having zero or negative values owing to their typically higher NIR reflectance compared to the green spectral reflectance. It has been demonstrated that NDWI thresholds are effective for eliminating exposed soil and terrestrial vegetation and retain open water features (McFeeters 1996; Qiao et al. 2011; Xu 2006). Suitable thresholds are influenced by the proportions of subpixel water/non-water

components. Nevertheless, many authors have applied NDWI > 0 as a threshold to detect presence of water (Gao 1996; Jain et al. 2005; McFeeters 1996).

We give a special relevance to the use of NDWI in Equation 3.6 to estimate the abundance of water in a pixel. While this index clearly provides an excellent separation of water from land as seen in (McFeeters 1996) and Jain et al. (2005), in this study we unmix pixels based on our assumption that a mixed pixel is composed of vegetation, soil and water components. Therefore reflectance in green and (ρ_G) and near infrared (ρ_{NIR}) can be expressed as:

$$\rho_G = \gamma_w \rho_{Gw} + \gamma_v \rho_{Gv} + \gamma_s \rho_{Gs} \qquad \text{Equation 3.3}$$

where ρ_{Gw} is the reflectance in the green band of pure water (endmember) pixels;

ρ_{Gv} is the reflectance in the green band of pure vegetation (endmember) pixels;

ρ_{Gs} is the reflectance in the green band of pure soil (endmember) pixels;

γ_w is the fractional abundance of water;

γ_v is the fractional abundance of vegetation and

γ_s is the fractional abundance of soil.

and

$$\rho_{NIR} = \gamma_w \rho_{NIRw} + \gamma_v \rho_{NIRv} + \gamma_s \rho_{NIRs} \qquad \text{Equation 3.4}$$

where ρ_{NIRw} is the reflectance values in the NIR band of pure water (endmember) pixels;

ρ_{NIRv} is the reflectance values in the NIR band of pure vegetation (endmember) pixels and

ρ_{NIRs} is the reflectance values in the NIR band of pure soil (endmember) pixels.

The fractional abundance of soil γ_s can be obtained as:

$$\gamma_s = 1 - \gamma_v - \gamma_w \qquad \text{Equation 3.5}$$

Incorporating Equation 3.3, Equation 3.4 and Equation 3.5 into Equation 3.2 the γ_w within a pixel can be expressed as:

$$\gamma_w = \frac{\gamma_v \times (D - F) - \gamma_v NDWI \times (E - C) + F - NDWI \times E}{NDWI \times (A - E) + (F - B)} \qquad \text{Equation 3.6}$$

With coefficients A, B, C, D, E, and F being the sums and differences of the endmembers reflectance:

$$A = \rho_{Gw} + \rho_{NIRw} \quad \text{Equation 3.7}$$

$$B = \rho_{Gw} - \rho_{NIRw} \quad \text{Equation 3.8}$$

$$C = \rho_{Gv} + \rho_{NIRv} \quad \text{Equation 3.9}$$

$$D = \rho_{Gv} - \rho_{NIRv} \quad \text{Equation 3.10}$$

$$E = \rho_{Gs} + \rho_{NIRs} \quad \text{Equation 3.11}$$

$$F = \rho_{Gs} - \rho_{NIRs} \quad \text{Equation 3.12}$$

γ_v can be estimated as a function of NDVI as described in Gutman & Ignatov (1998):

$$\gamma_v = \frac{\text{NDVI} - NDVI_0}{NDVI_{inf} - NDVI_0} \quad \text{Equation 3.13}$$

where $NDVI_0$ is the NDVI value of a reference pure water pixel and
$NDVI_{inf}$ NDVI value respectively of a reference pure vegetation pixel.

We adopted a modification of Equation 3.13 applied by Gutman & Ignatov (1998) to estimate the fractional abundance of aquatic vegetation by setting $NDVI_{inf}$ to be equal to the maximum NDVI value of a pure vegetation pixel, while$NDVI_0$ was set to the lowest NDVI value of an open (pure) water pixel within the study area. Selecting the maximum and minimum NDVI values ensures that the derived fractional vegetation cover values in the range from zero to one, given the characteristics of a spatially heterogeneous flooded area. Accuracy was evaluated by comparing the fractional abundance estimated with MERIS FR data with the reference map produced using the TM images. Using γ_v estimated with Equation 3.13 in Equation 3.6 modulates the pixel reflectance at constant γ_w, leading to indices-based spectral unmixing (IBSU).

3.3.6 Automatic selection of endmembers

As explained above, we identified three endmembers, namely pure water, pure vegetation and pure soil. The analyses described above, however, documented a significant variability of the reflectance values within each member, with the consequence that the estimated fractional abundances varied with the choice of the pixels to determine the reflectance spectrum of each endmember. To obtain robust estimates of the reflectance spectra of endmembers we devised a

two-stage procedure. In Stage 1 a number of samples for each endmember are selected, applying thresholds on ρ_G and ρ_{NIR}. The threshold values define typical ranges of the spectral reflectance of water, vegetation and soil. The two thresholds will vary within each endmember. Stage 2 gives an ensemble estimate of the abundances by random extraction of spectral samples from the Stage 1 sets, determining N realisations of the fractional abundances by applying Equation 3.6 and using the median of the N realisations as final estimate of γ_w.

At Stage 1 pure water pixels have been defined as the pixels where ρ_G is greater than ρ_{NIR} (McFeeters 1996). Pure vegetation pixels have been identified on the basis of NDVI values. At first a maximum NDVI value has been evaluated as the 90th percentile of the NDVI values in the image. Then a sample of pixels within a spectral neighbourhood of this maximum value, i.e., within a range of ±0.1 NDVI, was extracted. Pure soil pixels were at first identified by the following conditions: $\rho_{NIR} > \rho_{RED} > \rho_{GREEN}$, $\rho_{NIR} < 0.32$, $\rho_{NIR} > 0.16$ and NDVI < 0.14.The thresholds for soil endmembers were adapted by using as reference the spectral signature of wet and dry soil as found in Agapiou et al. (2016). This procedure yields a number of spectral samples for each endmember. A robust estimate of γ_w is obtained by extracting 40 realisations of the spectral endmembers, applying the unmixing method described above, (Equation 3.6 and Equation 3.13) to each realisation and determining the median $\gamma_w$for each pixel, which yields the final map of γ_w.

The selection of spectral samples was evaluated with the support of a visual inspection of a true colour composite (R = red G = green and B = blue) of the high-resolution (TM) images. Vegetation, water and bare soil are clearly visible in this image and we evaluated whether the location of the spectral samples selected with the criteria described above was correct. Finally, the MERIS and TM reflectance spectra of a number of samples for each endmember were inspected to evaluate whether the selection of samples had been correct. Particularly, the SWIR reflectance in the TM bands 5 and 7 was used to verify the selection based on the reflectance at shorter wavelengths.

In order to evaluate the impact of the choice of endmembers on the results, a sensitivity analysis was performed. The set of endmember pixels was selected by the automatic procedure. The retrieval of the water fractional abundance was repeated 40 times, with each iteration using 20 pixels from the full set of the automatically selected pixels for each endmember. This procedure was repeated three times, each time changing randomly one of the endmember, i.e., soil, vegetation or water, and keeping fixed the remaining endmembers.

NDVI values for full vegetation cover and water were required to solve Equation 3.13. These values are estimates of the maximum and the minimum values of NDVI. To mitigate the impact of outliers, the percentiles 0.5% and 99.5% of the NDVI frequency distribution were used to estimate $NDVI_0$ and $NDVI_{inf}$ respectively.

3.3.7 Accuracy assessment

Accuracy assessment performed in this work mainly relied on the comparison of γ_w estimated with MERIS versus TM, which was used as reference since it was the highest spatial resolution product available on the selected dates. LSU is a widely used method used to map fractional abundance of land features and we also used it as a reference to evaluate our method. It has to be noted that LSU was applied using all the fifteen MERIS and 7 TM spectral bands, while our method used only three spectral bands, which are green, red and near infrared.

Two comparative analyses were performed:

1. Comparison between MERIS versus TM based γ_w obtained with the IBSU (Equation 3.5 and Equation 3.6) to evaluate the impact of image spatial resolution on the γ_w estimated with our method. To compare the γ_w estimated with the MERIS data with the one estimated with TM a grid was constructed with each cell being 1200 m × 1200 m. The mean γ_w of each cell was calculated for both data sets and the cell averages compared. The arbitrary 1200 m × 1200 m grid was selected to sample the same area with both TM and MERIS. Cells of this size included a sufficient number (sixteen) of MERIS pixels.

2. Comparison between MERIS versus TM γ_w estimated with Equation 3.6 and Equation 3.13 with the γ_w obtained with Equation 3.1.

To summarise, inundation maps were produced for each selected image by following these four steps: (1) Perform image pre-processing; (2) Calculate NDWI, NDVI and fractional vegetation cover; (3) Select (automatically) endmembers; and (4) Calculate γ_w with Equation 3.6 and Equation 3.13 using 40 different combinations of endmembers. Accuracy was assessed by comparing the MERIS γ_w map with the TM γ_w map and with the map obtained by applying LSU to the MERIS image data.

3.4 RESULTS

3.4.1 Detection of water and vegetation features with MERIS and TM spectral indices

To evaluate whether the NDVI and NDWI correctly captured water and vegetation features, samples of both indices were taken along four arbitrary transects plotted in Figure 3.3 and Figure 3.4, respectively. In both cases MERIS data was resampled to the TM spatial resolution (30 m) using a nearest neighbour method. Apart from one sample in Transect 1 where the higher spatial resolution of TM image allowed the detection of a narrow water feature (Figure 3.3c), the MERIS and TM data detected the same water features and abundant vegetation. Moreover, the NDWI and NDVI values obtained with MERIS and TM were generally very similar. At a few samples in Transects 3 and 4, taken over prominent water features Figure 3.3e and Figure 3.3f, the MERIS NDWI values were higher than TM (close to 1). Conversely, the MERIS NDVI values at the same location (Figure 3.4e and Figure 3.4f) were much lower than in the TM image. This seems to suggest that, in spite of an increase in mixed pixels due to the lower resolution of MERIS, open water features were well represented by high NDWI and low NDVI values.

To evaluate the consistency of NDVI and NDWI derived from MERIS versus TM, we extracted a larger sample of water features and vegetation cover, using as reference a true colour TM composite image (R: Band 4; G: Band 3; and B Band 2). Compared to TM the image, generally water and vegetation features were better separated by MERIS-based NDWI and NDVI values (Figure 3.5), due to the outliers in the distribution of TM NDVI and NDWI of water and vegetation. The latter implies a smaller class diameter and larger inter-class distance with MERIS data. In general, there seems to be a strong agreement, as shown by the large overlap in the scatter plot (Figure 3.5), between the NDWI and NDVI values of vegetation features as measured by the two sensors.

Finally, we compared the TM and MERIS NDWI and NDVI over the entire study area. The frequency distributions of NDWI and NDVI, as determined with the MERIS and TM images on 17 April 2008, are shown in Figure 3.6. The motivation of this analysis was to evaluate whether MERIS could act as a majority filter when sampling very heterogeneous pixels, assigning to the full pixel the spectral features of the land cover more abundant within the pixel. Figure 3.6 clearly shows that the frequency distributions are comparable, confirming the evidence provided by the smaller samples analysed in Figure 3.3, Figure 3.3 and Figure 3.5. Only relative

frequencies can be compared given the very different numbers of MERIS and TM pixels for a given area of interest.

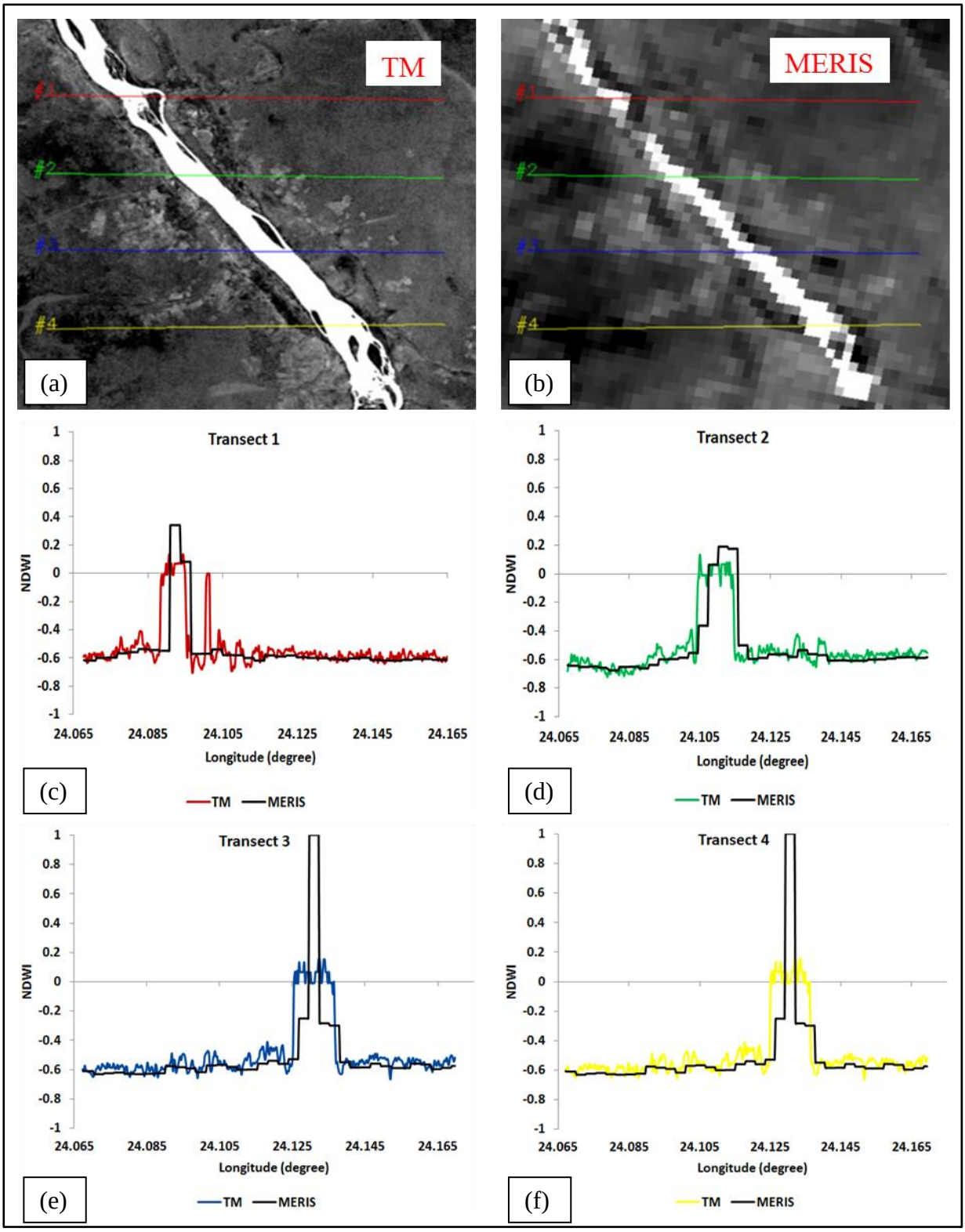

Figure 3.3 NDWI calculated from (a) TM and (b) MERIS images acquired on 17 April 2008 as sampled along four transects (c–f)

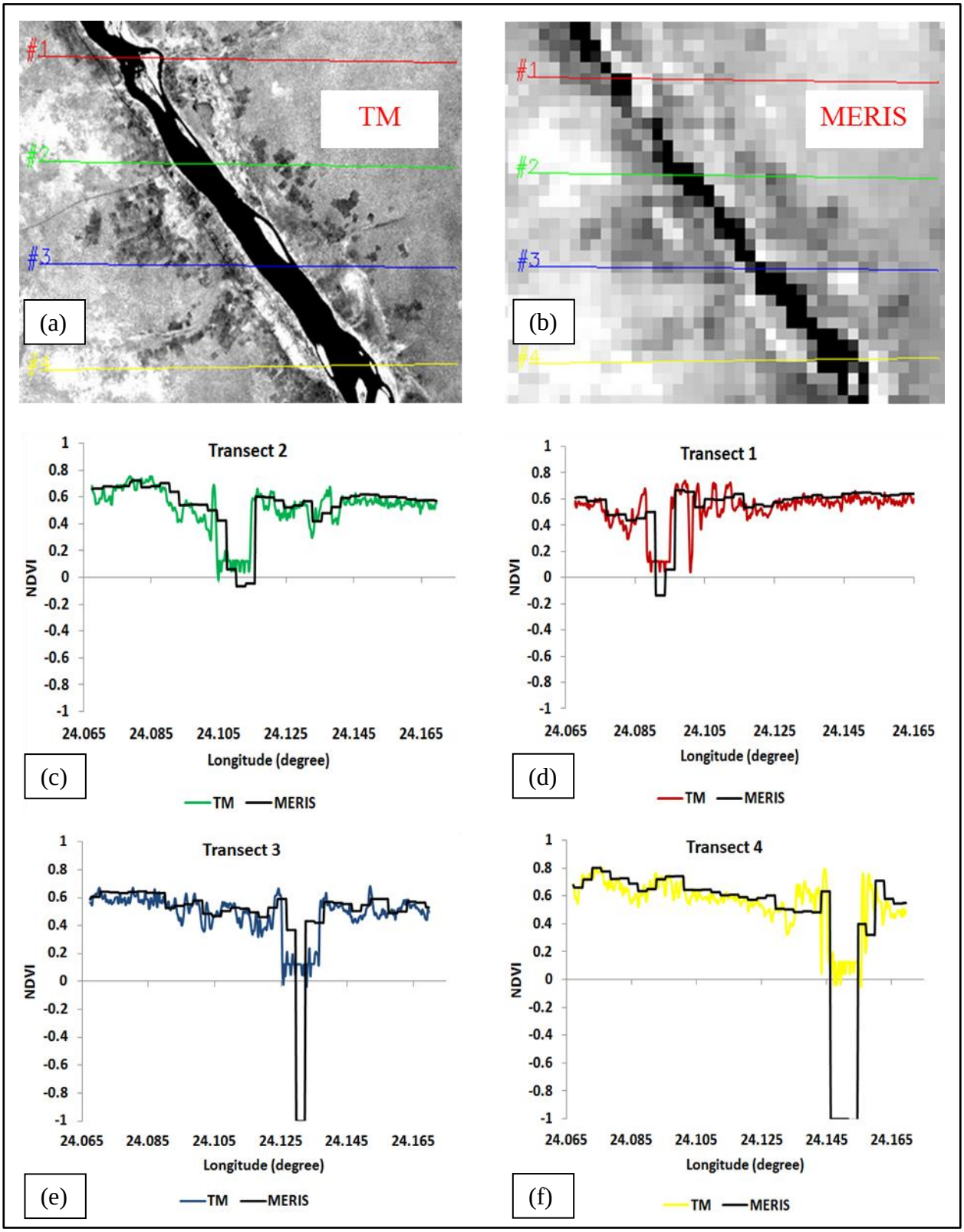

Figure 3.4 NDVI calculated from (a) TM and (b) MERIS images acquired on 17 April 2008 as sampled along four transects (c–f)

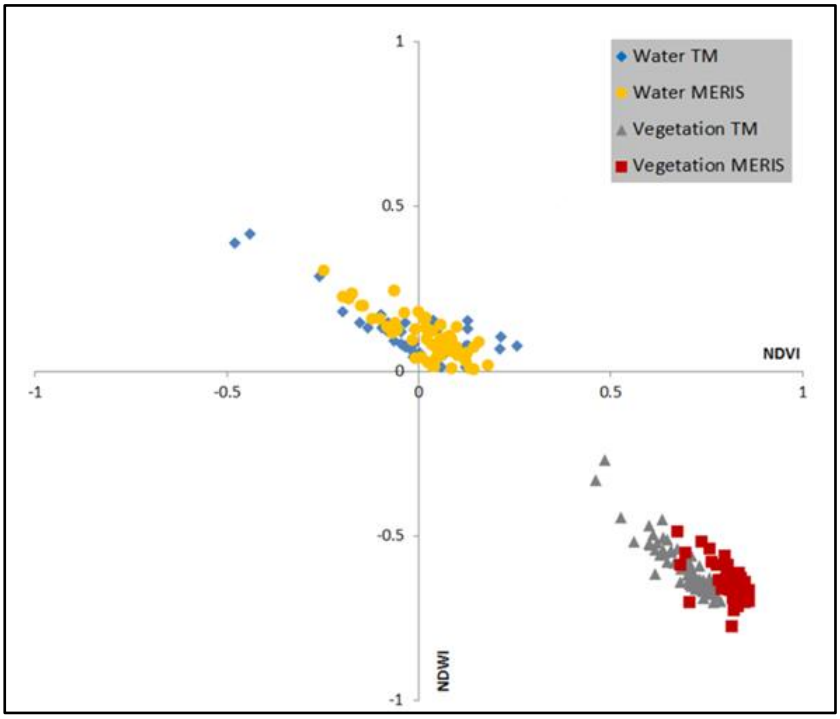

Figure 3.5 Scatter plot of TM versus MERIS NDVI and NDWI over water and vegetation features

The NDWI histograms, particularly the median values, are similar, i.e., mixed water features are captured in a comparable way by the two sensors, which suggest that the coarser spatial resolution of MERIS is not a major constraint on the retrieval of inundated areas. In contrast, the tails of the frequency distributions clearly show the spatial filtering effect of the MERIS lower spatial resolution. The TM observations capture both very high and very low values of NDWI and NDVI due to the higher spatial resolution. This gives a TM frequency distribution with extended tails not present in the MERIS frequency distribution.

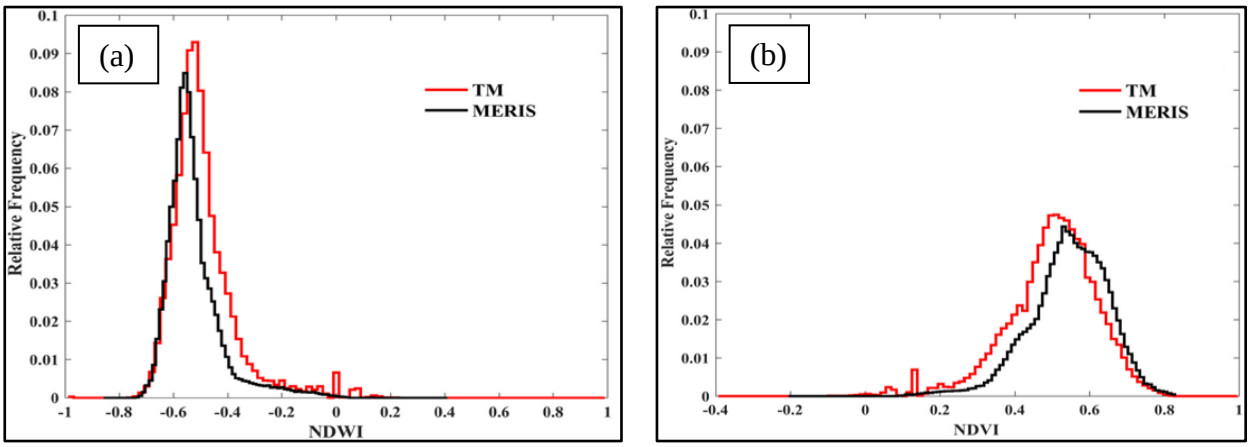

Figure 3.6 Histograms of (a) NDWI and (b) NDVI as generated from MERIS and TM images acquired on 17 April 2008

The small difference in the distributions of NDVI can be accommodated by using different values for $NDVI_{inf}$ and $NDVI_0$ (Table 3.3) when estimating vegetation fractional cover with

either MERIS or TM data. Evidence of some small water and vegetation features captured by TM but not by MERIS (due to its coarser spatial resolution) is noticeable at around NDWI 0–0.2 and NDVI 0–0.1 respectively (see Figure 3.6)**.** This can also be due to mixed pixels of two or more land cover classes in a portion smaller than the pixel resolution.

3.4.2 Endmember selection

The accuracy of the novel IBSU approach and of LSU depends on whether suitable spectral endmembers under dry and wet conditions can be accurately selected. This is particularly challenging for the soil endmember. It is, however, known that the spectral reflectance of soil varies as a function of physical, chemical and biological soil characteristics such as soil moisture content, soil texture (proportion of sand, silt and clay), surface roughness, iron oxide and organic matter content. Spectral reflectance of the water, vegetation and soil endmembers in the green and NIR bands (Table 3.2) were extracted from the MERIS and TM image data using the automatic selection procedure.

Table 3.2 Mean NIR and green spectral reflectance of the automatically selected water, vegetation and soil endmembers (standard deviations shown in brackets)

Image dates	*ρ_{Gw}	ρ_{NIRw}	ρ_{Gv}	ρ_{NIRv}	ρ_{Gs}	ρ_{NIRs}
MERIS 17 April 2008	0.051 (±0.011)	0.034 (±0.012)	0.060 (±0.08)	0.241 (±0.033)	0.081 (±0.016)	0.198 (±0.043)
TM 17 April 2008	0.038 (±0.049)	0.030 (±0.021)	0.060 (±0.011)	0.234 (±0.034)	0.105 (±0.016)	0.252 (±0.026)
MERIS 23 May 2009	0.041 (±0.016)	0.023 (±0.012)	0.056 (±0.009)	0.214 (±0.030)	0.071 (±0.018)	0.187 (±0.057)
TM 22 May 2009	0.026 (±0.046)	0.020 (±0.017)	0.055 (±0.011)	0.204 (±0.033)	0.090 (±0.019)	0.215 (±0.029)

*ρ_{Gw} is reflectance in green for pure water pixel; ρNIRw is reflectance in NIR for pure water pixel, ρGv is for reflectance in green for pure vegetation pixel, ρNIRv Reflectance in NIR for pure vegetation pixel, ρGs reflectance in green for pure soil pixel and ρNIRs reflectance in NIR for pure soil pixel.

MERIS has slightly higher mean water reflectance in the green band (ρ_{Gw}) as compared to TM data. There is no significant difference in the ρ_{Gv} endmember selection between MERIS and TM. A slight difference in near infrared reflectance of vegetation endmembers can be observed when comparing different dates, i.e., the ρ_{NIRv} in April 2008 is higher than that of May 2009 for both sensors. Moreover, ρ_{NIRv} is also slightly different if comparing MERIS and TM values in the same date of May 2009, but this is probably related to the different dates and times of the MERIS and TM observations. In general, MERIS shows much higher reflectance values than TM in both green and NIR for water and vegetation endmembers for the two dates. However, it is the opposite for soil endmembers on both dates. Nevertheless, the scatter plot of green versus NIR reflectance (Figure 3.7) show a good separability of water, soil and vegetation endmembers.

Figure 3.7 shows that differences in the mean reflectance of the mean land cover types are significant and the correlation of NIR and green reflectance reduces the internal diameter of each class, thus improving separability. Water pixels are clustered at the left bottom corner of the 2D plane (Figure 3.7) due to water high absorption of the NIR radiation and high reflectance of the green radiation. The distribution of the MERIS and TM endmembers are comparable.

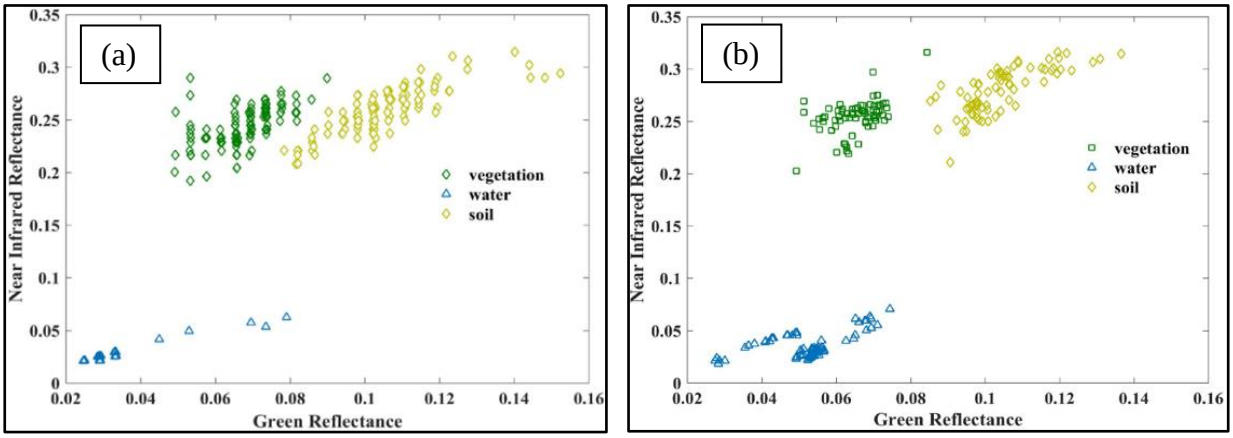

Figure 3.7 Scatter plot of green versus NIR spectral reflectance of an endmembers sample selected automatically from (a) TM and (b) MERIS images on 17 April 2008

The visual inspection of the correspondence of soil, water and vegetation endmembers with the land cover suggested, in a first instance, a correct identification of pure pixels (Figure 3.8). In MERIS images the selected soil endmembers pixels are approximatively selected in the same area as TM (Figure 3.8) even if it is clear that most of the pixels are a mixture of different soils at high and low absorption in NIR, respectively corresponding to wet and dry soils. In a few cases they include a small amount of vegetation (see Figure 3.8).

It remains a challenge, however, to select, even manually, sufficiently large targets to yield pure spectral endmembers in the MERIS images due to the heterogeneity of the study area. Thus, we considered the automatic selection of soil endmembers based on a satisfactory procedure (described in 3.3.6) to narrow down the range of possible endmember reflectance, but not sufficient to obtain the final endmembers. However, the high standard deviation of water endmember selected in TM compared to the other endmembers (Table 3.2) may impact the γ_w estimates, so the selection of endmembers was further refined as described in Section 3.3.6.

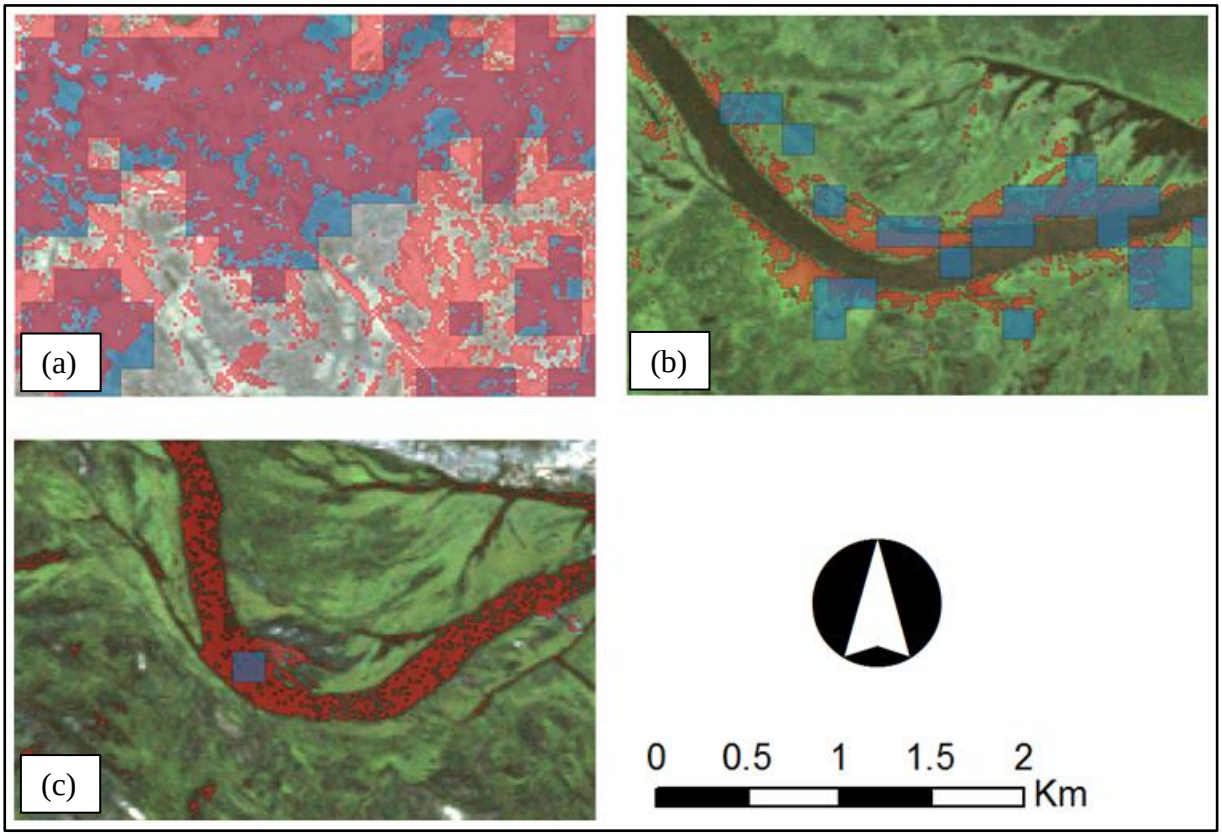

Figure 3.8 Different extents of (a) soil, (b) vegetation and (c) water endmembers selected by the automatic procedure explained in Section 2.6 from TM (red shade) and MERIS images (blue shade) on 17 April 2008 over TM true colour composite (RGB)

Forty realisations of the endmembers were generated and applied in SU (Figure 3.9). The results (Figure 3.9a) show that at the spatial resolution of the TM images, γ_w cannot be estimated with just one selection of endmembers, since the variability across the forty realisations remains large. One realisation appears sufficient to select the vegetation and soil endmembers (Figure 3.9c–f). The final γ_w map was then generated taking the median γ_w for each pixel.

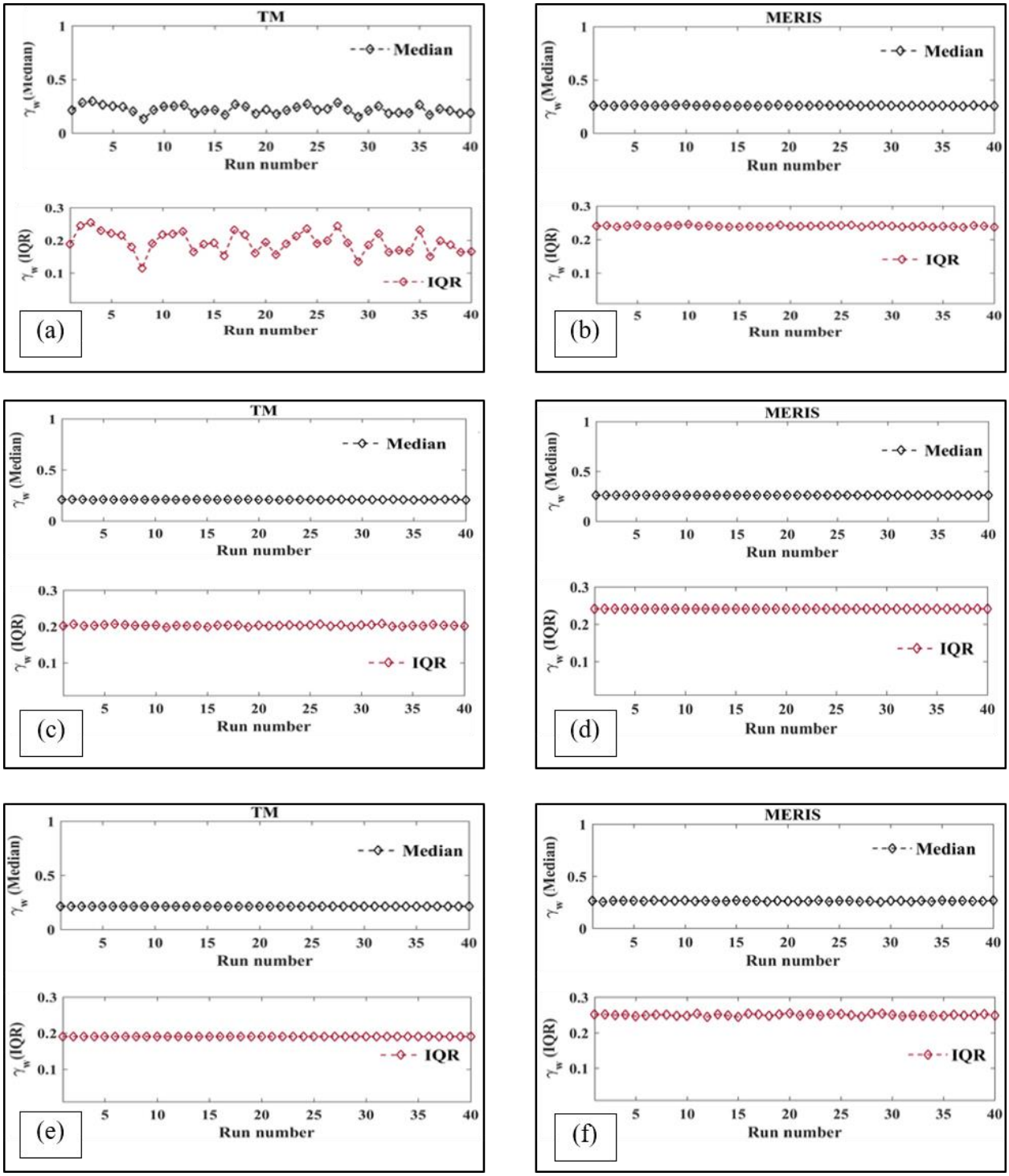

Figure 3.9 Medians (black diamonds) and interquartile range (IQR) (red diamonds) of the γ_w distributions calculated with the proposed IBSU method for the Caprivi study area from TM and MERIS images on 17 April 2008 by randomly changing water (a,b), vegetation (c,d) and soil (e,f) endmembers

As shown in Figure 3.10 this gives a stable estimate of γ_w, since both the median and the interquartile range stabilize after averaging over some twenty realisations.

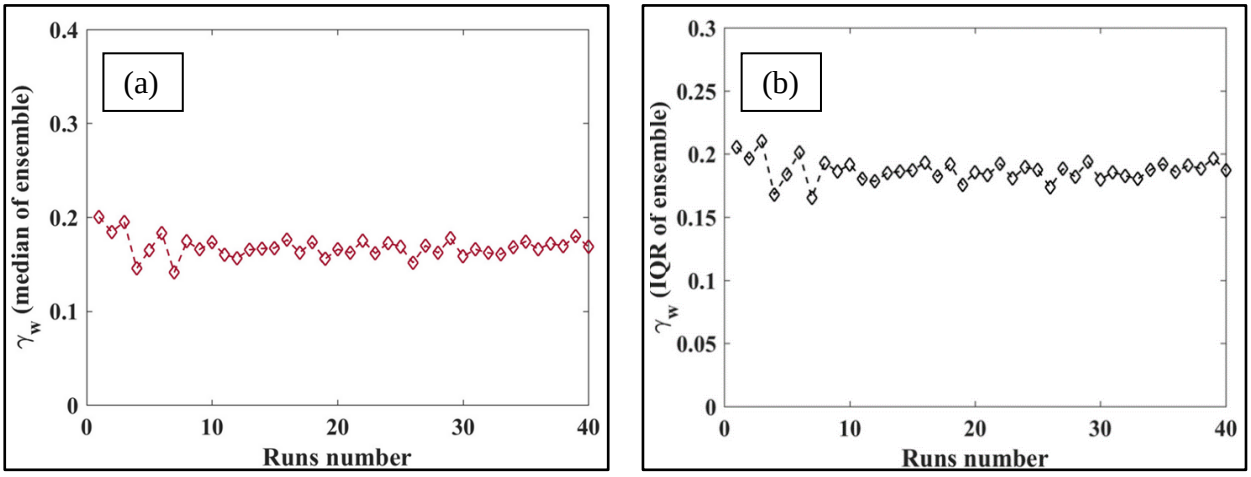

Figure 3.10 (a) Medians; (b) interquartile range (IQR) of ensemble γ_w calculated over the study area as a function of number of runs included in the ensemble

As can be seen in Table 3.3, there is a difference of 0.02 between the $NDVI_{inf}$ of MERIS and TM $NDVI_{inf}$ for the 17 April 2008 images. However, there is a much larger difference of 0.12 in $NDVI_0$ for the same image pair. The value of $NDVI_{inf}$ for the images used in the study was found to be in the range of 0.64–0.74.

Table 3.3 Mean values of $NDVI_{inf}$ and $NDVI_0$ calculated respectively as percentiles 99.5 and 0.5 of NDVI distribution within the study area

Image date	$NDVI_{inf}$	$NDVI_0$
MERIS 17 April 2008	0.69	0.17
TM 17 April 2008	0.67	0.05
MERIS 23 May 2009	0.74	0.05
TM 22 May 2009	0.64	0.00

3.4.3 Spectral indices-based unmixing versus linear spectral unmixing

The γ_w was estimated for both the MERIS-TM image pairs by applying the procedure explained in Section 2.5. The resulting γ_w maps are shown in Figure 3.11. Resultants cell-wise mean values of γ_w, estimated by IBSU with MERIS and TM images over 1200 m × 1200 m cells are shown in Figure 3.12. The bulk of the estimates with TM data is in good agreement with MERIS estimates, i.e., the black zone indicating a high number of observations, while this representation emphasised outliers in the MERIS retrievals, i.e., the spikes in both Figure 3.12a and Figure 3.12b.

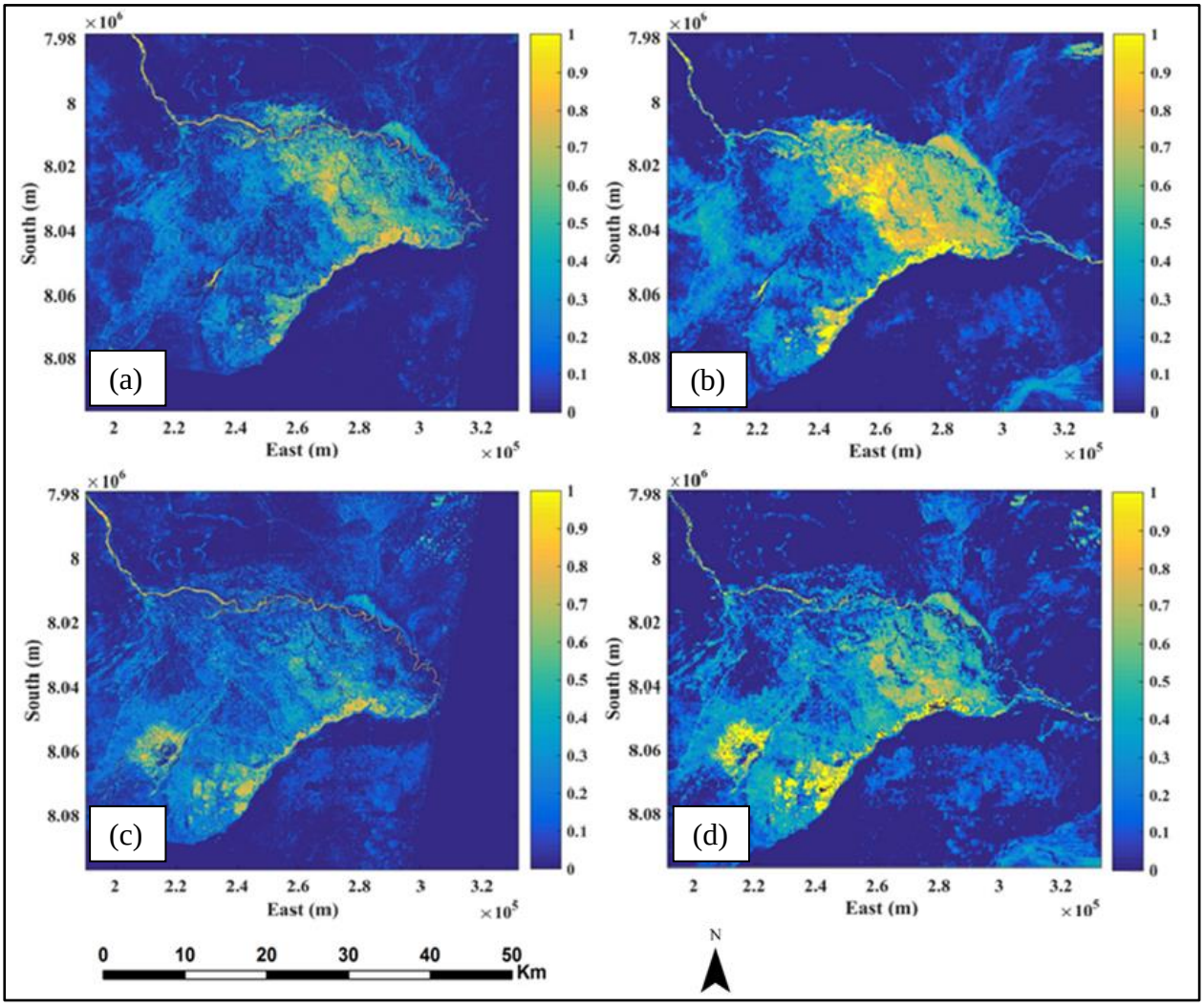

Figure 3.11 The γ_w calculated with the 17 April 2008 (a) TM and (b) MERIS images, compared to the γ_w derived from the (c) 22 May 2009 and (d) 23 May 2009 MERIS images

At a glance it seems that there is a good agreement between MERIS and TM γ_w retrievals, particularly when the spatial patterns and individual features are visually compared. The low resolution images underestimate γ_w in areas with relatively low γ_w (e.g., γ_w < 0.3), particularly when there is also a large proportion of vegetation mixed with water. MERIS overestimates γ_w where γ_w > 0.3 for 17 April 2008 (Figure 3.12a). This is also due to fragmentation of pixels, particularly with vegetation plus water and wet soil, where the lower spatial resolution leads to MERIS sampling to mimic a majority filter, i.e., to assign the entire footprint to the dominant class.

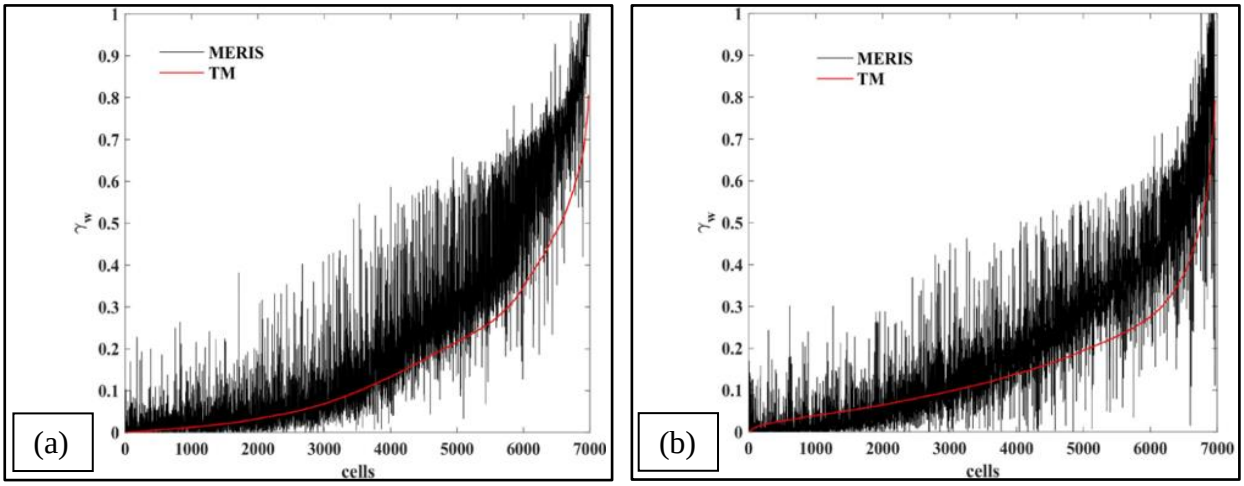

Figure 3.12 Mean fractional abundance estimated by spectral indices unmixing method over the 1.2 km × 1.2 km cells of an arbitrary grid in (a) April 2008 and (b) May 2009 images indices-based spectral unmixing

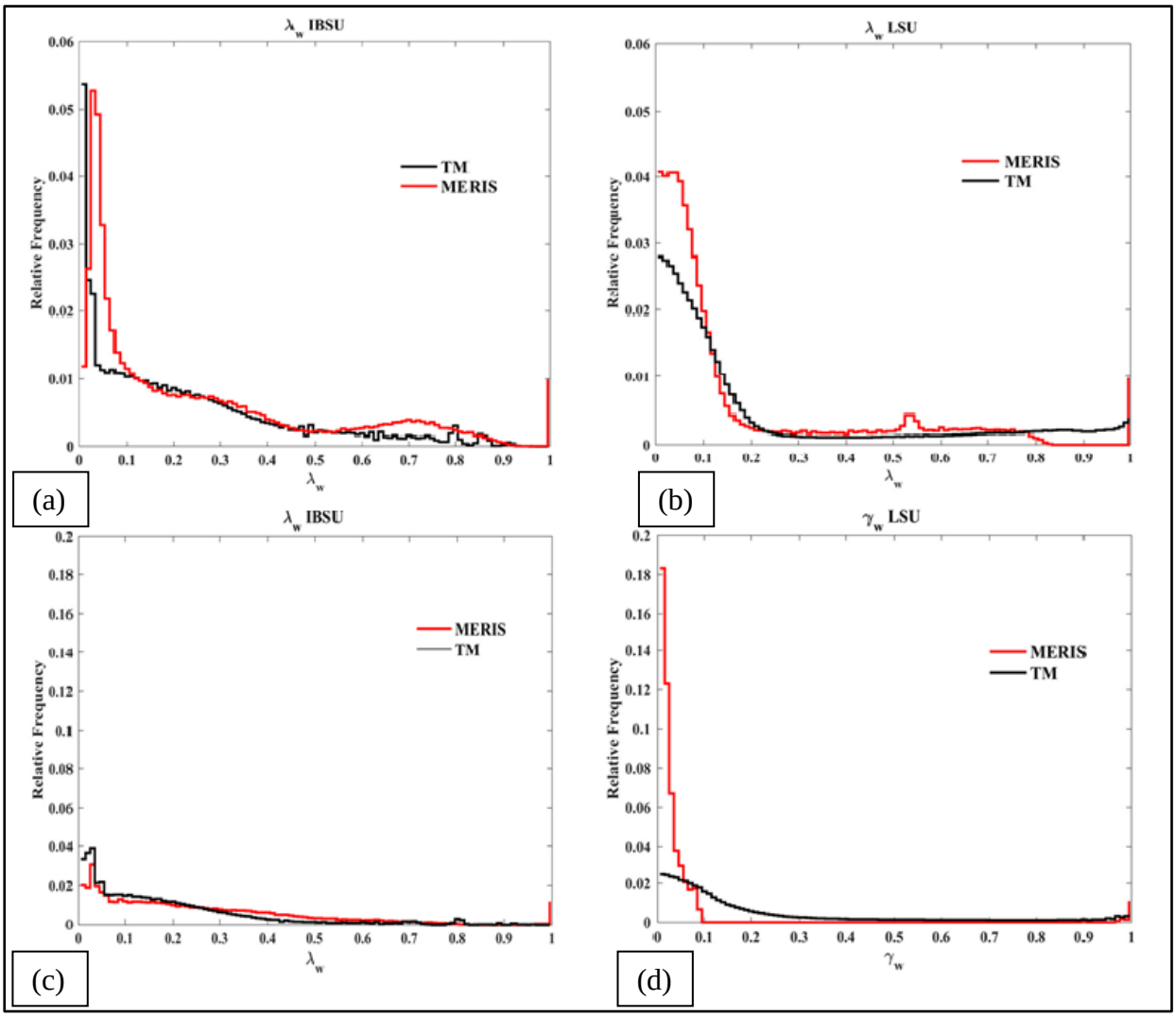

Figure 3.13 Histograms of γ_w retrieved with MERIS and TM data: (a) IBSU on 17 April 2008; (b) LSU on 17 April 2008; (c) IBSU on 22 (TM) (MERIS) and 23 May 2009; (d) LSU on 22 (TM) and 23 (MERIS) May 2009

When the frequency distributions (Figure 3.13a and Figure 3.13c) are compared it is evident that the TM and MERIS retrievals are in good agreement at values of γ_w between 0.3 and 0.5. MERIS mostly overestimates γ_w at high and low values for both IBSU and LSU.

The frequency distributions of γ_w estimated by LSU show relatively large differences between TM and MERIS retrievals on both dates, while the IBSU retrievals are comparable. The fractional abundances calculated using LSU have in all the cases a larger spatial variability compared to those obtained with IBSU (Figure 3.14).

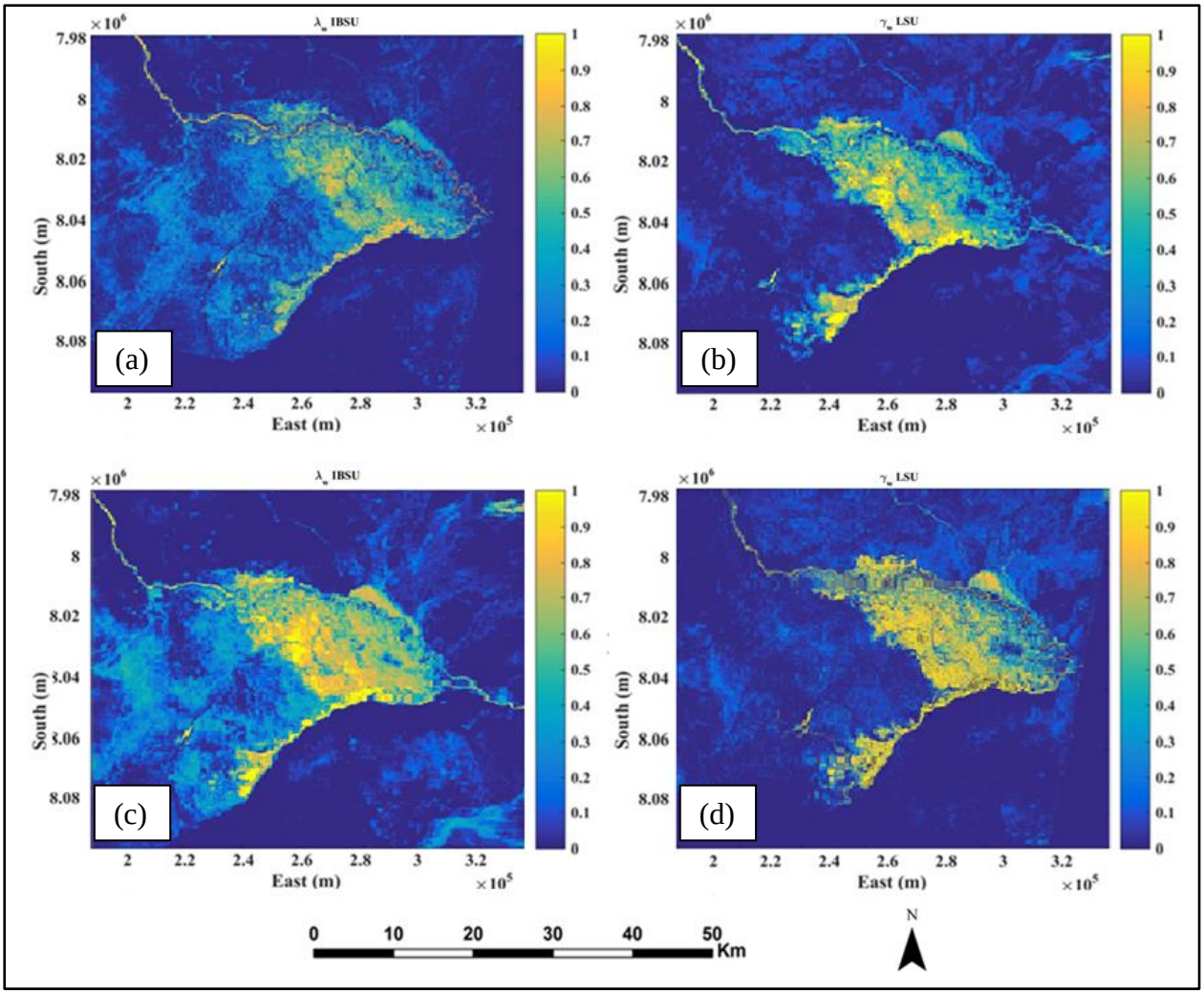

Figure 3.14 The γ_w maps produced by applying (a) IBSU and (b) LSU on the 17 April 2008 TM image, compared to (c) IBSU and (d) LSU applied to the MERIS image of the same date

3.5 DISCUSSION

Remote sensing holds much potential for flood monitoring, but because floods can occur rapidly and affect large areas, sensors with frequent revisit times and large swath widths are required. Most existing optical sensors with these characteristics have relatively coarse spatial resolution. Mapping water surfaces with such imagery has been shown to be challenging (Gebbinck &

Schouten 1995), mainly due to the inability of lower spatial resolution imagery to adequately characterise pixel fragmentation, i.e., the so-called mixed pixel effect. This effect is augmented in vegetated floodplains (Thomas et al. 2015) where the spectral response of vegetation weakens water signatures. For instance, in this study, it was found that NDWI and NDVI derived from low (300 m) MERIS images were generally higher over water surfaces than those generated from high-resolution (30 m) TM images. This finding is in accordance with Cheruiyot et al. (2014), who found that MERIS had higher reflectance values over water surfaces in the green band compared to TM. Most studies (Huang, Chen & Wu 2014; Islam, Bala & Haque 2010; Jain et al. 2006) that make use of coarse-resolution optical imagery for flood mapping do not adequately account for the effects of mixed pixels.

SU has been shown to reduce the effect of mixed pixels, as the measured spectrum of a pixel is decomposed into a collection of spectral endmembers and a set of corresponding fractional abundances within the pixel. However, the success of SU is highly dependent on the quality of spectral endmembers. Selecting pure endmembers in vegetated floodplains is particularly difficult (Sarker et al. 2015; Zurita-Milla et al. 2011). This is demonstrated in Figure 3.14a and b where both the low (MERIS) and high-resolution (TM) data contain γ_w, even in the areas with dense vegetation. Our proposed IBSU method reduces this effect and produced consistent water fraction maps, as evident in Figure 3.13b and Figure 3.14d. However, in Figure 3.11b and c it is clear that the γ_w derived from MERIS included larger areas with high values of water fraction. Lake Liambezi (southwest of the flood plain) did not flood in April 2008, but did flood in May 2009. This result is supported by Mazvimavi & Wolski (2006), which confirmed that Zambezi water will push back into the Chobe River causing floods in the southern part of the flood plain during late May. Homogeneous areas, such as the Zambezi River and Lake Liambezi, generally agreed well with the reference data. When the frequency distributions (Figure 3.13a and c) are compared it is evident that the TM and MERIS retrievals are in good agreement at γ_w values between 0.3 and 0.5. MERIS mostly overestimated γ_w at high and low fractions for both IBSU and LSU. These results show that detection accuracy of water may vary with the portion of the pixel occupied with water.

Authors in Plaza et al. (2004) and Zurita-Milla et al. (2011) argued that the best endmember selection method must consider both spatial and spectral information. We adopted this principle in estimating the fractional abundance of water by automatically selecting an ensemble of endmembers (Figure 3.8) to a produce more complete and robust unmixing results based on only three bands (red, green and NIR). This is in contrast to Boardman (1993) in which a spectral

library was derived based on all bands of all pixels. Spectral bands are also often highly correlated leading to spectral information redundancy (Keshava & Mustard 2002). In addition, materials of different physical composition may exhibit similar spectral properties in a given wavelength range or have spectral properties that cannot be mathematically defined by a linear combination (Keshava & Mustard 2002). Our proposed IBSU allows the type and number of endmembers to vary within each pixel, which yields more accurate fractional information than conventional unmixing methods. IBSU is straight forward and relatively easy to implement because it integrates only two well-known indices, namely NDWI and NDVI. Despite of its simplicity, it was able to successfully model the complex flooded and vegetated landscape of the Caprivi region.

Although the results clearly demonstrate the advantages of using the proposed IBSU method, the accuracy of the results in this study were estimated by using higher resolution (30 m) TM images as reference. This is not ideal as such imagery also contains some degree of mixed pixels. Ideally, in situ data should have be used for verification purposes, but given the temporal nature of flood events and the difficulty in accessing flooded areas; such an approach will in most cases be ineffective. It would thus be of great value if the proposed method can be compared against synchronous, very high-resolution (<10 m) imagery, such as the image data acquired by the Multi-Spectral Imager onboard the S2 satellites, to get a better sense of how well the unmixing procedures are performing.

3.6 CONCLUSION

Timely and frequent observations of flood plains can provide information needed to mitigate the social, economic and environmental impacts of floods. While it is advisable to use finer spatial resolution image data to accurately map flood plains, coarse-resolution products remain best suited for flood monitoring, since they have more frequent revisits and better coverage. It is necessary to understand which remote sensing techniques work best for flood mapping with coarse-resolution products, especially in heterogeneous environments. In this study, we described and demonstrated a new method, called IBSU, to map inundated areas in heterogeneous environments using coarse-resolution MERIS image data and TM as reference. The method mitigates the mixed pixel effect of coarse-resolution imagery and has the advantage of using fewer bands. A new method was developed and applied to obtain ensemble estimates of spectral endmembers and of fractional abundances. Moreover, the combination of NDWI and NDVI into the same equation (Equation 3.6) yielded a nonlinear relationship between γ_w and endmember spectral reflectance.

The results demonstrate that inundated areas can be adequately monitored by coarse-resolution data such as MERIS FR. Notwithstanding the complexity and fragmentation of the Caprivi Basin landscape, the proposed IBSU method produced results that are comparable to those generated using high-resolution TM data. The method, as it stands now, can be used to monitor the floodplain by using the data acquired by OLCI on board S3. LSU shows, instead, relatively large differences between TM and MERIS retrievals, detecting larger spatial variability when compared to the retrievals by the MERIS IBSU method.

Considering the recent launch of the S3 satellite, which offers daily revisit frequency, 300 m spatial resolution and MERIS-like spectral sampling by OLCI, we conclude that the proposed inundation detection technique is a useful method to quickly identify the extent of flooding in large and heterogeneous river basins with a fully automated procedure. More work is needed, however, to investigate how the technique can be used for operational (automated) inundation monitoring. Ideally, inundated areas mapped using SAR data should be incorporated into monitoring systems, especially in areas with persistent cloud coverage. Although some constellations of commercial high-resolution satellites are capable of providing frequent observations (through tasking), the cost of such acquisitions is often prohibitively expensive, especially over large floodplains. Therefore, our study focused on using freely available data.

CHAPTER 4: FLOOD EXTENT MAPPING WITHIN THE CAPRIVI FLOODPLAIN USING SENTINEL-1 TIME SERIES ANALYSIS

4.1 ABSTRACT

The use of synthetic aperture radar (SAR) data has become increasingly relevant for mapping and monitoring floods. Remotely sensed SAR data enable cost-effective, robust and efficient monitoring of large and inaccessible floodplains. Its use of this data has largely been limited by the availability of sensors with sufficiently high spatial resolution and short enough revisit times. The establishment of the Sentinel-1 (S1) satellite constellation carrying a C-band SAR system allows for continuous monitoring of floods at frequent intervals. The purpose of operational flood monitoring services is to promptly and accurately map flood extents from their onset until return to non-flooded conditions. This study evaluates the efficacy of S1 time series data for mapping temporary flooded vegetation (FV) in complex environments. A novel algorithm based on statistical time series modelling of flooded (F) and a non-flooded (NF) S1 pixels is proposed. For each new available image, the probability of temporary flooded conditions is tested against historical images. Specifically, changes in land cover characteristics are considered in the procedure. The resulting inundation maps were compared to those produced using Landsat-8 Operational Land Imager (OLI) imagery and in situ observations. The flood map derived from the proposed algorithm show good spatial agreement with the Landsat-based maps. Overall classification accuracies suggest fused VH and VH/VV images are more effective (84.5%) than VH (78.7%) images alone. The classification accuracies from VH polarisations are significantly lower ($z > 1.96$) compared to those obtained from fused products. These results demonstrate that the fusion of VH/VV and VV has the potential to improve flood mapping in vegetated floodplains.

Keywords: Flooded vegetation, Sentinel-1, SAR, time series, land cover, flood mapping

4.2 INTRODUCTION

Riparian areas, such as the Caprivi flood plain, are flooded almost every year due to excess rainfall in the upper catchments (Zhao et al. 2018). Riverine flooding affects ecological (e.g., ecosystem productivity, species distribution and occurrence, nutrients and sediment dynamics) and socio-economic systems (e.g., causing loss of life, water-borne diseases, destruction of shelter and infrastructure damage). Accurate and detailed near real-time images about the extent of inundated areas provides important information that could guide the identification of the most

prone areas and provide data necessary for mitigating flood hazards (Hong et al. 2015; Twele et al. 2016). In situ observations of flooding are severely limited by the inaccessibility of such areas due to flooding, poor road infrastructure, slide soils and dense vegetation. Remote sensing (RS) techniques that make use of synthetic aperture radar (SAR) and multispectral data have been widely recognised as an alternative method for mapping floods over large geographical and inaccessible areas (Townsend 2001; Twele et al. 2016).

Multispectral imagery is easily interpretable and the extraction of open water from such data is relatively straightforward (Acharya et al. 2016). However, cloud conditions associated with flood events can limit the application of multispectral imagery for flood mapping. In contrast, SAR sensors have all-weather/day-night imaging capabilities (Martinis, Plank & Ćwik 2018). Furthermore, SAR has been shown to partly penetrate vegetation canopies depending on wavelength and polarisation, which helps to observe partly obscured surface water that is difficult to detect using sensors operating in the infrared and visible range of the electromagnetic spectrum (EMS) (Plank et al. 2017; Tsyganskaya et al. 2018b; White et al. 2014).

SAR data have been successfully used for flood mapping in a number of studies. Examples include Kuenzer et al. (2013), Schlaffer et al. (2015), Hong et al. (2015), Giustarini et al. (2016) and Bioresita et al. (2018). These studies focused on detecting open water, assuming perfectly smooth surfaces of high dielectric constants that reflect most radiation away from side-looking SAR sensors. Open water regions were thus identified as regions of low backscatter. This approach successfully delineates open water in most cases, but the presence of emergent vegetation and wind increase backscatter to such an extent that inundated areas display similar backscatter characteristics to those of dry land surfaces (Tsyganskaya et al. 2018b). This is often the case when trees, grass, shrubs and crops are flooded or partially flooded. Under such conditions, a high backscatter is returned due to double-bounce and diffuse backscattering (Plank et al. 2017). The interaction between the SAR signal and the vegetation canopy is volumetric, thus the fraction of vegetation in a given pixel resolution has a significant impact on the SAR signal (Srivastava et al. 2009). This makes flood detection in vegetated areas more challenging than for open water features.

Recently, there have been significant improvements in SAR-based algorithms for observing the influence of flooded vegetation (FV) (Cazals et al. 2016; Mleczko & Mróz 2018; Muro et al. 2016; Plank et al. 2017; Twele et al. 2016; White et al. 2014). The commonality of these algorithms is that they all make use of thresholding to initialise the classification process. However, accuracy of thresholding varies dramatically depending on to the land cover (LC)

characteristics (e.g. rough soil surface, vegetation) within the scene. Theoretical electromagnetic backscattering models have traditionally been used to define appropriate threshold values for mapping FV (Pulvirenti et al. 2013). However, such approaches require detailed soil, vegetation and LC maps to accurately estimate thresholds – data that are often unavailable. There is thus a need for approaches that automatically determine the optimal threshold value for a scene without the need for ancillary data. Such techniques must take into account double bouncing caused by vegetation and the diffuse backscatter from dry and bare surfaces. Martinis, Twele & Voigt (2009) pioneered an approach that applies a split-based automatic thresholding procedure on TerraSAR-X data for near real-time (NRT) flood detection. Other examples of this approach include Matgen et al. (2011), who performed thresholding by modelling the flood class using a nonlinear fitting algorithm under the gamma distribution assumption. Schumann et al. (2010) and Pulvirenti et al. (2012) computed threshold values from the global grey level histograms of SAR data using the popular Otsu algorithm (Otsu 1975). The Otsu method finds a threshold that minimises the inter-class variance between two classes e.g. water and non-water areas.

Automatic processing chains based on thresholding are ideal for rapid flood mapping activities and improve the delivery time of emergency information. Twele et al. (2016) proposed an automated Sentinel-1 (S1) based processing chain for detecting and monitoring floods in NRT. The algorithm was applied to individual SAR images to detect open water. Although an individual SAR image can provide a reasonable estimate of the flood extent, setting a threshold for flood probability based on a single image is risky and inflexible, especially in vegetated flood plains as local variations in LC are difficult to deduce from a single image. However, by analysing a series of SAR images additional information, such as temporary FV, can be extracted by considering backscatter trends and relating changes in backscatter to in situ observations. Temporary FV refers to vegetation that is covered with water after heavy rains or during a flood event (Tsyganskaya et al. 2018a).

This study presents a rapid, simple and semi-automated pixel-based technique for mapping open water, temporary open water and FV over a large and complex region. The method is based on a S1 time series and does not require any ancillary data such as river levels and land cover. For each new available image, the probability of flooded conditions is estimated using the observations from the previous images, and is tested against the probability of dry land conditions. A pixel-adaptive modelling and testing procedure is applied to the cross-polarized backscatter VH and to the polarization ratio VH/VV. User intervention is needed only during the

initial algorithm calibration step, where the desired balance between false flood positives and negatives must be determined.

4.3 MATERIALS

4.3.1 Study area

The proposed technique was evaluated in the Caprivi floodplain, which is on the border between Namibia, Zambia, Zimbabwe and Botswana (Figure 4.1). The Caprivi is an extensive flat sand-filled inland Kalahari basin with elevations ranging from 950 to 980 m.a.s.l. The flood plain is complex and surrounded by four rivers namely the Zambezi (fourth longest river in Africa), Cuando/Kwando, Linyanti and Chobe (Long, Fatoyinbo & Policelli 2014; Skakun et al. 2014). These rivers have different hydrological regimes with diverse habitats, vegetation and aquatic life (Van der Waal 1990). The Zambezi River has a typical autumn flood regime, with a peak flow from March-May. The Chobe River flows in a south-western direction when the Zambezi River starts flooding and changes direction towards the Zambezi (north-east) when the levels of the Zambezi start subsiding. The Kwando and Linyanti Rivers normally flood in June and July respectively (Long, Fatoyinbo & Policelli 2014).

The Caprivi flood plain is a typical savannah ecosystem, consisting of sparsely distributed impalila, riverine, mopane and Kalahari woodlands interspersed with open thick stemmed grasslands (Mendelsohn, Robets & Hines 1997). The main economic activity of the area is tourism, subsistence agriculture and commercial fishing. The Caprivi people have adapted to the flooding cycles by migrating to temporary accommodation in elevated campsites (established by the government) during the wet season. When the floodwater recedes, the communities return to their homes to continue with their agricultural activities.

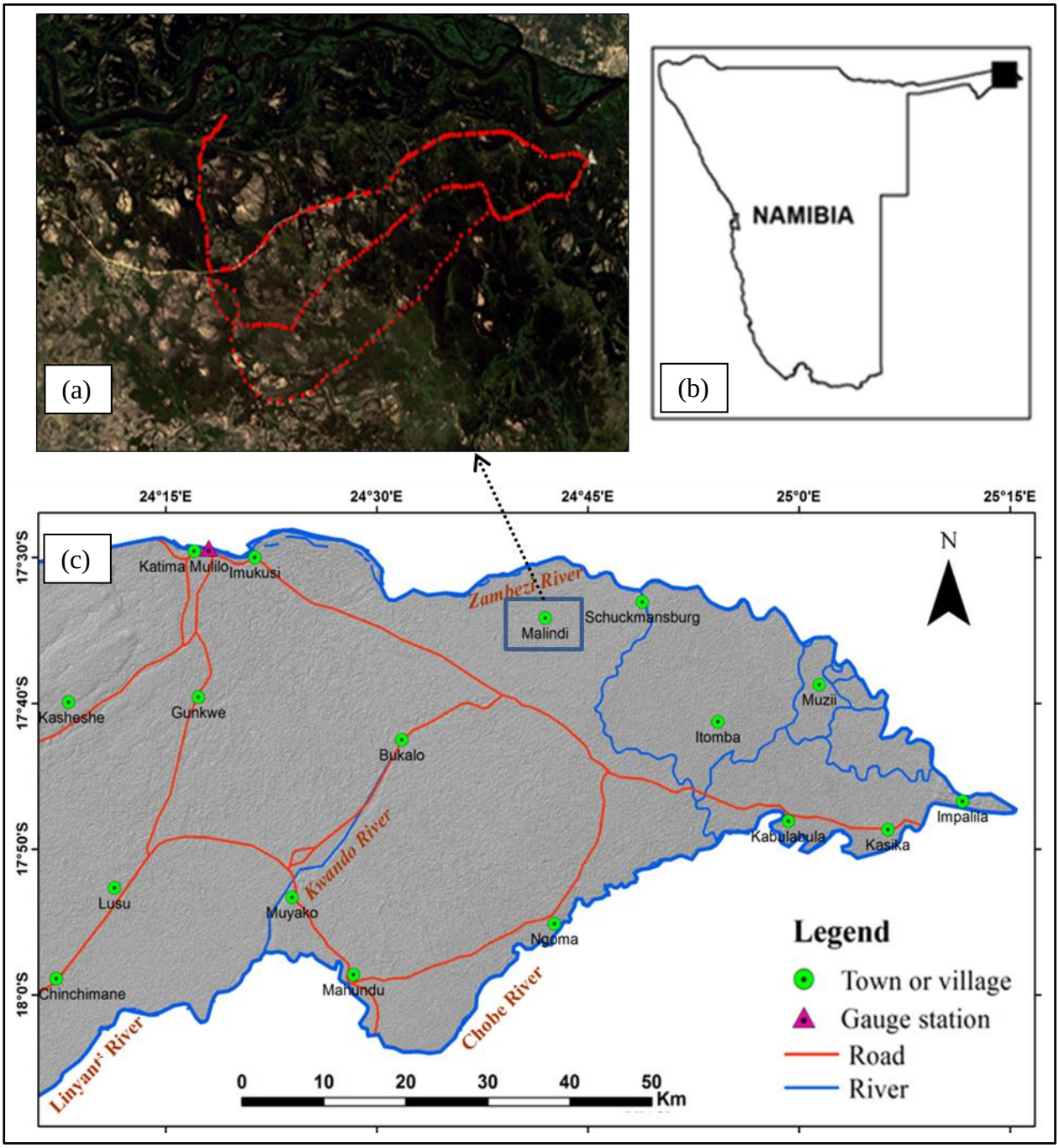

Figure 4.1 Location map of the (a) collected ground observations overlayed on a true colour image (4, 3, 2) of Landsat-8 (10 April 2017), (b) Caprivi area and (c) study area

4.3.2 In situ data collection

In situ observations (Figure 4.1) in the form of global positioning system (GPS) readings were collected for different vegetation types and flood levels during a flood event. The field surveys were conducted from 4–7 April 2017 using a Trimble differential GPS with a sub-metre accuracy. The samples were stratified according to LC, although some samples were inaccessible during the field survey. The visited locations were recorded and were used to extract spectral

data and backscatter dB values from Landsat-8 OLI (LS) and S1 data respectively. The major LC classes observed at the sampled locations were dry soil, temporary open water, open water, flooded vegetation and non-flooded vegetation. Redundant locations were deleted resulting in 725 samples, 125 for each LC type. The samples were also labelled as flooded and non-flooded.

Figure 4.2 shows the rainfall records in the Caprivi floodplain at Katimo Mlilo (Figure 4.1) for the period 1 July 2015 to 31 October 2018 based on the data from Integrated Multi-satellite Retrievals for Global Precipitation Measurement Mission (IMERG). The figure shows that rainfall started around mid-October and ended in early April from 2015 to 2018.

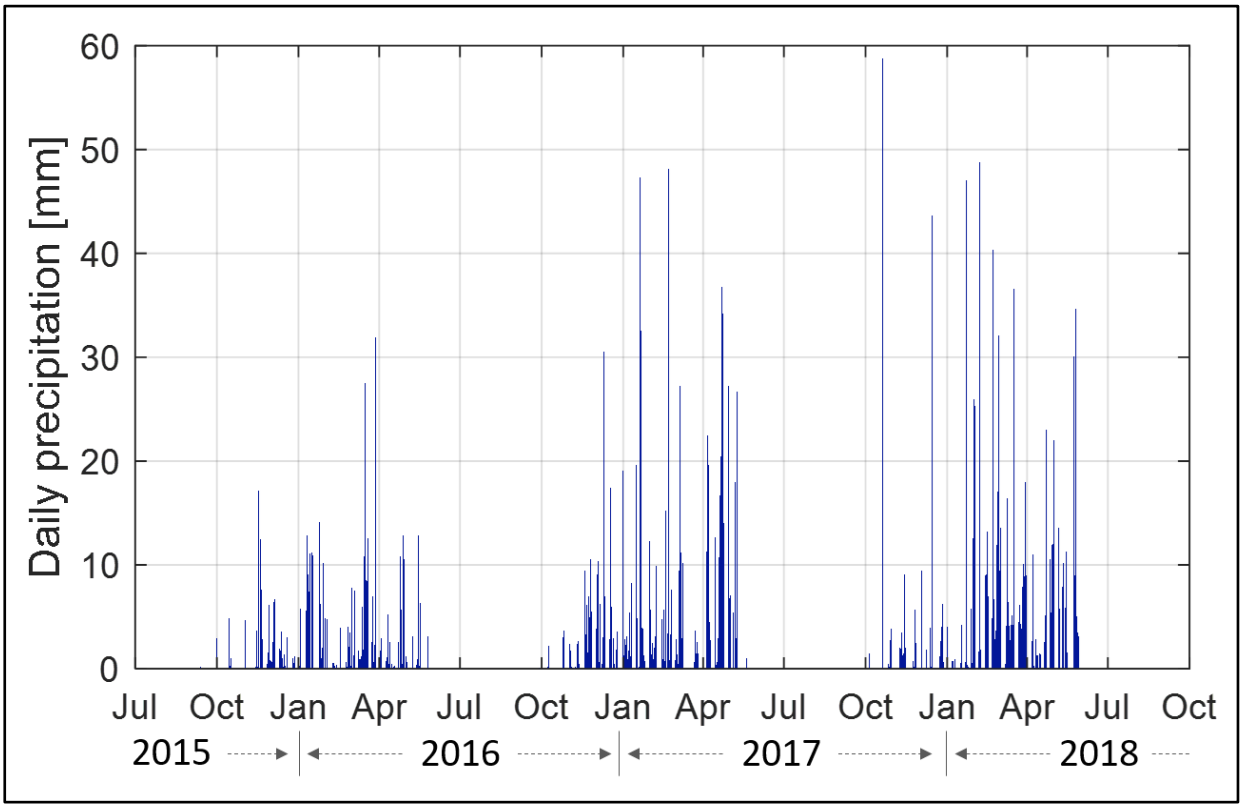

Figure 4.2 Rainfall events in the Caprivi floodplain from July 2015 to October 2018

The peak rainfall occurs between January and March. Therefore, the floods in Caprivi are not as a result of excessive rainfall received in the area. Towards the end of the rainy season, large volumes of upstream water break the banks of the Zambezi River.

4.3.3 Remote sensing data collection

For the period from December 2016 to September 2018, the test area is covered by 55 S1 Interferometric Wide Swath (IW) acquisitions with a regular sampling of 12 days. Only one satellite (Sentinel-1B) in the ascending orbit (6 PM local time) is active over the region. The Ground Range Detected (GRD) products were used for the study. As outlined in Table 4.1, the

images have a spatial ground resolution of 20 x 22 m (ground range and azimuth) with an estimated equivalent number of looks (ENL) of 4.4. Both the VH and the VV polarized images underwent the standard pre-processing operations described in the following section. The study area is illuminated with incidence angles ranging from 33 to 39 degrees. Therefore, it is assumed that the impact of a six-degree difference on backscatter is negligible.

Table 4.1 Outline of the Sentinel-1 and Landsat-8 OLI datasets used in this study

SENTINEL-1		LANDSAT-8	
Satellite	Sentinel-1B	Instrument	Operational Land Imager (OLI)
Mode	Ascending	Acquisition time	10 AM
Acquisition time	6 PM	Product	USGS Surface Reflectance
Incidence angles	33° - 36°	Resolution	30 m
Product	Ground Range Detected	Cloud Coverage	< 40 %
Resolution	20 m (azimuth) x 5 m (ground range)	Number of images	27 (February 2017 - August 2018)
Number of images	55 (December 2016 - September 2018)		

The images of 25 March and 6 April 2017 represented the flood peak and correspond well to the field survey. It also closely matches the cloud free Landsat-8 OLI (L8) images (25 March and 10 April 2017) which were used for algorithm calibration and validation.

4.4 Backscatter analysis

The interaction of water with vegetation and soil changes the nature and intensity of the SAR polarimetric mechanisms (Martinis 2017). Although this study focuses on the Caprivi region, similar pattern elements can be observed in regions with similar climate, landscape morphology and vegetation patterns.

During the onset of the rainy season (from November to February), the backscatter gradually increases in both the co-polarized and cross-polarized components as vegetation canopies develop and water content in both the soil and the vegetation increases. The occurrence of a flood event manifests itself through abrupt changes in the signal amplitude or/and in the nature of the scattering mechanisms (Pradhan, Sameen & Kalantar 2017). Such changes are LC dependent.

Short grass has different backscatter patterns compared to taller grass or shrubs, as graphically illustrated in Figure 4.3. Short vegetation (blue line in Figure 4.3a) show a sudden backscatter suppression as soon as the soil is flooded. Bragg surface scattering due to wind-blown waves and

short vegetation standing out from the water is expected during the entire flood period, characterised by extremely low VH and VV, especially the latter as it is more sensitive to the roughness of the water surface.

In the case of tall vegetation, with vertically oriented elements in the plant geometric structure, a more diverse temporal trajectory can be expected. When the signal penetrates the canopy and reaches the water surface, double-bounce reflection and multiple scattering occur (Plank et al. 2017; Tsyganskaya et al. 2018b). The water-plant interaction attenuates the co-polarization channels (HH and VV), while it has negligible effects on the cross-polarization (HV and VH) intensities. The VH backscatter shows a slight decrease because of the reduction of the above-water vegetation volume. The VH/VV ratio is the most sensitive indicator of FV in a dual polarization system, given that the VV enhancement is larger than the drop in VH. For grasses and sparse shrubs, i.e. the dominant vegetation in semi-arid areas, the increase in VV occurs at the beginning and end of the flood event when the water is shallow, as shown by the red-coloured line in Figure 4.3a. The backscatter drops to bare soil levels when the water is high enough to submerge most of the plant structure. It can reach and even fall below the noise equivalent sigma nought (NESZ) power in the case of open and smooth water surface. In such flooded conditions, the VH intensity is the most suited indicator for detecting the presence of (open) water. In support of these considerations and further assisted by Figure 4.3, four different LC regions in the dual polarization backscatter domain can be identified, namely:

a) a double-bounce region with high (> 10 dB) VH/VV ratio values (this region typically delineates FV and man-made structures);

b) a low overall backscatter region, with low (< -20 dB) VH and low (< -15 dB) VV backscatter values, typically associated with open and calm water surfaces (in the absence of wind) and dry bare soil;

c) a medium backscatter region, with moderate VH and VV values, which includes a variety of LC conditions ranging from vegetated surfaces (grasses, shrubs and crops) to wet bare soil; and

d) a high overall backscatter region, with high VH (> -15 dB) and high VV (> -10 dB) values, mainly comprising dense vegetation.

Therefore, the cross-polarisation and the co-polarisation intensities as well as their temporal trajectories are essential for delineating and mapping FV.

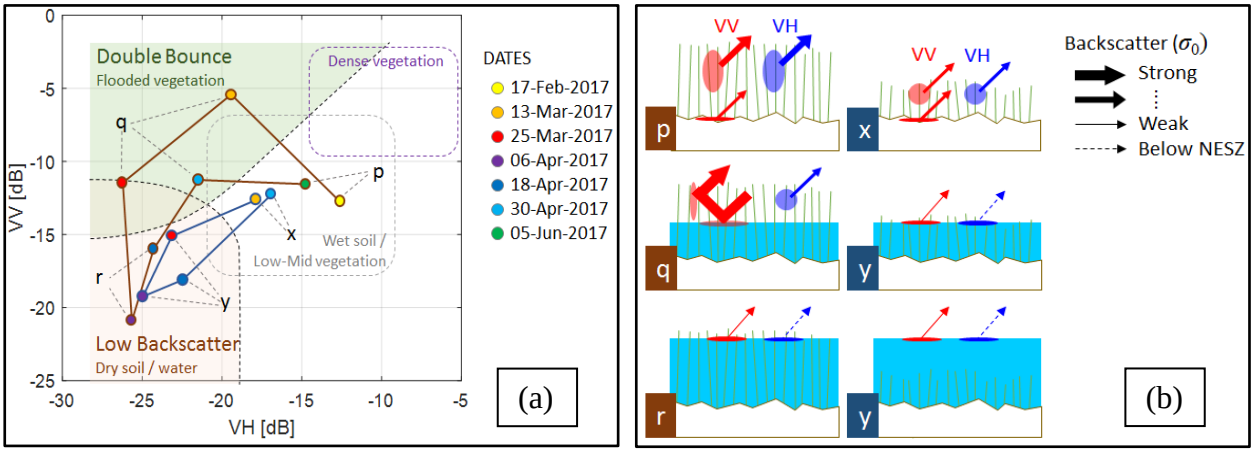

Figure 4.3 The (a) Sentinel-1 time series in the VH and VV plane of two different pixels before, during and after the flood event. The first location (dark red line) has tall grass and shrubs whereas the second (blue line) has short grass. The coloured markers show the temporal information. In the first location, the flooding period started earlier and ended later than in the second location. (b) Schematic representation of the scattering mechanisms for the different LC types and different flood levels. Note: The scenarios r and y essentially produce the same mechanism type and NESZ is the noise equivalent sigma zero. The double-bounce reflection from the water vegetation interaction is indicated by the thick VV arrow in q.

4.5 METHODS

Based on the conceptual analysis presented in the previous section, a novel approach for the continuous monitoring of floods, from their onset until the return to non-flooded conditions, is proposed. The mapping algorithm is entirely based on S1 data, whereas its calibration and validation are based on optical and in situ data. The use of digital elevation models (DEMs), a common ancillary data source for spatial flood constraining, was not considered since the Caprivi floodplain is extremely flat, with an estimated total elevation range of 28 m over a 3 000 km^2 area. As conveyed by the flowchart in Figure 4.4, when a new S1 product is available at time *t*, a new processing cycle, or iteration, is carried out. The cycle receives as inputs the pre-processed VH and VV images at time *t* the stack of the past *L* images and the intermediate products generated by the previous iteration at time *t−1*, comprising the land and water signature models (discussed in section 4.5.1.1) and the flood map output. Every cycle includes a pre-processing, modelling and classification step. The modelling and classification steps, highlighted by the blue-coloured frame in the flowchart, are applied independently to the cross-polarized backscatter, $\sigma^0(VH)$ and to the polarization ratio $\sigma^0(\frac{VH}{VV})$. Although not explicitly reported in Figure 4.4, two distinct sets of intermediate products are thus returned at the end of the iteration.

4.5.1.1 Pre-processing

The S1 VH and VV GRD products are radiometrically calibrated, terrain-corrected and projected to a geographic coordinate system using the Sentinel Application Platform (SNAP). The two polarisation channels are speckle filtered by applying a refined Lee-sigma filter. The polarization ratio (in dB) is computed through simple band subtraction.

4.5.1.2 Modelling

For every up-to-date image at time, or epoch, *t*, the observed pixel feature, y_t, is tested against two probability models: 1) a dry/non-flooded (NF) land model and 2) a flooded (F) land model. The model parameters are predicted from the previous observations and are thus computed at time $t-1$. Simple unimodal Gaussian distributions have been adopted for both models. The outcome of the testing procedure, illustrated in section 4.5.1.3, with pixels labelled as either NF (non-flooded) or F (flooded).

4.5.1.2.1 NF model

The observed feature of a generic pixel with NF conditions at time *t* is described by:

$$y_t \sim \mathcal{N}(\mu_t, v_t) \qquad \text{Equation 4.1}$$

where μ_t is the theoretical mean and
v_t is the variance of the probability density function (PDF) model.

Note that the generic nomenclature y_t can represent either VH or the ratio VH/VV, expressed in dB. The set of the *L* previous observations is defined as:

$$y_t = \{y_n, n = (t-L), \ldots, (t-1)\} \qquad \text{Equation 4.2}$$

where $\boldsymbol{Y}_t$ the observed feature at time *t* is not included.

The observation area is extended to a spatial neighbourhood of Ω of the pixel by defining

$$\boldsymbol{Y}_t = \{\boldsymbol{y}_t, \forall\, pixel \in \Omega\} \qquad \text{Equation 4.3}$$

where Ω is the spatial neighbourhood of the pixel.

Under the assumption of process stationarity, the NF distribution parameters can be estimated from the samples in Equation 4.2 and Equation 4.3 by means of:

$$\check{\mu}_t = \langle \boldsymbol{y}_t \rangle \quad \text{Equation 4.4}$$

$$\check{v}_t = \text{var}\,(\mathbf{Y}_t) \quad \text{Equation 4.5}$$

where $\langle . \rangle$ represents the sample mean and

$(.)$ represents the sample variance estimators.

Note that the assumption of stationarity is reasonable only for short temporal intervals (a maximum of 1-1.5 months) and thus for low L values. Since the Caprivi area is covered by S1 data every 12-days, L was set to three. The neighbourhood Ω was set to a 5 × 5 spatial window centred on the pixel. The decision to account for a spatial neighbourhood in the variance was motivated by the intrinsic higher uncertainty of variance estimations compared to those of means. The bound was implemented as a function of $\check{\mu}^{[VH]}$, i.e. the estimated $\check{\mu}$ for VH [dB]. This constraint is expressed as:

$$v = \max\left\{\check{v}\left[0.16\left(\check{\mu}^{[VH]} + 25\right) + v_0\right]^2\right\} \quad \text{Equation 4.6}$$

where v_0 is set at -3.5 for VH and

v_0 is set at -3.5 + $\sqrt{2}$ for VH/VV.

For the VH feature case, the application of Equation 4.6 leads, for instance, to a minimum standard deviation of 3.5 dB and 1 dB for estimated $\check{\mu}$ values of -25 and -10 dB respectively. It is reasonable to assume that weak scatterers, with normalized radar cross-section close to the NESZ (reported at -25 dB for S1), are more affected by the thermal noise than stronger scatterers.

4.5.1.2.2 F model

Similarly, to the NF case, the flooded pixels are statistically modelled as:

$$y_t \sim \mathcal{N}(\mu_t^F, v_t^F) \quad \text{Equation 4.7}$$

In this case, however, the model is not pixel-adaptive. The same set of parameters μ^F, v^F is adopted for all the pixels. To account for all the pixels classified as flooded in the previous iteration, the parameters are estimated as:

$$\breve{\mu}_t^F = \langle y_{t-1,} \forall \text{ F } pixel\ at\ (t-1) \rangle \quad \text{Equation 4.8}$$

$$\breve{v}_t^F = var(y_{t-1}, \forall \text{ F } pixel\ at\ (t-1)) \quad \text{Equation 4.9}$$

The same constraint expressed in Equation 4.6 for the NF case is applied to $\breve{v}^F$. The model initialization is based on the Zambezi and Chobe River area at the beginning of the time-series. When the image at time $t-1$ does not offer enough flooded pixels, the last significantly flooded image or the reference/initial river-based parameters are used.

4.5.1.3 Classification

For every pixel, the algorithm performs at time *t* one of the following two tests (Figure 4.4), depending on the class label (F or NF) at time *t*-1:

- NF2F: a NF to F change, test if the pixel was classified was NF; or
- F2NF: an F to NF change, test if the pixel was classified as F.

The tests are based on the likelihoods computed from the distributions defined in Equation 4.10 and Equation 4.11. In the NF2F case the generalised likelihood ratio test takes the expression:

$$LR = \frac{\ell_F(t)}{\ell_{NF}(t)} = \frac{P(y_t|\mu_t^F, v_t^F)}{P(y_t|\mu_t, v_t)} \underset{NF}{\overset{F}{\gtrless}} \gamma \quad \text{Equation 4.10}$$

where ℓ_F and ℓ_{NF} are the two likelihood functions evaluated for the observation y_t.

The expression conveys that a change from NF to F conditions is accepted if the probability of the pixel being flooded is γ times larger than that of being not flooded, with $\gamma > 1$. A large γ value would yield few false positives, defined as pixels erroneously classified as F, but a large number of false negatives (missed flood pixels). Small values of γ would intuitively lead to the opposite performance outcome.

For flooded pixels the F2NF test is instead performed, defined as:

$$LR = \frac{\ell_{NF}(t)}{\ell_F(t)} = \frac{P\left(y_t|\mu_{t_{start}}, v_{t_{start}}\right)}{P(y_t|, \mu_t^F, v_t^F)} \underset{F}{\overset{NF}{\gtrless}} \beta \quad \text{Equation 4.11}$$

where $\beta > 1$ regulates the return of the surface to dry conditions and

t_{start} refers to the time of the last NF observation of the pixel in the time series.

The PDF parameters μ_t and ν_t stop being updated when the pixel is labelled as flooded. A pixel therefore returns to its NF status when its backscatter tends to its pre-flood backscatter level and farther from the overall flooded area signature.

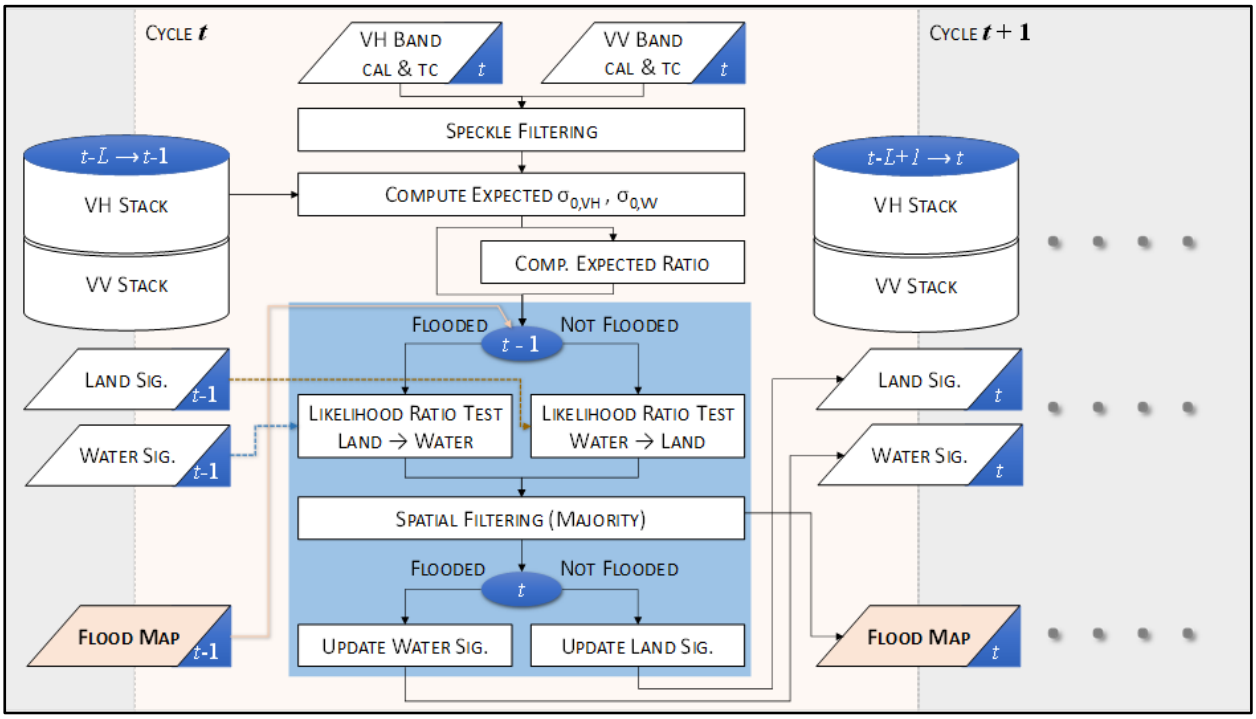

Figure 4.4 Flowchart for the cycle/iteration *t* of the flood mapping algorithm. The blue-coloured frame represents the processing block that is identically applied to both the VH and VH/VV inputs. Note that the flowchart does not include the map fusion step. Fusion is performed as post-processing step (Section 4.5.1.4).

The assembled outcome from the tests (Equation 4.10) and (Equation 4.11) is spatially processed to remove outliers, by applying a majority filter with a 5 × 5 window size. The model parameters for the next iteration, at time $t + 1$, are calculated by Equation 4.4, Equation 4.5, Equation 4.8 and Equation 4.9.

4.5.1.4 Flood map fusion

The flood mapping process is extended by fusing the VH output with VH/VV output. In light of the analysis in Section 4.4, the two flood maps can be combined as shown in Table 4.2 to produce three land cover classes namely non-flooded land (NF), flooded vegetation (FV) and temporary water (TW).

Table 4.2 Classes produced by fusing the VH and VH/VV maps

		VH/VV Map	
		NF	F
VH Map	NF	NF	FV
	F	TW	FV

Note: F is flooded areas; NF is non-flooded areas; TW is temporary open water; FV is flooded vegetation

4.5.2 Calibration and validation

4.5.2.1 Calibration and cross-validation with Landsat

The performance of the proposed algorithm was evaluated by comparing the classification results to LS8 derived maps. These were produced by thresholding the normalized difference wetness index (NDWI) (McFeeters 1996) with a value of -0.25, as suggested by Bangira et al. (2017). NDWI is calculated as follows:

$$\text{NDWI} = \frac{\rho_G - \rho_{NIR}}{\rho_G + \rho_{NIR}} \qquad \text{Equation 4.12}$$

where ρ_g is spectral reflectance in the green (band 2) region of the spectrum and

ρ_{NIR} is spectral reflectance in the near infrared (band 5) regions of the spectrum.

The comparison is carried out on the total flooded area obtained by merging (Boolean union) the FV and TW pixel sets (see Table 4.2) or, equivalently, by merging the F pixels from the VH and VH/VV maps. Two performance indicators are defined for both calibration and validation purposes:

$$False\ S1\ positives = \frac{\#(S1\ flood\ AND\ LS8\ dry)}{\#S1\ flood} \qquad \text{Equation 4.13}$$

$$False\ S1\ negatives = \frac{\#(S1\ dry\ AND\ LS8\ flood)}{\#LS8\ flood} \qquad \text{Equation 4.14}$$

These metrics can be regarded as the user's and producer's accuracy for the water class, where the classified data are the S1-based maps and the reference data are the LS8-based maps. The expressions (Equation 4.13 and Equation 4.14) are evaluated by matching the closest LS8 map (in time) to the S1-based map under assessment over an area of 800 km^2.

The calibration procedure aims to achieve the best trade-off between false S1 positives and negatives during the two flood transition phases: the flood expansion phase and the flood

recession phase. The first iteration is exploited to tune the threshold γ, hence regulating the change rate from NF to F conditions, whereas the latter is used to tune β. In this study, the calibration was performed on the 2017 season. A supervised decision, based on the maps generated for the 25 March, 12 May and 29 June 2017 acquisitions, was made. However, for all these dates a concurrent LS8 acquisition was available. The performance analysis is reported in Figure 4.5. The value of γ was set to four (resulting in 27% false S1 positives and 21% false S1 negatives) thus slightly favouring an aggressive flood alarm strategy over a conservative one. For the flood recession scenario, the performance trade-off is complicated by the dominance of false negatives over the false positives. Although the selection of large β values can reduce the false negatives during the flood recession phase, it can block the return to NF conditions, thereby increasing the number of false positives after the end of the flood. As conveyed in Figure 4.5a, a value of β > 10 would lead to flooded area extents larger than 100 km^2, compared to the 25 km^2 estimate of the LS8 based map. The configuration β = four provided a good false positive balance throughout the year.

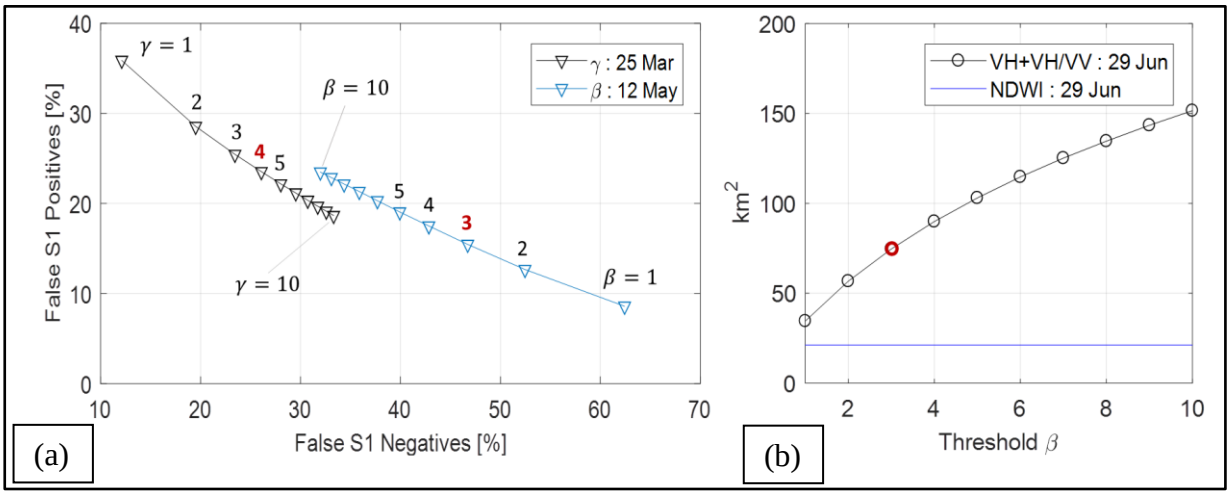

Figure 4.5 The (a) performance of the algorithm for different likelihood ratio thresholds γ and β evaluated on the LS and S1 images, collected on 25 March 2017 (flood peak) and 12 May 2017 (flood recession) and (b) estimated flooded area by algorithm (VH + VH/VV) and by the LS NDWI thresholding method on the images collected on 29 June 2017. The selected thresholds (γ = 4 and β=3) are highlighted

4.5.2.2 Validation with in situ data

The flood classification results produced by the algorithm were assessed using the observations collected during the in situ survey. The evaluation was performed on the maps generated from the 06 April 2017 S1 acquisition, as it closely matched the in situ observations (07 April). Several classification accuracy measures were implemented, namely the producer's accuracy (PA), user's accuracy (UA), overall accuracy (OA) and Kappa (K) (Foody 2004). In contrast to Equation 4.13 and Equation 4.14, the PA and UA were applied on both the NF and F classes and

the average accuracies were considered. A McNemar's test (Lu, Wang & Zhang 2017) was also performed to assess the statistical significance of the improvements brought by the map fusion (VH + VH/VV) compared to using a single feature (VH or VH/VV). Differences were considered as statistically significant at the 5% confidence level, thus, for a Z value greater than 1.96.

4.6 RESULTS

4.6.1 Model analysis on exemplary time-series

This section overviews the application of the proposed modelling technique and classification concepts (Equation 4.2 to Equation 4.11) on an actual time series S1 data covering a section of the Caprivi floodplain is herewith analysed. Two land cover features, namely short grass and tall grass, are used for demonstration purposes. The first series (Figure 4.6) represents a field (Reference Point 1:latitude: -17.5950; longitude: 24.6137) covered with short grass (the same represented by the blue line in Figure 4.3, whereas the second series (Figure 4.7) represents a field covered by thicker grass (Reference Point 2: latitude: -17.5853; longitude: 24.6496).

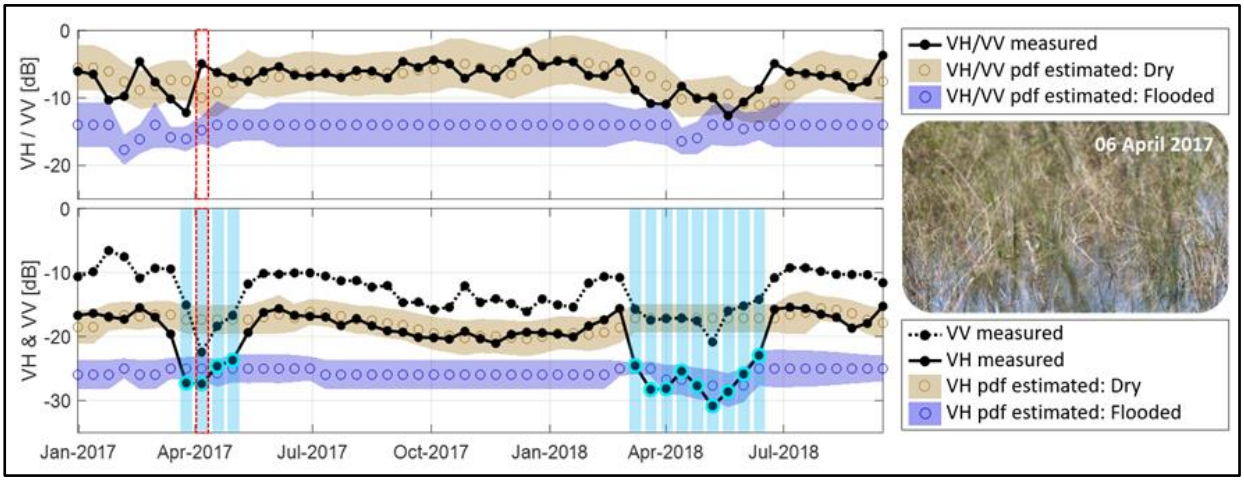

Figure 4.6 Example of S1 time series for a pixel at Reference Point 1 (short grass). The blue vertical bars show the flooded dates as mapped by the VH and VV algorithms respectively. The means (circle markers) and standard deviations (width of band) of the probability density functions (PDFs) of the dry/non-flooded (brown) and of the flooded (purple). The date of the ground campaign date is highlighted by the red vertical bars.

In the short grass scenario, the temporal behaviour of VH and VV intensities are similar. The VH/VV dynamics are constant (around the -12 dB) during the dry months, between June and February. When the flood starts, for example around March 2017, the dB values drop sharply by about eight to nine dB.

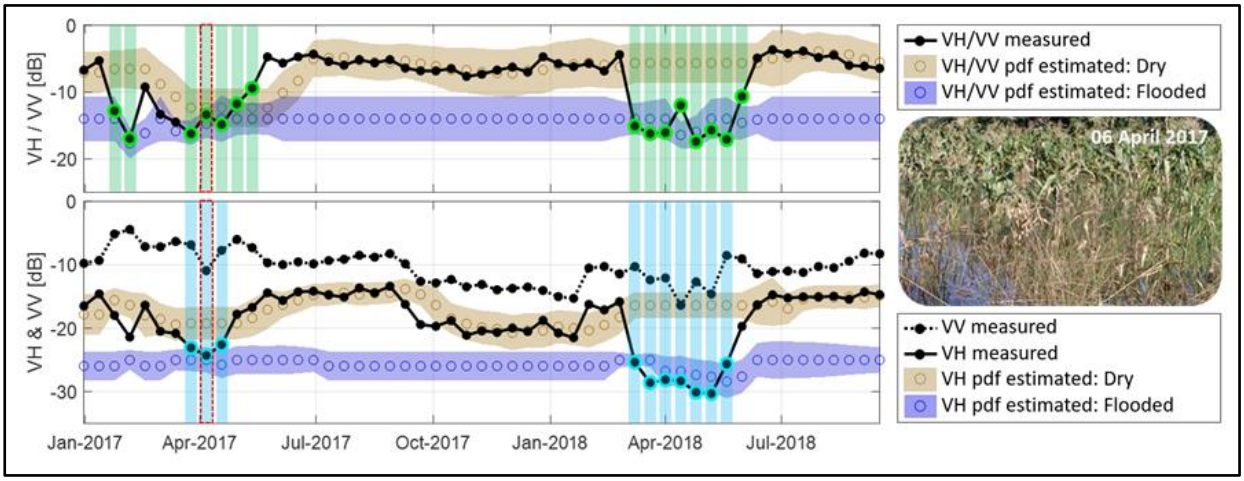

Figure 4.7 Example of S1 time series for a pixel at Reference Point 1 (short grass). The blue and green vertical bars show the flooded dates as mapped by the VH and VH/VV algorithms respectively. The means (circle markers) and standard deviations (width of band) of the probability density functions (PDFs) of the dry/non-flooded (brown) and of the flooded (purple). The date of the ground campaign date is highlighted by the red vertical bars.

A difference between 2017 and 2018 was registered at Reference Point 2 (tall grass). A double bounce mechanism was observed by the VH/VV classifier in both years. However, the intensity of the double bounce mechanism was significantly stronger in 2017, as signified by the higher VH and VV backscatter levels (around +6 dB) from March to April.

From Figure 4.6 and Figure 4.7, it is clear that the model provides a generalisation of events, especially dry (NF) conditions. There is also a slight lag after the flood event. This smoothing effect, caused by setting the temporal integration to L = 3 samples, is important as it helps to stabilise the changes. Some criticalities might arise when VH/VV decrease insignificantly during the flood onset, as shown in Figure 4.7 during March 2017. It can be observed that in such critical scenario the classifier manages to produce a reasonable output, hardly distinguishable from a user-supervised labelling intervention.

4.6.2 Potential of the fusion of VH and VH/VV in mapping flooded vegetation

Figure 4.8 depicts the changes in flooded area in the study region when VH, VH/VV and the fused product (VH + VH/VV) are classified. The VH/VV ratio highlighted the double bounce effect of FV, while VH missed it, thus the union of VH and VH/VV shows the total flood extent.

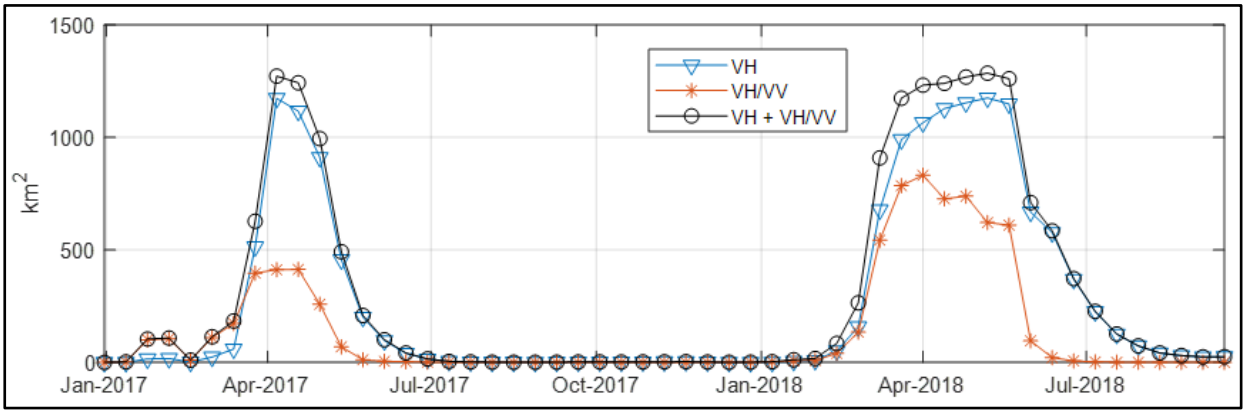

Figure 4.8 The multi-temporal comparison of the flooded area extracted from VH, VH/VV and the union of the two

The time to maximum flood extent is very short, unlike the time it takes for the flood to recede. Under short grass conditions, around February, the VH/VV ratio provides a better representation of the flood extent than the VH band.

The classification accuracy assessment of the proposed method was done based on the VH and the fused product for 6 April 2017. Figure 4.9 shows the PA, UA, OA and K values for the VH and VH+VH/VV flood maps. For the TW class, the UA and PA are 84.7% and 83.8% respectively when the VH dataset is used as input, while for when the VH+VH/VV dataset is used it is 93.4 and 85.2% respectively. In comparison, the accuracy of the NF class is lower, with 85.3% (UA) and 79.2% (PA) for VH, and 88.7% (UA) and 82.8% (PA) for the VH+VH/VV dataset. In terms of TW, the fused dataset achieved the highest improvement in UA (8.7%), while the PA for TW achieved the least improvement (1.4%) over the VH.

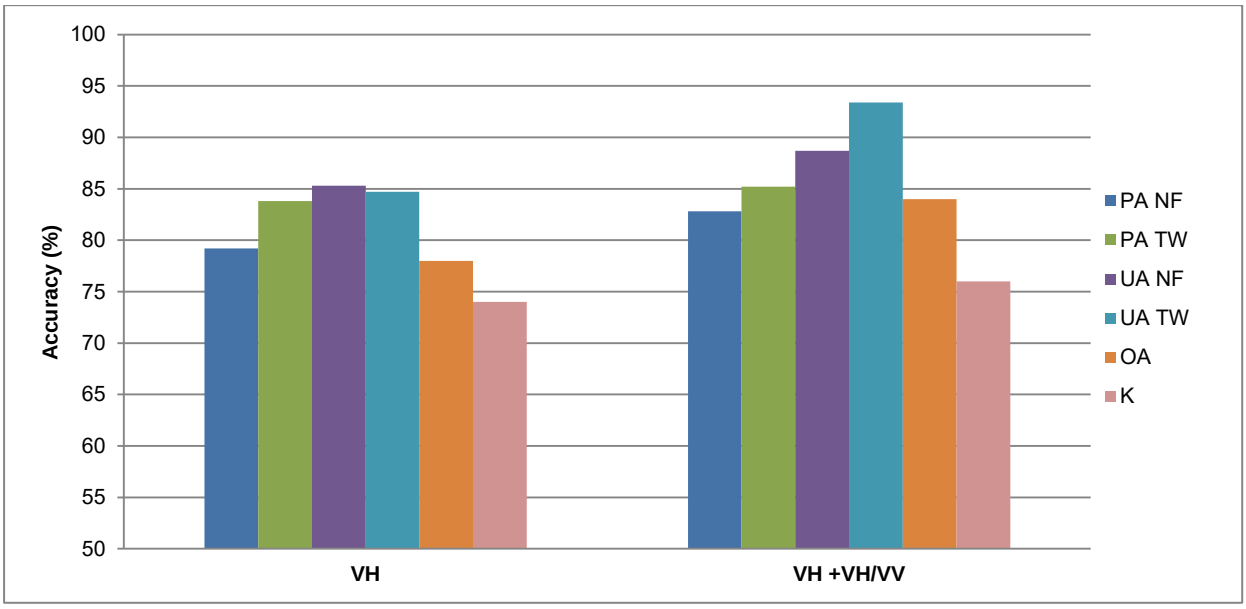

Figure 4.9 Classification accuracy results for the time series approach for VH and fusion of VH and VH/VV images for 6 April 2017

On average, the OA achieved on the classification of the fused dataset is about 5% higher compared to the VH-based classification. The McNemar's test showed that the difference in accuracies when the VH and VH+VH/VV datasets were used as input are statistically significant ($Z > 1.96$) in classification accuracies between VH and VH+VH/VV.

4.6.3 Classification performance when a fusion of VH and VH/VV polarisation and NDWI is used

Figure 4.10 compares the derived flooded extent (area) for the period between January and October 2018 when the S1 and LS8 datasets were used as input to the classifications. Only the valid (non-cloudy) LS8 observations within the region of interest were used and the comparison only considers the F and NF classes. Overall, the union of VH and VH/VV based on LS8 dataset showed a larger flood extent compared to S1. In 2018, the duration of the inundated area was much longer than the previous year. As the flood starts to recede, the difference between the flood extents derived from the two data sets increases and eventually become equal during dry periods.

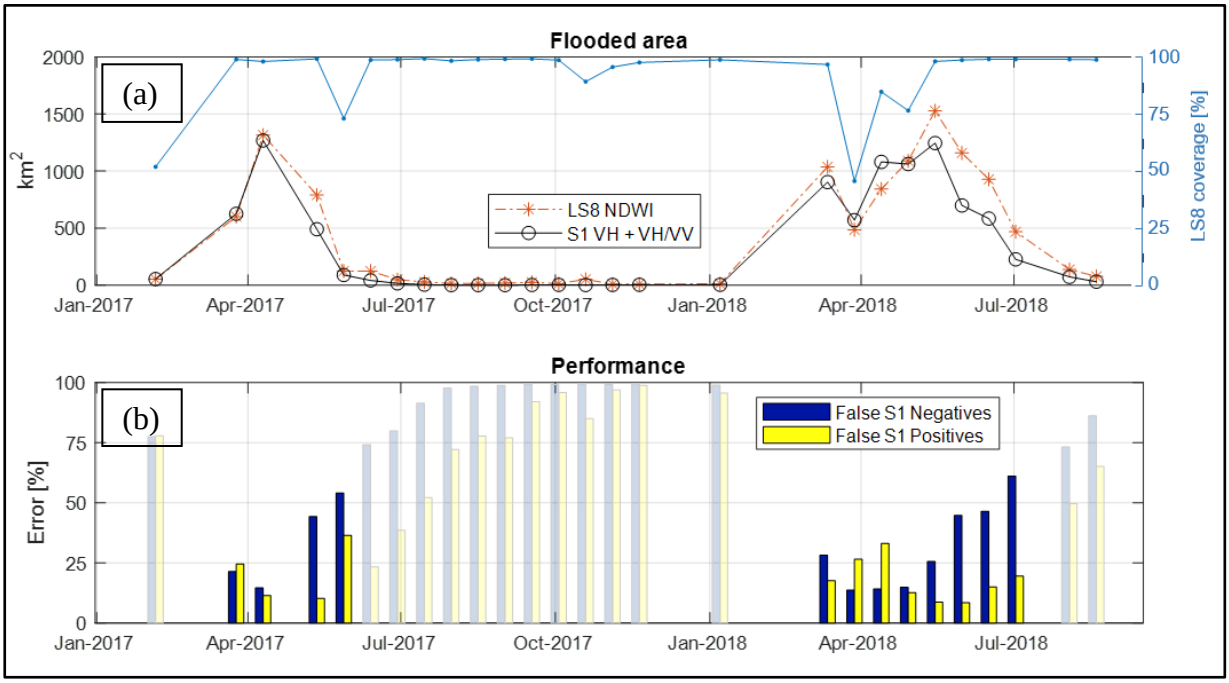

Figure 4.10 Total flood extent (TW + FV) extracted from the Landsat-derived NDWI dataset compared to the Sentinel-1 derived maps, with the (a) blue line representing the percentage of inundation extent. The two performance metrics are shown with saturated colours in (b), while images with marginal inundation extents are shown with desaturated colours.

Figure 4.10b shows that S1-based flood maps have a high proportion of false negatives, which implies that the S1-based flood maps showed a smaller inundation extent when compared to

LS8-based flood maps. The percentage of false negatives is higher during flood recession than at the onset of the flood and during the flood peak.

Figure 4.11 shows a spatial and temporal comparison of the flooded area extent derived from the proposed algorithm and LS8 datasets. The two NDWI images and the flood maps derived from the union of the VH and VH/VV datasets display the flood extent for non-flooded (NF) vegetation. During the flood event (25 March 2017), the map generated using the proposed model show a larger flood extent compared to the one derived from the NDWI. During the flood recession (12 May 2017), flood maps from the proposed method show larger areas of S1 negative.

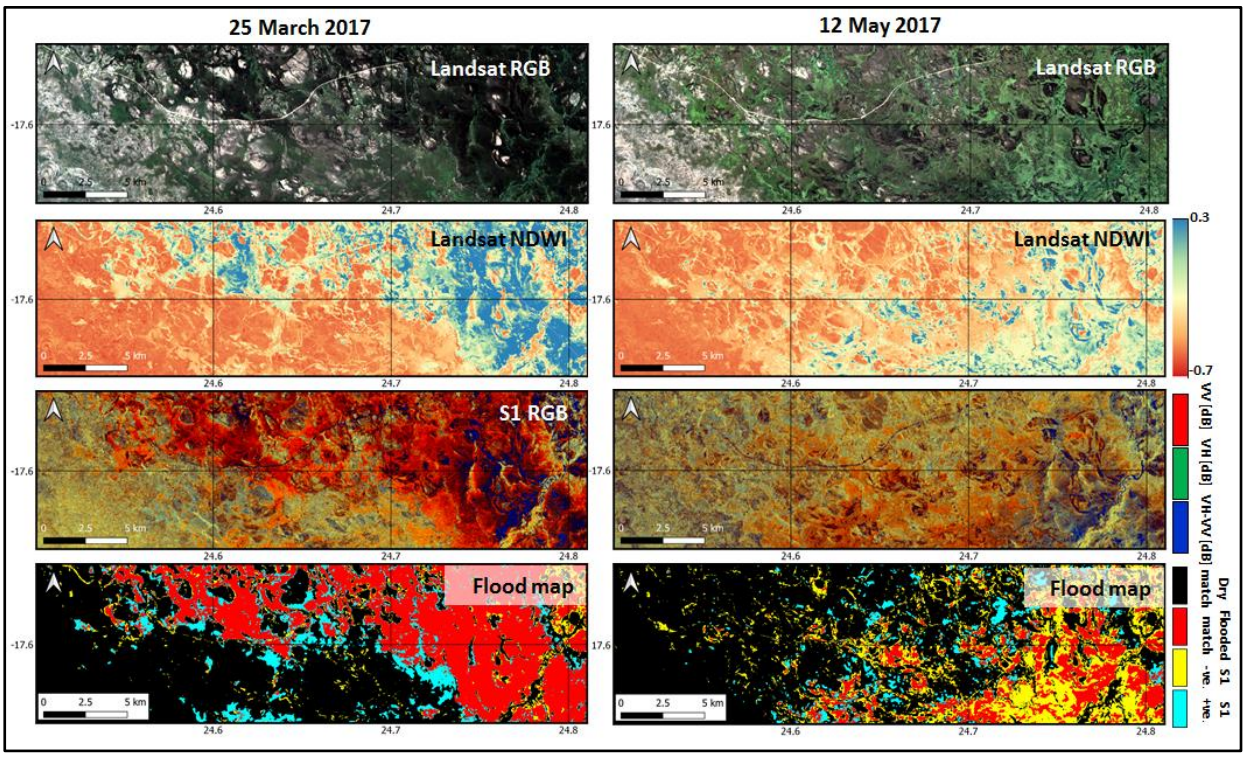

Figure 4.11 Comparison during flood peak (25 March 2017) and recession (12 May 2017) in the area surrounding the Malindi village, with (a) showing an RGB colour composite (3, 2, 1) and (b) an NDWI derived from Landsat. The Sentinel-1 polarisations (VV, VH, VH/VV) are shown as a colour composite (c), while the flood maps generated by the merging (union) of the TW and FV maps are shown in (d). The matching pixels between the NDWI and the merged S1 dataset are depicted in black and red for the dry (non-flooded) and the flooded areas respectively. The (false) S1 negatives and positives are shown with yellow and magenta.

Figure 4.12 shows the time series of the final flood maps covering the entire Caprivi flood plain based on the fusion of VH and VH/VV for the period from 13 March to 12 May 2017. From these maps it is clear that the inundation started in the north along the Zambezi River along the

Chobe River in the south-east. The flood then progresses to the east. Overall, the eastern parts of the floodplain experiences most of the inundation.

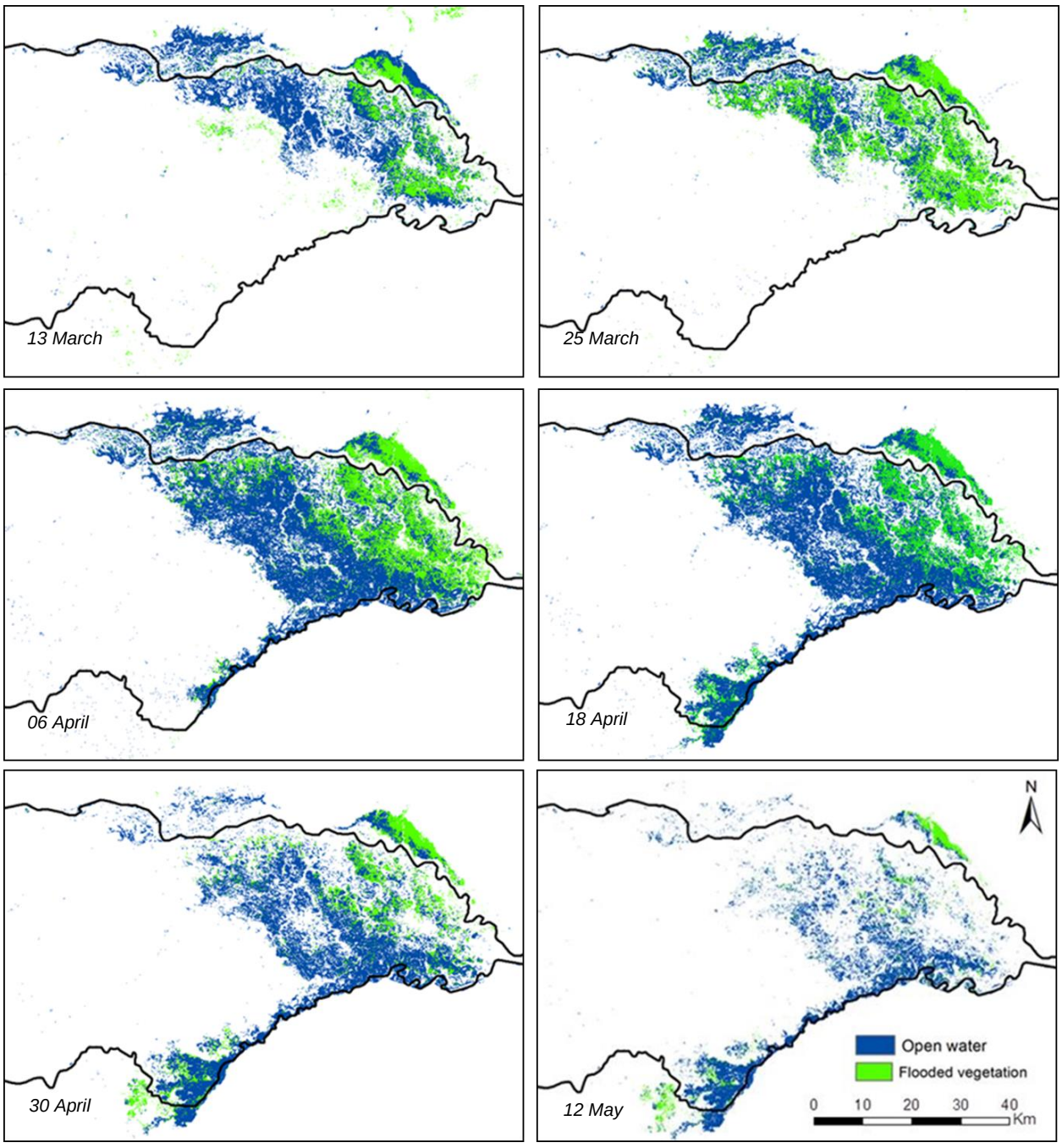

Figure 4.12 Flood maps of the Caprivi floodplain from 13 March 2017 to 12 May 2017 as produced using the union of the VH and VH/VV time series results.

4.7 DISCUSSION

The principal aim of this study was to explore the suitability of using a S1 time series for mapping the flood extent in a vegetated floodplain. Specifically, the study investigated the potential of the unique data acquisition properties of S1, notably dual polarisation (VH+VV),

steep incidence angles (30.4° – 46.2°), large coverage (250 km swath width), high spatial resolution (20 m) and short revisit time (six days) for monitoring the inundation extent of vegetated floodplains.

FV and temporary open water respectively showed an increase and decrease in the backscatter values during the April 2017 flood event (Figure 4.6 and Figure 4.7). The increase in backscatter during the beginning of the wet season is as a result of diffuse scattering from the wet soil (Amazirh et al. 2018). The low backscatter of temporary open water is caused by specular reflection in which much of the emitted radar energy is reflected away from the sensor (Martinis & Rieke 2015). The increase in backscatter during flood events can be explained by the double-bounce interactions of the radar signal with the calm water surface that partly covers vegetation (e.g., branches and trunks) (Plank et al. 2017; Tsyganskaya et al. 2018b; Twele et al. 2016). Previous studies (Plank et al. 2017; Tsyganskaya et al. 2018a; Zhao et al. 2014) observed similar backscatter characteristics of flooded vegetation and temporary open water. These temporal changes in backscatter values are difficult to deduce from a single image, but from a series of SAR images, they can be compared to infer additional information.

This study found that the VH polarisation is more sensitive than VV to FV due to the effect of double-bounce scattering, which mainly depends on the vegetation characteristics and roughness of the water surface (Amazirh et al. 2018). The same sensitivity of VH polarisations to FV was observed in Tsyganskaya et al. (2018a) and Westra et al. (2010). However, Manjusree et al. (2012) argued that a VV polarisation is better than a VH polarisation for identifying partially submerged vegetation.

Overall classification results obtained from the proposed multi-temporal technique were comparable to those obtained using the cloud-free LS8 and in situ observations. The superior performance of the fused VH and VH/VV maps is primarily attributed to the ability of the VH/VV data to represent the effect of FV. The relevance of VH/VV in monitoring FV has been shown (Tsyganskaya et al. 2018a), but the addition of VH improved the results in our case study, which is a new finding. The dual polarisation of S1 thus offers a good characterisation of FV, which is typical of many floodplains.

The study showed that LC has an impact on the observed backscatter and the selection of thresholds. In previous studies, absolute backscatter threshold values were applied for the extraction of flood extent on individual images using either VH, HH or VV (Plank et al. 2017). This can lead to misclassifications and limit the applicability of the method for operational use.

The limitations of the selection of a suitable backscatter threshold can be overcome by averaging the backscatter values over the time series, and thereby consider LC changes. The use of a single polarisation will enable the detection of open water and disregard flooded vegetation. Furthermore, unlike other studies (Plank et al. 2017; Tsyganskaya et al. 2018a) the proposed method does not require ancillary data sets to map the flood extent.

This study has shown that C-band radar and optical sensors have similar capabilities in detecting flooded areas. The observed flood extent during the flood peak, based on the union of VH and VH/VV, was very similar to the NDWI-based map. However, polarimetric radar signals clearly have an intrinsic potential to distinguish between the two-flooded conditions, namely open water and flooded vegetation. The sensitivity of the C-band to partially submerged vegetation is particularly high for vegetation with vertical structures such as stems and trunks as it leads to double bounce. In contrast, NDWI is more influenced by the amount of open water and the liquid water content of the vegetation recorded in a pixel. In addition, the ability of SAR to acquire images during cloud cover gives the statistical modelling developed in this study an advantage over methods that make use of optical data. Although optical imagery is easy to interpret, the proposed SAR-based multi-temporal technique is more suitable for flood mapping as it is not affected by cloud cover and considers LC changes.

In this study, the S1-based flood maps were compared to maps generated from optical images. However, it will be insightful to compare the produced maps to those generated with other SAR systems (e.g. RADARSAT-2) as it would provide a more in-depth understanding of the backscatter patterns. In addition, the developed method was tested over an area with a flat terrain. It is not clear how the method will perform in other of landscapes with more dramatic relief. It is likely that the inclusion of ancillary data (e.g. DEMs) will improve the performance of the technique, but more work is needed to integrate such data into the workflow.

4.8 CONCLUSION

This study evaluated the potential of S1 SAR images for mapping a flood event (April 2017) in the Caprivi floodplain using novel statistical time series modelling of FV, TW and NF areas. The method uses time series analysis to detect inundation extent by taking LC characteristics into consideration. The technique was applied to VV, VH and VH/VV ratio polarisations. A multi-temporal inspection of backscatter characteristics showed that the ratio between VH and VV captures the effect of FV better than when the features are used on their own.

Based on the findings if this study we conclude that:

(a) S1 SAR is an invaluable primary data source for flood monitoring;

(b) VH/VV ratios are superior to VH polarisations for flood mapping; and

(c) the fusion of VH and VH/VV in a time series approach is well suited to map temporary surface water partly obscured by vegetation, thus eliminating the limitation of flood extent underestimation in vegetated floodplains.

Another major advantage of the proposed method is that the classification thresholds are automatically selected by considering previous pixel conditions, which allows the technique to be fully automated for near real-time flood extent mapping.

CHAPTER 5: COMPARING THRESHOLDING WITH MACHINE LEARNING CLASSIFIERS FOR MAPPING COMPLEX WATER BODIES[3]

5.1 ABSTRACT

Small reservoirs play an important role in mining, industries and agriculture, but are very dynamic in nature. Accurate and up-to-date maps of surface water storage and distribution are invaluable for informing decisions relating to water security, flood monitoring and water resources management. Satellite remote sensing is an effective way of monitoring the dynamics of surface waterbodies over large areas. The European Space Agency (ESA) has recently launched constellations of Sentinel-1(S1) and Sentinel-2 (S2) satellites carrying C-band synthetic aperture radar (SAR) and a multispectral imaging radiometer respectively. The constellations improve global coverage of remotely sensed imagery and enable the development of near real-time operational products. This unprecedented data availability leads to an urgent need for developing fully automatic, feasible and accurate retrieval methods for mapping and monitoring waterbodies. Mapping of waterbodies can take advantage of the synthesis of SAR and multispectral remote sensing data in order to increase classification accuracy. In this study, we propose an approach that combines automatic thresholding of near-concurrent normalized difference wetness index (NDWI) (generated from S2) and VH backscatter bands (generated from S1) for the mapping of waterbodies (mainly reservoirs and dams) with diverse spectral and spatial characteristics. Waterbodies of different sizes and varying levels of turbidity, sedimentation and eutrophication were targeted. The resulting maps are compared to the classification performances of five machine learning algorithms (MLAs), namely decision tree (DT), k-nearest neighbour (*k*-NN), random forest (RF), and two implementations of the support vector machine (SVM). Several experiments were carried out to better understand the complexities involved in mapping spectrally and spatially complex waterbodies. It was found that the combination of multispectral indices with SAR data is highly beneficial for classifying complex waterbodies and that the proposed thresholding approach classified waterbodies with an

---

[3] Bangira T, van Niekerk A, Menenti M 2018. Comparing thresholding with machine learning classifiers for mapping complex water bodies (In review)

overall classification accuracy of 89.3%. However, the varying concentrations of suspended sediments (turbidity), dissolved particles and aquatic plants negatively affected the classification accuracies of the proposed method, whereas the MLAs (SVM in particular) were less sensitive to such variations. The main disadvantage of using MLAs for operational waterbody mapping is the requirement of suitable training samples, representing both water and non-water land covers. The dynamic nature of reservoirs (many reservoirs are depleted at least once a year) makes the re-use of training data unfeasible. The study thus concludes that the combination fully automated thresholding techniques with SAR and optical data is viable for classifying complex waterbodies, but that further refinements are required to improve accuracies.

Keywords: waterbody mapping, machine learning, thresholding, optically complex, remote sensing

5.2 INTRODUCTION

Communities in developing countries rely on freshwater stored in small waterbodies for agricultural, domestic, mining and industrial use (Araujo, Abiodun & Crespo 2016). These water resources are highly susceptible to climate variations and are often not sufficient to withstand long periods of drought. Recently, the water resources of the Cape Winelands District of South Africa have been under severe pressure due to drought conditions brought about by the El Niño weather cycle (Botai et al. 2017). Agriculture plays a critical role in this region's economy (Gilbertson, Kemp & Van Niekerk 2017), with wine production alone contributing to more than 30% of its regional gross domestic product (RGDP). The wine production industry furthermore provides more than 8% of the employment in the Western Cape Province (DAFF 2018). The district is well-known for perennial crop irrigation of grapes (mostly wine production) and fruits (apples, pears, peaches, olives and citrus) (Botai et al. 2017). In contrast to other parts of southern Africa, the area has a semi-arid, Mediterranean climate with a mean annual rainfall of about 400 mm (Hoffman et al. 2009), and as such receives winter rainfall when demand for irrigation water is relatively low. In contrast, the growing season occurs during the dry and hot months when rainfall is low (about 20% of the total annual) and water demand for irrigation is at its apex (Engelbrecht et al. 2015).

During the recent drought (2015–2018), water reserves in the principal reservoirs were reduced to below 17% in April 2018, necessitating the implementation of drastic water restrictions by as much as 80% of normal usage for crop irrigation and industrial and domestic use (Evans 2018). Authorities were confronted with difficult decisions about how to best manage the limited available water resources and minimise the inevitable socio-economic impacts. Many

limitations of existing procedures and gaps in available information sources were exposed. One of the biggest needs was to determine how resilient the agricultural industry, in particular the perennial crops sector, would be to severe water restrictions. This proved to be challenging given that no operational systems are in place to quantify and monitor how much water is stored in privately owned and managed reservoirs (dams). Most of these dams are ungauged, and setting up, maintaining and managing conventional in situ surveys, gauge stations and telemetry systems would be prohibitively expensive and time-consuming (Bangira et al. 2015).

Satellite remote sensing techniques have been shown to provide a viable alternative for monitoring water bodies. Satellite data can provide macroscopic, real-time, dynamic and cost-effective information, and Earth observation procedures can be set up to provide operational (autonomous) monitoring of water resources (Du et al. 2016; Hanqiu 2005). Several methods have been proposed to classify surface water areas using either multispectral (Bangira et al. 2017; Du et al. 2016; Yang et al. 2017) or SAR remotely sensed data (Pham-Duc, Prigent & Aires 2017; Schlaffer et al. 2016). Popular techniques are image thresholding (rule-based classification) and supervised/unsupervised classification (Chini et al. 2017). Image thresholding is easy to implement, autonomous (thresholds that can be applied to images of different dates and areas are automatically generated) and computationally inexpensive (not time-consuming) (Du et al. 2016; Zhang et al. 2012b). During thresholding, a single threshold value within the image scene is determined and all pixels below (or above) it are classified as water or non-water. According to Pierdicca et al. (2013), the identification of a suitable threshold relies on a range of environmental factors, including atmospheric conditions, adjacency effects, mixed pixels, shadows and system factors such as viewing angle and pixel size (Li et al. 2015; Niroumand-Jadidi & Vitti 2017). Defining a robust threshold – one that will work effectively in different areas and on imagery acquired on different dates – has been cited by Feyisa et al. (2014) as being a very challenging task, especially in optically complex (e.g. flooded vegetation and sedimented and turbid water) environments. An alternative approach to finding a single "optimal" threshold that will work in multiple situations is to make use of automated, image – specific, threshold identification methods. Several such techniques have been proposed, among which Otsu's simple and robust algorithm (Otsu 1975) is one of the most utilised techniques for surface water mapping (Bangira et al. 2017; Chini et al. 2017; Du et al. 2016). The Otsu algorithm finds a threshold by maximising the inter-class variance and minimising the weighted within-class variance (Otsu 1975).

Supervised and unsupervised classification techniques have also been popular for mapping water features using remotely sensed data (Hasmadi, Pakhriazad & Shahrin 2009; Martinis, Twele & Voigt 2011). For instance, using 30 m multispectral Landsat TM, Xie et al. (2016b) obtained an accuracy of 96%, whereas Pradhan, Tehrany & Jebur (2016) achieved an accuracy of 58% using 3 m TerraSAR-X data to retrieve water (flooded) pixels based on the ISODATA unsupervised classification technique. The relatively low accuracy of the latter study was attributed to the presence of vegetation in the flooded area. Feng et al. (2015) employed supervised classification to map surface waterbodies with 30 m multispectral HJ-1B imagery and achieved 94% overall accuracies. Similarly, Verpoorter, Kutser & Tranvik (2012) achieved an accuracy of 95% using Landsat 7 ETM+ imagery. Although many authors agree that supervised classification is an efficient (accurate and fast) approach to map waterbodies, many highlight the need for prior definitions (training samples) to construct models capable of classifying unknown values. The generation and collection of training samples is time-consuming, expensive and tedious, often requiring extensive field visits. Nevertheless, recent implementations of non-parametric MLAs, including support vector machine (SVM), RF and DT, have demonstrated their value for mapping surface water. MLAs have the ability to generalise well using relatively small training sets and can handle large numbers of features (Gilbertson & Van Niekerk 2017).

In general, SAR and multispectral techniques are capable of accurately extracting water features if there is a significant contrast between water and non-water features in the data. However, the optical complexity of water affects the reflected spectral profile and backscatter values. For instance, the waterbodies in the Cape Winelands are characterised by varying concentrations of suspended sediments (turbidity), algae (e.g. chlorophylls, carotenoids), chemicals (e.g. nutrients, pesticides and metals), dissolved organic matter and aquatic plants. This makes it difficult to develop reliable, universal and autonomous supervised remote sensing-based water extraction methods. To date, the remote sensing research community has given very little attention to how these variations affect waterbody mapping. Notable exceptions include Hong et al. (2015) and Yang & Chen (2017) who used RADARSAT-1 (16 m), Landsat TM (30 m) and S2 (10 m) data to map optically complex waterbodies. The latter study mapped optically complex waterbodies in urban areas and concluded that it is necessary to find the most appropriate and practical water identification methods regardless of the physical and chemical characteristics of waterbodies.

The ESA recently launched a constellation of high spatial and temporal resolution satellites, namely S1 and S2, carrying C-band SAR and multispectral sensors respectively (Donlon et al. 2012). Thanks to their dual-satellite-per-orbit configurations, S1 and S2 have relatively high

revisit times of six and five days respectively. To our knowledge, no research has evaluated how data from these satellites can be combined to improve classification accuracies of waterbodies in complex environments such as the Winelands District of South Africa.

Taking into account the challenges of mapping waterbodies with diverse physical and chemical characteristics, the objectives of this study are:

1. To compare the performance of simple rule-based methods, i.e. the application of dynamic thresholds that can be easily incorporated into operational workflows, to the performance of supervised learning approaches (i.e. MLAs);

2. To investigate how variations in the water optics (caused by physical and chemical variations) influence classification accuracies.

Thresholding and MLAs were applied to a range of features derived from S1 (SAR) and S2 (multispectral) data. This included a range of existing and new water indices and texture measures. Five popular MLAs, namely DTs, RF, *k*-NN, *c*-SVM and SVM were implemented to serve as a benchmark against which the autonomous rule-based techniques could be compared. The study concludes by assessing the value of combining SAR and multispectral thresholding rules for mapping optically complex waterbodies.

5.3 MATERIALS AND METHODS

5.3.1 Study area

A 40×45km study area located in the Cape Winelands district of South Africa was chosen for the comparisons. The area (Figure 5.1) was chosen because it is the major wine and fruit producing region in South Africa and because of the optical complexity of the dams and reservoirs located therein. The area has a Mediterranean climate characterised by warm, dry summers and cool, wet winters (Hoffman et al. 2009). It receives a mean annual rainfall of about 400 mm and has a mean annual minimum and maximum temperature of 11°C and 22°C respectively. Approximately 80% of precipitation falls within the winter months of April to September, hence the demand for summer irrigation (Engelbrecht et al. 2015).

The Cape Winelands district has a complex topography, ranging from coastal plains to mega-anticlinal complex mountain ranges separated by synclinal valleys. During the rainy months, the high mountain ranges receive rainfall of up to 2000 mm (Van Niekerk & Joubert 2011) and catchments naturally collect rainfall runoff and channel it to rivers that feed reservoirs in valleys.

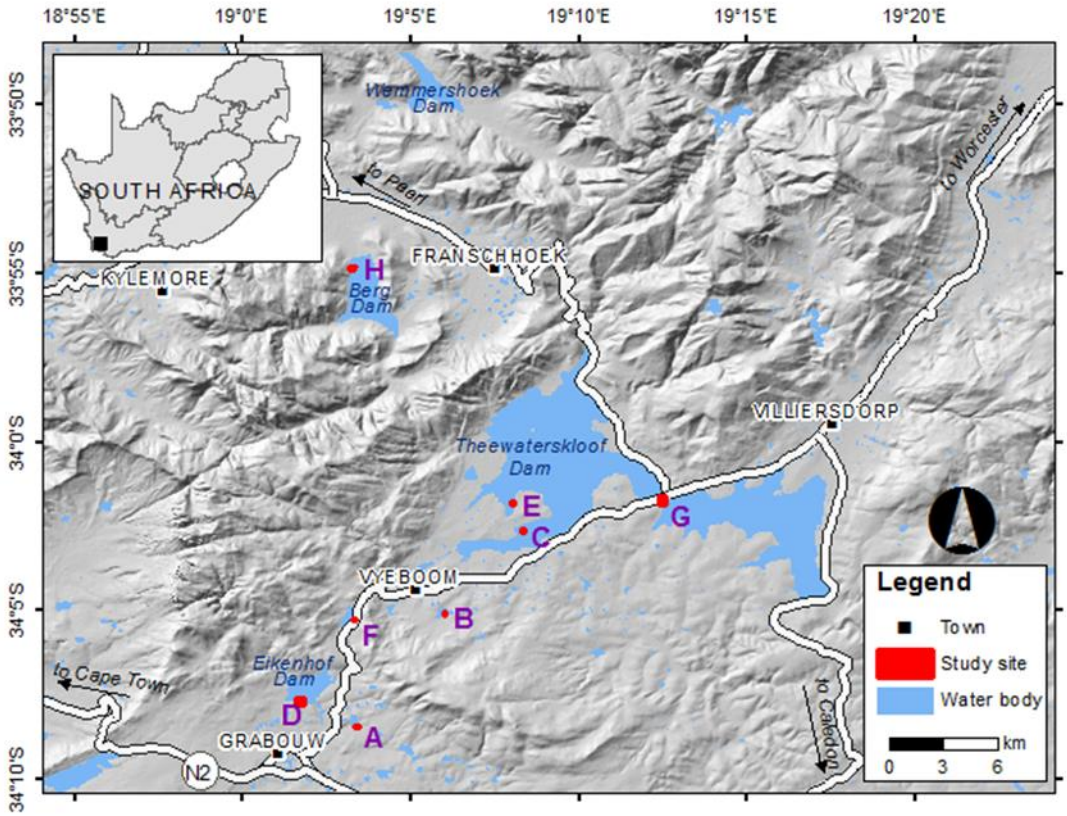

Figure 5.1 Study area and location of field survey sites

The geology of the area is dominated by pre-Cambrian metamorphosed shales and fine sandstones of marine origin, known as the Malmesbury group (Wooldridge 2003). Soils on hillslopes are generally shallower than in valleys and are highly associated with erosion and transportation regimes resulting in sedimentation of waterbodies (Meadows 2003).

The suitable climate and presence of rivers and dams have led to agricultural activities and urbanisation. Fertilisers containing phosphorous and nitrogen are widely used to increase crop harvests. These nutrients are carried by runoff from agricultural areas to waterbodies, resulting in eutrophication.

5.3.2 Data collection and preparation

5.3.2.1 Test sites and data collection

To investigate the performance of thresholding and MLAs in the extraction of waterbodies, eight test sites (Figure 5.1) located in areas with diverse land cover/use featuring different types of waterbodies (Table 5.1) were chosen to evaluate the performance of the proposed methods.

Table 5.1 Description of the physical characteristics of the study sites

Site	Description
Site A	Very shallow with low eutrophication and turbidity
Site B	Shallow with moderate turbidity and eutrophication
Site C	Clear with moderate eutrophication
Site D	Shallow and humic-rich (black) water
Site E	Very shallow and eutrophic
Site F	Shallow, sedimented and humic-rich (black) water
Site G	Shallow and moderate turbidity
Site H	Shallow, clear and wind-induced turbulence

The in situ data used for accuracy assessment of the classification results were collected using a handheld global positioning system (GPS) receiver (three meters accuracy) during four field surveys on dates that corresponded closely with satellite acquisitions (Table 5.2) to get an accurate representation of the relationship between the remotely sensed water features and ground observations.

Table 5.2 Sentinel image acquisition and field visit dates

Field visit	Sentinel-1 image	Sentinel-2 image
27 October 2016	27 October 2016	23 October 2016
26 November 2016	25 November 2016	22 November 2016
28 January 2017	31 January 2017	31 January 2017
25 February 2017	24 February 2017	03 March 2017

An in situ reference point was defined as a 10 m x 10 m plot (corresponding to a S2 pixel) and each plot were assigned a single land cover label based on majority coverage. For the MLAs, a broad five-class classification scheme was adopted, namely water, built-up, shadow, bare ground and vegetation, which was subsequently reduced (reclassified) to two classes, namely water and non-water. The latter two-class classification scheme was also used in the thresholding experiments.

5.3.2.2 Multispectral image pre-processing

The S2 multispectral images used in this study have 13 bands of which four bands (blue, green, red and NIR) have a spatial resolution of 10 m; six bands (including SWIR) have a spatial resolution of 20 m; and three have a 60 m resolution (coastal aerosol, water vapour and SWIR-Cirrus bands). The images were atmospherically corrected using the Sen2cor algorithm available in the Sentinel Application Platform (SNAP) toolbox, which uses the Climate Change Initiative (CCI) land cover data use to characterise atmospheric conditions at the time of acquisition. The

process was carried out at 10 m resolution resulting in the output excluding the 60 m bands (Bands 1, 9 and 10) (Louis et al. 2016). Thus, ten bands were preserved for further analysis.

5.3.2.3 SAR data pre-processing

The S1 constellation consists of two SAR satellites (S1A and S1B) that record C-band (5.405 GHz) backscatter at incidence angles ranging from 29–46°. Four-cloud free Sentinel-2 level-1C image and four interferometric wide (IW) swath mode Level-1 ground range detected (GRD) S1 scenes were downloaded from ESA's Scientific Data Hub (https://scihub.copernicus.eu/dhus/). IW images have large swath widths (250 km) and moderately high spatial resolutions (5×20 m). IW offers dual polarisation capability, which can provide more information about ground surfaces as compared to single polarisations. Only HV and VV polarisations were available over the study area.

The S1 toolbox (S-1 TBX) available in SNAP was used for the pre-processing of the SAR dataset. Figure 5.2 shows the pre-processing chain followed.

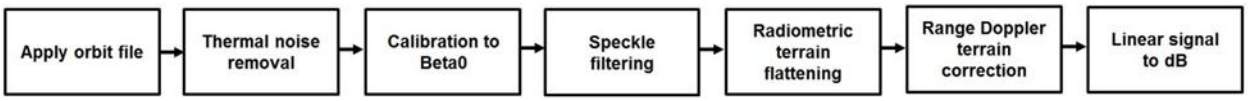

Figure 5.2 Pre-processing steps for Sentinel-1 data

The images were projected and resampled using nearest neighbour to 10 m resolution. The Universal Transverse Mercator (UTM) WGS84 coordinate system (zone 34 South) was used to allow for pixel-to-pixel comparison with the S2 images.

5.3.3 Feature set generation for classification

In addition to the ten S2 spectral and two HV and VV S1 polarisation bands, a range of supplementary features was generated and used as input to the classification methods. Table 5.3 outlines the 252 (63 per image capture date) features considered. To reduce the number of variables (feature dimensionality), Bands 5 (vegetation red-edge), 7 (vegetation red-edge), 8a (narrow NIR) and 12 (SWIR) were excluded as they were highly correlated with Bands 6, 8 and 11 respectively.

Table 5.3 Features used as input to the thresholding and MLAs

Data type	Type	Subtype	Description	Total features
Sentinel-1	Speckle filters	HV	Boxcar, none, median(5x5), Lee-sigma, refined Lee, frost, gamma MAP, IDAN and Lee	9
		VV		9
	Band ratios	$\frac{HV}{VV}$	Boxcar, none, median(5x5), Lee-sigma, refined Lee, frost, gamma MAP, IDAN and Lee	9
Sentinel-2	Spectral indices	Reflectance bands and mean of the six bands	B2, B3, B4, B6, B8, B11 and Mean	7
		normalized difference spectral indices (NDSIs)	Band combinations from Sentinel-2 bands (B2, B3, B4, B6, B8, B11) e.g. (B2-B3)/(B2+B3)	16
		Pan-sharpening of SWIR (Band 11)	Band combinations from P1 of B11	5
			Band combinations from P2 of B11	5
	Textural features	GLCM	Correlation, Homogeneity	2
		GLDV	Contrast, Entropy, Mean	3
	Image transforms	Principle components (PC`s)	PC1 and PC2	2

Note: P1=ATWT pan-sharpening, P2=Gram-Schmidt pan-sharpening, PC=principal component and B=band

The S2 spectral bands were used to develop NDSIs, which include the normalised difference water index (NDWI) (McFeeters 1996), normalized difference moisture index (NDMI) (Wilson & Sader 2002), modified normalized difference water index (MNDWI) (Xu 2006) and water ratio index (WRI) (Shen & Li 2010) indices. Table 5.4 shows the calculation of the popular indices. Band 11 was downscaled from 20 m to 10 m (e.g. for generating a 10 m resolution MNDWI) using pan-sharpening, where Band 8 was employed as the panchromatic (PAN) band as suggested by Du et al. (2016).

Table 5.4 Calculation of the popular indices-based on Sentinel-2 reflectance bands

Index	Equation
Normalized difference water index	NDWI = $\frac{Band\ 3-Band\ 8}{Band\ 3+Band\ 8}$
Normalized difference moisture index	NDMI = $\frac{Band\ 8-Band\ 11}{Band\ 8+Band\ 11}$
Modified normalized difference water index	MNDWI = $\frac{Band\ 3-Band\ 11}{Band\ 3+Band\ 11}$
Water ratio index	WRI = $\frac{Band\ 3+Band\ 4}{Band\ 8+Band\ 11}$
Automated water extraction index	AWEI = $4(Band\ 3 - Band\ 11) - (0.25Band\ 8 + 2.75Band11)$

Two popular pan-sharpening algorithms were used, namely Gram-Schmidt (GS) (Laben & Brower 2000) and À Trous Wavelet Transform (ATWT) (Shensa 1992). Several other NDSIs generated from other S2 band combinations (not included in the hand-selected water indices) and

the mean of all bands (i.e. brightness) were included to investigate whether they were useful for water feature detection.

Principal component analysis (PCA) was performed on all S2 bands per image and the two first components (PC1 and PC2) with the largest Eigenvalues were retained (Kalantari et al. 2014). Two types of textural measures, namely the grey level co-occurrence matrix (GLCM) and grey level difference vector (GLDV), were generated from each PC1. These measures quantify differences in the grey levels within a local window (Haralick, Shanmugam & Dinstein 1973). In this study the window size was set to (5 x 5) pixels as suggested by Zhang et al. (2017). The GLDV texture measures employed were contrast, entropy and mean, while correlation and homogeneity were selected from the GLCM analyses.

Nine popular speckle filters available in SNAP, namely boxcar, none, median (5×5), Lee-sigma, refined Lee, frost, gamma MAP, IDAN and Lee, were applied to the HV and VV SAR polarisations (Argenti et al. 2013).

5.3.4 Experimental design

The thresholding results were compared to the classifications produced by the MLAs to get a sense of relative performance (i.e. the MLA results were used as benchmarks against which the autonomous rule-based approaches could be compared). The classification experiments were applied for each site separately and in combination to better understand how variations in waterbody types influence accuracies. Table 5.5 summarises the experiments, classification methods and input features. The thresholding classified each feature individually, whereas MLAs considered them all in combination.

Table 5.5 Experiments carried out

Experiment set	Classification method	Input features	Number of experiments
A	Thresholding	Each feature individually	252 x 9 = 2268
B	*k*-NN	All features combined	1 x 9 = 9
C	DT	All features combined	1 x 9 = 9
D	RF	All features combined	1 x 9 = 9
E	SVM	All features combined	1 x 9 = 9
F	*c*-SVM	All features combined	1 x 9 = 9

5.3.5 Image thresholding

Threshold selection is a key step in using rule-based approaches for waterbody mapping. Several researchers have noted the difficulty of selecting robust threshold values, as image variables (e.g.

spectral indices and backscatter) are often dynamic vary both temporally and spatially among regions, depending on different image and water characteristics.

The use of a deterministic threshold (e.g. zero in NDWI) can either overestimate or underestimate surface water areas. Various automatic threshold selection methods have consequently been proposed in the literature (Al-Bayati & El-Zaart 2013). In this study, waterbody masks were extracted from each of the 252 features (Table 5.3) by applying a threshold dynamically generated with the Otsu algorithm (Otsu 1975). The algorithm is a widely used automatic thresholding method aimed at maximising inter-class variance and minimising intra-class variance (Du et al. 2016; Schlaffer et al. 2015). The thresholding experiments per feature (Table 5.5) and per each site were automated in Matlab software.

Otsu automatically defines a threshold value t that divides the image into two classes. In this study, the two classes were set to water and non-water. The threshold value t separating these classes was determined as follows:

$$\delta^2 = \mathrm{P_{nw}} \cdot (\mathrm{M_{nw}} - M)^2 + \mathrm{P}_w \cdot (\mathrm{M}_w - \mathrm{M})^2 \quad \text{Equation 5.1}$$

$$\mathrm{M} = \mathrm{P_{nw}} \cdot \mathrm{M}_{nw} + \mathrm{P}_w \cdot \mathrm{M}_w \quad \text{Equation 5.2}$$

$$\mathrm{P}_{nw} + \mathrm{P}_w = 1 \quad \text{Equation 5.3}$$

$$\mathrm{t}^* = \underset{a \le t \le b}{Arg\ Max} \{\mathrm{P_{nw}} \cdot (\mathrm{M_{nw}} - \mathrm{M})^2 + \mathrm{P_w} \cdot (\mathrm{M_w} - \mathrm{M})^2\} \quad \text{Equation 5.4}$$

where P_{nw} is the probabilities of one pixel belonging to non-water class;
P_w is the probabilities of one pixel belonging to water class;
M_{nw} is the mean values of the non-water class;
M_w is an arbitrary multiplier representing the upper standardised range value; and
M is the mean value of the feature image.

5.3.6 Machine learning

The Supervised Learning and Image Classification Environment (SLICE) software developed by the Centre for Geographical Analysis at Stellenbosch University (Myburgh & Van Niekerk 2014) was used for the supervised machine learning classification. SLICE was developed using the C++ programming language and libraries from OpenCV (Open Source Computer Vision

Library) 2.2 (Garage 2011) and Libsvm (Library for Support Vector Machines) (Chang & Lin 2011).

SLICE integrates five popular machine learning algorithms, namely DTs, *k*-NN, RF, constant optimisation parameter SVM (*c*-SVM) and SVM. These machine-learning techniques are well established in remote sensing applications, mainly thanks to their flexibility, simplicity and computational efficiency (Myburgh & Van Niekerk 2014; Zheng et al. 2015).

SVM is a non-parametric supervised classification technique based on a statistical learning theory, and aims to determine the location of decision boundaries by maximising the margin between classes (Vapnik 2013). In the case of two linearly separable classes, SVM selects from among the infinite number of linear decision boundaries the optimal separating hyperplane (OSH), which minimises the generalisation error. The OSH ensures a maximum margin between the hyperplane and the closest training samples (dubbed support vectors) of each class and it is calculated by standard quadratic programming optimisation techniques (Pal & Mather 2005). The support vectors are the only training samples used in the classification. When the data are not linearly separable in two dimensions, SVM is extended by introducing slack variables and applying a kernel function to solve the optimisation problem in higher-dimensional space (Steinwart & Christmann 2008). Commonly used kernels are linear, polynomial and the radial basis function (RBF). The performance of SVM largely depends on the choice of the kernel function and the assignment of kernel parameters (Pal & Mather 2005). The RBF kernel usually trains much faster by mapping every point to a Gaussian function and was chosen for this study, as recommended by Jia, Wu & Li (2013). The *c* parameter in *c*-SVM helps to optimise SVM since the value is tuned based on the input data. The range of *c* is from zero to infinity. For large values of *c*, the optimisation will choose a smaller-margin hyperplane whereas a very small value of *c* will cause the optimiser to look for a larger-margin separating hyperplane, even if that hyperplane misclassifies more points.

DT classifier is a predictive, flexible and comprehensive classification algorithm that labels an unknown class using a sequence of rules that leads to a classification decision (Sun, Yu & Goldberg 2011). A decision tree is composed of a root node, a set of interior nodes and terminal nodes (termed leaf nodes). The root node and interior nodes are linked to decision stages, while the terminal nodes represent the final classification. The classification process is implemented by a set of rules that determines the path to be followed, starting from the root node and ending at one terminal node that represents the label for the object being classified. At each nonterminal node, a decision is made about the path to the next node. The efficiency and performance of this

algorithm strongly depends on the set of rules controlling a decision tree and the nature of decisions being set (Mather & Tso 2016).

RF is an ensemble machine learning method consisting of a combination of DT classifiers (Pal 2005). All trees are trained with the same features but on various training sets, which are generated randomly from the original training data. After training, each tree assigns a class label to the test data. Finally, the results of all decision trees are fused and the majority of votes determine the class label for each land cover (Amani et al. 2017). Depth and minimum sample number are the two important tuning parameters in the RF algorithm. In this study, the DT and RF classifiers were parameterised according to the suggestions in the OpenCV library documentation presented by Garage (2011), i.e. the maximum depth was set to 50, the minimum number of samples was set to one and pruning harshness was set to the minimum.

The *k*-NN classifier is a distance rule-based technique often employed in image classification. The rule assigns an unknown sample to the class that occurs most frequently among its *k*-nearest neighbours (Aggarwal (Compiler and ed) 2014; Campbell & Wynne 2011). The basic functioning behind *k*-NN is that the group of *k* samples in the calibration dataset that are nearest (in feature space) to an unknown sample is used to infer (through a majority vote) its membership (Qian et al. 2015; Thanh Noi & Kappas 2018). Therefore, *k* is the key tuning parameter in this classifier and largely determines the performance of the classifier. For this study *k* was set to 1, as proposed by (Qian et al. 2015).

5.3.7 Accuracy assessment

A 3:2 sample split ratio was used for classifier training and accuracy assessment, i.e. 40% of the samples was randomly excluded from classifier training and used exclusively for assessing the accuracy of the resulting classifier, as suggested by Gilbertson, Kemp & Van Niekerk (2017). To compare the performance of each classifier, the same training (input) and testing (validation) dataset were used for all the classification experiments to ensure that differences in accuracy could be attributed to the nature of the class allocation processes. The same set of samples was used for assessing the accuracies of the thresholding and machine learning classification results.

A confusion matrix, producer's accuracy (PA), user's accuracy (UA), overall accuracy (OA) and the kappa coefficient (K) were generated for each classification experiment. OA is easily interpreted as it represents the percentage of classified pixels in the image that have been correctly labelled (Campbell & Wynne 2011), while K can be used to assess statistical differences between classifications (Foody & Mathur 2004).

The statistical significance of the accuracy differences among experiments was evaluated using non-parametric statistical tests, namely McNemar's (Adedokun & Burgess 2011) and Friedman's test, as implemented in the Statistical Package for Social Sciences (SPSS). Differences were considered as statistically significant at $P<0.05$.

5.4 RESULTS

5.4.1 Thresholding

Table 5.6 lists the results of the six best performing Otsu-based thresholding experiments (named T1–T6 for easier notation). Compared to the S1 features, higher accuracies were achieved when thresholding was applied to the S2 variables, with only one SAR-based experiment (T2) being among the six best results. When considering the combination of all the study sites, NDWI (T1), derived from the green and NIR S2 bands, was the most successful in separating water from other land covers with an OA of 81.6% and K of 0.73. The second best performing feature was the S1 VH band (T2), derived from the refined Lee (RL) filter, with OA and K values of 77.7% and 0.67 respectively. According to McNemar's test, the difference between T1 and T2 is statistically significant. The second best performing S2 feature (OA of 71.8%) was the MNDWI, derived from the green band, and the ATWT pan-sharpened SWIR S2 Band 11 (T3). This result was significantly lower than both T1 and T2, but not significantly higher than when individual bands (T4 and T5) were used as input to the thresholding algorithm. The accuracy levels dropped off sharply in T6 when Gram-Schmidt pan-sharpening was used for MNDWI.

Generally, thresholding was more successful when each site was classified individually (i.e. using a locally adapted threshold). For instance, the mean OA of the per site NDWI (T1) classifications was 90.7%, which is significantly higher than the 81.6% OA achieved when all the sites were classified in combination. A similar pattern is observed for the other features (all differences between mean OAs per site and OAs of all sites combined were statistically significant), although the variation among site-specific classifications varied considerably. Notably, the standard deviation (SD) of the NDWI (T1) classifications was 1.57%, while for $MNDWI_{GS}$ (T6) and $MNDWI_{ATWT}$ (T3) it was 13.2% and 11.8% respectively, which brings the stability of the latter two features into question. The stability of the S1 VH RL speckle filter (T2) was better (SD of 3.1) than that of the two MNDWI-based features (T3 and T6), but still significantly lower than that of NDWI (T1). This suggests that no single threshold could accurately separate water and non-water land covers in all sites. This is supported by Figure 5.3a, b and c which demonstrates the temporal variability of NDWI, MNDWI and VH/VV for the

points taken at the same waterbody (Site G) on different dates. Furthermore, Figure 5.3d shows the spectral variability within the same waterbody based on a S2 image acquired on 22 November 2016.

Table 5.6 Overall accuracies (OAs), kappa coefficients (K), mean ($\bar{x}$) and standard deviation (δ) values for the six best performing thresholding features.

Site	Thresholding												Average			
	T1		T2		T3		T4		T5		T6		OA		K	
	NDWI		VH $Band_{RL}$		$MNDWI_{ATWT}$		Band 8		Band 11_{ATWT}		$MNDWI_{GS}$					
	OA	K	OA	K	OA	K	OA	K	OA	K	OA	K	$\bar{x}$	δ	$\bar{x}$	δ
Site A	88.2	0.83	85.5	0.65	73.2	0.59	74	0.53	63.7	0.53	64.2	0.51	77.6	9.5	0.50	0.27
Site B	91.8	0.84	88.5	0.77	68.3	0.58	77.6	0.55	75.4	0.51	71.6	0.54	76.8	12.1	0.40	0.38
Site C	90.8	0.83	88.4	0.77	93.6	0.87	81.2	0.73	78	0.57	84.2	0.89	86.9	7.1	0.78	0.15
Site D	91.6	0.89	89.6	0.79	75.8	0.62	76.7	0.53	65.9	0.51	65.7	0.51	77.8	11.4	0.49	0.30
Site E	90.7	0.81	89.5	0.79	94.6	0.89	80.8	0.62	75.9	0.52	85.1	0.92	87.1	8.0	0.78	0.17
Site F	89.1	0.78	88.7	0.77	65.9	0.55	78.9	0.58	73.1	0.57	64.3	0.51	75.4	16.0	0.38	0.37
Site G	96.1	0.92	92.4	0.85	98.2	0.91	88.8	0.78	88.6	0.77	93.2	0.93	90.5	6.0	0.81	0.11
Site H	90.3	0.81	82.8	0.71	91.1	0.82	76.3	0.53	75.7	0.52	70.4	0.54	83.9	11.0	0.63	0.20
Mean	90.7	0.82	86.3	0.70	85.2	0.67	81.3	0.61	77.8	0.55	75.2	0.73	82.8	5.8	0.7	0.13
SD	1.57	0.03	3.1	0.10	11.8	0.20	4.5	0.10	6.2	0.05	13.2	0.15	6.73	4.75	0.11	0.06
All sites	81.6	0.76	77.7	0.71	73.8	0.69	69.5	0.57	67.7	0.57	65.2	0.56	72.3	6.25	0.64	0.08

Notes: GS = Gram-Schmidt; ATWT = pan-sharpening à Trous wavelet transform; RL= refined Lee speckle filtering. Kappa values greater than 0.8 are highlighted in red.

The accuracies among study sites varied substantially. Site G, which is slightly turbid and eutrophic achieved the highest mean OA (90.5%), while the lowest accuracy was recorded at site F (mean OA 75.4%). The latter site is a shallow dam with humic-rich water from a slow-moving channel flowing through forested plantations (Eucalyptus pine and swamps, Table 5.1). MNDWI (T3) showed the highest accuracy for delineating sites C, E and H. These sites represent clear and eutrophic water. Thresholding of NDWI (T1) produced the best results when humic water sites were classified (i.e. A, B, D and F), while T2 (SAR backscatter) performed generally well (>82%) in all sites. This suggests that the SAR data were less affected by the optical variabilities among the waterbodies. A Friedman's test showed that the difference between feature type and optical variability of water are statistically significant (P = 0.002).

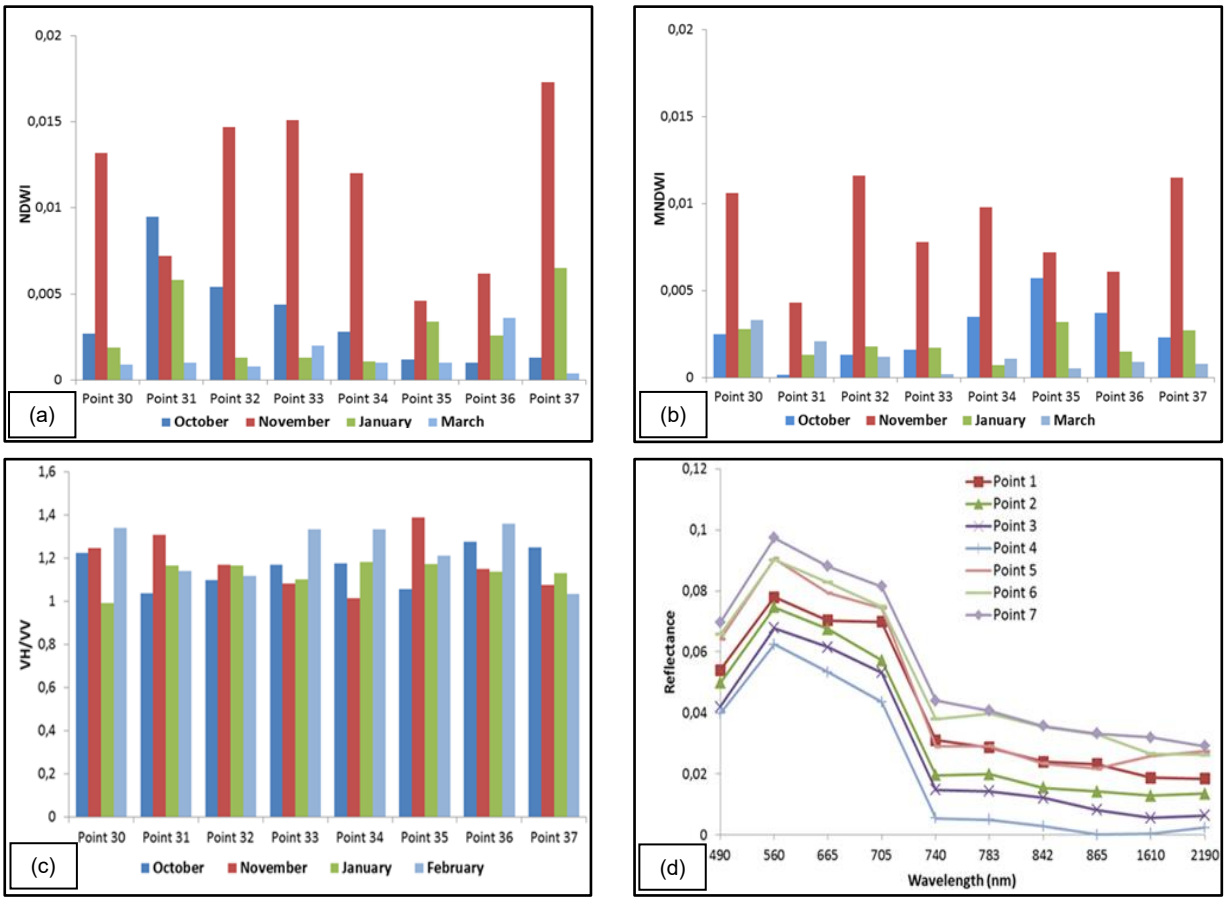

Figure 5.3 The water points collected on the same waterbody (Site G) showing the temporal and spatial variability in (a) NDWI, (b) MNDWI, (c) VH/VV on different dates and (d) spectral variability on Sentinel-2 image of 22 November 2016

Unlike the other indices tested, NDWI was found to have the ability to spectrally differentiate surface water with different characteristics located among different land cover types, including shadows or dark areas. For instance Figure 5.4 shows that MNDWI incorrectly classified humic-rich water as non-water and confused shadows with water (Figure 5.5). Details of confusion matrices, including commission and omission errors when applying NDWI, MNDWI and $VHBand_{RL,}$ are shown in Appendix A. The waterbodies were better captured by NDWI in all cases.

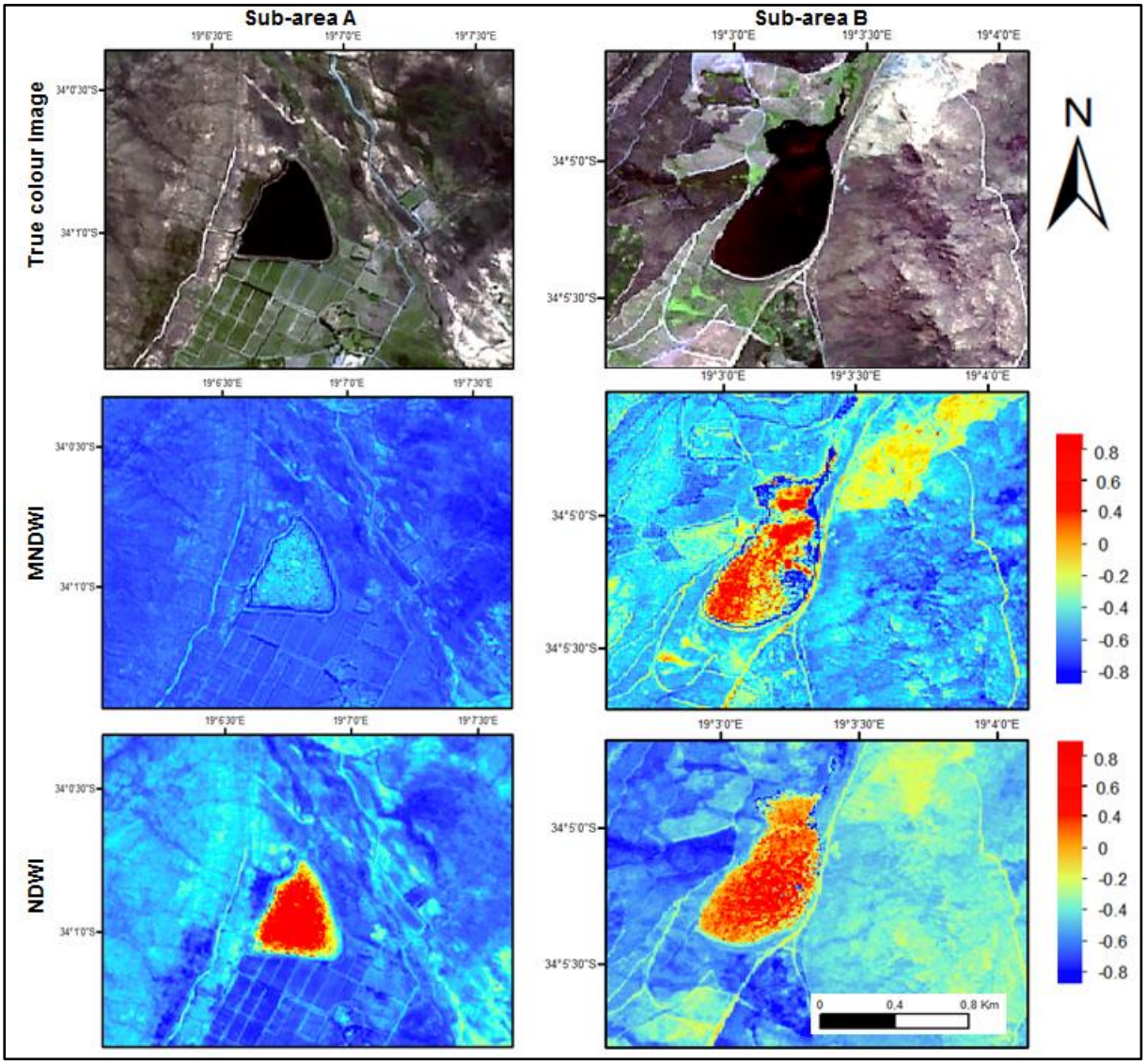

Figure 5.4 Detailed (large-scale) examples of the 10 m true colour maps of Sentinel-2 (4, 3, 2), MNDWI and NDWI images. The first column represents site A and the second column is for site F. Values greater than -0.2 were classified as water

Shadows and water are spectrally similar and were consequently difficult to discriminate, as depicted by large errors of omission and commission in the shadow class with all the MNDWI, NDWI and VH $Band_{RL}$. For example, for MNDWI, a higher commission error in the shadow class was detected (47%) (mainly due to misclassification of water), which is also reflected in the high omission error (16.5%). Furthermore, this is supported by the visualisation of false positives for MNDWI, especially in mountainous terrain (Figure 5.5).

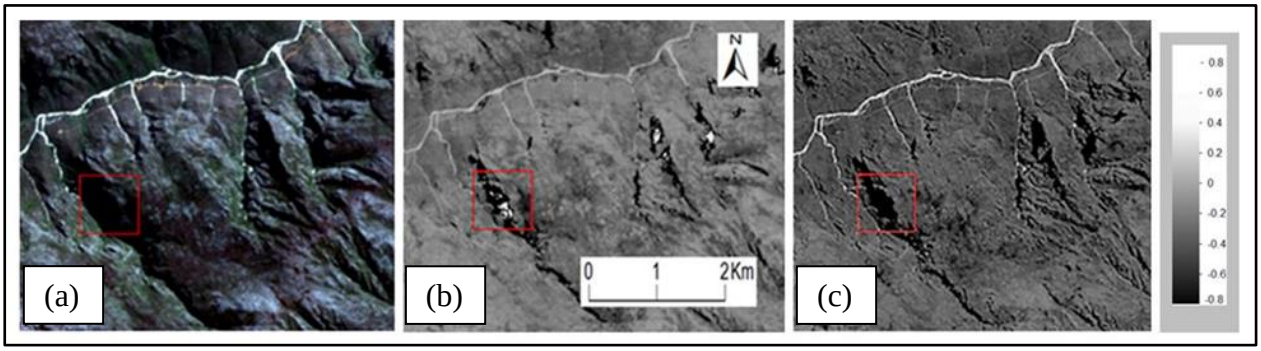

Figure 5.5 Visual comparison of a Sentinel-2 (a) true colour image (4, 3, 2), (b) MNDWI and (c) NDWI misrepresentation of shadows by MNDWI. Values greater than -0.2 were classified as water

Figure 5.6 provides a qualitative comparison of T1 and T2 in test site F generated from images captured on 31 January 2017. In general, it seems that T1 classified water with greater accuracy than T2; however T1 (marked with green squares) and T2 (marked with red squares) omitted water in some areas (Figure 5.6). To reduce these errors and in the interest of finding a solution to classify water automatically and accurately, an additional experiment (called "T1+T2") was carried out in which T1 and T2 were intersected (i.e. using the Boolean operator OR).

Figure 5.6 The visualisation of water masks derived from T1 (NDWI), T2 (SAR VH band) and T1+T2 (fusion of T1 and T2). An aerial photograph of October 2014 was used at which time the water level was lower than those at T1 and T2.

Visual inspection of Figure 5.6 suggests that T1+T2 resulted in better accuracy of surface water mapping compared to either T1 or T2. The accuracy of T1+T2 was significantly (8%) higher than that of T1, achieving an OA of 89.3%.

5.4.2 Benchmarking thresholding to machine learning

Table 5.7 summarises the machine learning classification results. Generally, all the classifiers performed well at classifying slightly turbid water (site G). SVM significantly outperformed the other classifiers when the classifications were carried per individual site, with site G recording the highest mean OA of 95.9%. This result is significantly higher (P = 0.03) than the second best classifier *c*-SVM (mean OA = 93.3%). On average, DT was the worst performing classifier (mean OA of 88.4%) when the classifications were carried out per site, except for site G (94.6%) where it outperformed RF (92.5%) and *k*-NN (93.8%). With a SD of 3.7, DT was also the least stable of the five classifiers. The *c*-SVM was the second best performing classifier, but it did not perform well at classifying sites D and E (relative to *k*-NN and RF).

Table 5.7 Overall accuracies (OAs), kappa coefficients (K), mean ($\bar{x}$) and standard deviation (δ) values for the machine learning algorithms (MLAs)

Site	CLASSIFFIER										OVERALL AVERAGE			
	SVM		*c*-SVM		*k*-NN		RF		DT		OA		K	
	OA	K	OA	K	OA	K	OA	K	OA	K	$\bar{x}$	δ	$\bar{x}$	δ
Site A	95.8	0.91	92.7	0.90	87.2	0.85	88.7	0.86	81.7	0.79	89.2	4.73	0.86	0.05
Site B	97.4	0.93	94.2	0.91	89.0	0.87	89.8	0.86	85.0	0.82	91	4.07	0.88	0.05
Site C	96.8	0.94	94.4	0.91	90.5	0.89	89.3	0.86	86.2	0.83	91.2	3.39	0.88	0.04
Site D	95	0.94	90.7	0.92	91.8	0.90	91.3	0.89	90.2	0.89	93.9	1.89	0.91	0.02
Site E	96.3	0.88	93.3	0.95	93.6	0.90	91.4	0.89	91.2	0.89	93	1.52	0.90	0.03
Site F	94.5	0.90	92.2	0.90	89.7	0.87	88.7	0.86	86.2	0.83	90	2.1	0.87	0.03
Site G	98.2	0.96	95.7	0.95	93.8	0.89	92.5	0.89	94.6	0.95	94	2.67	0.93	0.03
Site H	94.6	0.91	94.3	0.93	91.5	0.89	92.7	0.90	91.3	0.90	93	1.08	0.91	0.02
Mean	95.9	0.93	93.3	0.92	90.8	0.9	90.5	0.88	88.4	0.89	91.8	2.89	0.90	0.03
SD	2.17	0.03	1.1	0.02	2.26	0.02	2.6	0.04	3.7	0.03	2.37	0.93	0.03	0.01
All sites	91.7	0.82	89.6	0.81	80.7	0.78	79.5	0.77	78.7	0.76	81.2	2.32	0.79	0.03

SVM consistently outperformed the other classifiers, with an OA and K values of 91.7% and 0.82 respectively when all sites were combined. This was significantly higher (P = 0.03) than the second best performing classifier *c*-SVM, which achieved an OA of 89.6%. DT delivered the poorest overall classification results (OA = 78.7%), followed by RF (79.5%) and *k*-NN (80.7%). The accuracies of all classifiers dropped significantly when all the sites were classified in combination (i.e. when the complexity of the target classes increased), with RF and *k*-NN being the most affected (reduction in mean OA of more than 10%).

The OAs of the MLAs and best thresholding classifications are graphically compared in Figure 5.7. SVM and *c*-SVM performed the best, regardless of the characteristics of the waterbody. T1 performed better than the worst performing machine learning classifier (*k*-NN) at sites A, B and C, which are characterised by moderately eutrophic water. At site D (humic water), T1 achieved a 1.5% higher OA than *c*-SVM. Although T3 was the worst performing classification when all sites were combined, it performed on par with the machine learning classifiers at sites C, E, G and H. For instance, at site E its accuracy was significantly (1.3%) higher than what was obtained with *c*-SVM.

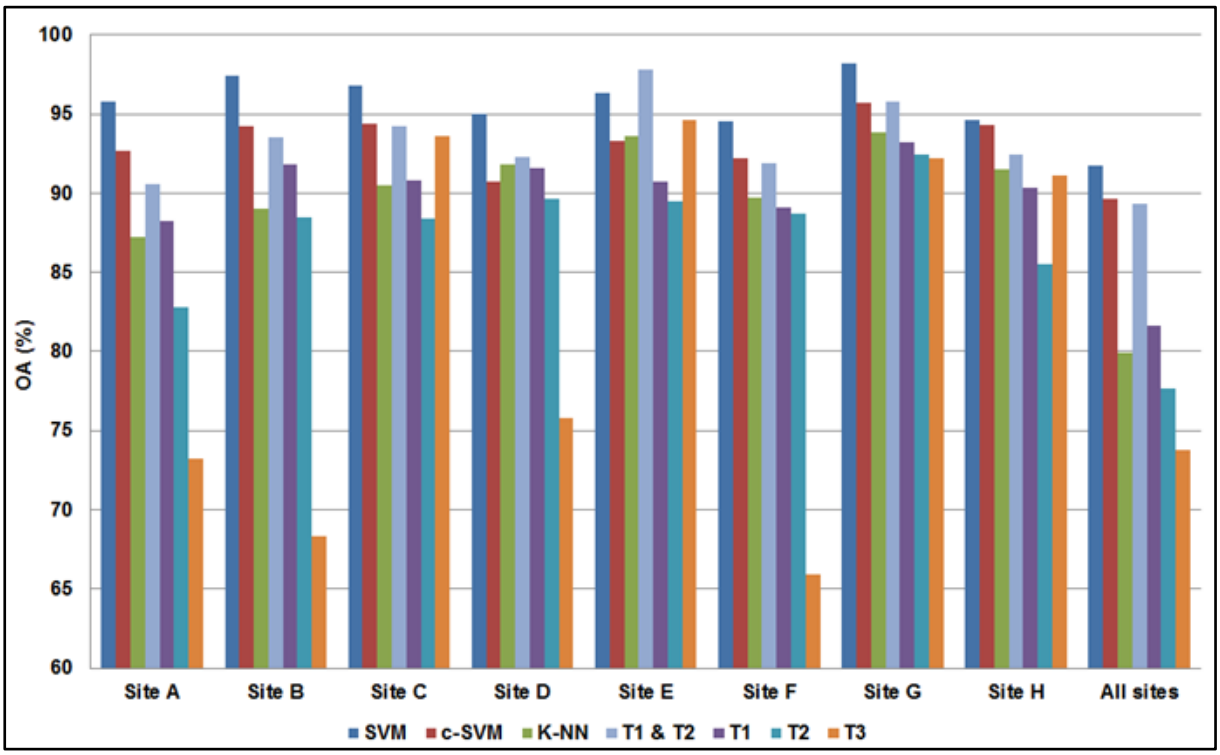

Figure 5.7 Comparison between thresholding and MLAs for all sites

Although SVM was superior, the fusion of the T1 and T2 rulesets improved the threshold-based classification outcome to achieve competitive results. T1+T2 achieved a higher accuracy than *k*-NN at all individual sites and at site D; it outperformed c-SVM by about 2.7%. At site E (eutrophic waterbody), T1+T2 attained the highest accuracy, while at sites C and G, its accuracy was almost on par with that of *c*-SVM. It is important to note that the fusion of T1 and T2 did not improve the OAs at sites D and H by much. Figure 5.7 show that all the classifiers struggled (OAs below 95%) at sites D, F and H. These sites are characterised by humic-rich water and are located in mountainous terrain.

5.5 DISCUSSION

The results show that the characteristics of the water, type of classifier and input feature dataset had a significant impact on the accuracies of the surface water classifications. With the multispectral data, the selection of the spectral index had a significant impact on accuracies. MNDWI's lower OA compared to NDWI was mainly due to the under classification of humic-rich water (Figure 5.4) and over classification of shadows (Figure 5.5).

NDWI was able to highlight dark, turbid and eutrophic water more effectively than MNDWI. This finding contrast with those of Xu (2006) and Zhai et al. (2015) who noted that MNDWI provided better discriminatory power than NDWI for shadowed and dark areas in close spectral proximity to water. Zhai et al. (2015) found that MNDWI performed substantially better than NDWI in mapping waterbodies that have similar spectral profiles to shadows, while Xu (2006) showed that MNDWI performed significantly better than NDWI for extracting turbid water, which has a high spectral resemblance to some non-water classes. It should be noted, however, that these studies used spectral bands from Landsat 7 and Landsat-8, which differ from S2 bands used in this study. However, our observations support those of Rokni et al. (2014) and Zhou et al. (2017) who found NDWI to be superior to other indices in delineating shallow and turbid lakes respectively. A likely explanation for NDWI performing better than MNDWI in our study was the study region. The latter index is known to be more effective than NDWI in suppressing built-up features (Du et al. 2016; Yang et al. 2017) and our study region is mostly rural. Nevertheless, the different OAs of NDWI and MNDWI suggest that the NIR and SWIR bands were more sensitive to the variations in physical and chemical properties of water than the green band.

It was observed that the SAR VH band classified water more accurately than the VV band did, irrespective of the targeted water characteristics. Classification errors at site H were mainly due to windy conditions at the time of acquisition, which created waves on the water surface and resulted in high backscatter signals. The VV polarisation produced higher backscatter values over water surfaces than the VH polarisation, which suggests that the former configuration is more sensitive to variations between water and non-water features. A bigger difference between the backscatter responses of land and water features was noted in the VH polarisation than in the VV polarisation. This corresponds well with Clement, Kilsby & Moore (2018) who also noted that VH outperformed VV polarisation for turbid water mapping. Our study observed that the refined Lee speckle filter can suppress the speckle effect and maintain details of the water

boundary (Pham-Duc, Prigent & Aires 2017), which is important for the identification of water pixels at the water/soil interface.

In this study, the semi-automated MLAs were used for benchmarking the autonomous thresholding results. All multispectral and SAR features were included in the MLAs to produce a best-case scenario. Although inequality within the waterbodies (e.g. depth, colour and sediment variations) has been shown to affect classification results when using remotely sensed data (Gómez-Palacios, Torres & Reinoso 2017), this study has proved SVM to be less sensitive to intra-class variations compared to other classifiers. Moreover, SVM was credited with its ability to effectively separate classes that are spectrally similar (e.g. humic-rich water and shadows). This was likely a major contributing factor to its outstanding performance in this study.

Challenges relating to different applications and data used were encountered when attempts were made to directly compare the findings of this study with those of previous studies. The majority of the published studies that focus on the use of MLAs for the supervised classification of remote sensing data have been done for vegetation and crop type classification using Landsat data. However, the outcomes of this study are closely related to those of Sarp & Ozcelik (2017) who revealed that machine learning algorithms marginally outperform thresholding.

Although MLAs (specifically SVM) outperformed the thresholding methods in individual sites and when the sites were combined (i.e. when complexity increased), the main drawback of supervised MLAs is their dependence on training data. The application of supervised approaches is limited to regions for which representative samples of labelled data are available. Once training samples are established, they can be reused and applied to images with different dates and even of different areas. However, the accuracy of the resulting classifications is usually negatively affected (Hasmadi, Pakhriazad & Shahrin 2009; Ireland, Volpi & Petropoulos 2015; Verhulp & Van Niekerk 2017), mainly due to temporal and regional variations. Waterbodies are highly dynamic as they continuously fill up and empty, which makes the re-use of training sets very challenging and limits the operational implementation of supervised techniques for monitoring changes in surface water reservoirs.

Despite the relatively lower recorded accuracies of thresholding (compared to those of MLAs), it seems to be a viable solution for operational implementations. In contrast to supervised approaches that require training data and rule-set (expert system) approaches that make use of a set of static thresholds, thresholding generates dynamic rules (appropriate thresholds) that do not require human interaction or training data. However, our results show that the use of a single

feature (rule) for thresholding produced relatively poor and unstable results. Combining the outputs of different thresholding results produced much better and more robust results. For instance, we combined the two best thresholding outputs (NDWI and VH $Band_{RL}$) and found that the combination of these SAR and multispectral features significantly improved the accuracy and stability of the surface water classifications. More work is needed to investigate the efficacy of other combinations of thresholding outputs.

5.6 CONCLUSION

Accurate temporal and spatial changes for small waterbodies are critical for water security, drought monitoring and crop irrigation decision-making. Remote sensing offers a reliable, cost-effective and potentially autonomous alternative for surface water mapping of large and inaccessible areas. The recently launched S1 and S2 satellites provide fine spatial and temporal resolution remote sensing data, which makes it ideal for mapping waterbodies at regional and even global scales.

In this study, we proposed an approach that combines automatic thresholding of near-concurrent NDWI (generated from S1) and VH backscatter bands (generated from S1) for mapping waterbodies (mainly reservoirs and dams) with diverse spectral and spatial characteristics. Waterbodies of different sizes and varying levels of turbidity, sedimentation and eutrophication were targeted. The resulting maps were compared to the classification performances of five MLAs, namely DT, k-nearest neighbour (k-NN), RF and two implementations of the SVM. The results showed that the physical and chemical properties of water significantly affected classification accuracies. The performance of the best machine learning classifier (SVM) and thresholding (NDWI) dropped by more than 10% when the complexity of the task was increased (i.e. when the classifiers were applied to all sites in combination). However, the combination the two best thresholding results (NDWI and VH $Band_{RL}$) was relatively accurate and stable, likely because it takes advantage of both SAR and multispectral data. Although several heterogeneous sites were used to evaluate the results, more work is needed to test whether the dynamic NDWI–VH $Band_{RL}$ rule-set will be as effective in other areas, on other water types, during different seasons and under contrasting conditions. Other indices such as the automated water extraction index (AWEI) and tasselled cap wetness transformation should also be evaluated when the coefficients for S2 bands are made available.

In summary, the techniques and datasets evaluated in this study show much promise for the accurate classification of optically complex waterbodies. Moreover, the relatively accurate and

stable classifications achieved when the multispectral and SAR data were fused and automatically thresholded are very encouraging and may provide a viable solution for the operational monitoring of surface waterbodies in the Winelands district of South Africa. The implementation of this technique will provide invaluable information for water management and water security.

CHAPTER 6: LAND SURFACE WATER MAPPING USING REMOTE SENSING IN COMPLEX AND HETEROGENEOUS ENVIRONMENTS: CONCLUSION

6.1 INTRODUCTION

Mapping of surface water (LSW) is of particular importance for monitoring flood events and water resources (Kundzewicz et al. 2014; Mueller et al. 2016). According to the Intergovernmental Panel on Climate Change (IPCC (2014), global climate change and the occurrence and severity of floods and droughts are projected to be more pronounced in the near future than previously foreseen. The impacts of these events will likely be more destructive in developing countries, particularly those in Africa, where the adaptive capacity is low and community vulnerability high (IPCC 2014; Long, Fatoyinbo & Policelli 2014). Responsible organisations in these countries are often inadequately equipped to monitor the impacts of climate change on LSW resources and risks.

Recently, there has been an improved understanding of the connection between climate change and the dynamics of LSW resources (Amitrano et al. 2018; Bessinger 2016; Ouled et al. 2018; Sadegh et al. 2017). In situ hydrological data are useful in quantifying the temporal and spatial changes of LSW resources. Studies have used field surveys data to monitor seasonal and long-term climatic changes of LSW resources (Correia et al. 1998; Hess et al. 1995). These surveys are limited in temporal and spatial coverage, however, and are thus inadequate for monitoring dynamics in LSW over large areas. This inadequacy is pronounced in developing countries where financial constraints make it difficult to carry out field surveys regularly (Rahman & Di 2017). Further, even in well-resourced, developed nations, it is not economically viable or practical to implement frequent field surveys for monitoring LSW resources. On the other hand, space-borne remote sensing has been proposed as an alternative approach for mapping and monitoring LSW resources over large areas and at short temporal intervals (Makapela et al. 2015; Yan et al. 2015). However, most RS applications for LSW mapping have not given much attention to the effects of surrounding land covers, partly submerged vegetation, as well as dissolved and suspended substances in water (Plank et al. 2017). According to Song et al. (2014), the increased level of turbidity and the presence of water underneath the vegetation can increase backscatter and reflectance values of water. This can result in underestimation of wetlands and inundation extents in vegetated floodplains (Plank et al. 2017; Wei et al. 2017) and optically complex (e.g. turbid and eutrophic) waterbodies (Sarp & Ozcelik 2017). Therefore, effective

LSW mapping requires an understanding of the impacts of these complexities on SAR backscatter and reflectance values.

The next section revisits the research aims and objectives in order to critically reflect on the value of this study.

6.1 RESEARCH OBJECTIVES REVISITED

The primary aim of the research was to evaluate the potential of remotely sensed data with different temporal, spatial and radiometric properties to map LSW under complex conditions.

The first objective (see Section 6.2) was to review the literature on the trade-offs between conventional (i.e. field-based) and remote sensing techniques for mapping LSW. In Chapter 2 we reviewed the literature on different classification methods, i.e. visual interpretation, supervised classification, unsupervised classification and expert systems, applied to SAR and multispectral data for LSW mapping. The review of the use of satellite RS for LSW mapping showed that only a few studies targeted the mapping of heterogeneous and optically complex waterbodies. The review also highlighted the challenges associated with the use of RS for this purpose. The trade-offs between pixel size and revisit time were cited by many researchers as a major limitation of RS for mapping flooded vegetation in near real-time. This drawback, coupled with the growing demand for near real-time information on flood monitoring, has motivated many researchers to embark on linear spectral unmixing, unsupervised classification (e.g. thresholding), as well as multisensory and data fusion approaches.

The second objective of the study was to develop a technique whereby surface water can be mapped in the presence of vegetation using high temporal and low spatial resolution RS data. MERIS imagery was chosen to map a historical flood event in the Caprivi floodplain using a novel spectral unmixing approach (Chapter 3). MERIS images are similar to the Ocean and Land Colour Instrument (OLCI) imagery acquired by the recently launched Sentinel-3 (S3) satellite. A challenge to spectral unmixing for flooded area mapping is the estimation of spectral endmembers, i.e. pure spectra of land cover features. In this study, an unmixing method based on an ensemble of spectral endmembers was developed to take into account spectral variability within each endmember. Specifically, the fractional abundance of water (γ_w) was estimated by applying a new spectral indices-based unmixing algorithm using three spectral bands. The NDWI was applied to delineate the water surface and combined with NDVI to account for partly submerged vegetation within inundated areas. The quality of the flood map was assessed against high (30 m) spatial resolution Landsat Thematic Mapper (TM) images on two different dates (17

April 2008 and 22 May 2009) during which floods occurred. The findings show that both the spatial and the frequency distribution of the fractional abundance of water extracted from the MERIS data were in good agreement with the TM retrievals. In contrast, conventional linear unmixing, performed using the all the available bands in each image, resulted in relatively large differences between TM and MERIS retrievals.

Flood maps derived from SAR data are critical for accurate flood monitoring. SAR has the capability to penetrate the vegetation canopy to a certain extent depending on the wavelength and its sensitivity to water underneath the vegetation (Tsyganskaya et al. 2018b). From the literature it was established that most studies make use of single SAR images and land use and land cover (LULC) maps for estimating flood extent. The principle of such an approach is to find a satellite-observed backscatter value below which a pixel can be regarded as being flooded. This approach is, however, limiting as the threshold applying to flood conditions does not take local land surface characteristics (e.g. rough soil surface, vegetation) affecting backscatter observations into account. An evaluation of the utility of a time series of Sentinel-1 (S1) SAR data for mapping flooded vegetation (Chapter 4) thus addressed the third objective of the research. A time series classification technique based on the Bayesian probability was developed. A quantitative assessment of the derived inundated area during a flood event on 7 April 2017 was done using Landsat OLI images. It was shown that, compared to S1 SAR images, the optical Landsat images overestimated the flooded area by about 11%. The evaluation showed that setting a fixed backscatter value as a threshold for estimating the probability of a pixel being flooded is inflexible and that it is difficult to capture local land surface characteristics from a single image; however, additional information can be extracted from a time series statistics of SAR images.

Chapter 5 investigated the value of combining multispectral and SAR data for mapping small and fragmented surface waterbodies, thereby addressing the final objective of this research. MLAs were used to benchmark a range of autonomous thresholding experiments. The study showed that combining multispectral indices with SAR data is highly beneficial for classifying complex waterbodies and that the proposed thresholding approach classified waterbodies with an overall classification accuracy of 89.3%. Although MLAs classified the complex waterbodies with higher accuracy (91.7%) than thresholding, they require training data to be collected (and updated) and as such cannot be fully automated. In contrast, fully automated thresholding can be operationalised to map and monitor LSW over large and in complex areas with relatively high and stable accuracies.

6.2 RESEARCH VALUE AND CONTRIBUTION

This study has contributed to existing knowledge on LSW mapping to aid flood monitoring and water security management, particularly in turbid, vegetated, sedimented and eutrophic waterbodies. Many communities in developing countries rely on such LSW for agricultural production, as well as domestic and industrial use (Botai et al. 2017). The trade-off between pixel size and revisit time was addressed by developing and demonstrating a novel spectral unmixing method (Chapter 3). The combined ability to capture variability of spectral endmembers and thresholds is novel. The developed method makes use of ensemble estimation of spectral endmembers to capture and take into account spectral variability within each endmember and can be used to improve the accuracy of flood extent mapping in the heterogeneous environments.

Chapter 4 showed that local land surface characteristics are difficult to deduce from a single SAR image, but that invaluable information on LSW can be extracted from a series of images. This finding is novel and the fusion of VH and VH/VV polarisations to derive the extent of flooded vegetation also contributes to existing knowledge.

Another contribution of this research was the integration of SAR and multispectral indices to improve the classification accuracy of optically complex waterbodies. The varying concentrations of suspended sediments (turbidity), dissolved particles and aquatic plants negatively affect the classification accuracies of Earth observation methods, although it seems that MLAs (SVM in particular) are less sensitive to such variations. The dynamic nature of reservoirs (many reservoirs are depleted at least once a year) makes the re-use of training data unfeasible, which lends support to implementing fully automated thresholding techniques that combines SAR and optical data for mapping and monitoring complex waterbodies.

An additional benefit of the study is the range of flood and LSW maps generated in the Southern African region. The maps act as proof of the concept of the use of SAR and multispectral data in the region and will hopefully create awareness of the value of RS data and techniques for operational LSW monitoring. At the very least, these maps can be used to calibrate and validate other techniques such as hydraulic models (Dimitriadis et al. 2016; Shen et al. 2015).

6.3 LIMITATIONS, RECOMMENDATIONS AND SUGGESTIONS FOR FUTURE STUDIES

As with most research, this study has several limitations, which should be addressed in future work. For this research, the assumptions were that multispectral and SAR images can be easily classified into land and water based on different spectral and SAR backscatter returns respectively. This assumption works well in clear open water bodies. The case studies for this research are complex areas characterised with turbid, sedimented and merged vegetation, which have impacts on the spectral profile and backscatter return. For the SAR images, flooded vegetation had high backscatter values similar to dry features. Delineating these complex environments using multispectral images, however, proved to be difficult as well. The spectral signature from different bands was a mixture of vegetation, water, wet soil and sediments. In addition, the LSW under vegetation canopies and at the boundaries between water and non-water classes was erroneously excluded in the flooded class. The complexity of these environments together with the trade-offs between spatial and temporal resolutions of satellite data make mapping of LSW in these environments complicated.

The spectral unmixing developed in Chapter 3 was used to map a historical flood event based on MERIS data from the now decommissioned Envisat satellite. The technique needs to be tested on new datasets, for instance those acquired by the OLCI instrument on board S3, which have technical similarities to the MERIS image data. In addition, the accuracy of the spectral unmixing method was assessed using Landsat imagery with a spatial resolution of 30 m. Higher resolution imagery would have been better, but was not available for the historical event. It is recommended that the technique is carried out in an area for which very high resolution (VHR) imagery such as S-2 is available during or shortly after a flood event.

Coarse spatial resolution imagery is typically used for real-time flood mapping. The spectral unmixing method developed in this research (Chapter 3) requires substantial manual inputs (e.g. selection of pure endmembers). More work is needed to automatically select pure endmembers. Furthermore, there is a need for developing algorithms to spatially upscale coarse-resolution remote sensing data to produce datasets with acceptable spatial and temporal resolution for LSW monitoring, particularly in heterogeneous environments. Future experiments should test the utility of the new datasets with coarse spatial resolutions and frequent revisit times, with S-3 / OLCI data being a logical candidate.

This study did not consider the impact of different types of flooded vegetation on SAR backscatter (Chapter 4). Future studies should differentiate backscatter according to vegetation types, specifically tall graminoids (e.g. grass and reeds), shrubs and dense forests. Another limitation of the study was the per-pixel classification approach used. Future studies should assess the value of using object-based classification techniques, which could reduce noise and improve depiction of real-word objects.

The mapping of complex waterbodies using RS techniques (Chapter 5) was applied to a relatively small area (40×45 km) in the Western Cape province of South Africa. Although the waterbodies in the area are highly diverse, it would be worth testing the suggested multispectral and SAR thresholding technique in a larger area and in different landscape types to assess the robustness thereof. Other automatic thresholding algorithms (i.e. in addition to Otsu used in this research), such as histogram-shape-based, entropy-based and attribute-based techniques, should be tested. The levels of turbidity and chlorophyll concentration of these water bodies were not tested. It is therefore, recommended that future studies have to quantitatively evaluate the physical and chemical properties of the waterbodies.

6.4 CONCLUSION

The purpose of this study was to evaluate the performance and strength of remote sensing data for mapping flooded vegetation, as well as turbid, sedimented and eutrophic water. One of the main findings is that SAR backscatter and multispectral signatures are strongly affected by variations in suspended, dissolved, chemical and physical constituents of water, which in turn impacts classification accuracies. The research concludes that the fusion of SAR and optical data, combined with the use of fully automated thresholding techniques, is a viable solution for mapping and monitoring complex waterbodies, but that further refinements are required to improve accuracies. Based on the results of this work, it was shown that a time series of SAR data backscatter statistics of a specific area can be characterised year round under a range of conditions. These backscatter statistics can be utilised to precisely determine whether a specific area is flooded or not, irrespective of weather conditions or time of day.

The future of RS for LSW mapping looks promising. The advent of very high resolution EO data such as Kompsat-3A, DEIMOS-2, WorldView-4, Pleiades-Neo 1-4[4] and CartoSat-2 (C-F), in

[4] Not yet launched

conjunction with the continuous improvements in image classification techniques (e.g. data fusion and MLAs) and the increasing public awareness of EO data through platforms such as social media, television and newspaper articles, will likely promote the increased use of EO methods and efficient monitoring of LSW resources in developing countries. There is need to integrate LiDAR altimetry (water level) with hyperspectral data and multi – frequency polarised SAR to find out if different EM signals improve the classification accuracy for mapping heterogeneous and complex environments. Moreover, the use of emerging technologies such as smartphones equipped with very high resolution cameras and UAVs will likely improve access to data needed for LSW mapping.

RS has been recognised as an effective alternative to conventional methods of monitoring LSW as it reduces costs and time associated with obtaining information about the extent of LSW. LSW, which include temporary surface water features, is highly susceptible to climate variations. Increased impacts of climate change on LSW have resulted in regional floods and water shortages, which have considerable ecological, social and economic consequences. LSW maps and techniques developed in this study is critical for flood status monitoring, water resources planning and disaster management, and will as such hopefully reduce the impact of floods and droughts on vulnerable communities living in southern Africa.

REFERENCES

Acharya TD, Lee DH, Yang IT & Lee JK 2016. Identification of Water Bodies in a Landsat 8 OLI Image Using a J48 Decision Tree. *Sensors* 16: 1075.

Adedokun OA & Burgess WD 2011. Analysis of paired dichotomous data: A gentle introduction to the McNemar test in SPSS. *Journal of MultiDisciplinary Evaluation* 8: 125-131.

Agapiou A, Alexakis DD, Themistocleous K & Hadjimitsis DG 2016. Water leakage detection using remote sensing, field spectroscopy and GIS in semiarid areas of Cyprus. *Urban Water Journal* 13: 221-231.

Aggarwal CC (Compiler and ed) 2014. *Data classification: algorithms and applications.* London: CRC Press.

Aimar A 2017. Managing water crisis in the North African Region with particular reference to Jijel Region. *Environmental Change and Human Security in Africa and the Middle East*, 219-237. Cham: Springer International Publishing.

Al-Bayati M & El-Zaart A 2013. Automatic thresholding techniques for SAR images. Proceedings of the International Conference of Soft Computing held 02-03 November Dubai, United Arab Emirates.

Alcântara E, Barbosa C, Stech J, Novo E & Shimabukuro Y 2009. Improving the spectral unmixing algorithm to map water turbidity Distributions. *Environmental Modelling & Software* 24: 1051-1061.

Ali A, Quadir DA & Huh OK 1989. Study of river flood hydrology in Bangladesh with AVHRR data. *International Journal of Remote Sensing* 10: 1873-1891.

Ali BMH, Lifu Z, Shudong W, Gaozhen J, Shanlong L & Qingxi T 2013. Comparison of MNDWI and DFI for water mapping in flooding season. 2013 IEEE International Geoscience and Remote Sensing Symposium - IGARSS held 21-26 July 2013 Australia (Melbourne, Victoria).

Amani M, Salehi B, Mahdavi S, Granger J & Brisco B 2017. Wetland classification in Newfoundland and Labrador using multi-source SAR and optical data integration. *GIScience & Remote Sensing* 54: 779-796.

Amarsaikhan D, Saandar M, Ganzorig M, Blotevogel HH, Egshiglen E, Gantuyal R, Nergui B & Enkhjargal D 2012. Comparison of multisource image fusion methods and land cover classification. *International Journal of Remote Sensing* 33: 2532-2550.

Amazirh A, Merlin O, Er-Raki S, Gao Q, Rivalland V, Malbeteau Y, Khabba S & Escorihuela MJ 2018. Retrieving surface soil moisture at high spatio-temporal resolution from a synergy

between Sentinel-1 radar and Landsat thermal data: A study case over bare soil. *Remote Sensing of Environment* 211: 321-337.

Amitrano D, Di Martino G, Iodice A, Riccio D & Ruello G 2018. Unsupervised rapid flood mapping using Sentinel-1 GRD SAR images. *IEEE Transactions on Geoscience and Remote Sensing* 56: 3290-3299.

Araujo JA, Abiodun BJ & Crespo O 2016. Impacts of drought on grape yields in Western Cape, South Africa. *Theoretical and Applied Climatology* 123: 117-130.

Argenti F, Lapini A, Bianchi T & Alparone L 2013. A tutorial on speckle reduction in synthetic aperture radar images. *IEEE Geoscience and Remote Sensing Magazine* 1: 6-35.

Bangira T, Alfieri S, Menenti M, van Niekerk A & Vekerdy Z 2017. A spectral unmixing method with ensemble estimation of endmembers: Application to flood mapping in the Caprivi floodplain. *Remote Sensing* 9: 1013.

Bangira T, Maathuis BH, Dube T & Gara TW 2015. Investigating flash floods potential areas using ASCAT and TRMM satellites in the Western Cape Province, South Africa. *Geocarto International* 30: 737-754.

Barati S, Rayegani B, Saati M, Sharifi A & Nasri M 2011. Comparison the accuracies of different spectral indices for estimation of vegetation cover fraction in sparse vegetated areas. *The Egyptian Journal of Remote Sensing and Space Science* 14: 49-56.

Barton IJ & Bathols JM 1989. Monitoring floods with AVHRR. *Remote Sensing of Environment* 30: 89-94.

Bello OM & Aina YA 2014. Satellite remote sensing as a tool in disaster management and sustainable development: towards a synergistic approach. *Procedia-Social and Behavioral Sciences* 120: 365-373.

Berger M, Moreno J, Johannessen JA, Levelt PF & Hanssen RF 2012. ESA's sentinel missions in support of Earth system science. *Remote Sensing of Environment* 120: 84-90.

Bessinger M 2016. Flood mapping in the Zambezi Region using Synthetic Aperture Radar. Master's thesis. Stellenbosch: Stellenbosch University, Department of Geography and Environmental Studies.

Bhagat VS & Sonawane KR 2011. Use of Landsat ETM+ data for delineation of water bodies in hilly zones. *Journal of Hydroinformatics* 13: 661-671.

Bioresita F, Puissant A, Stumpf A & Malet JP 2018. A method for automatic and rapid mapping of water surfaces from Sentinel-1 imagery. *Remote Sensing* 10: 217.

Bioucas-Dias JM, Plaza A, Dobigeon N, Parente M, Du Q, Gader P & Chanussot J 2012. Hyperspectral unmixing overview: Geometrical, statistical and sparse regression-based

approaches. *IEEE journal of selected topics in applied earth observations and remote sensing* 5: 354-379.

Blaes X, Vanhalle L & Defourny P 2005. Efficiency of crop identification based on optical and SAR image time series. *Remote Sensing of Environment* 96: 352-365.

Blaschke T 2010. Object based image analysis for remote sensing. *ISPRS Journal of Photogrammetry and Remote Sensing* 65: 2-16.

Blasco F, Bellan MF & Chaudhury MU 1992. Estimating the extent of floods in Bangladesh using SPOT data. *Remote Sensing of Environment* 39: 167-178.

Boardman JW 1993. Automating spectral unmixing of AVIRIS data using convex geometry concepts. Fourth Annual JPL Airborne Geoscience Workshop held 25-29 October. Arlington, Virginia.

Borga M, Anagnostou EN, Blöschl G & Creutin JD 2011. Flash flood forecasting, warning and risk management: the HYDRATE project. *Environmental Science & Policy* 14: 834-844.

Botai C, Botai J, de Wit J, Ncongwane K & Adeola A 2017. Drought characteristics over the Western Cape Province, South Africa. *Water* 9: 876.

Brakenridge GR, Nghiem SV, Anderson E & Mic R 2007. Orbital microwave measurement of river discharge and ice status. *Water Resources Research* 43.

Breiman L 2001. Random forests. *Machine learning* 45: 5-32.

Brisco B 2015. Mapping and monitoring surface water and wetlands with synthetic aperture radar. *Remote Sensing of Wetlands: Applications and Advances*: 119-136.

Brisco B, Kapfer M, Hirose T, Tedford B & Liu J 2011. Evaluation of C-band polarization diversity and polarimetry for wetland mapping. *Canadian Journal of Remote Sensing* 37: 82-92.

Brivio PA, Colombo R, Maggi M & Tomasoni R 2002. Integration of remote sensing data and GIS for accurate mapping of flooded areas. *International Journal of Remote Sensing* 23: 429-441.

Burke J, Pricope N & Blum J 2016. Thermal imagery-derived surface inundation modeling to assess flood risk in a flood-pulsed savannah watershed in Botswana and Namibia. *Remote Sensing* 8: 676.

Bwangoy JRB, Hansen MC, Roy DP, Grandi GD & Justice CO 2010. Wetland mapping in the Congo Basin using optical and radar remotely sensed data and derived topographical indices. *Remote Sensing of Environment* 114: 73-86.

Campbell JB & Wynne RH 2011. *Introduction to remote sensing.* 5th ed. New York: Guilford Press.

Canty MJ 2014. *Image analysis, classification and change detection in remote sensing: with algorithms for ENVI/IDL and Python.* Boca Raton: CRC Press.

Carlson TN & Ripley DA 1997. On the relation between NDVI, fractional vegetation cover and leaf area index. *Remote sensing of Environment* 62: 241-252.

Cazals C, Rapinel S, Frison PL, Bonis A, Mercier G, Mallet C, Corgne S & Rudant JP 2016. Mapping and characterization of hydrological dynamics in a coastal marsh using high temporal resolution Sentinel-1A images. *Remote Sensing* 8: 570.

Chan YK & Koo VC 2008. An introduction to synthetic aperture radar (SAR). *Progress In Electromagnetics Research* 2: 27-60.

Chang C-C & Lin C-J 2011. LIBSVM: A library for support vector machines. *ACM Transactions on Intelligent Systems and Technology* 2: 1-27.

Chavez P, Sides SC & Anderson JA 1991. Comparison of three different methods to merge multiresolution and multispectral data: Landsat TM and SPOT panchromatic *Photogrammetric Engineering and remote sensing* 57: 295-303.

Chen B, Chen L, Lu M & Xu B 2017. Wetland mapping by fusing fine spatial and hyperspectral resolution images. *Ecological Modelling* 353: 95-106.

Cheruiyot E, Mito C, Menenti M, Gorte B, Koenders R & Akdim N 2014. Evaluating MERIS-based aquatic vegetation mapping in Lake Victoria. *Remote Sensing* 6: 7762.

Chini M, Hostache R, Giustarini L & Matgen P 2017. A hierarchical split-based approach for parametric thresholding of SAR images: Flood inundation as a test case. *IEEE Transactions on Geoscience and Remote Sensing* 55: 6975-6988.

Chopra R, Verma VK & Sharma PK 2001. Mapping, monitoring and conservation of Harike wetland ecosystem, Punjab, India, through remote sensing. *International Journal of Remote Sensing* 22: 89-98.

Chuvieco E 2016. *Fundamentals of Satellite Remote Sensing: An Environmental Approach.* 2nd ed. Boca Raton: CRC press.

Clement MA, Kilsby CG & Moore P 2018. Multi-temporal synthetic aperture radar flood mapping using change detection. *Journal of Flood Risk Management*: 152-168.

Congalton RG & Green K 2008. *Assessing the accuracy of remotely sensed data: principles and practices.* 2nd ed. Boca Raton: CRC press.

Corcoran J, Knight J, Brisco B, Kaya S, Cull A & Murnaghan K 2012. The integration of optical, topographic and radar data for wetland mapping in northern Minnesota. *Canadian Journal of Remote Sensing* 37: 564-582.

Correia FN, Rego FC, Saraiva MDG & Ramos I 1998. Coupling GIS with hydrologic and hydraulic flood modelling. *Water Resources Management* 12: 229-249.

Costa MPF 2004. Use of SAR satellites for mapping zonation of vegetation communities in the Amazon floodplain. *International Journal of Remote Sensing* 25: 1817-1835.

Costa MPF, Niemann O, Novo E & Ahern F 2002. Biophysical properties and mapping of aquatic vegetation during the hydrological cycle of the Amazon floodplain using JERS-1 and RADARSAT. *International Journal of Remote Sensing* 23: 1401-1426.

Costabile P & Macchione F 2015. Enhancing river model set-up for 2-D dynamic flood modelling. *Environmental Modelling & Software* 67: 89-107.

Costabile P, Macchione F, Natale L & Petaccia G 2015. Flood mapping using LIDAR DEM. Limitations of the 1-D modeling highlighted by the 2-D approach. *Natural Hazards* 77: 181-204.

Čotar K, Oštir K & Kokalj Ž 2016. Radar satellite imagery and automatic detection of water bodies. *Geodetski glasnik* 50: 5-15.

Cracknell AP 1998. Review article synergy in remote sensing-What's in a pixel? *International Journal of Remote Sensing* 19: 2025-2047.

Crétaux JF, Jelinski W, Calmant S, Kouraev A, Vuglinski V, Bergé-Nguyen M, Gennero MC, Nino F, Abarca Del Rio R, Cazenave A & Maisongrande P 2011. SOLS: A lake database to monitor in the Near Real-time (NRT) water level and storage variations from remote sensing data. *Advances in Space Research* 47: 1497-1507.

D'Addabbo A, Refice A, Pasquariello G, Lovergine FP, Capolongo D & Manfreda S 2016. A Bayesian network for flood detection combining SAR imagery and ancillary data. *IEEE Transactions on Geoscience and Remote Sensing* 54: 3612-3625.

D'Andrimont R & Defourny P 2018. Monitoring African water bodies from twice-daily MODIS observation. *GIScience & Remote Sensing* 55: 130-153.

D'Andrimont R, Marlier C & Defourny P 2017. Hyperspatial and multi-source waterbody mapping: A framework to handle heterogeneities from observations and targets over large areas. *Remote Sensing* 9: 211.

DAFF 2018. Abstract of Western Cape Province agricultural statistics 2018 [online]. Pretoria, South Africa: Department of Agriculture, Forestry and Fisheries. Available from http://www.daff.gov.za/Daffweb3/Portals/0/Statistics%20and%20Economic%20Analysis/Statistical%20Information/Abstract%202018.pdf [Accessed 23 April 2018].

Dao P & Liou Y-A 2015. Object-based flood mapping and affected rice field estimation with Landsat 8 OLI and MODIS data. *Remote Sensing* 7: 5077.

Dasari K, Anjaneyulu L, Jayasri PV & Prasad AVV 2015. Importance of speckle filtering in image classification of SAR data. International Conference on Microwave, Optical and Communication Engineering (ICMOCE) held 30 July 2015. Bhubaneswar, Odisha, India.

Davranche A, Lefebvre G & Poulin B 2010. Wetland monitoring using classification trees and SPOT-5 seasonal time series. *Remote Sensing of Environment* 114: 552-562.

De Sherbinin A 2014. Climate change hotspots mapping: What have we learned? *Climatic Change* 123: 23-37.

Desai B, Maskrey A, Peduzzi P, De Bono A & Herold C 2015. Making development sustainable: The future of disaster risk management, global assessment report on disaster risk reduction. Geneva: United Nations Office for Disaster Risk Reduction (UNISDR).

Di Baldassarre G, Schumann G, Bates PD, Freer JE & Beven KJ 2010. Flood-plain mapping: a critical discussion of deterministic and probabilistic approaches. *Hydrological Sciences Journal* 55: 364-376.

Di Baldassarre G, Schumann G, Brandimarte L & Bates P 2011. Timely low resolution SAR imagery to support floodplain modelling: a case study review. *Surveys in geophysics* 32: 255-269.

Dimitriadis P, Tegos A, Oikonomou A, Pagana V, Koukouvinos A, Mamassis N, Koutsoyiannis D & Efstratiadis A 2016. Comparative evaluation of 1D and quasi-2D hydraulic models based on benchmark and real-world applications for uncertainty assessment in flood mapping. *Journal of Hydrology* 534: 478-492.

Dong Y, Milne A & Forster B 2000. A review of SAR speckle filters: texture restoration and preservation. IEEE 2000 International Geoscience and Remote Sensing Symposium : taking the pulse of the planet, the role of remote sensing in managing the environment held 24-28 July, 2000. Hilton Hawaiian Village, Honolulu, Hawaii, USA.

Donlon C, Berruti B, Buongiorno A, Ferreira MH, Féménias P, Frerick J, Goryl P, Klein U, Laur H, Mavrocordatos C, Nieke J, Rebhan H, Seitz B, Stroede J & Sciarra R 2012. The Global Monitoring for Environment and Security (GMES) Sentinel-3 mission. *Remote Sensing of Environment* 120: 37-57.

Dosio A & Panitz H-J 2016. Climate change projections for CORDEX-Africa with COSMO-CLM regional climate model and differences with the driving global climate models. *Climate Dynamics* 46: 1599-1625.

Du Y, Zhang Y, Ling F, Wang Q, Li W & Li X 2016. Water bodies' mapping from Sentinel-2 imagery with modified normalized difference water index at 10-m spatial resolution produced by sharpening the SWIR band. *Remote Sensing* 8: 354.

Du Z, Li W, Zhou D, Tian L, Ling F, Wang H, Gui Y & Sun B 2014. Analysis of Landsat-8 OLI imagery for land surface water mapping. *Remote Sensing Letters* 5: 672-681.

El-Magd IA & Tanton T 2003. Improvements in land use mapping for irrigated agriculture from satellite sensor data using a multi-stage maximum likelihood classification. *International Journal of Remote Sensing* 24: 4197-4206.

Engelbrecht CJ, Landman WA, Engelbrecht FA & Malherbe J 2015. A synoptic decomposition of rainfall over the Cape south coast of South Africa. *Climate Dynamics* 44: 2589-2607.

Evans J 2018. Western Cape dam levels drop even more. *Mail & Guardian.* 05 March 2018. Johannesburg, South Africa: https://mg.co.za/article/2018-03-05-western-cape-dam-levels-drop-even-more [Accessed 29 June 2018].

Fan FM, Collischonn W, Quiroz KJ, Sorribas MV, Buarque DC & Siqueira VA 2016. Flood forecasting on the Tocantins River using ensemble rainfall forecasts and Near Real-time (NRT) satellite rainfall estimates. *Journal of Flood Risk Management* 9: 278-288.

Feng Q, Gong J, Liu J & Li Y 2015. Flood mapping based on multiple endmember spectral mixture analysis and random forest classifier—The case of Yuyao, China. *Remote Sensing* 7: 12539.

Feng Q, Liu J & Gong J 2015. Urban flood mapping based on unmanned aerial vehicle remote sensing and random forest classifier—A case of Yuyao, China. *Water* 7: 1437.

Ferro-Famil L & Pottier E 2016. Synthetic aperture radar imaging *Microwave remote sensing of land surface*, 1-65. Amsterdam: Elsevier.

Feyisa GL, Meilby H, Fensholt R & Proud SR 2014. Automated water extraction index (AWEI): A new technique for surface water mapping using Landsat imagery. *Remote Sensing of Environment* 140: 23-35.

Finkl CW & Makowski C 2017. *Coastal Wetlands: Alteration and Remediation.* Cham: Springer.

Foody GM 2000. Estimation of sub-pixel land cover composition in the presence of untrained classes. *Computers & Geosciences* 26: 469-478.

Foody GM 2004. Thematic map comparison: Evaluating the statistical significance of differences in classification accuracy. *Photogrammetric Engineering & Remote Sensing* 70: 627-633.

Foody GM & Mathur A 2004. A relative evaluation of multiclass image classification by support vector machines. *IEEE Transactions on Geoscience and Remote Sensing* 42: 1335-1343.

Franceschetti G & Lanari R 2018. *Synthetic aperture radar processing.* Boca Raton: CRC press.

Franklin SE, Skeries EM, Stefanuk MA & Ahmed OS 2018. Wetland classification using RADARSAT-2 SAR quad-polarization and Landsat-8 OLI spectral response data: a case study in the Hudson Bay Lowlands Ecoregion. *International Journal of Remote Sensing* 39: 1615-1627.

Ganaie HA, Hashaia H & Kalota D 2013. Delineation of flood prone area using normalized difference water index (NDWI) and transect method: A case study of Kashmir Valley. *International Journal of Remote Sensing Applications* 3: 53-58.

Gao BC 1996. NDWI, a normalized difference water index for remote sensing of vegetation liquid water from space. *Remote sensing of environment* 58: 257-266.

Gao Q, Zribi M, Escorihuela M & Baghdadi N 2017. Synergetic use of Sentinel-1 and Sentinel-2 data for soil moisture mapping at 100 m resolution. *Sensors* 17: 1966.

Garage W 2011. OpenCV 2.0 and 2.2 open source computer vision library. *Internet: http://opencv. willowgarage. com/wiki/[Jan. 15, 2011]*.

Gascon F, Cadau E, Colin O, Hoersch B, Isola C, Fernández BL & Martimort P 2014. Copernicus Sentinel-2 mission: products, algorithms and Cal/Val. Proceedings of Earth Observing Systems XIX held 17-21 August 2014. San Diego Convention Center San Diego, California, United States.

Gaughan AE, Staub CG, Hoell A, Weaver A & Waylen PR 2016. Inter-and intra-annual precipitation variability and associated relationships to ENSO and the IOD in southern Africa. *International Journal of Climatology* 36: 1643-1656.

Gebbinck MSK & Schouten TE 1995. Decomposition of mixed pixels. Proceedings of Image and Signal Processing for Remote Sensing II held 25-27 September 1995. Paris, France.

Geudtner D, Torres R, Snoeij P, Davidson M & Rommen B 2014. Sentinel-1 system capabilities and applications. Geoscience and Remote Sensing Symposium (IGARSS), 2014 IEEE International held 13-18 July 2014. Quebec, Canada.

Ghassemian H 2016. A review of remote sensing image fusion methods. *Information Fusion* 32: 75-89.

Giardino C, Bresciani M, Villa P & Martinelli A 2010. Application of remote sensing in water resource management: The case study of Lake Trasimeno, Italy. *Water Resources Management* 24: 3885-3899.

Gilbertson JK, Kemp J & Van Niekerk A 2017. Effect of pan-sharpening multi-temporal Landsat 8 imagery for crop type differentiation using different classification techniques. *Computers and Electronics in Agriculture* 134: 151-159.

Gilbertson JK & Van Niekerk A 2017. Value of dimensionality reduction for crop differentiation with multi-temporal imagery and machine learning. *Computers and Electronics in Agriculture* 142: 50-58.

Giustarini L, Hostache R, Kavetski D, Chini M, Corato G, Schlaffer S & Matgen P 2016. Probabilistic flood mapping using synthetic aperture radar data. *IEEE Transactions on Geoscience and Remote Sensing* 54: 6958-6969.

Giustarini L, Vernieuwe H, Verwaeren J, Chini M, Hostache R, Matgen P, Verhoest NEC & De Baets B 2015. Accounting for image uncertainty in SAR-based flood mapping. *International Journal of Applied Earth Observation and Geoinformation* 34: 70-77.

Glasbey CA 1993. An analysis of histogram-based thresholding algorithms. *CVGIP: Graphical models and image processing* 55: 532-537.

Gómez-Palacios D, Torres MA & Reinoso E 2017. Flood mapping through principal component analysis of multitemporal satellite imagery considering the alteration of water spectral properties due to turbidity conditions. *Geomatics, Natural Hazards and Risk* 8: 607-623.

Gorelick N, Hancher M, Dixon M, Ilyushchenko S, Thau D & Moore R 2017. Google Earth Engine: Planetary-scale geospatial analysis for everyone. *Remote Sensing of Environment* 202: 18-27.

Goward SN, Masek JG, Williams DL, Irons JR & Thompson RJ 2001. The Landsat 7 mission: Terrestrial research and applications for the 21st century. *Remote Sensing of Environment* 78: 3-12.

Greifeneder F, Wagner W, Sabel D & Naeimi V 2014. Suitability of SAR imagery for automatic flood mapping in the Lower Mekong basin. *International journal of remote sensing* 35: 2857-2874.

Gstaiger V, Huth J, Gebhardt S, Wehrmann T & Kuenzer C 2012. Multi-sensoral and automated derivation of inundated areas using TerraSAR-X and ENVISAT ASAR data. *International Journal of Remote Sensing* 33: 7291-7304.

Gumindoga W, Makurira H, Phiri M & Nhapi I 2016. Estimating runoff from ungauged catchments for reservoir water balance in the Lower Middle Zambezi Basin. *Water SA* 42: 641-649.

Gutman G & Ignatov A 1998. The derivation of the green vegetation fraction from NOAA/AVHRR data for use in numerical weather prediction models. *International Journal of remote sensing* 19: 1533-1543.

Haddeland I, Heinke J, Biemans H, Eisner S, Flörke M, Hanasaki N, Konzmann M, Ludwig F, Masaki Y & Schewe J 2014. Global water resources affected by human interventions and climate change. *Proceedings of the National Academy of Sciences* 111: 3251-3256.

Halimi A, Dobigeon N, Tourneret J-Y & Honeine P 2015. A new Bayesian unmixing algorithm for hyperspectral images mitigating endmember variability. Proceedings of 2015 IEEE International Conference on Acoustics, Speech and Signal Processing (ICASSP) held 19-24 April 2015. Brisbane, Australia.

Hallberg GR, Hoyer BE & Rango A 1973. Application of ERTS-1 imagery to flood inundation mapping. Paper presented on symposium of Significant results obtained from the Earth Resources Satellite 1 held on 1 May 1973. NASA, United States of America.

Hanqiu X 2005. A Study on Information Extraction of Waterbody with the Modified Normalized Difference Water Index (MNDWI). *Journal of Remote Sensing* 5: 589-595.

Haralick RM, Shanmugam K & Dinstein I 1973. Textural features for image classification. *IEEE Transactions on Systems, Man, and Cybernetics* SMC-3: 610-621.

Hasmadi M, Pakhriazad H & Shahrin M 2009. Evaluating supervised and unsupervised techniques for land cover mapping using remote sensing data. *Geografia: Malaysian Journal of Society and Space* 5: 1-10.

Heege T, Kiselev V, Wettle M & Hung NN 2014. Operational multi-sensor monitoring of turbidity for the entire Mekong Delta. *International Journal of Remote Sensing* 35: 2910-2926.

Henderson FM, Lewis AJ, American Society for P & Remote S 1998. *Principles and applications of imaging radar.* New York Wiley.

Hess LL & Melack JM 2003. Remote sensing of vegetation and flooding on Magela Creek Floodplain (Northern Territory, Australia) with the SIR-C synthetic aperture RADAR. *Hydrobiologia* 500: 65-82.

Hess LL, Melack JM, Filoso S & Wang Y 1995. Delineation of inundated area and vegetation along the Amazon floodplain with the SIR-C synthetic aperture radar. *IEEE Transactions on Geoscience and Remote Sensing* 33: 896-904.

Hess LL, Melack JM & Simonett DS 1990. Radar detection of flooding beneath the forest canopy: a review. *International Journal of Remote Sensing* 11: 1313-1325.

Hoell A, Funk C, Zinke J & Harrison L 2017a. Modulation of the Southern Africa precipitation response to the El Niño Southern Oscillation by the subtropical Indian Ocean Dipole. *Climate Dynamics* 48: 2529-2540.

Hoell A, Gaughan AE, Shukla S & Magadzire T 2017b. The Hydrologic Effects of Synchronous El Niño–Southern Oscillation and Subtropical Indian Ocean Dipole Events over Southern Africa. *Journal of Hydrometeorology* 18: 2407-2424.

Hoffman MT, Carrick P, Gillson L & West A 2009. Drought, climate change and vegetation response in the succulent karoo, South Africa. *South African Journal of Science* 105: 54-60.

Holderness T & Turpin E 2015. From social media to geosocial intelligence: Crowdsourcing civic co-management for flood response in Jakarta, Indonesia. *Social media for government services*, 115-133. Cham: Springer.

Hong S, Jang H, Kim N & Sohn H-G 2015. Water area extraction using RADARSAT SAR imagery combined with Landsat imagery and terrain information. *Sensors* 15: 6652-6667.

Horritt M, Mason D, Cobby D, Davenport I & Bates P 2003. Waterline mapping in flooded vegetation from airborne SAR imagery. *Remote Sensing of Environment* 85: 271-281.

Horritt M, Mason D & Luckman A 2001. Flood boundary delineation from synthetic aperture radar imagery using a statistical active contour model. *International Journal of Remote Sensing* 22: 2489-2507.

Huang C, Chen Y & Wu J 2014. Mapping spatio-temporal flood inundation dynamics at large river basin scale using time-series flow data and MODIS imagery. *International Journal of Applied Earth Observation and Geoinformation* 26: 350-362.

Huang C, Chen Y, Zhang S, Li L, Shi K & Liu R 2016. Surface water mapping from Suomi NPP-VIIRS imagery at 30 m resolution via blending with Landsat data. *Remote Sensing* 8: 631.

Huang C, Peng Y, Lang M, Yeo I-Y & McCarty G 2014. Wetland inundation mapping and change monitoring using Landsat and airborne LiDAR data. *Remote Sensing of Environment* 141: 231-242.

Huang C, Wylie B, Yang L, Homer C & Zylstra G 2002. Derivation of a tasselled cap transformation based on Landsat 7 at satellite reflectance. *International Journal of Remote Sensing* 23: 1741-1748.

Huang X, Tan H, Zhou J, Yang T, Benjamin A, Wen S, Li S, Liu A, Li X, Fen S & Li X 2008. Flood hazard in Hunan Province of China: an economic loss analysis. *Natural Hazards* 47: 65-73.

Hui F, Xu B, Huang H, Yu Q & Gong P 2008. Modelling spatial-temporal change of Poyang Lake using multitemporal Landsat imagery. *International Journal of Remote Sensing* 29: 5767-5784.

Imhoff M, Story M, Vermillion C, Khan F & Polcyn F 1986. Forest canopy characterization and vegetation penetration assessment with space-borne radar. *IEEE Transactions on Geoscience and Remote Sensing*: 535-542.

IPCC 2014. *Climate change 2014: synthesis report. Contribution of Working Groups I, II and III to the fifth assessment report of the Intergovernmental Panel on Climate Change.* Geneva: IPCC.

Ireland G, Volpi M & Petropoulos G 2015. Examining the capability of supervised machine learning classifiers in extracting flooded areas from Landsat TM imagery: A case study from a Mediterranean flood. *Remote Sensing* 7: 3372.

Irwin K, Beaulne D, Braun A & Fotopoulos G 2017. Fusion of SAR, optical imagery and airborne LiDAR for surface water detection. *Remote Sensing* 9: 890.

Islam AS, Bala SK & Haque M 2010. Flood inundation map of Bangladesh using MODIS time-series images. *Journal of Flood Risk Management* 3: 210-222.

Jafarzadegan K & Merwade V 2017. A DEM-based approach for large-scale floodplain mapping in ungauged watersheds. *Journal of Hydrology* 550: 650-662.

Jain SK, Saraf AK, Goswami A & Ahmad T 2006. Flood inundation mapping using NOAA AVHRR data. *Water Resources Management* 20: 949-959.

Jain SK, Singh R, Jain M & Lohani A 2005. Delineation of flood-prone areas using remote sensing techniques. *Water Resources Management* 19: 333-347.

Jawahar C, Biswas PK & Ray A 1997. Investigations on fuzzy thresholding based on fuzzy clustering. *Pattern Recognition* 30: 1605-1613.

Jay S & Guillaume M 2014. A novel maximum likelihood based method for mapping depth and water quality from hyperspectral remote-sensing data. *Remote Sensing of Environment* 147: 121-132.

Ji L, Zhang L & Wylie B 2009. Analysis of dynamic thresholds for the normalized difference water index. *Photogrammetric Engineering & Remote Sensing* 75: 1307-1317.

Jia K, Wei X, Gu X, Yao Y, Xie X & Li B 2014. Land cover classification using Landsat 8 operational land imager data in Beijing, China. *Geocarto International* 29: 941-951.

Jia K, Wu B & Li Q 2013. Crop classification using HJ satellite multispectral data in the North China Plain. *Journal of Applied Remote Sensing* 7: 073576-073576.

Jiang Z, Qi J, Su S, Zhang Z & Wu J 2012. Waterbody delineation using index composition and HIS transformation. *International Journal of Remote Sensing* 33: 3402-3421.

Joshi N, Baumann M, Ehammer A, Fensholt R, Grogan K, Hostert P, Jepsen MR, Kuemmerle T, Meyfroidt P & Mitchard ET 2016. A review of the application of optical and radar remote sensing data fusion to land use mapping and monitoring. *Remote Sensing* 8: 70.

Jung Y, Kim D, Kim D, Kim M & Lee S 2014. Simplified flood inundation mapping based on flood elevation-discharge rating curves using satellite images in gauged watersheds. *Water* 6: 1280.

Kalantari Z, Nickman A, Lyon SW, Olofsson B & Folkeson L 2014. A method for mapping flood hazard along roads. *Journal of Environmental Management* 133: 69-77.

Kaplan G 2018. Sentinel-2 Pan Sharpening—Comparative Analysis. *Paper presented at the 2nd International Electronic Conference on Remote Sensing held online on 22 March–5 April 2018.* 2: 345.

Kaplan G & Avdan U 2018. Sentinel-1 and Sentinel-2 data fusion for wetlands mapping: Balikdami, Turkey. *International Archives of the Photogrammetry, Remote Sensing & Spatial Information Sciences* 42: 729-734.

Kapur JN, Sahoo PK & Wong AK 1985. A new method for gray-level picture thresholding using the entropy of the histogram. *Computer vision, graphics, and image processing* 29: 273-285.

Karpatne A, Khandelwal A, Chen X, Mithal V, Faghmous J & Kumar V 2016. Global monitoring of inland water dynamics: State-of-the-Art, challenges, and opportunities. *Computational Sustainability*, 121-147. Cham: Springer International Publishing.

Kauth RJ & Thomas G 1976. The tasselled cap-a graphic description of the spectral-temporal development of agricultural crops as seen by Landsat. Paper delivered at the Laboratory for Applications of Remote Sensing (LARS) held 29 June -1 July 1976. West Lafayette, Indiana.

Kelman I 2015. Climate change and the Sendai framework for disaster risk reduction. *International Journal of Disaster Risk Science* 6: 117-127.

Keshava N 2003. A survey of spectral unmixing algorithms. *Lincoln Laboratory Journal* 14: 55-78.

Keshava N & Mustard JF 2002. Spectral unmixing. *IEEE Signal Processing Magazine* 19: 44-57.

Khan SI, Hong Y, Wang J, Yilmaz KK, Gourley JJ, Adler RF, Brakenridge GR, Policelli F, Habib S & Irwin D 2011. Satellite remote sensing and hydrologic modeling for flood inundation mapping in Lake Victoria basin: implications for hydrologic prediction in ungauged basins. *IEEE Transactions on Geoscience and Remote Sensing* 49: 85-95.

Khan U, Minallah N, Junaid A, Gul K & Ahmad N 2015. Parallelepiped and Mahalanobis distance based classification for forestry identification in Pakistan. Paper delivered at

International Conference on Emerging Technologies (ICET) held 19-20 December 2015. Peshawar Services Club, Peshawar, Pakistan.

Kittler J & Illingworth J 1986. Minimum error thresholding. *Pattern recognition* 19: 41-47.

Klemas V 2015. Remote sensing of floods and flood-prone areas: An overview. *Journal of Coastal Research* 31: 1005-1013.

Kuenzer C, Guo H, Huth J, Leinenkugel P, Li X & Dech S 2013. Flood mapping and flood dynamics of the Mekong Delta: ENVISAT-ASAR-WSM based time series analysis. *Remote Sensing* 5: 687.

Kumar R & Acharya P 2016. Flood hazard and risk assessment of 2014 floods in Kashmir Valley: a space-based multisensor approach. *Natural Hazards : Journal of the International Society for the Prevention and Mitigation of Natural Hazards* 84: 437-464.

Kundzewicz Z, Krysanova V, Benestad R, Hov Ø, Piniewski M & Otto I 2018. Uncertainty in climate change impacts on water resources. *Environmental Science & Policy* 79: 1-8.

Kundzewicz ZW, Kanae S, Seneviratne SI, Handmer J, Nicholls N, Peduzzi P, Mechler R, Bouwer LM, Arnell N & Mach K 2014. Flood risk and climate change: global and regional perspectives. *Hydrological Sciences Journal* 59: 1-28.

Kusangaya S, Warburton ML, Van Garderen EA & Jewitt GP 2014. Impacts of climate change on water resources in southern Africa: A review. *Physics and Chemistry of the Earth, Parts A/B/C* 67: 47-54.

Laben CA & Brower BV 2000. Process for enhancing the spatial resolution of multispectral imagery using pan-sharpening. U.S. Patent 6 011 875, 4 January 2000.

Lang M, Bourgeau-Chavez LL, Tiner RW & Klemas VV 2015. Advances in remotely sensed data and techniques for wetland mapping and monitoring. *Remote Sensing of Wetlands: Applications and Advances*: 79-118.

Lang MW, Townsend PA & Kasischke ES 2008. Influence of incidence angle on detecting flooded forests using C-HH synthetic aperture radar data. *Remote Sensing of Environment* 112: 3898-3907.

Lässig J, Kersting K & Morik K 2016. *Computational Sustainability.* Cham: Springer.

Leung C-K & Lam F 1996. Performance analysis for a class of iterative image thresholding algorithms. *Pattern Recognition* 29: 1523-1530.

Levin N 1999. *Fundamentals of remote sensing, 1st Hydrographic Data Management Course.* Trieste: International Maritime Academy.

Li H, Jing L & Tang Y 2017. Assessment of pansharpening methods applied to WorldView-2 imagery fusion. *Sensors* 17: 89.

Li L, Chen Y, Xu T, Liu R, Shi K & Huang C 2015. Super-resolution mapping of wetland inundation from remote sensing imagery based on integration of back-propagation neural network and genetic algorithm. *Remote Sensing of Environment* 164: 142-154.

Li W, Du Z, Ling F, Zhou D, Wang H, Gui Y, Sun B & Zhang X 2013. A comparison of land surface water mapping using the normalized difference water index from TM, ETM+ and ALI. *Remote Sensing* 5: 5530-5549.

Li Y, Martinis S, Plank S & Ludwig R 2018. An automatic change detection approach for rapid flood mapping in Sentinel-1 SAR data. *International Journal of Applied Earth Observation and Geoinformation* 73: 123-135.

Li Z & Guo X 2015. Remote sensing of terrestrial non-photosynthetic vegetation using hyperspectral, multispectral, SAR, and LiDAR data. *Progress in Physical Geography: Earth and Environment* 40: 276-304.

Lie W-N 1993. An efficient threshold-evaluation algorithm for image segmentation based on spatial graylevel co-occurrences. *Signal Processing* 33: 121-126.

Lillesand T, Kiefer RW & Chipman J 2014. *Remote sensing and image interpretation.* New York: John Wiley & Sons.

Liu T, Abd-Elrahman A, Morton J & Wilhelm VL 2018. Comparing fully convolutional networks, random forest, support vector machine, and patch-based deep convolutional neural networks for object-based wetland mapping using images from small unmanned aircraft system. *GIScience & Remote Sensing* 55: 243-264.

Liu Y & Srihari SN 1997. Document image binarization based on texture analysis. *IEEE Transactions on Pattern Analysis and Machine Intelligence* 2181: 254-264.

Liu Z, Yao Z & Wang R 2016. Assessing methods of identifying open waterbodies using Landsat 8 OLI imagery. *Environmental Earth Sciences* 75: 873.

Long S, Fatoyinbo T, E & Policelli F 2014. Flood extent mapping for Namibia using change detection and thresholding with SAR. *Environmental Research Letters* 9: 035002.

Louis J, Debaecker V, Pflug B, Main-Knorn M, Bieniarz J, Mueller-Wilm U, Cadau E & Gascon F 2016. Sentinel-2 Sen2Cor: L2A processor for users. Paper presented at Living Planet Symposium held 9-13 May 2016. Prague, Czech Republic.

Lu S, Wu B, Yan N & Wang H 2011. Waterbody mapping method with HJ-1A/B satellite imagery. *International Journal of Applied Earth Observation and Geoinformation* 13: 428-434.

Lu Y, Wang M & Zhang G 2017. A new revised version of McNemar's test for paired binary data. *Communications in Statistics - Theory and Methods*: 1-15.

MacAlister C & Mahaxay M 2009. Mapping wetlands in the Lower Mekong Basin for wetland resource and conservation management using Landsat ETM images and field survey data. *Journal of Environmental Management* 90: 2130-2137.

Mahalanobis A, Vijaya Kumar BVK & Sims SRF 1996. Distance-classifier correlation filters for multiclass target recognition. *Applied Optics* 35: 3127-3133.

Mahdianpari M, Salehi B, Mohammadimanesh F & Motagh M 2017. Random forest wetland classification using ALOS-2 L-band, RADARSAT-2 C-band, and TerraSAR-X imagery. *ISPRS Journal of Photogrammetry and Remote Sensing* 130: 13-31.

Maillard P, Alencar-Silva T & Clausi D 2008. An evaluation of RADARSAT-1 and ASTER data for mapping Veredas (palm swamps). *Sensors* 8: 6055.

Makapela L, Newby T, Gibson L, Majozi N, Mathieu R, Ramoelo A, Mengistu M, Jewitt G, Chetty HBK & Clark D 2015. *Review of the Earth Observations and remote sensing in water resource management in South Africa.* Publication No KV 329/15. South African water research commission (WRC). Pretoria.

Malherbe J, Dieppois B, Maluleke P, Van Staden M & Pillay DL 2016. South African droughts and decadal variability. *Natural Hazards* 80: 657-681.

Manakos I & Lavender S 2014. Remote sensing in support of the geo-information in Europe. In Manakos I & Braun M (eds) *Land Use and Land Cover Mapping in Europe: Practices & Trends*, 3-10. Dordrecht: Springer Netherlands.

Manavalan R 2017. SAR image analysis techniques for flood area mapping - literature survey. *Earth Science Informatics* 10: 1-14.

Manavalan R, Rao YS & Krishna Mohan B 2017. Comparative flood area analysis of C-band VH, VV, and L-band HH polarizations SAR data. *International Journal of Remote Sensing* 38: 4645-4654.

Manhique AJ, Reason CJC, Silinto B, Zucula J, Raiva I, Congolo F & Mavume AF 2015. Extreme rainfall and floods in southern Africa in January 2013 and associated circulation patterns. *Natural Hazards* 77: 679-691.

Manjusree P, Prasanna Kumar L, Bhatt CM, Rao GS & Bhanumurthy V 2012. Optimization of threshold ranges for rapid flood inundation mapping by evaluating backscatter profiles of high incidence angle SAR images. *International Journal of Disaster Risk Science* 3: 113-122.

Marcus WA & Fonstad MA 2008. Optical remote mapping of rivers at sub-meter resolutions and watershed extents. *Earth Surface Processes and Landforms* 33: 4-24.

Martin R, Brabyn L & Beard C 2014. Effects of class granularity and cofactors on the performance of unsupervised classification of wetlands using multi-spectral aerial photography. *Journal of Spatial Science* 59: 269-282.

Martin S 2014. *An introduction to ocean remote sensing.* London: Cambridge University Press.

Martinez J-M & Le Toan T 2007. Mapping of flood dynamics and spatial distribution of vegetation in the Amazon floodplain using multitemporal SAR data. *Remote Sensing of Environment* 108: 209-223.

Martinis S 2017. Improving flood mapping in arid areas using Sentinel-1 time series data. Paper delivered at IEEE International Geoscience and Remote Sensing Symposium (IGARSS) held 23-28 July 2017. Fort Worth, TX, USA.

Martinis S, Kersten J & Twele A 2015. A fully automated TerraSAR-X based flood service. *ISPRS Journal of Photogrammetry and Remote Sensing* 104: 203-212.

Martinis S, Kuenzer C, Wendleder A, Huth J, Twele A, Roth A & Dech S 2015. Comparing four operational SAR-based water and flood detection approaches. *International Journal of Remote Sensing* 36: 3519-3543.

Martinis S, Plank S & Ćwik K 2018. The use of Sentinel-1 time-series data to improve flood monitoring in arid areas. *Remote Sensing* 10: 583.

Martinis S & Rieke C 2015. Backscatter analysis using multi-temporal and multi-frequency SAR data in the context of flood mapping at river Saale, Germany. *Remote Sensing* 7: 7732.

Martinis S, Twele A & Voigt S 2009. Towards operational Near Real-time (NRT) flood detection using a split-based automatic thresholding procedure on high resolution TerraSAR-X data. *Natural Hazards and Earth System Sciences* 9: 303-314.

Martinis S, Twele A & Voigt S 2011. Unsupervised extraction of flood-induced backscatter changes in SAR data using Markov image modeling on irregular graphs. *IEEE Transactions on Geoscience and Remote Sensing* 49: 251-263.

Masocha M & Skidmore AK 2011. Integrating conventional classifiers with a GIS expert system to increase the accuracy of invasive species mapping. *International Journal of Applied Earth Observation and Geoinformation* 13: 487-494.

Mason DC, Davenport IJ, Neal JC, Schumann GJ-P & Bates PD 2012. Near Real-time (NRT) flood detection in urban and rural areas using high-resolution synthetic aperture radar images. *IEEE transactions on Geoscience and Remote Sensing* 50: 3041-3052.

Mason SJ & Goddard L 2001. Probabilistic precipitation anomalies associated with ENSO. *Bulletin of the American Meteorological Society* 82: 619-638.

Matgen P 2011. Surface and subsurface water from space: on the integration of microwave remote sensing observations with flood prediction systems. Doctoral dissertation. Delft: TU Delft, Delft University of Technology, Department of Geoscience and Remote Sensing.

Matgen P, Hostache R, Schumann G, Pfister L, Hoffmann L & Savenije H 2011. Towards an automated SAR-based flood monitoring system: Lessons learned from two case studies. *Physics and Chemistry of the Earth, Parts A/B/C* 36: 241-252.

Mather P & Tso B 2016. *Classification methods for remotely sensed data.* Boca Raton: CRC press.

Matthew MW, Adler-Golden SM, Berk A, Richtsmeier SC, Levine RY, Bernstein LS, Acharya PK, Anderson GP, Felde GW & Hoke ML 2000. Status of atmospheric correction using a MODTRAN4-based algorithm. Paper presented at AeroSense 2000 held 24-28 April 2000. Orlando, Florida, USA.

Mazvimavi D & Wolski P 2006. Long-term variations of annual flows of the Okavango and Zambezi Rivers. *Physics and Chemistry of the Earth, Parts A/B/C* 31: 944-951.

McCallum I, Liu W, See L, Mechler R, Keating A, Hochrainer-Stigler S, Mochizuki J, Fritz S, Dugar S, Arestegui M, Szoenyi M, Bayas J-CL, Burek P, French A & Moorthy I 2016. Technologies to support community flood disaster risk reduction. *International Journal of Disaster Risk Science* 7: 198-204.

McFeeters SK 1996. The use of the Normalized Difference Water Index (NDWI) in the delineation of open water features. *International Journal of Remote Sensing* 17: 1425-1432.

Meadows ME 2003. Soil erosion in the Swartland, Western Cape Province, South Africa: implications of past and present policy and practice. *Environmental Science & Policy* 6: 17-28.

Memon AA, Muhammad S, Rahman S & Haq M 2015. Flood monitoring and damage assessment using water indices: A case study of Pakistan flood-2012. *The Egyptian Journal of Remote Sensing and Space Science* 18: 99-106.

Menarguez MA 2015. Global waterbody mapping from 1984 to 2014 using high resolution multispectral satellite imagery. Doctoral dissertation. Oklahoma: University of Oklahoma, Department of Geography.

Mendelsohn J, Robets C & Hines C 1997. *An environmental profile and atlas of Caprivi.* Windhoek: Directorate of Environmental Affairs.

Miah MM 1988. *Flood in Bangladesh : a hydromorphological study of the 1987 flood.* Dhaka: Academic Publishers.

Millard K & Richardson M 2013. Wetland mapping with LiDAR derivatives, SAR polarimetric decompositions, and LiDAR–SAR fusion using a random forest classifier. *Canadian Journal of Remote Sensing* 39: 290-307.

Mishra AK & Singh VP 2010. A review of drought concepts. *Journal of Hydrology* 391: 202-216.

Mleczko M & Mróz M 2018. Wetland mapping using SAR data from the Sentinel-1A and TanDEM-X missions: A comparative study in the Biebrza floodplain (Poland). *Remote Sensing* 10: 78.

Momo MR, Silva HDS, Severo DL, Cordero A, Tachini M & Refosco JC 2015. Cloud services for mapping susceptible flood areas Paper pesented at Ninth International Conference on Complex, Intelligent and Software Intensive Systems (CISIS) held 8-10 July 2015. Regional University of Blumenau (FURB), Blumenau, Brazil.

Moore GK & North GW 1974. Flood inundation in the South Eastern United States from aircraft and satellite imagery *JAWRA Journal of the American Water Resources Association* 10: 1082-1096.

Moreira A 2013. Synthetic aperture radar (SAR): Principles and applications [online]. Germany: German Aerospace Center

Available from https://earth.esa.int/documents/10174/642943/6-LTC2013-SAR-Moreira.pdf [Accessed 20 May 2018].

Morrison RB & Cooley M 1973. Assessment of flood damage in Arizona by means of ERTS-1 imagery. Paper presented on symposium of Significant results obtained from the Earth Resources Satellite 1 held on 1 May 1973. NASA, United States of America.

Mountrakis G, Im J & Ogole C 2011. Support vector machines in remote sensing: A review. *ISPRS Journal of Photogrammetry and Remote Sensing* 66: 247-259.

Mtamba J, Van der Velde R, Ndomba P, Zoltán V & Mtalo F 2015. Use of RADARSAT-2 and Landsat TM Images for Spatial Parameterization of Manning's Roughness Coefficient in Hydraulic Modeling. *Remote Sensing* 7: 836.

Mueller N, Lewis A, Roberts D, Ring S, Melrose R, Sixsmith J, Lymburner L, McIntyre A, Tan P & Curnow S 2016. Water observations from space: Mapping surface water from 25years of Landsat imagery across Australia. *Remote Sensing of Environment* 174: 341-352.

Muro J, Canty M, Conradsen K, Hüttich C, Nielsen A, Skriver H, Remy F, Strauch A, Thonfeld F & Menz G 2016. Short-term change detection in wetlands using Sentinel-1 time series. *Remote Sensing* 8: 795.

Myburgh G & Van Niekerk A 2014. Impact of training set size on object-based land cover classification: A comparison of three classifiers. *International Journal of Applied Geospatial Research* 5: 49-67.

Nandi I, Srivastava PK & Shah K 2017. Floodplain mapping through support vector machine and optical/infrared images from Landsat 8 OLI/TIRS sensors: Case study from Varanasi. *Water Resources Management* 31: 1157-1171.

Nason GP & Silverman BW 1995. The stationary wavelet transform and some statistical applications. In Antoniadis A & Oppenheim G (eds) *Wavelets and Statistics*, 281-299. New York: Springer New York.

Nieke J, Mavrocordatos C, Donlon C, Berruti B, Garnier T, Riti JB & Delclaud Y 2015. Ocean and Land Colour Imager (OLCI) on Sentinel-3. *Optical Payloads for Space Missions*: 223.

Niroumand-Jadidi M & Vitti A 2017. Reconstruction of river boundaries at sub-pixel resolution: Estimation and spatial allocation of water fractions. *ISPRS International Journal of Geo-Information* 6: 383.

O'Grady D, Leblanc M & Bass A 2014. The use of radar satellite data from multiple incidence angles improves surface water mapping. *Remote Sensing of Environment* 140: 652-664.

O'Gorman L 1997. Binarization and multithresholding of document images using connectivity. *CVGIP: Graphical Models and Image Processing* 56: 494-506.

O'Grady D, Leblanc M & Gillieson D 2013. Relationship of local incidence angle with satellite Radar backscatter for different surface conditions. *International Journal of Applied Earth Observation and Geoinformation* 24: 42-53.

Oberstadler R, Honsch H & Huth D 1997. Assessment of the mapping capabilities of ERS-1 SAR data for flood mapping: a case study in Germany. *Hydrological Processes* 11: 1415-1425.

Olivo J-C 1994. Automatic threshold selection using the wavelet transform. *CVGIP: Graphical Models and Image Processing* 56: 205-218.

Ormsby JP, Blanchard BJ & Blanchard AJ 1985. Detection of lowland flooding using active microwave systems. *Photogrammetric Engineering and Remote Sensing* 51: 317-329.

Otsu N 1975. A threshold selection method from gray-level histograms. *Automatica* 11: 23-27.

Ouchi K 2013. Recent trend and advance of synthetic aperture radar with selected topics. *Remote Sensing* 5: 716-807.

Ouled SM, Hammami I, Foucher S & Lepage R 2018. Flood extent mapping from time-series SAR images based on texture analysis and data fusion. *Remote Sensing* 10: 237.

Ouma YO & Tateishi R 2006. A water index for rapid mapping of shoreline changes of five East African Rift Valley lakes: an empirical analysis using Landsat TM and ETM+ data. *International Journal of Remote Sensing* 27: 3153-3181.

Ozesmi SL & Bauer ME 2002. Satellite remote sensing of wetlands. *Wetlands Ecology and Management* 10: 381-402.

Pal M 2005. Random forest classifier for remote sensing classification. *International Journal of Remote Sensing* 26: 217-222.

Pal M & Mather PM 2005. Support vector machines for classification in remote sensing. *International Journal of Remote Sensing* 26: 1007-1011.

Papaioannou G, Vasiliades L & Loukas A 2015. Multi-criteria analysis framework for potential flood prone areas mapping. *Water Resources Management* 29: 399-418.

Papaioannou G, Vasiliades L, Loukas A & Aronica GT 2017. Probabilistic flood inundation mapping at ungauged streams due to roughness coefficient uncertainty in hydraulic modelling. *Advances in Geosciences* 44: 23.

Parent JR, Volin JC & Civco DL 2015. A fully-automated approach to land cover mapping with airborne LiDAR and high resolution multispectral imagery in a forested suburban landscape. *ISPRS Journal of Photogrammetry and Remote Sensing* 104: 18-29.

Parmuchi MG, Karszenbaum H & Kandus P 2002. Mapping wetlands using multi-temporal RADARSAT-1 data and a decision-based classifier. *Canadian Journal of Remote Sensing* 28: 175-186.

Pauw T 2012. Assessment of SPOT 5 and ERS-2 OBIA for mapping wetlands. Master's thesis. Stellenbosch: Stellenbosch University, Department of Geography and Environmental Studies.

Pekel J-F, Cottam A, Gorelick N & Belward AS 2016. High-resolution mapping of global surface water and its long-term changes. *Nature* 540: 418.

Petropoulos GP, Kalaitzidis C & Vadrevu PK 2012. Support vector machines and object-based classification for obtaining land-use/cover cartography from Hyperion hyperspectral imagery. *Computers & Geosciences* 41: 99-107.

Pham-Duc B, Prigent C & Aires F 2017. Surface water monitoring within Cambodia and the Vietnamese Mekong Delta over a year, with Sentinel-1 SAR observations. *Water* 9: 366.

Pierdicca N, Pulvirenti L & Chini M 2013. Dealing with flood mapping using SAR data in the presence of wind or heavy precipitation. Paper delivered at SPIE Remote Sensing Conference on SAR Image Analysis, Modeling and Techniques XIII held 23 - 26 September 2013., Internationales Congress Center Dresden, Germany.

Pierdicca N, Pulvirenti L & Chini M 2018. Flood mapping in vegetated and urban areas and other challenges: Models and methods. In Refice A, D'Addabbo A & Capolongo D (eds) *Flood Monitoring through Remote Sensing*, 135-179. Cham: Springer International Publishing.

Pierdicca N, Pulvirenti L, Chini M, Guerriero L & Candela L 2013. Observing floods from space: Experience gained from COSMO-SkyMed observations. *Acta Astronautica* 84: 122-133.

Plank S, Jüssi M, Martinis S & Twele A 2017. Mapping of flooded vegetation by means of polarimetric Sentinel-1 and ALOS-2/PALSAR-2 imagery. *International Journal of Remote Sensing* 38: 3831-3850.

Plaza A, Martínez P, Pérez R & Plaza J 2004. A quantitative and comparative analysis of endmember extraction algorithms from hyperspectral data. *IEEE transactions on geoscience and remote sensing* 42: 650-663.

Pohl C & Van Genderen JL 1998. Review article multisensor image fusion in remote sensing: concepts, methods and applications. *International journal of remote sensing* 19: 823-854.

Pohl C & Van Genderen JL 2017. Remote sensing image fusion : a practical guide. Boca Raton, FL: CRC Press.

Pope KO, Rejmankova E, Paris JF & Woodruff R 1997. Detecting seasonal flooding cycles in marshes of the Yucatan Peninsula with SIR-C polarimetric radar imagery. *Remote Sensing of Environment* 59: 157-166.

Pradhan B, Hagemann U, Tehrany MS & Prechtel N 2014. An easy to use ArcMap based texture analysis program for extraction of flooded areas from TerraSAR-X satellite image. *Computers & Geosciences* 63: 34-43.

Pradhan B, Sameen MI & Kalantar B 2017. Optimized rule-based flood mapping technique using multitemporal RADARSAT-2 images in the Tropical Region. *IEEE Journal of Selected Topics in Applied Earth Observations and Remote Sensing* 10: 3190-3199.

Pradhan B, Tehrany MS & Jebur MN 2016. A new semiautomated detection mapping of flood extent from TerraSAR-X satellite image using rule-based classification and Taguchi optimization techniques. *IEEE Transactions on Geoscience and Remote Sensing* 54: 4331-4342.

Pricope NG 2013. Variable-source flood pulsing in a semi-arid transboundary watershed: the Chobe River, Botswana and Namibia. *Environmental Monitoring and Assessment* 185: 1883-1906.

Pulvirenti L, Chini M, Marzano FS, Pierdicca N, Mori S, Guerriero L, Boni G & Candela L 2012. Detection of floods and heavy rain using Cosmo-SkyMed data: The event in Northwestern Italy of November 2011. Paper presented at IEEE International Geoscience and Remote Sensing Symposium held 22-27 July 2012. Munich, Germany.

Pulvirenti L, Chini M, Pierdicca N & Boni G 2016a. Use of SAR Data for Detecting Floodwater in Urban and Agricultural Areas: The Role of the Interferometric Coherence. *IEEE Transactions on Geoscience and Remote Sensing* 54: 1532-1544.

Pulvirenti L, Chini M, Pierdicca N, Guerriero L & Ferrazzoli P 2011a. Flood monitoring using multi-temporal COSMO-SkyMed data: Image segmentation and signature interpretation. *Remote Sensing of Environment* 115: 990-1002.

Pulvirenti L, Pierdicca N, Chini M & Guerriero L 2011b. An algorithm for operational flood mapping from synthetic aperture radar (SAR) data using fuzzy logic. *Natural Hazards and Earth System Sciences* 11: 529.

Pulvirenti L, Pierdicca N, Chini M & Guerriero L 2013. Monitoring flood evolution in vegetated areas using COSMO-SkyMed data: The Tuscany 2009 case study. *IEEE Journal of Selected Topics in Applied Earth Observations and Remote Sensing* 6: 1807-1816.

Pulvirenti L, Pierdicca N, Squicciarino G, Boni G, Chini M & Benedetto C 2016b. Polarimetric SAR data for improving flood mapping: An investigation over rice flooded fields. Paper presented at Geoscience and Remote Sensing Symposium (IGARSS) held 10-15 July 2016. Beijing, China.

Qian Y, Zhou W, Yan J, Li W & Han L 2015. Comparing machine learning classifiers for object-based land cover classification using very high resolution imagery. *Remote Sensing* 7: 153-168.

Qiao C, Luo J, Sheng Y, Shen Z, Zhu Z & Ming D 2011. An Adaptive Water Extraction Method from Remote Sensing Image Based on NDWI. *Journal of the Indian Society of Remote Sensing* 40: 421-433.

Rahman H & Dedieu G 1994. SMAC: a simplified method for the atmospheric correction of satellite measurements in the solar spectrum. *International Journal of Remote Sensing* 15: 123-143.

Rahman MS & Di L 2017. The state of the art of spaceborne remote sensing in flood management. *Natural Hazards* 85: 1223-1248.

Ramsey E, Rangoonwala A & Bannister T 2013. Coastal flood inundation monitoring with satellite C-band and L-band synthetic aperture radar data. *JAWRA Journal of the American Water Resources Association* 49: 1239-1260.

Ranchin T & Wald L 2000. Fusion of high spatial and spectral resolution images: the ARSIS concept and its implementation. *Photogrammetric Engineering and Remote Sensing* 66: 49-61.

Rebelo L 2010. Eco-hydrological characterization of inland wetlands in Africa using L-Band SAR. *IEEE Journal of Selected Topics in Applied Earth Observations and Remote Sensing* 3: 554-559.

Refice A, Capolongo D, Pasquariello G, D'Addabbo A, Bovenga F, Nutricato R, Lovergine FP & Pietranera L 2014. SAR and InSAR for flood monitoring: Examples with COSMO-SkyMed data. *IEEE Journal of Selected Topics in Applied Earth Observations and Remote Sensing* 7: 2711-2722.

Revilla-Romero B, Hirpa F, Pozo J, Salamon P, Brakenridge R, Pappenberger F & De Groeve T 2015. On the use of global flood forecasts and satellite-derived inundation maps for flood monitoring in data-scarse regions. *Remote Sensing* 7: 15702.

Rodriguez-Galiano VF, Ghimire B, Rogan J, Chica-Olmo M & Rigol-Sanchez JP 2012. An assessment of the effectiveness of a random forest classifier for land-cover classification. *ISPRS Journal of Photogrammetry and Remote Sensing* 67: 93-104.

Rogers AS & Kearney MS 2004. Reducing signature variability in unmixing coastal marsh Thematic Mapper scenes using spectral indices. *International Journal of Remote Sensing* 25: 2317-2335.

Rokni K, Ahmad A, Selamat A & Hazini S 2014. Water feature extraction and change detection using multitemporal Landsat imagery. *Remote Sensing* 6: 4173-4189.

Rokni K, Ahmad A, Solaimani K & Hazini S 2015. A new approach for surface water change detection: Integration of pixel level image fusion and image classification techniques. *International Journal of Applied Earth Observation and Geoinformation* 34: 226-234.

Sadegh M, Love C, Farahmand A, Mehran A, Tourian M & AghaKouchak A 2017. Multi-sensor remote sensing of drought from space. *Remote Sensing of Hydrological Extremes*, 219-247. Cham: Springer.

Sandholt I, Nyborg L, Fog B, Lô M, Bocoum O & Rasmussen K 2003. Remote sensing techniques for flood monitoring in the Senegal River Valley. *Geografisk Tidsskrift-Danish Journal of Geography* 103: 71-81.

Santoro M, Wegmüller U, Lamarche C, Bontemps S, Defourny P & Arino O 2015. Strengths and weaknesses of multi-year Envisat ASAR backscatter measurements to map permanent open waterbodies at global scale. *Remote Sensing of Environment* 171: 185-201.

Sarker CD, Jia X, Wang L, Fraser D & Lymburner L 2015. Spectral unmixing with estimated adaptive endmember index using extended support vector machine. *Spatial Diversity and Dynamics in Resources and Urban Development*, 37-71. Cham: Springer.

Sarp G & Ozcelik M 2017. Waterbody extraction and change detection using time series: A case study of Lake Burdur, Turkey. *Journal of Taibah University for Science* 11: 381-391.

Sauvola J & Pietikäinen M 2000. Adaptive document image binarization. *Pattern recognition* 33: 225-236.

Schlaffer S, Chini M, Dettmering D & Wagner W 2016. Mapping wetlands in Zambia using seasonal backscatter signatures derived from ENVISAT ASAR time series. *Remote Sensing* 8: 402.

Schlaffer S, Matgen P, Hollaus M & Wagner W 2015. Flood detection from multi-temporal SAR data using harmonic analysis and change detection. *International Journal of Applied Earth Observation and Geoinformation* 38: 15-24.

Schowengerdt RA 2012. *Techniques for image processing and classifications in remote sensing.* New York: Academic Press.

Schumann G, Di Baldassarre G, Alsdorf D & Bates P 2010. Near Real-time (NRT) flood wave approximation on large rivers from space: Application to the River Po, Italy. *Water Resources Research* 46.

Schwertz EL, Spicer BE & Svehlak HT 1977. Near real-time mapping of the 1975 Mississipi River flood in Louisiana using Landsat imagery. *JAWRA Journal of the American Water Resources Association* 13: 107-115.

Settle JJ & Drake NA 1993. Linear mixing and the estimation of ground cover proportions. *International Journal of Remote Sensing* 14: 1159-1177.

Sezgin M & Sankur B 2004. Survey over image thresholding techniques and quantitative performance evaluation. *Journal of Electronic imaging* 13: 146-166.

Shah-Hosseini R, Safari A & Homayouni S 2018. Estimation of natural hazard damages through the fusion of change maps obtained from optical and radar earth observations. *Proceedings* 2: 365.

Shang H, Jia L & Menenti M 2015. Analyzing the inundation pattern of the Poyang Lake floodplain by passive microwave data. *Journal of Hydrometeorology* 16: 652-667.

Shen D, Wang J, Cheng X, Rui Y & Ye S 2015. Integration of 2-D hydraulic model and high-resolution lidar-derived DEM for floodplain flow modeling. *Hydrology and Earth System Sciences* 19: 3605-3616.

Shen L & Li C 2010. Waterbody extraction from Landsat ETM+ imagery using adaboost algorithm. Paper presented at 18th International Conference on Geoinformatics held 18-20 June 2010. Beijing, China.

Shensa MJ 1992. The discrete wavelet transform: wedding the a trous and Mallat algorithms. *IEEE Transactions on Signal Processing* 40: 2464-2482.

Singh KV, Setia R, Sahoo S, Prasad A & Pateriya B 2015. Evaluation of NDWI and MNDWI for assessment of waterlogging by integrating digital elevation model and groundwater level. *Geocarto International* 30: 650-661.

Sisodia PS, Tiwari V & Kumar A 2014a. Analysis of supervised maximum likelihood classification for remote sensing image. Paper presented at Recent Advances and Innovations in Engineering (ICRAIE) held 9-11 May 2014. Jaipur, India.

Sisodia PS, Tiwari V & Kumar A 2014b. A comparative analysis of remote sensing image classification techniques. Paper presented at International Conference on Advances in Computing, Communications and Informatics (ICACCI) held 24-27 September 2014. Delhi, India.

Sivakumar M, Roy P, Harmsen K & Saha S 2004. Satellite remote sensing and GIS applications in agricultural meteorology. Paper presented at the Training Workshop held on 7-11 July 2003. Dehradun, India.

Skakun S 2012. A neural network approach to flood mapping using satellite imagery. *Computing and Informatics* 29: 1013-1024.

Skakun S, Kussul N, Shelestov A & Kussul O 2014. Flood hazard and flood risk assessment using a time series of satellite images: A case study in Namibia. *Risk Analysis* 34: 1521-1537.

Skakun S, Kussul N, Shelestov AY, Lavreniuk M & Kussul O 2016. Efficiency assessment of multitemporal C-Band RADARSAT-2 intensity and Landsat-8 surface reflectance satellite imagery for crop classification in Ukraine. *IEEE Journal of Selected Topics in Applied Earth Observations and Remote Sensing* 9: 3712-3719.

Skidmore AK, Watford F, Luckananurug P & Ryan P 1996. An operational GIS expert system for mapping forest soils. *Photogrammetric Engineering and Remote Sensing* 62: 501-511.

Skidmore AK, Woodgate PW & Richards JA 1986. Classification of the Riverina forests of south east Australia using co-registered Landsat MSS and SIR-B radar data. *Remote sensing for resources development and environmental management. Proc. 7th ISPRS Commission VII symposium, Enschede, 1986. Vol. 1*: 517-519.

Smith RB 2012. Introduction to hyperspectral imaging [online]. Available from http://www.microimages.com/documentation/Tutorials/hyprspec.pdf [Accessed 3 June 2018].

Song C, Huang B, Ke L & Richards KS 2014. Remote sensing of alpine lake water environment changes on the Tibetan Plateau and surroundings: A review. *ISPRS Journal of Photogrammetry and Remote Sensing* 92: 26-37.

Song Y-S, Sohn H-G & Park C-H 2007. Efficient water area classification using RADARSAT-1 SAR imagery in a high relief mountainous environment. *Photogrammetric Engineering & Remote Sensing* 73: 285-296.

Srivastava HS, Patel P, Sharma Y & Navalgund RR 2009. Multi-frequency and multi-polarized SAR response to thin vegetation and scattered trees. *Current Science (00113891)* 97.

Stagakis S, Vanikiotis T & Sykioti O 2016. Estimating forest species abundance through linear unmixing of CHRIS/PROBA imagery. *ISPRS Journal of Photogrammetry and Remote Sensing* 119: 79-89.

Steinwart I & Christmann A 2008. *Support vector machines.* Cham: Springer Science & Business Media.

Sun D, Yu Y & Goldberg MD 2011. Deriving water fraction and flood maps from MODIS images using a decision tree approach. *IEEE Journal of Selected Topics in Applied Earth Observations and Remote Sensing* 4: 814-825.

Sun F, Sun W, Chen J & Gong P 2012. Comparison and improvement of methods for identifying waterbodies in remotely sensed imagery. *International Journal of Remote Sensing* 33: 6854-6875.

Tanguy M, Chokmani K, Bernier M, Poulin J & Raymond S 2017. River flood mapping in urban areas combining RADARSAT-2 data and flood return period data. *Remote Sensing of Environment* 198: 442-459.

Tehrany MS, Pradhan B & Jebur MN 2014. Flood susceptibility mapping using a novel ensemble weights-of-evidence and support vector machine models in GIS. *Journal of Hydrology* 512: 332-343.

Tehrany MS, Pradhan B & Jebuv MN 2014. A comparative assessment between object and pixel-based classification approaches for land use/land cover mapping using SPOT 5 imagery. *Geocarto International* 29: 351-369.

Tempfli K, Huurneman G, Bakker W, Janssen LL, Feringa W, Gieske A, Grabmaier K, Hecker C, Horn J & Kerle N 2009. *Principles of remote sensing: an introductory textbook. (ITC Educational Textbook Series).* Enschede: ITC.

Teng J, Jakeman AJ, Vaze J, Croke BFW, Dutta D & Kim S 2017. Flood inundation modelling: A review of methods, recent advances and uncertainty analysis. *Environmental Modelling & Software* 90: 201-216.

Thanh Noi P & Kappas M 2018. Comparison of random forest, k-nearest neighbour, and support vector machine classifiers for land cover classification using Sentinel-2 imagery. *Sensors* 18: 18.

Thomas RF, Kingsford RT, Lu Y, Cox SJ, Sims NC & Hunter SJ 2015. Mapping inundation in the heterogeneous floodplain wetlands of the Macquarie Marshes, using Landsat Thematic Mapper. *Journal of Hydrology* 524: 194-213.

Thomas RF, Kingsford RT, Lu Y & Hunter SJ 2011. Landsat mapping of annual inundation (1979–2006) of the Macquarie Marshes in semi-arid Australia. *International Journal of Remote Sensing* 32: 4545-4569.

Tiner RW, Lang MW & Klemas VV 2015. *Remote sensing of wetlands: applications and advances.* Boca Raton: CRC Press.

Torbick N & Salas W 2015. Mapping agricultural wetlands in the Sacramento Valley, USA with satellite remote sensing. *Wetlands Ecology and Management* 23: 79-94.

Townsend PA 2001. Mapping seasonal flooding in forested wetlands using multi-temporal RADARSAT. *Photogrammetric engineering and remote sensing* 67: 857-864.

Townsend PA & Walsh SJ 1998. Modeling floodplain inundation using an integrated GIS with RADAR and optical remote sensing. *Geomorphology* 21: 295-312.

Töyrä J, Pietroniro A & Martz LW 2001. Multisensor hydrologic assessment of a freshwater wetland. *Remote Sensing of Environment* 75: 162-173.

Töyrä J, Pietroniro A, Martz LW & Prowse TD 2002. A multi-sensor approach to wetland flood monitoring. *HYP Hydrological Processes* 16: 1569-1581.

Traore SB, Ali A, Tinni SH, Samake M, Garba I, Maigari I, Alhassane A, Samba A, Diao MB, Atta S, Dieye PO, Nacro HB & Bouafou KGM 2014. AGRHYMET: A drought monitoring and capacity building center in the West Africa Region. *Weather and Climate Extremes* 3: 22-30.

Tsyganskaya V, Martinis S, Marzahn P & Ludwig R 2018a. Detection of temporary flooded vegetation using Sentinel-1 time series data. *Remote Sensing* 10: 1286.

Tsyganskaya V, Martinis S, Marzahn P & Ludwig R 2018b. SAR-based detection of flooded vegetation – a review of characteristics and approaches. *International Journal of Remote Sensing* 39: 2255-2293.

Tu T-M, Su S-C, Shyu H-C & Huang PS 2001. A new look at IHS-like image fusion methods. *Information fusion* 2: 177-186.

Tulbure MG & Broich M 2013. Spatiotemporal dynamic of surface water bodies using Landsat time-series data from 1999 to 2011. *ISPRS Journal of Photogrammetry and Remote Sensing* 79: 44-52.

Twele A, Cao W, Plank S & Martinis S 2016. Sentinel-1-based flood mapping: a fully automated processing chain. *International Journal of Remote Sensing* 37: 2990-3004.

UNICEF 2012. Extreme flooding causes grave danger, Namibia [online]. Available from http://www.unicef.org/infobycountry/namibia_namibian_floods.html [Accessed 27 September 2017].

Van der Waal B 1990. Aspects of the fishery of the Eastern Caprivi, Namibia. *Madoqua* 17: 1-16.

Van Niekerk A & Joubert SJ 2011. Input variable selection for interpolating high-resolution climate surfaces for the Western Cape. *Water SA* 37.

Vapnik V 2013. *The nature of statistical learning theory*. Cham: Springer science & business media.

Verhulp J & Van Niekerk A 2017. Transferability of decision trees for land cover classification in a heterogeneous area. *South African Journal of Geomatics* 6: 30-46.

Verpoorter C, Kutser T & Tranvik L 2012. Automated mapping of water bodies using Landsat multispectral data. *Limnology and Oceanography: Methods* 10: 1037-1050.

Vikhamar D & Solberg R 2003. Snow-cover mapping in forests by constrained linear spectral unmixing of MODIS data. *Remote Sensing of Environment* 88: 309-323.

Vivone G, Alparone L, Chanussot J, Dalla Mura M, Garzelli A, Licciardi GA, Restaino R & Wald L 2015. A critical comparison among pansharpening algorithms. *IEEE Transactions on Geoscience and Remote Sensing* 53: 2565-2586.

Wang F, Koopmans BN & Pohl C 1996. The 1995 Flood in the Netherlands monitored from Space-a multisensor approach. *Euopean Space Agency-Publications-ESA SP* 383: 469-472.

Wang Q, Shi W, Li Z & Atkinson PM 2016. Fusion of Sentinel-2 images. *Remote Sensing of Environment* 187: 241-252.

Wang R-Q, Mao H, Wang Y, Rae C & Shaw W 2018. Hyper-resolution monitoring of urban flooding with social media and crowdsourcing data. *Computers & Geosciences* 111: 139-147.

Wang S, Baig MHA, Zhang L, Jiang H, Ji Y, Zhao H & Tian J 2015. A simple enhanced water index (EWI) for percent surface water estimation using Landsat data. *IEEE Journal of Selected Topics in Applied Earth Observations and Remote Sensing* 8: 90-97.

Wang Y, Colby JD & Mulcahy KA 2002. An efficient method for mapping flood extent in a coastal floodplain using Landsat TM and DEM data. *International Journal of Remote Sensing* 23: 3681-3696.

Wang Y, Hess LL, Filoso S & Melack JM 1995. Understanding the radar backscattering from flooded and nonflooded Amazonian forests: Results from canopy backscatter modeling. *Remote Sensing of Environment* 54: 324-332.

Wei X, Li Q, Zhang M, Giles-Hansen K, Liu W, Fan H, Wang Y, Zhou G, Piao S & Liu S 2017. Vegetation cover—another dominant factor in determining global water resources in forested regions. *Global change biology*.

Welch R 1987. Merging multiresolution SPOT HRV and Landsat TM data. *Photogrammetric Engineering & Remote Sensing* 53: 301-303.

Westra T, Wulf RD, Coillie FV & Crabbe S 2010. Optimal Envisat advanced synthetic aperture radar image parameters for mapping and monitoring Sahelian floodplains. *Journal of Applied Remote Sensing* 4: 04-35.

White JM & Rohrer GD 1983. Image thresholding for optical character recognition and other applications requiring character image extraction. *IBM Journal of research and development* 27: 400-411.

White L, Brisco B, Dabboor M, Schmitt A & Pratt A 2015. A collection of SAR methodologies for monitoring wetlands. *Remote Sensing* 7: 7615.

White L, Brisco B, Pregitzer M, Tedford B & Boychuk L 2014. RADARSAT-2 beam mode selection for surface water and flooded vegetation mapping. *Canadian Journal of Remote Sensing* 40: 135-151.

Whyte A, Ferentinos KP & Petropoulos GP 2018. A new synergistic approach for monitoring wetlands using Sentinels -1 and 2 data with object-based machine learning algorithms. *Environmental Modelling & Software* 104: 40-54.

Wiesnet DR, McGinnis DF & Pritchard JA 1974. Mapping of the 1973 Mississippi river floods by the NOAA-2 satellite. *JAWRA Journal of the American Water Resources Association* 10: 1040-1049.

Wilson EH & Sader SA 2002. Detection of forest harvest type using multiple dates of Landsat TM imagery. *Remote Sensing of Environment* 80: 385-396.

Winkler K, Gessner U & Hochschild V 2017. Identifying droughts affecting agriculture in Africa based on remote sensing time series between 2000–2016: Rainfall anomalies and vegetation condition in the context of ENSO. *Remote Sensing* 9: 831.

Woodhouse IH 2017. *Introduction to microwave remote sensing.* Cham: CRC press.

Wooldridge J 2003. Geology and terroir in the Western Cape winelands. *Wineland, décembre*: 85-87.

Xiao X, Boles S, Liu J, Zhuang D, Frolking S, Li C, Salas W & Moore Iii B 2005. Mapping paddy rice agriculture in southern China using multi-temporal MODIS images. *Remote Sensing of Environment* 95: 480-492.

Xie H, Luo X, Xu X, Pan H & Tong X 2016a. Automated subpixel surface water mapping from heterogeneous urban environments using Landsat 8 OLI imagery. *Remote Sensing* 8: 584.

Xie H, Luo X, Xu X, Pan H & Tong X 2016b. Evaluation of Landsat 8 OLI imagery for unsupervised inland water extraction. *International Journal of Remote Sensing* 37: 1826-1844.

Xu H 2006. Modification of normalised difference water index (NDWI) to enhance open water features in remotely sensed imagery. *International Journal of Remote Sensing* 27: 3025-3033.

Yan K, Di Baldassarre G, Solomatine DP & Schumann GJP 2015. A review of low-cost space-borne data for flood modelling: topography, flood extent and water level. *Hydrological Processes* 29: 3368-3387.

Yang C, Everitt JH, Du Q, Luo B & Chanussot J 2013. Using high-resolution airborne and satellite imagery to assess crop growth and yield variability for precision agriculture. *Proceedings of the IEEE* 101: 582-592.

Yang J & Du X 2017. An enhanced water index in extracting water bodies from Landsat TM imagery. *Annals of GIS* 23: 141-148.

Yang X & Chen L 2017. Evaluation of automated urban surface water extraction from Sentinel-2A imagery using different water indices.

Yang X, Zhao S, Qin X, Zhao N & Liang L 2017. Mapping of urban surface water bodies from Sentinel-2 MSI Imagery at 10 m resolution via NDWI-based image sharpening. *Remote Sensing* 9: 596.

Yanowitz SD & Bruckstein AM 1989. A new method for image segmentation. *Computer Vision, Graphics, and Image Processing* 46: 82-95.

Yesou H, Pottier E, Mercier G, Grizonnet M, Haouet S, Giros A, Faivre R, Huber C & Michel J 2016. Synergy of Sentinel-1 and Sentinel-2 imagery for wetland monitoring information extraction from continuous flow of sentinel images applied to water bodies and vegetation mapping and monitoring. Paper presented at Geoscience and Remote Sensing Symposium (IGARSS) held 10-15 July 2016. Beijing, China.

Yu J, Chen D, Lin Y & Ye S 2017. Comparison of linear and nonlinear spectral unmixing approaches: a case study with multispectral TM imagery. *International Journal of Remote Sensing* 38: 773-795.

Zhai K, Wu X, Qin Y & Du P 2015. Comparison of surface water extraction performances of different classic water indices using OLI and TM imageries in different situations. *Geo-spatial Information Science* 18: 32-42.

Zhang F, Zhu X & Liu D 2014. Blending MODIS and Landsat images for urban flood mapping. *International Journal of Remote Sensing* 35: 3237-3253.

Zhang J 2010. Multi-source remote sensing data fusion: status and trends. *International Journal of Image and Data Fusion* 1: 5-24.

Zhang M, Zeng Y, Huang W & Li S 2018. Combining spatiotemporal fusion and object-based image analysis for improving wetland mapping in complex and heterogeneous urban landscapes. *Geocarto International*: 1-29.

Zhang R, Sun D, Yu Y & Goldberg MD 2012a. Mapping nighttime flood from MODIS observations using support vector machines. *Photogrammetric Engineering & Remote Sensing* 78: 1151-1161.

Zhang X-K, Zhang X, Lan Q & Baig MHA 2012b. Automated detection of coastline using Landsat TM based on water index and edge detection methods. Paper presented at Second International Workshop on Earth Observation and Remote Sensing Applications held 8-11 June 2012. Shanghai, China.

Zhang X, Cui J, Wang W & Lin C 2017. A study for texture feature extraction of high-resolution satellite images based on a direction measure and gray level co-occurrence matrix fusion algorithm. *Sensors* 17: 1474.

Zhao G, Pang B, Xu Z, Yue J & Tu T 2018. Mapping flood susceptibility in mountainous areas on a national scale in China. *Science of The Total Environment* 615: 1133-1142.

Zhao L, Yang J, Li P & Zhang L 2014. Seasonal inundation monitoring and vegetation pattern mapping of the Erguna floodplain by means of a RADARSAT-2 fully polarimetric time series. *Remote Sensing of Environment* 152: 426-440.

Zheng B, Myint SW, Thenkabail PS & Aggarwal RM 2015. A support vector machine to identify irrigated crop types using time-series Landsat NDVI data. *International Journal of Applied Earth Observation and Geoinformation* 34: 103-112.

Zhou Y, Dong J, Xiao X, Xiao T, Yang Z, Zhao G, Zou Z & Qin Y 2017. Open surface water mapping algorithms: A comparison of water-related spectral indices and sensors. *Water* 9: 256.

Zurita-Milla R, Gómez-Chova L, Guanter L, Clevers JG & Camps-Valls G 2011. Multitemporal unmixing of medium-spatial-resolution satellite images: A case study using MERIS images for land-cover mapping. *IEEE Transactions on geoscience and remote sensing* 49: 4308-4317.

APPENDIX

CONFUSION MATRICES

Table A. 1 NDWI confusion matrix

	Water	Trees & shrubs	Bare & built	Grass	Shadow	TOTALS	PA*%	EO†%
Water	3607	69	88	54	183	4160	86.7	13.3
Trees & shrubs	67	2645	123	326	68	3329	79.5	20.5
Bare & built	104	87	4162	189	248	4990	83.4	16.6
Grass	27	458	101	1794	66	2496	71.9	28.1
Shadow	119	38	62	21	1425	1665	85.6	14.4
TOTALS	3924	3297	4536	2384	1990	16640		
CA‡%	91.9	80.2	91.7	75.3	71.6			
EC§%	8.1	19.8	8.3	24.7	28.4			
Overall accuracy	**81.6**							
Overall kappa	**0.76**							

*PA = Producer's accuracy; †EO = Errors of omission; ‡CA = Consumer's accuracy; EC = Errors of commission

Table A. 2 VH Band confusion matrix

	Water	Trees & shrubs	Bare & built	Grass	Shadow	TOTALS	PA*%	EO†%
Water	3597	83	79	89	262	4110	86.5	13.5
Trees & shrubs	88	2679	60	218	284	3329	80.5	19.5
Bare & built	179	193	3805	381	145	4703	76.3	23.7
Grass	41	303	158	1920	49	2471	76.9	23.1
Shadow	168	104	162	63	1168	1665	70.1	29.9
TOTALS	4073	3362	4264	2671	1908	16640		
CA‡%	88.3	79.7	89.2	71.9	61.2			
EC§%	11.7	20.3	10.8	28.1	38.8			
Overall accuracy	**77.7**							
Overall kappa	**0.71**							

*PA = Producer's accuracy; †EO = Errors of omission; ‡CA = Consumer's accuracy; EC = Errors of commission

Table A. 3 MNDWI confusion matrix

	Water	Trees & shrubs	Bare & built	Grass	Shadow	TOTALS	PA*%	EO†%
Water	3271	85	189	56	469	4160	83.5	16.5
Trees & shrubs	69	2879	97	128	56	3329	78.2	21.8
Bare & built	90	126	4271	147	186	4990	73.8	26.2
Grass	49	401	93	1625	48	2496	74.1	25.9
Shadow	463	49	97	89	857	1665	70.2	29.8
TOTALS	3942	3540	4747	2045	1616			
CA‡%	83	81.3	89	79.5	53			
EC§%	17	18.7	11	20.5	47			
Overall accuracy	**73.8**							
Overall kappa	**0.69**							

*PA = Producer's accuracy; †EO = Errors of omission; ‡CA = Consumer's accuracy; EC = Errors of commission